SGP-TR-199

Modeling and Characterization of Hydraulic Stimulation and Induced Seismicity in Geothermal and Shale Gas Reservoirs

Mark McClure

December 2012

Stanford Geothermal Program
Interdisciplinary Research in
Engineering and Earth Sciences
STANFORD UNIVERSITY
Stanford, California

Abstract

The classical concept of hydraulic fracturing is that large, wing-shaped tensile fractures propagate away from the wellbore. However, in low matrix permeability settings such as Enhanced Geothermal Systems (EGS) and gas shale, hydraulic fracturing creates complex networks that may contain both newly formed fractures and stimulated natural fractures.

In this research, the overall approach has been to integrate field observations, laboratory observations, and understanding of fundamental physical processes into computational modeling that is specifically designed for complex hydraulic fracturing and to apply the modeling to develop deeper understanding and to solve practical problems.

A computational model was developed that coupled fluid flow, stresses induced by fracture opening and sliding, transmissivity coupling to deformation, friction evolution, and fracture propagation in two-dimensional discrete fracture networks. The model is efficient enough to simulate networks with thousands of fractures. A variety of novel techniques were developed to enable the model to be accurate, efficient, realistic, and convergent to discretization refinement in time and space. Testing demonstrated that simulation results are affected profoundly by the stresses induced by fracture deformation, justifying the considerable effort required to include these stresses in the model.

Four conceptual models were formulated that represent the main hypotheses about stimulation mechanism from the literature of hydraulic fracturing. We refer to the stimulation mechanisms as Pure Opening Mode (POM), Pure Shear Stimulation (PSS),

Mixed-Mechanism Stimulation (MMS), and Primary Fracturing with Shear Stimulation Leakoff (PFSSL). Computational models were used to investigate the properties of each mechanism. Geological factors that affect stimulation mechanism were identified. Techniques for diagnosing stimulation mechanism were devised that incorporate interpretation of bottom hole pressure during injection, shut-in, and production, microseismic relocations, and wellbore image logs. A Tendency to Shear Stimulation (TSS) test was proposed as a way to help diagnose the mechanism by unambiguously measuring a formation's ability to experience shear stimulation. Modeling results suggested several potential sources for error in estimation of the least principal stress in low matrix permeability settings. The Crack-like Shear Stimulation (CSS) mechanism was identified as a potentially important physical process that may control the spreading of shear stimulation through the interaction of fluid flow, deformation, and slip-transmissivity coupling.

The computational model also has the capability to couple fluid flow with rate and state earthquake simulation. The model was used to investigate the interaction of fluid flow, permeability evolution, and induced seismicity during injection into a single large fault. Using the model, a variety of observations about induced seismicity in EGS were explained. Producing fluid back after injection and gradually reducing injection pressure during stimulation were identified as strategies for minimizing induced seismicity.

A review of historical EGS projects demonstrated that the severity of induced seismicity has been correlated to the degree of brittle fault zone development in the interval of injection. The fracture networks at each project were categorized along a continuum from thick, porous fault zones to thin cracks. Observations from specific EGS projects fell across the full continuum, a result that has implications not only for induced seismicity, but for fractured reservoirs in general.

A pressure transient analysis was performed using data from the EGS project at Soultz-sous-Forêts. At Soultz, fluid injection induced slip and transmissivity enhancement in large fault zones. The pressure transient analysis showed that these fault zones are best described as slabs of single porosity, single permeability material. Evidence of dual porosity behavior was not found.

Acknowledgements

Thank you to my advisor Dr. Roland Horne. Roland has been tirelessly supportive and always pushed to get the best out of me. Not only has Roland been a tremendous mentor for research, he has had a profoundly positive influence on the direction that my life has taken over the years. I do not think that you could ask for more from an advisor.

There have been many people who have been very generous to meet with me informally as I have pursued my PhD and let me tap into their knowledge and expertise. First, thank you to Dr. Mark Zoback and Dr. David Pollard, who I met with particularly frequently and have been very influential. Also thank you to Dr. Eric Dunham, Dr. Paul Segall, and Dr. Hamdi Tchelepi.

Thank you to Dr. Pollard for providing the code COMP2DD, which was used to verify the accuracy of the model used in Chapter 2. Thank you to Dr. Dunham for providing an earthquake simulation code that was used to verify the accuracy of the model used in Chapter 4.

Dr. Andrew Bradley was influential in the development of the modeling described in Chapters 2, 3, and 4. Most importantly, his matrix multiplication code Hmmvp is integrated into the simulator used in Chapters 2 and 3, and it plays a crucial role in making the simulator efficient. Not only was he very generous to share his code, he modified it so that it could be better integrated with the simulator, and he spent time helping me to implement it.

Thank you to Dr. Albert Genter and Dr. Nicolas Cuenot for supplying the data from the Soultz EGS project that was used in Chapter 6. In gathering information for Chapter 5, I contacted several people from around the world who supplied me with data,

Table of Contents

List of Tables

List of Figures

Chapter 1

1 Introduction

1.1 Background

Hydraulic fracturing is used widely in the exploitation of oil, gas, and geothermal resources (Beckwith, 2010; Tester, 2007). In some settings, hydraulic fracturing is used to improve the connection between a well and a productive reservoir (Martin and Economides, 2010). In other settings, hydraulic fracturing is used to engineer the reservoir, creating or stimulating fractures in a low permeability matrix. Two examples of the latter case are gas shale stimulation (Bowker, 2007; Warpinski et al., 2009; King, 2010) and Enhanced Geothermal Systems, or "EGS" (Tester, 2007).

This research was concerned with modeling and characterization of the fracturing process during hydraulic stimulation in very low matrix permeability settings such as EGS and gas shale. It is natural to consider hydraulic stimulation in very low matrix permeability rock separately from stimulation in other settings. In most settings, fracturing during hydraulic stimulation is typically conceptualized as one (or perhaps a few) large, continuous, opening mode fractures propagating through the wellbore (Smith and Shlyapobersky, 2000). In very low permeability rock, the process of stimulation is typically conceptualized as a complex network of newly forming fractures and/or natural

fractures that slip and open (Fisher et al., 2004; Bowker, 2007; Gale et al., 2007; Cipolla et al., 2008; King, 2010; Pine and Batchelor, 1984; Murphy and Fehler, 1986; Brown, 1989; Ito, 2003; Ito and Hayashi, 2003; Evans, Moriya, et al., 2005; Ledésert et al., 2010).

The two main examples of stimulation in very low matrix permeability, EGS and gas shale, have significant importance to global energy and environmental issues. Gas shale production has grown tremendously in the past decade. Gas shale is now major source of energy in the United States, and production is expected to increase dramatically worldwide (Moniz, 2011). EGS has been a topic of research for decades, and currently several companies are attempting to produce electricity from EGS commercially. However, at present, EGS has not reached its potential for contributing significantly to the energy sector because wells with economically sufficient productivity have not yet been demonstrated (Tester, 2007).

Historically, production of gas shale was limited because shale has very low permeability, and wells drilled into shale formations were unproductive. However, in the past ten to twenty years, horizontal drilling and improved techniques for hydraulic fracturing have changed the economics of gas shale production. Horizontal drilling allows extended laterals do be drilled through shale formations, increasing contact between the wellbore and the reservoir. Hydraulic fracturing further increases connectivity to the formation by creating or stimulating fractures that act as conduits for flow, allowing gas to flow to the wellbore from more distant volumes of rock. Improvements in gas shale stimulation design over the past two decades have included zonal isolation for multiple stage stimulation and the use of slickwater and lower volumes of proppant, which increases fracture network surface area and reduces cost (King, 2010).

The concept of Enhanced Geothermal Systems (EGS) was devised as a way to increase the magnitude of economically recoverable geothermal resources. To produce geothermal energy, it is necessary to have high formation temperature, sufficient fluid to carry heat from the reservoir, and high formation permeability to transport the fluid through the subsurface at a high flow rate. Temperatures high enough to produce geothermal electricity are present within a depth of 5 km (reasonable for conventional

drilling) across a significant percentage of the Earth's surface. However, in most places, permeability adequate to achieve economic production is not present at those depths. The concept of EGS is to use hydraulic fracturing to generate permeability, and then circulate fluid in a closed loop between injector and production wells. Since the concept was first demonstrated by researchers at Los Alamos National Laboratory at Fenton Hill, New Mexico in the 1970s, EGS projects have been pursued around at the world at sites such as Rosemanowes, UK, Ogachi, Japan, Hijiori, Japan, Soultz-sous-Forêts, France, Cooper Basin, Australia, and Desert Peak, USA. These projects have demonstrated technical feasibility of EGS, but so far have not demonstrated the high, sustained flow rates needed for economic feasibility (Tester, 2007).

EGS does not typically involve emission of greenhouse gases (Tester, 2007), and electricity production from natural gas emits significantly less CO_2 than from coal (Moniz, 2011), though the latter point has been the subject of recent controversy over the issue of how much methane leaks during drilling, completion, and extraction (Howarth et al., 2011; Cathles et al., 2012). Because natural gas and EGS are abundant, widespread energy sources, they can contribute to energy independence for a variety of countries around the world, including the United States. A potential application for natural gas is in automobile transportation, which would reduce reliance on oil (Moniz, 2011).

Both EGS and gas shale need to be developed responsibly. Concerns that gas shale hydraulic fracturing could lead to groundwater contamination have been raised (Moniz, 2011). In EGS, induced seismicity has been a persistent issue, though it has never caused more than very minor property damage (Majer et al., 2007).

There are significant opportunities for research into hydraulic fracture modeling to contribute to the fields of EGS and natural gas shale. For EGS to become economically viable, stimulation design needs to be improved so that higher flow rates can be achieved through the subsurface with lower (or zero) energy consumption from pumping. Furthermore, fracture networks must be created that achieve good heat sweep efficiency and prevent short-circuiting of cold injected water.

In order to manage concerns about induced seismicity, better methods are needed for prediction and mitigation of seismic hazard. Induced seismicity is an important issue for

EGS (Majer et al., 2007; Cladouhos et al., 2010), oil and gas hydraulic fracturing (Holland, 2011; Baisch and Vörös, 2011), CO_2 sequestration (Cappa and Rutqvist, 2011; Nicol et al., 2011; Zoback and Gorelick, 2012), and other settings (McGarr et al., 2002).

Natural gas shale has already been proven to be economic, but further gains in productivity and efficiency could be made. Potential applications of modeling include stimulation optimization, formation evaluation, and prediction of future production.

1.2 Modeling Philosophy

The challenges of performing computational modeling of hydraulic stimulation in EGS and gas shale are both conceptual and technical. These challenges are connected, and this research attempts to make contributions from both perspectives.

Conceptually, the challenge of stimulation modeling is that fracturing and permeability generation occur deep in the earth and cannot be observed directly. Direct observational data (such as core, image logs, or production logs) are limited in spatial extent to the wellbore. Data sources that interrogate the full spatial domain of the reservoir (such as microseismic or pressure transients) are indirect, incomplete, potentially inaccurate, and require interpretation that relies on assumptions that may or may not be well founded. Because of these difficulties, it is a major challenge to answer a basic question: "what physical processes contribute to stimulation and fluid storage during hydraulic fracturing?" Because of the data limitations, nonuniqueness is a major problem. A great variety of models or explanations might be constructed that are consistent with the limited available data.

Technically, the challenge of stimulation modeling is that a great variety of physical processes are taking place at different scale in a discontinuous and complex spatial domain. As in all modeling, a tradeoff exists between realism (including physical processes and spatial detail) and feasibility (CPU time and memory). An important choice in this dissertation has been to use discrete fracture network (DFN) modeling, in which distinct, individual fractures are included in the stimulation model. In contrast to DFN models, Effective Continuum Models (ECM) use volumetric discretizations that

average physical properties within a Representative Elemental Volume (REV). With DFN modeling, the processes of hydraulic fracturing can be described in greater detail, but DFN modeling is significantly more computationally intensive.

The technical and conceptual challenges of stimulation modeling are closely linked. Modeling can be used to develop improved understanding, yet models require an adequate understanding of the process to be modeled. In performing the research for this dissertation, the following process was followed. First, gather available data from field scale hydraulic fracturing projects, both direct wellbore observations and indirect field scale observations. Second, consider all important physical processes and determine how these processes have already been characterized in the literature, either through fundamental physical laws, laboratory experiments, geological outcrop studies, or modeling. In many aspects, the fundamental physical processes governing hydraulic stimulation are understood reasonably well, at least to a first degree of approximation. Third, using the direct observations from field scale projects, understanding of the relevant physical processes and ideas already present in the literature, develop a hypothesis or collection of hypotheses about the overall mechanisms taking place during hydraulic stimulation. Fourth, construct a computational model that is consistent with the conceptual hypothesis (or hypotheses) and that includes all physical processes that are expected to have a first order effect on the results (keeping in mind that different processes are important depending on conclusions drawn from the model). Fifth, perform forward simulations with computational model and determine whether the results are consistent with the available field scale observations. Sixth, apply the model to answer useful questions: How do the various processes interact? How do the processes affect the results? If model results are not consistent with field scale observation, why not? Can the results be used to confirm or refute various hypotheses? Hypotheses can never be proven with complete certainty, but consistency with observation increases the probability that they are correct (Oreskes et al., 1994), or at least useful. Seventh, if a hypothesis about conceptual model is tentatively accepted, apply the model for practical applications such as optimization of stimulation design.

1.3 Scope of Work

In Chapter 2, the details of the stimulation model used in Chapter 3 are described, and results from testing and verification are presented. The model couples fluid flow, stresses induced by fracture deformation, transmissivity, and friction evolution in two-dimensional discrete fracture networks. New methods of solution and specialized techniques were developed to ensure model efficiency and realistic behavior. The modeling code is perhaps the most efficient currently in existence that fully couples fluid flow with stresses induced by fracture sliding and opening in a discrete fracture network. In the past, the primary limitation of coupled fluid flow-deformation discrete fracture models has been that problem size was limited. Chapter 2 demonstrates that the modeling code is able to model problems with thousands of fractures efficiently. Simulation results from Chapter 2 demonstrate the profound effect of induced stresses on model behavior.

In Chapter 3, four hypotheses about the mechanism of hydraulic stimulation are presented: pure opening mode (POM), pure shear stimulation (PSS), mixed-mechanism stimulation (MMS), and primary fracturing with shear stimulation leakoff (PFSSL). A computational model was used to perform simulations representative of each hypothesis, and their properties were investigated. Based on results from the modeling and review of the literature, geological processes were identified that may affect stimulation mechanism. Techniques were demonstrated that could be used in practice to diagnose stimulation mechanism. These techniques involve interpretation of down hole pressure during injection, shut-in, and production, microseismic relocations, and wellbore image logs. A Tendency for Shear Stimulation (TSS) test is proposed as a way to directly measure the ability of a formation to experience shear stimulation and to help diagnose mechanism. A variety of processes were identified that could cause incorrect interpretation of the least principal stress in low matrix permeability settings. An important physical process was investigated, crack-like shear stimulation (CSS), that had a fundamental effect on the simulation results in Chapters 2, 3, and 4. Simulations showed that the CSS mechanism could allow stimulation to propagate at a rate insensitive

to the initial formation diffusivity, a result that is in contrast to assumptions sometimes made in the literature.

A key idea in Chapter 3 is that uncertainty and disagreement exists about the correct conceptual model for stimulation mechanism in EGS and gas shale. This uncertainty is very important because assumptions about the mechanism of stimulation affect every aspect of reservoir engineering, modeling, and formation evaluation. The diagnostic methodologies and conceptual ideas described in Chapter 3 will lead to a better fundamental understanding of hydraulic fracturing in low matrix permeability settings. Chapter 3 is an attempt to answer the basic question: "what is going on during hydraulic stimulation?"

The model used in Chapter 4 couples fluid flow, fracture deformation, and rate and state friction evolution. The model was used to explain post-injection seismicity, increasing event magnitude over the course of stimulation, and the tendency for hypocenters to be located at the edge of the stimulated region. The idea of crack-like shear stimulation was further explored, and it was shown how CSS can occur smoothly or episodically, depending on whether slip is seismic or aseismic. Two techniques were found that could be used to reduce the severity of induced seismicity from stimulation: producing fluid back after injection and gradually decreasing injection pressure over time. Overall, this chapter shows the utility of coupling earthquake modeling with fluid flow modeling. Further research on this topic could lead to improved insight into the processes of induced seismicity, practical recommendations for mitigation, and improved estimations of induced seismicity hazard analysis.

In Chapter 5, a review of historical EGS projects is summarized. The most important result of Chapter 5 is that there is a striking variability in fault thickness between different projects. In some EGS projects, meters thick, porous fault zones are present. In other EGS projects, the thickest fractures are cracks millimeters thick. It was found that the severity of induced seismicity at historical EGS projects was correlated directly with the observed degree of brittle fault zone development. Degree of brittle fault zone development is not the only variable that affects induced seismicity hazard, but our result confirms that it is an important variable to include in hazard analysis. Aside from

induced seismicity, the results have broad implications for reservoir and stimulation engineering in fractured reservoirs because they demonstrate that qualitatively different types of "fractures" are found in different EGS reservoirs.

In Chapter 6, a pressure transient analysis study is described that used data from the EGS project at Soultz, France. At Soultz, fluid flow and deformation is localized into relatively large scale fault zones. Three alternative hypotheses were developed regarding the distribution of the permeability and porosity within the fault zones. It was found that the observed pressure transients were most consistent with the idea that individual fault zones are effectively a single porosity, single permeability medium. The alternative hypothesis, which was not found to be consistent with the data, was that the fault zones could be considered dual porosity features, with high transmissivity fractures leaking off into a porous, high storativity damage zones.

Variable definitions are given in Table 7-1.

Chapter 2

2 Modeling Methodology, Validation, and Testing

This chapter describes the development and testing of a model that couples fluid-flow, deformation, friction weakening, and permeability evolution in large, complex two-dimensional discrete fracture networks. The model can be used to explore the behavior of hydraulic stimulation in settings where matrix permeability is low and preexisting fractures play an important role, such as Enhanced Geothermal Systems and gas shale. The model can be used to describe pure shear stimulation, mixed-mechanism stimulation, or pure opening-mode stimulation. Convergence to grid refinement was demonstrated, and simulation settings required for acceptable accuracy were identified. A variety of novel techniques to ensure efficiency and realistic model behavior were conceived, implemented, and tested. It was demonstrated that the simulation methodology can also be used as an efficient method for directly solving quasistatic fracture contact problems. Demonstration results show how stresses induced by fracture deformation during stimulation directly impact the mechanism of propagation and the resulting fracture network. The model assumes that flow is single-phase, isothermal, matrix permeability is negligible, and deformation is small strain in an infinite, homogeneous, linearly elastic

medium. The model requires the paths of newly forming tensile fractures to be specified in advance, a limitation that could be overcome in future development.

2.1 Introduction

Computational modeling of hydraulic fracturing can be used for stimulation optimization, long term production forecasting, basic research into fundamental mechanisms, and investigation of novel techniques. However, modelers face daunting challenges: a variety of complex physical processes, limited and imperfect information, and a heterogeneous and discontinuous spatial domain. Because of these difficulties, it is necessary to make trade-offs between efficiency, spatial resolution, and inclusion of physical processes.

The classical conceptual model of hydraulic fracturing is that a single opening-mode fracture propagates away from the wellbore (Khristianovich and Zheltov, 1955; Perkins and Kern, 1961; Geertsma and de Klerk, 1969; Nordgren, 1972). This conceptual model is still used in hydraulic fracturing design and modeling in conventional settings (Economides and Nolte, 2000; Meyer & Associates, 2011; Adachi et al., 2007). However, in settings with complex fracture networks, classical hydraulic fracturing models may be overly simplified.

This chapter describes the development and testing of a two-dimensional hydraulic stimulation model that has been developed specifically for simulating hydraulic fracturing in settings with very low matrix permeability and where preexisting fractures play an important role, such as Enhanced Geothermal Systems (EGS) or gas shale. The model simulates fluid flow in a discrete fracture network (DFN), directly discretizing individual fractures (e.g., Karimi-Fard et al, 2004; Golder Associates, 2009). The DFN approach is distinct from effective continuum modeling, which averages fracture properties into effective properties over volumetric grid blocks (Warren and Root, 1963; Kazemi et al., 1976; Lemmonier, 2010). The model calculates the stresses induced by opening and sliding along individual fractures and couples opening and slip to fracture transmissivity. The model couples deformation with flow using iterative coupling (Kim

et al., 2011) and is efficient enough to simulate problems involving thousands of individual fractures in a few hours or days on a single processor. The model assumes flow is single-phase and isothermal, matrix permeability is negligible, and deformation is small strain in an infinite, linearly elastic medium. The model was written using C++.

The model has several other specific limitations. The model can simulate propagation of new tensile fractures, but the locations of the potentially forming new fractures must be specified in advance (Sections 2.2.3.8 and 2.2.4.1). In practice, a large number of potentially forming fractures can be specified throughout the model, which allows the simulator significant freedom in determining the overall propagation of stimulation (Sections 2.2.4.1, 2.3.3.2, and 2.4.3). The model sometimes encounters problems at low-angle fracture intersections ($< 10°$) as a consequence of its use of the boundary element method to calculate stresses induced by deformation. In practice, this limitation can be handled either by not permitting models to contain low-angle intersections (Section 2.2.4.1) or by implementing a special penalty method (Sections 2.2.5.6, 2.3.4, and 2.4.3)

An earlier version of the model (described in Chapter 4) was used to study induced seismicity by performing rate and state friction earthquake simulation. That ability is retained in the current model, but rate and state friction simulations are very intensive computationally and are not the focus of this chapter. Most simulations described in this chapter were performed with a constant coefficient of friction. As a compromise between rate and state friction and constant coefficient of friction, static/dynamic friction was implemented and tested in the work described in this chapter (Sections 2.2.5.3, 2.3.3.1, and 2.4.2.5). Static/dynamic friction is a more efficient, but less rigorous, way of modeling seismicity than rate and state. There are several other differences between the model described in this chapter (which is also used in Chapter 3) and the model in Chapter 4. The most important differences are related to time stepping (implicit Euler versus third-order Runge-Kutta) and coupling (explicit versus iterative).

Earlier versions of the model used in this chapter were used to investigate shear stimulation and induced seismicity in fracture networks (McClure and Horne, 2010a; 2010b). The model described in this chapter has significant improvements on the earlier

versions. The most important differences are that the model in this chapter is more efficient, handles fracture opening much more realistically, and is fully convergent to discretization refinement in time.

The philosophy of development has been to construct a model that is realistic and efficient enough to simulate the most important physical processes that take place during hydraulic stimulation in large, complex fracture networks in very low permeability rock. In some cases, special treatments are used in the model to enforce realistic behavior in the fracture network. Our guiding principle is that a model should include as much realism as needed to reasonably capture the physical processes that significantly affect the results of the model for a given purpose.

Because the boundary element method is used, temperature is constant, and matrix permeability is zero, it is only necessary to discretize the fractures, not the volume around the fractures. As a result, the problem size is reduced dramatically. With iterative and approximate methods, it is possible to solve the large, dense systems of equations associated with the use of the boundary element method efficiently in a coupled, implicit fluid flow and geomechanical simulator.

The chapter is divided into several parts. In Sections 2.1.1 and 2.1.2, the literature is reviewed to identify other numerical models that have been used for complex hydraulic fracturing. In the Methodology (Section 2.2), the model is described in detail. Topics include governing and constitutive equations, numerical methods for mechanical and fluid flow calculations, the coupling scheme between the mechanical and flow equations, handling of mechanical inequality constraints and changing stress boundary conditions, stochastic generation of discrete fracture networks, spatial discretization of fracture networks, and several specialized topics particular to the model, including efficient matrix multiplication, adaptive domain adjustment, handling of regions near opening crack tips, and a technique for handling difficulties associated with low-angle fracture intersections.

In Sections 2.3 and 2.4, the results of simulations on four different fracture networks are presented and discussed. These simulations (1) verify the accuracy of the mechanical calculations, (2) verify convergence from discretization refinement in both time and

space, (3) test sensitivity to error tolerances, and (4) test the effect of various special simulation options, including the use of dynamic/static friction for seismicity modeling, ignoring or including stresses caused by normal displacement of "closed" fractures (in this dissertation, the word "open" is used to refer to a fracture whose walls have mechanically separated because fluid pressure exceeds normal stress, and the word "closed" is used to refer to a fracture with walls that are in contact), and an adjustment to handle low-angle fracture intersections.

The primary purpose of simulations described in this chapter was to test the accuracy, efficiency, and versatility of the model and to identify optimal simulation parameters. In addition, there are some interesting physical insights that can be drawn from the results. The results demonstrate that stresses induced by deformation affect the propagation of stimulation profoundly, justifying the considerable effort required to integrate them fully into a discrete fracture network simulator.

In Chapter 3, there is discussion of the variety of conceptual models that have been used in the literature to describe the complex fracturing mechanisms taking place in EGS and gas shale. These models involve either opening and propagation of new fractures, sliding of preexisting fractures, or combinations of both. At a given site, establishing the correct conceptual model should be considered a fundamental requirement for successful application of modeling and reservoir engineering.

2.1.1 Discrete Fracture Network Modeling

In discrete fracture network (DFN) modeling, the equations of fluid flow are solved on each individual fracture. Figure 2-1 shows an example of a discrete fracture network (this is Model B, discussed in Sections 2.3.3.1 and 2.4.2). The network is two-dimensional, and the fractures should be considered vertical, strike-slip fractures viewed in plan view (equivalently, they could be considered normal fractures viewed in cross-section).
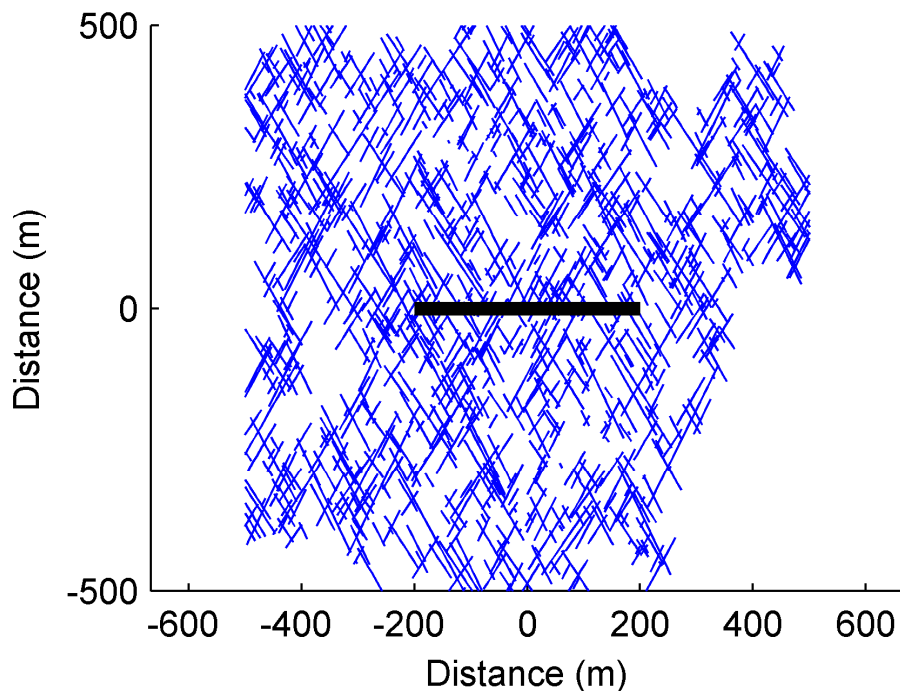
Figure 2-1: Example of a discrete fracture network. The blue lines are preexisting fractures and the thick black line represents the wellbore.

There are several reasons why DFN models are particularly useful for describing complex hydraulic fracturing in low permeability medium. In low permeability rock, individual fractures that are in close proximity but not touching are not well connected hydraulically. As a result, fluid flow between locations is dependent on idiosyncrasies of the fracture network geometry. Connectivity can be highly unpredictable, with weak connections between two nearby locations, but strong connection between more distant locations (McCabe et al., 1983; Cacas et al., 1990; Abelin et al, 1991). In hydraulically stimulated, fractured, low matrix permeability reservoirs, production logs typically show that productivity can be highly variable along individual wells within the same rock unit (Baria et al., 2004; Dezayes et al., 2010; Miller et al., 2011). Discrete fracture models are better at describing this sort of highly channelized, unpredictable behavior.

Stress perturbation can be handled much more accurately with a DFN. The stresses caused by fracture opening or sliding are very heterogeneous spatially, and effects on neighboring fractures are dependent on the relative orientations and locations. Stresses caused by fracture deformation have major effects on the process of stimulation, as

described in this chapter (see Section 2.4.2.6 for an example of what happens when induced stresses are neglected) and also in McClure and Horne (2010a).

2.1.2 Review of Stimulation Models

There is an incredible diversity of hydraulic stimulation modeling described in the literature. The diversity reflects the profound uncertainty that exists about mechanisms of stimulation in the subsurface, the difficulty of validating the underlying assumptions of a given model, the great number of numerical methods available, and different choices about balancing realism and efficiency. This section reviews models of hydraulic fracturing found in the literature. Models that treat hydraulic stimulation as a single planar fracture propagating away from a wellbore are used widely in the industry and in academia (Adachi et al., 2007; Meyer and Associates, 2012). However, this section focuses on models intended for more complex settings.

In some modeling of unconventional fracturing, effective continuum modeling has been used (Yamamoto, 1997; Taron and Elsworth, 2009; Vassilellis et al., 2011; Lee and Ghassemi, 2011; Kelkar et al., 2012). These models average flow from multiple fractures into effective continuum properties. Other models use hybrid approaches that combine aspects of continuum models with aspects of discrete fracture models (Xu et al., 2010; Meyer and Bazan, 2011; Palmer et al., 2007).

Some discrete fracture models neglect the stresses caused by deformation of fractures. Neglecting stress interaction reduces the complexity of the implementation significantly and increases efficiency. With this approach, it is possible to perform simulations on large, reservoir-scale discrete fracture networks. In some of these models, fluid flow is calculated by upscaling the DFN to an effective continuum model (Lanyon et al., 1993; Fakcharoenphol et al., 2012; Tezuka et al., 2005; Jing et al., 2000; Willis-Richards et al., 1996; Kohl and Mégel, 2007; Rahman et al., 2002; Cladouhos et al., 2011; Wang and Ghassemi, 2012; Du et al., 2011). In other models, discrete fracture network are used directly without upscaling to effective continuum models (Bruel, 1995; Bruel, 2007; Sausse et al., 2008; Dershowitz et al., 2010).

A variety of numerical methods have been used to calculate stresses induced by deformation in discrete fracture networks. These methods include finite element (Heuze et al., 1990; Swenson and Hardeman, 1997; Rahman and Rahman 2009; Lee and Ghassemi, 2011; Fu et al., 2012; Kelkar et al., 2012), finite difference (Hicks et al., 1996; Taron and Elsworth, 2009; Roussel and Sharma, 2011), boundary element (Asgian, 1989; Zhang and Jeffrey, 2006; Cheng, 2009; Olson and Dahi-Taleghani, 2009; Zhou and Ghassemi, 2011; Weng et al., 2011; Meyer and Bazan, 2011; Safari and Ghassemi, 2011; Jeffrey et al., 2012; Tarasovs and Ghassemi, 2012; Sesetty and Ghassemi, 2012), block-spring model (Baisch et al., 2010), extended finite element (Dahi-Taleghani and Olson, 2011; Keshavarzi and Mohammadi, 2012), distinct element method (Pine and Cundall, 1985; Last and Harper, 1990; Rachez and Gentier, 2010; Nagel et al., 2011), hybrid finite element/discrete element (Rogers et al., 2011), and the particle-based distinct element method (Suk Min and Ghassemi, 2010; Deng et al., 2011; Zhao and Young, 2011; Damjanac et al., 2010). An overview of the numerical methods used in rock mechanics (including all of these methods) can be found in Jing (2003).

The majority of published results using coupled geomechanical-fluid flow models in discrete fracture networks have involved a limited number of fractures. Some studies have investigated induced slip on one or a few preexisting fractures (Baisch et al., 2010; Zhou and Ghassemi, 2011; Safari and Ghassemi, 2011). Some have investigated one or a few propagating and preexisting fractures (Heuze et al., 1990; Zhang and Jeffrey, 2006; Rahman and Rahman 2009; Suk Min and Ghassemi, 2010; Deng et al., 2011; Zhao and Young, 2011; Dahi-Taleghani and Olson, 2011; Jeffrey et al., 2012; Sesetty and Ghassemi 2012; Cheng, 2009; Keshavarzi and Mohammadi, 2012). Some have investigated induced slip on a network of preexisting fractures (no propagation of new fractures) of up to a few dozen fractures (Pine and Cundall, 1985; Asgian, 1989; Last and Harper, 1990; Hicks et al., 1996; Swenson and Hardeman, 1997; Rachez and Gentier 2010). Some have investigated propagation of multiple fractures with no preexisting fractures (Tarasovs and Ghassemi, 2012; Roussel and Sharma, 2011). Some have combined propagation of new fractures and preexisting fractures on networks up to dozens of fractures (Damjanac et al., 2010; Nagel et al., 2011, 2012; Fu et al., 2012, Weng et al., 2011; Rogers et al., 2011).

As the size and complexity of the fracture network increases, the challenge of geomechanical discrete fracture modeling grows considerably. Finite element and finite difference methods require discretization of the area (in two dimensions) or the volume (in three dimensions) around the fractures, and this can lead to a very large number of elements for complex networks and arbitrary fracture geometries. Boundary element methods (BEM) avoid the need to discretize around fractures, but if they are applied directly, they are inefficient for very large problems because they require solution of dense matrices. That disadvantage is mitigated in the model described in this chapter because iterative and approximate methods are used to improve efficiency of the BEM solutions. Other disadvantages are that the BEM typically cannot handle arbitrary rock properties and heterogeneity and struggles to handle low angle fracture intersections accurately (as discussed in Sections 2.3.4 and 2.4.4). Extended finite element methods may eventually become a powerful technique for hydraulic fracturing modeling but are relatively new and have not yet been demonstrated on complex networks.

Particle based distinct element models have several advantages. They are versatile because they have the ability to handle arbitrary rock properties and they can avoid discretization difficulties by employing a loose discretization of the volume around fractures. However, these models do not provide solutions that are convergent to grid refinement. Macroscopic rock properties such as Young's modulus are emergent properties of the model, and model inputs (including the coarseness of the discretization itself) must be tuned with trial and error to find settings that match desired behavior (Potyondy and Cundall, 2004).

2.2 Methodology

The model described in this chapter computes fluid flow and deformation in a discrete fracture network. As an input, the model requires a realization of the preexisting fracture network. The model has the ability to represent propagation of new fractures, but the potential locations of new fractures must be specified in advance.

Because the boundary element method is used and fluid flow in the matrix surrounding the fractures is assumed negligible, it is not necessary to discretize the volume around the fractures, significantly reducing the number of elements in the discretization.

In the following subsections, the modeling methodology is given in detail, including the governing and constitutive equations, numerical methods of solution, methods of discretization, methods of generating realizations of the preexisting (and potentially forming) discrete fracture network, and several special simulation techniques used for realism and efficiency.

2.2.1 Governing and Constitutive Equations

In the model, fluid flow is single-phase and isothermal. The unsteady-state fluid mass balance equation in a fracture is (adapted from Aziz and Settari, 1979):

$$\frac{\partial(\rho E)}{\partial t} = \nabla \cdot (q_{flux}e) + s_a,$$ 2-1

where s_a is a source term (mass per time for a unit of area of the fracture), t is time, E is void aperture (the pore volume per unit area of the fracture), ρ is fluid density, q_{flux} is mass flux (mass flow rate per cross-sectional area of flow), and e is the hydraulic aperture (the effective aperture for flow in the fracture).

Darcy flow is assumed, in which mass flux in a direction x_i is (Aziz and Settari, 1979):

$$q_{flux,i} = \frac{k\rho}{\mu_l}\frac{\partial P}{\partial x_i},$$ 2-2

where P is fluid pressure, μ_l is fluid viscosity, and k is permeability.

Fluid density and viscosity are functions of pressure (because the simulations were isothermal) and are interpolated from a polynomial curve fit based on values generated using the Matlab script XSteam 2.6 by Holmgren (2007) assuming a constant temperature of 200°C. A high temperature was used because of the application to geothermal energy.

The choice of higher temperature causes fluid density to be modestly lower and viscosity to be nearly a factor of ten lower, relative to room temperature.

The cubic law for fracture transmissivity (the product of permeability and hydraulic aperture) is (Jaeger et al., 2007):

$$T = ke = \frac{e^3}{12}.$$

2-3

Hydraulic aperture is equal to void aperture between two smooth plates but is lower than void aperture for rough surfaces such as rock fractures (Liu, 2005). A "fracture" in a DFN model may represent a crack, but it may also represent a more complex feature such as a fault zone. In the latter case, the void aperture may be much larger than the hydraulic aperture. The model allows e and E to be different.

For single-phase flow in a one-dimensional fracture, the mass flow rate q is:

$$q = \frac{Th\rho}{\mu_l} \frac{\partial P}{\partial x},$$

2-4

where h is the width of the flowing fracture (for example, the height of a vertical fracture).

Fluid flow boundary conditions (representing the wellbore) are either constant rate or constant pressure wellbore boundary conditions (Section 2.2.3.10). The boundaries of the spatial domain are impermeable to flow.

Stresses induced by deformation are calculated according to the equations of quasistatic equilibrium in a continuum assuming that body forces are equal to zero. These stresses are given by the vector equation (Jaeger et al., 2007):

$$\nabla^T T_s = 0,$$

2-5

where T_s is the stress tensor.

Linear elasticity in an isotropic, homogeneous body is assumed, giving the following relationship between stress and strain according to Hooke's law (Jaeger et al, 2007):

$$\mathrm{T}_s = \frac{2G v_p}{1 - 2v_p} trace(\varepsilon)I + 2G\varepsilon \,, \tag{2-6}$$

where *I* is the unit matrix, ε is the strain tensor, v_p is Poisson's ratio, and *G* is the shear modulus.

The shear cumulative displacement discontinuity at any point, *D*, is equal to the time integral of sliding velocity, *v*:

$$D = \int v dt \,. \tag{2-7}$$

A distinction is made between mechanically open and closed fractures. An open fracture is in tension such that the walls are physically separated and out of contact. A closed fracture bears compressive stress, and its walls are in contact.

For a closed fracture, Coulomb's law requires that shear stress be less than or equal to the frictional resistance to slip. We include an additional term, $v\eta$ (the radiation damping term), to approximate the effect of inertia during sliding at high velocities (Rice, 1993; Segall, 2010). The radiation damping coefficient, η, is defined to be equal to $G/(2v_s)$, where v_s is the shear wave velocity (Rice, 1993; Segall, 2010). The radiation damping term is on the order of several MPa, which means that the radiation damping term is small unless sliding velocity is at least centimeters per second. The Coulomb failure criterion with a radiation damping term is (Jaeger et al., 2007; Segall, 2010):

$$|\tau - \eta v| = \mu_f \sigma_n' + S_0 \,, \tag{2-8}$$

where μ_f is the coefficient of friction, S_0 is fracture cohesion, and σ_n' is the effective normal stress, defined as (Jaeger et al., 2007; Segall, 2010):

$$\sigma_n' = \sigma_n - P \,, \tag{2-9}$$

where compressive stresses are taken to be positive. For fractures with shear stress less than the frictional resistance to slip, shear deformation is assumed to be negligible.

Force balance requires that the effective normal stress of open fractures is zero. Because the fluid inside open fractures cannot support shear stress, the walls are stress free (Crouch and Starfield, 1983). These stress conditions can be stated:

$$\sigma_n' = 0, \qquad \text{2-10}$$

$$\tau - \eta v = 0. \qquad \text{2-11}$$

Relationships are used to relate effective normal stress and cumulative shear displacement to void and hydraulic aperture. These relationships are chosen so that there is not any discontinuity as elements transition between being open and closed. The aperture of a closed fracture is defined as (Willis-Richards et al., 1996; Rahman et al., 2002; Kohl and Mégel, 2007):

$$E = \frac{E_0}{1 + 9\sigma_n' / \sigma_{n,Eref}} + D_{E,eff} \tan \frac{\phi_{Edil}}{1 + 9\sigma_n' / \sigma_{n,Eref}}, \qquad \text{2-12}$$

where E_0, $\sigma_{n,Eref}$, and φ_{Edil} are specified constants. $D_{E,eff}$ is defined as equal to D if $D < D_{E,eff,max}$, and equal to $D_{E,eff,max}$ otherwise. The constants are allowed to be different for hydraulic aperture, e, and void aperture E. Non-zero φ_{Edil} corresponds to pore volume dilation with slip, and non-zero φ_{edil} corresponds to transmissivity enhancement with slip.

The void and hydraulic aperture of an open preexisting fracture is defined as:

$$E = E_0 + D_{E,eff} \tan \phi_{Edil} + E_{open}, \qquad \text{2-13}$$

$$e = e_0 + D_{e,eff} \tan \phi_{edil} + E_{open}, \qquad \text{2-14}$$

where E_{open} is the physical separation between the fracture walls.

The hydraulic and void apertures of newly formed fractures are treated differently than preexisting fractures. A value E_{hfres} is defined as the residual aperture of a newly formed fracture. Hydraulic aperture, e, is set equal to void aperture, E. The aperture of an open, newly formed fracture is:

$$E = E_{hfres} + E_{open},$$
<div align="right">2-15</div>

and the aperture of a closed, newly formed fracture is:

$$E = E_{hfres} \exp(-\sigma_n K_{hf}),$$
<div align="right">2-16</div>

where K_{hf} is a specified stiffness for closed hydraulic fracture elements.

If closed, the transmissivity of a newly formed fracture is defined as:

$$T = T_{hf,fac} E_{hfres},$$
<div align="right">2-17</div>

and if open, transmissivity is defined as:

$$T = T_{hf,fac} E_{hfres} + (E_{open})^3 / 12,$$
<div align="right">2-18</div>

where $T_{hf,res}$ is a specified constant. This treatment of transmissivity for newly forming fractures is used so that, if desired, they can be assigned a relatively high residual transmissivity. This might be desirable as a very simple way of approximating the effect of proppant in newly formed fractures, which would tend to cause higher residual transmissivity after closure (Fredd et al., 2001).

2.2.2 Initial Conditions

In the results shown here, the fluid pressure and stress state (defined by P, σ_{xx}, σ_{yy}, and σ_{xy}) were assumed to be constant everywhere in the model at the beginning of a simulation. In natural systems, the stress state or pore pressure may be spatially heterogeneous. For example, varying mechanical properties between layers can lead to significant stress heterogeneity and is believed to be responsible for vertical confinement of fractures (Warpinski et al., 1982; Teufel and Clark, 1984). If desired, spatially variable stress state could be incorporated into the model simply by changing the stress state of individual elements prior to initiating the simulation.

2.2.3 Methods of Solution

In this section, the numerical methods of solution for the governing equations are described. The simulator solves the unsteady-state mass balance equation, Equation 2-1, while simultaneously satisfying constitutive relations, updating stresses due to deformation, and satisfying the mechanical equations of force equilibrium. The fluid flow equations are solved using the finite volume method and the mechanical deformation problem is solved using the boundary element method of Shou and Crouch (1995). Time stepping is performed with the implicit Euler method, in which all equations and all unknowns are solved simultaneously in a coupled system of equations during every time step (Aziz and Settari, 1979).

2.2.3.1 Iterative Coupling

During each time step, the simulator solves for the primary variables: pressure, P, open aperture, E, and shear displacement, D, based on equations governing conservation of mass and momentum (details in Sections 2.2.3.4, 2.2.3.5, 2.2.3.6, and 2.2.3.7). Iterative coupling is used (Kim et al., 2011) to solve the system of equations. Iterative coupling is a strategy for solving a system of equations in which the system is split into parts and then solved sequentially until convergence. Figure 2-2 is a diagram of the iterative coupling approach.
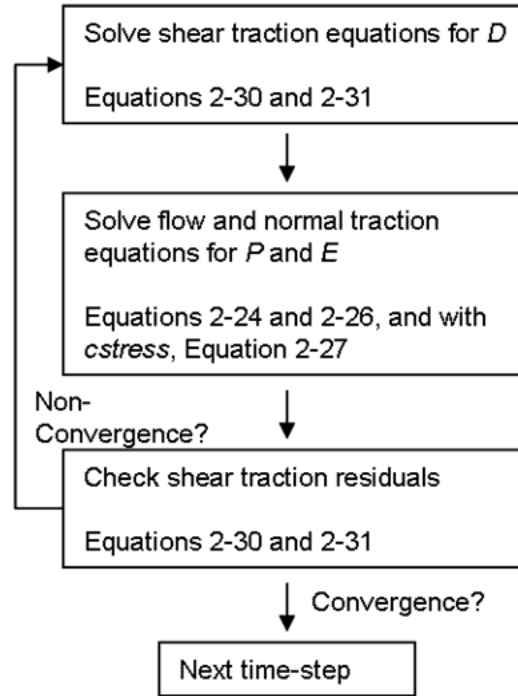
Figure 2-2: Summary of the iterative coupling approach for a single time step.

At the beginning of each time step, the shear stresses equations (Equations 2-8 and 2-11; or equivalently, 2-31 and 2-32) are solved as a system of equations with sliding displacements as unknowns while pressure and normal displacements are held constant (Section 2.2.3.5). Next the mass balance and normal stress equations (Equations 2-1, 2-10, and 2-12; or equivalently, 2-24, 2-26, 2-27) are solved with pressure and normal displacements as unknowns holding shear displacements fixed (Section 2.2.3.4). The shear stress residuals change during the solution to the flow and normal stress equations, and so after solving the flow and normal stress equations, shear stress residuals are rechecked. Convergence occurs if the shear stress residuals are below a certain threshold, *itertol*. The simulator iterates until convergence. In the simulations in this chapter, convergence typically occurred in less than ten iterations (most commonly three), with more iterations required for longer time steps.

2.2.3.2 Fracture Deformation: Displacement Discontinuity Method

Stresses induced by deformation are solved with the boundary element method for fracture deformation, the Displacement Discontinuity (DD) method. Quadratic basis functions were used according to the method of Shou and Crouch (1995). The method of

Shou and Crouch (1995) calculates the stresses induced by shear and normal displacement discontinuities by satisfying the equations of quasistatic equilibrium and compatibility for small strain deformation in an infinite, two-dimensional, homogeneous, isotropic, linearly elastic medium in plane strain. The problem reduces to finding the induced stresses $\Delta\tau$ and $\Delta\sigma$ at each element i caused by the shear displacements ΔD and opening displacements ΔE of each element j. Stresses and displacements are linearly related so that:

$$\Delta\sigma_{n,i} = \sum_{j=1}^{n} (B_{E,\sigma})_{ij} \Delta E_j ,$$
<div style="text-align:right">2-19</div>

$$\Delta\sigma_{n,i} = \sum_{j=1}^{n} (B_{D,\sigma})_{ij} \Delta D_j ,$$
<div style="text-align:right">2-20</div>

$$\Delta\tau_i = \sum_{j=1}^{n} (B_{E,\tau})_{ij} \Delta E_j ,$$
<div style="text-align:right">2-21</div>

$$\Delta\tau_i = \sum_{j=1}^{n} (B_{D,\tau})_{ij} \Delta D_j ,$$
<div style="text-align:right">2-22</div>

where $B_{E,\sigma}$, $B_{D,\sigma}$, $B_{E,\tau}$, and $B_{D,\tau}$ are a matrices of interaction coefficients calculated according to Crouch and Shou (1995). Interaction coefficients do not change during a simulation, and so they can be calculated once and then stored in memory.

The method of Shou and Crouch (1995) assumes strain plane deformation, which implies that the thickness of the deforming medium is infinite in the out-of-plane dimension. In three dimensions, the spatial extent of stress perturbation caused by a deforming fracture scales with the smallest dimension of the fracture (either width or length). Therefore, an implication of plane strain is that the spatial extent of stresses induced by fracture deformation scales linearly with the length of the fracture. In layered formations (more common in gas shale than in EGS), hydraulic fractures are typically confined to mechanical layers and can have length significantly greater than height. In this case, plane strain is not a good assumption. The Olson (2004) adjustment factor can be used to account for the effect of fracture height. Every interaction coefficient is multiplied by a factor:

$$G_{adj,ij} = 1 - \frac{d_{ij}^{\beta}}{(d_{ij}^2 + (h/\alpha)^2)^{\beta/2}} ,$$

<div align="right">2-23</div>

where h is the specified formation height, d is the distance between the centers of the two elements i and j, α is an empirical value equal to one, and β is an empirical value equal to 2.3 (Olson, 2004). If h is very large, then the adjustment factor is nearly one, and the method reduces to plane strain.

2.2.3.3 Stresses Induced by Normal Displacements of Closed Fractures

The simulator has the option to include (the *cstress* option) or not include (the *nocstress* option) the stresses induced by normal displacements of closed fractures.

The *nocstress* method can be justified because closed cracks experience very small opening displacements in response to significant changes in normal stress. From Barton et al. (1985), closed joints are most compliant at normal stresses below 10 MPa, and reducing normal stress from 10 MPa to 0 MPa leads to a normal displacement of 0.1 to 0.25 mm, depending on the stiffness of the joint. If a closed, 10 m long fracture experiences 0.1 mm of opening displacement, the approximate stress change (assuming plane strain) due to that displacement is less than 0.1 MPa (from Equation 2-46). Induced stresses would be even less for larger fractures because fracture stiffness is inversely proportional to size (Equation 2-46). As a result, the stresses induced by opening displacement of closed elements can be neglected with minor effect on the results unless the joints are very small or unusually compliant.

On the other hand, the *cstress* method may be useful because not all closed fractures are actually thin joints. For example, fault zones may be treated as fractures in a DFN, but in reality they can be centimeters to meters thick and be composed of a complex zone of porous material and fracturing (Chapter 5). In this case, the fractures represented in a DFN are not literally crack-like features. The void and hydraulic apertures are effective values that include the total effect of all sources of fluid storage and transmissivity in the fault zone. Because fault zones can have very high effective void aperture (if they are

thick, porous zones), they can contain a very significant amount of fluid, and as a result induce significantly greater displacement, strain, and stress than if they were thin cracks.

While the overall approach of the *cstress* option could be useful for modeling thick fault zones, there are some problems with the current implementation. The model calculates stresses induced by fracture normal displacements using the Shou and Crouch (1995) Displacement Discontinuity method. This method is intended to calculate the stresses induced by opening of a crack -- a displacement discontinuity in which a solid is parted and physically separated along a discrete plane. The physical process of fluid filling a porous, finite thickness fault zone is obviously different from the opening of a crack. One difference is that for the same amount of injected fluid, stresses induced by the opening of a crack are greater because the fluid is emplaced into a much thinner zone, resulting in a much greater strain (because strain is the ratio of displacement and size). Therefore it is not correct to model poroelastic swelling of a fault zone as the opening of a crack. This problem could be resolved in future work by replacing the Shou and Crouch (1995) method with a BEM designed for volumetric, poroelastic strain. Changing the BEM would affect the value of the interaction coefficients between elements, but the overall numerical approach of the *cstress* method (Section 2.2.4) would be unchanged.

2.2.3.4 Solution to the Fluid Flow and Normal Stress Equations

The fractures are discretized into discrete elements (Section 2.2.4.2). The unsteady-state mass balance equation, Equation 2-1, is solved implicitly using the finite volume method, which leads to a nonlinear system of equations that must be solved at each time step. Equations representing conditions for normal stress are included in the fluid flow system of equations.

With the *cstress* method, there is a $(2n) \times (2n)$ system of equations (n is the total number of elements), with pressure and void aperture of each element as unknowns. With the *nocstress* method, there is a $(n+m) \times (n+m)$ system of equations (m is the number of open elements), with pressure of each element and void aperture of each open element as unknowns. In typical simulations, m is much smaller than n, and so the *cstress* method can be significantly more computationally intensive.

From the finite volume method, a mass balance residual equation (from Equations 2-1 and 2-4) is written for each individual element m:

$$R_{m,mass} = \sum_{q=1}^{Q} T_{g,qm}^{n+1}(\frac{\rho}{\mu_l})_{qm}^{n+1}(P_q^{n+1} - P_m^{n+1}) + s_m^{n+1} - 2a_m h \frac{(E\rho)_m^{n+1} - (E\rho)_m^n}{dt^{n+1}},$$

2-24

where the superscript n denotes the previous time step, and superscript $n+1$ denotes the current time step, Q is the number of elements connected to element m, q is a dummy subscript referring to each of the elements connecting to element m, a is the element half-length, T_g is the geometric part of the transmissibility between two elements (referred to as geometric transmissibility, see Equation 2-25 for a definition), s_m is a source term such as a well (units of mass per time; positive s is flow into an element), and dt^{n+1} is the duration of the time step. The equations are solved fully implicitly by evaluating all terms at the upcoming time step. An exception is that when using the *cstress* option, the geometric transmissibility term is evaluated explicitly. The term $(\rho/\mu_l)_{qm}$ is evaluated with upstream weighting.

In this dissertation, the term "transmissivity" is used to refer to the ability of fluid to flow through a fracture (in general), and the term "transmissibility" is used to refer to the ability for water to flow between two numerical elements. The geometric transmissibilities are calculated using harmonic averaging. For a connection between adjacent elements not at a fracture intersection, geometric transmissibility is calculated as:

$$T_{g,qm} = \frac{2h(e_q^3/a_q)(e_m^3/a_m)}{12(e_q^3/a_q) + (e_m^3/a_m)}.$$

2-25

Geometric transmissibilities at fracture intersections are calculated according to the method of Karimi-Fard et al. (2004), which gives a way to calculate geometric transmissibilities between elements at fracture intersections without requiring a zero-dimensional element at the center of the intersection. In the Karimi-Fard et al. (2004) method, geometric transmissibility between two elements at a fracture intersection depends on all elements at the intersection.

For open elements (with either *nocstress* or *cstress*), the additional residual equation is (from Equation 2-10):

$$R_{E,o} = -\sigma_n' ,$$

2-26

and the additional unknown is E_{open} (or equivalently, E).

With the *cstress* method, fracture aperture is an additional unknown (and leads to an additional equation) for each closed element. For closed elements with the *cstress* method, the additional residual equation is (from Equation 2-12):

$$R_{E,c} = E - \frac{E_0}{1 + 9\sigma_n' / \sigma_{Enref}} - D_{E,eff}\, \tan \frac{\phi_{Edil}}{1 + 9\sigma_n' / \sigma_{Enref}} ,$$

2-27

with E as the additional unknown.

With the *nocstress* method, stresses induced by changes in aperture of closed elements are neglected. It is not necessary to include an additional unknown and equation for closed elements (such as Equation 2-27) because the empirical relations for fracture void and hydraulic aperture (Equation 2-12) can be substituted directly into the fluid flow residual equation (Equation 2-24). The hydraulic aperture is treated as a function of P, D, and σ_n, independent of E, and substituted into the fluid flow residual equation in both the *cstress* and the *nocstress* methods.

The system of equations is solved using an iterative method similar to Newton-Raphson iteration. In Newton-Raphson iteration, an iteration matrix is defined such that:

$$J_{ij} = \frac{\partial R_i}{\partial X_j} ,$$

2-28

where i reflects the row number, j reflects the column number, J_{ij} is an entry in the iteration matrix, R_i is an entry in the residual vector, and X_j is an entry in the vector of unknowns (Aziz and Settari, 1979). In Newton-Raphson iteration, the iteration matrix is called the Jacobian. However, we do not use the term Jacobian because, as discussed in this section, the iteration matrix used is not a full Jacobian. The algorithm makes a series

of guesses for X until certain convergence criteria are met. For each iteration, X is updated according to:

$$X_{new} = X_{prev} + dX \, ,$$

<div align="right">2-29</div>

where:

$$J * dX = -R \, .$$

<div align="right">2-30</div>

After each update of X, the residual vector is recalculated. Stresses are induced by changes in fracture aperture (changes in aperture of all elements if *cstress* is used, changes in aperture for open elements if *nocstress* is used), and so as a part of the residual update, the stresses at each element are updated based on the changes in aperture. The stress update requires matrix multiplication according to Equations 2-19 and 2-21. The two most computationally intensive steps in solving the system of equations are solving Equation 2-30 and updating the stresses.

In the DD method, normal displacements of each element affect the stress at every other element. As a result, the columns of the full Jacobian matrix corresponding to the normal displacements are dense. Solving a large, dense system of equations, as required by Equation 2-30, is extremely intensive computationally, and if attempted directly, would severely limit the practical size of the problem that could be solved. To handle this difficulty, an incomplete Jacobian matrix is used as an iteration matrix instead of a full Jacobian matrix.

The iteration matrix is equal to the full Jacobian matrix with interaction coefficients of absolute value below a certain threshold neglected. This approach can effectively solve the system of equations because the magnitude of interaction coefficients decays with the inverse of the square of distance (using the correction of Olson, 2004, coefficients decay even faster). As a result, the interaction coefficients of immediate neighbors are much larger than interaction coefficients of distant elements.

The threshold for inclusion in the iteration matrix is set to at 5% of the value of the self-interaction coefficient (the effect of an element's opening displacement on its own normal stress) for open elements and 30% for closed elements (if the *cstress* option is

used).   Using these thresholds, the iteration matrix typically includes five to ten interaction coefficients for each open element and even fewer for each closed element.

Neglecting values in the iteration matrix does not affect the accuracy of the answer; it only decreases the quality of the guesses based on Equation 2-28. After each *dX* update is calculated, the stresses caused by the changes in opening displacement are fully calculated according to Equations 2-19 and 2-21 without neglecting interaction coefficients.

Using an incomplete Jacobian increases the number of iterations required to reach convergence (relative to using a full Jacobian), but hugely reduces the computational burden of solving Equation 2-30. Because element interactions are affected mainly by near-neighbors (and time steps are short enough that variables change slightly between time steps), convergence is still possible in a reasonable number of iterations. Typically, the simulator achieves convergence in three or four iterations.

The iteration matrix is an unsymmetric sparse matrix. The publicly available code UMFPACK is used to solve the iteration matrix (Davis, 2004a, 2004b; Davis and Duff, 1997, 1999). Within UMFPACK, the publicly available codes AMD (Amestoy et al., 1996, 2004; Davis, 2006), BLAS (Lawson et al., 1979; Dongarra et al., 1988a, 1988b, 1990a, 1990b), and LAPACK (Anderson et al., 1999) are used.

Several criteria are used to judge convergence in the flow/opening stress equations. The change in the fluid pressure from iteration to another must be less than 0.001 MPa, and the change in opening displacement must be less than 1 micron. A normalized residual vector is calculated by multiplying each stress residual equation by 0.1, each mass balance residual by $dt/(2a_iE_ih\rho_i)$, and (if flow rate is specified) the wellbore residual equation by $1/s_m$. For convergence, the infinity norm of the normalized residual is required to be less than 10^{-4}. The Euclidean norm (scaled by the number of elements) is required to be less than 10^{-5}. If a constant pressure boundary condition is specified, the total flow rate into/out of the system is calculated, and the change in the calculated flow rate between iterations is required to be less than 10^{-5} kg/s.

If the nonlinear solver does not converge within a specified number of iterations, the time step is discarded and repeated with a smaller dt. In testing, it was found that nonconvergence was uncommon.

2.2.3.5 Solution to the Shear Stress Equations

The shear stress equations are solved with cumulative displacement, D, as the unknown (or equivalently, v or ΔD) holding fluid pressure and normal displacements constant. The sliding velocity v during a time step is equal to ΔD, the change in sliding displacement during a time step, divided by dt, the duration of the time step. The residual equations for closed and open elements are (from Equations 2-8 and 2-11):

$$R_{D,closed} = |\tau - \eta v| - \mu \sigma_n - S_0, \tag{2-31}$$

$$R_{D,open} = |\tau - \eta v| - S_{0,open}, \tag{2-32}$$

The shear stress residual equations are solved as a system of equations. The simulator identifies elements that have negative residual and a sliding velocity of zero and categorizes them as being "locked." The shear stiffness of locked elements is assumed to be infinite, and so locked elements have zero sliding velocity. Because the shear displacements of locked elements are not changing, they are excluded from the system of equations.

To be strictly correct, the cohesion term, $S_{0,open}$, should not be included for open elements because open fractures are not able to bear shear stress. The term is included because it offers a numerical convenience and has little effect on the results (as long as $S_{0,open}$ is small). Without the $S_{0,open}$ term, cohesion vanishes abruptly when closed elements become open elements. This causes very rapid sliding, which forces the simulator to take a large number of very short time steps. Because this process can happen frequently during a simulation (every time an element opens), it can significantly reduce efficiency. Possibly, abrupt loss of cohesion during fracture opening is a realistic process, and perhaps it is a cause of microseismicity. We are not aware of any discussion of this process in the literature. From the point of view of numerical modeling, the process is an inconvenience that increases simulation run-time drastically.

In the Shou and Crouch (1995) method, shear deformation of an element affects stress at every other element. The result is that the system of equations formed from Equations 2-31 and 2-32 is dense. As with the normal stress equations (Section 2.2.4), an iterative method similar to Newton-Raphson iteration is used. An iteration matrix is formed from the full Jacobian matrix, but entries with absolute value below a certain threshold are set to zero. All interaction coefficients less than a certain factor, $J_{mech,thresh}$ (in the simulations in this chapter, 0.01 was used), of an element's self-interaction coefficient are removed from the iteration matrix, resulting in a sparse system of equations. A series of iterations are performed until the infinity norm of the shear stress residuals is less than a prescribed tolerance, *mechtol*. Special complications are discussed in Sections 2.2.3.6 and 2.2.3.7. In the simulations in this chapter, convergence typically occurred in less than five or ten iterations.

The iteration matrix is an unsymmetric sparse matrix. The publicly available code UMFPACK is used to solve the matrix (Davis, 2004a, 2004b; Davis and Duff, 1997, 1999).

Compared to solving the system of equations directly, the iterative method radically improves the scaling of computation time with size. Direct solution of a dense matrix scales like n^3, where *n* is problem size. Assuming that solving the iteration matrix is a negligible cost, the iterative method reduces the problem to several matrix multiplications, which scale like n^2 (with direct multiplication). As discussed in Sections 2.2.5.1, 2.3.5, and 2.4.5), an efficient matrix multiplication technique is used that further reduces the problem scaling to between *n* and $n\log(n)$.

Because the iteration matrix is a general sparse matrix, solving the matrix may not necessarily be a trivial computational expense for larger problems or for larger values of $J_{mech,thresh}$. If the cost of solving the iteration matrix system became prohibitive (in testing for this chapter, it did not), a banded iteration matrix could be used. A banded iteration matrix would require more iterations because it would not be able to include interactions between nearby elements in adjacent fractures (which are particularly important at fracture intersections). However, the solution of banded matrices is very efficient, and so solution time of the iteration matrix could be guaranteed to be small.

2.2.3.6 Inequality Constraints on Fracture Deformations

To enforce realistic behavior, two inequality constraints are imposed for fracture deformations. The walls of open fractures may not interpenetrate ($E_{open} \geq 0$), and a fracture may not slide backwards against the direction of shear stress ($\tau \Delta D \geq 0$). During every iteration of the flow/normal stress subloop, prior to updating stresses caused by the changes in displacement, the model checks each element to see if the applied displacement will violate an inequality constraint. If an applied displacement will result in the violation of an inequality constraint, the applied displacement is adjusted so that equality will be satisfied (resulting in E_{open} and ΔD being equal to zero).

Adjustments to enforce the constraints are made frequently by the simulator. The iterative solution algorithm used to solve the systems of equations is not aware of the constraints, and so whenever an element transitions from open to closed or from sliding to not sliding, the Newton update overshoots zero (E_{open} or ΔD equal to zero), and an adjustment must be applied. These adjustments tend to be small and typically have a minor effect on convergence.

However, because adjustments are nonsmooth perturbations to the residual equations, they have the potential to cause nonconvergence. Convergence problems did not occur for any of the simulations performed for this chapter, but with testing, it was found that convergence could sometimes be a problem when solving the shear stress residual equations on very complex, dense, and/or poorly discretized fracture networks. If nonconvergence occurs, the simulator automatically reduces time step duration. With sufficient reduction in time step, displacements can always be made small enough to assure convergence. However, frequent time step reduction due to convergence failure leads to poor efficiency and is not desirable for optimal performance.

The shear stress residual equations can fail to converge if a complex cluster of intersecting fractures is poorly discretized. In this case, a group of elements can interact in such a way that the iteration matrix consistently attempts to make updates that violate the constraint. A cycle results as the updates violate the constraint and then are reset. Unlike the normal stress element residual equation (Equation 2-26), the shear stress

residual equation of closed elements (Equation 2-31) contains both normal and shear stress, which increases the potential for complex interactions between elements.

The tendency to for nonconvergence is affected by the number of elements included in the iteration matrix.   With more elements included in the iteration matrix, nonconvergence is more likely because there is greater potential for complex interactions between neighboring elements.   However, the system converges more rapidly if more elements are included.   Therefore, a trade-off exists between efficiency (including more elements in the iteration matrix, which reduces the number of iterations required) and robustness (including fewer elements in the iteration matrix to prevent the possibility of reverse sliding).   Including too many elements in the iteration matrix can lead to reduced efficiency if the time required to solve the iteration matrix becomes nonnegligible compared to the time required to update stresses.   The most robust iteration matrix has zeros everywhere except the main diagonal, but this matrix may require hundreds of iterations for convergence.   For these reasons, the user specified parameter $J_{mech,thresh}$, which determines the number of elements included in the iteration matrix, has an important impact on efficiency and robustness.   For the simulations in this chapter, $J_{mech,thresh}$ equal to 0.01 was used.

In the simulations in this paper, convergence failure of the shear stress residual equations did not ever occur.   However, convergence failure is possible in poorly discretized networks.   If this is happens, the best solution is to refine the discretization. An alternative approach is to use a larger value of $J_{mech,thresh}$.

2.2.3.7 Changing Mechanical Boundary Conditions

As discussed in Sections 2.2.3.4 and 2.2.3.5, different forms of the stress equilibrium equation are solved depending on whether an element is open, sliding, or locked (Equations 2-26, 2-27, 2-31, and 2-32).   A major issue for the simulator is that element status may change during a time step, and so it is not known in advance which equations to solve for each element.   The issue of changing boundary conditions is handled in two ways: frequent checking of element status between iterations and time stepping.

The use of time stepping is advantageous because deformation is always small for a sufficiently short time step. Time step duration plays a direct role in the residual equations: in the accumulation term of Equation 2-24 and the radiation damping term of Equations 2-31 and 2-32. Reducing time step sufficiently always enable the simulator to converge because the residual equations do not contain discontinuities (although there are discontinuities in the derivative of the residual equations).

Typically, time step reduction to enable convergence is not necessary because the combination of iterative methods and frequent checking of element status allows convergence to be achieved in the vast majority of cases. Iterative methods are used in both the flow/normal stress and the shear stress subloops. The effect of these iterative methods is that fractures are deformed gradually as they converge to the solution. Changing element status can be problematic because it creates discontinuities in the derivative of the residual equations that worsen convergence. However, because the equations are solved with iterative methods that apply a series of small deformations, the effect of the discontinuities is dampened and typically convergence can be achieved. The need for gradual deformation is another reason why including too many elements in the iteration matrix (using a $J_{mech,thresh}$ that is too low) could be problematic for robustness.

As these gradual deformations are applied, element status is checked constantly. Elements are checked for opening and closing after every iteration in the flow/normal stress subloop and checked for opening/sliding/locking after every iteration in the shear stress subloop. An exception is that elements that are locked at the beginning of the shear stress subloop are not checked during every iteration of that subloop -- they are assumed to remain locked. If dynamic friction weakening is used (Section 2.2.5.3), the status of all elements is checked after every iteration of the shear stress subloop. After the shear stress subloop has converged (before beginning the flow/normal stress subloop), element status is checked for every element, even the previously locked elements. Finally, after the flow/normal stress subloop, before evaluating the overall coupling error for the iterative coupling, the element status is checked a final time.

Convergence problems could hypothetically occur if elements entered a cycle in which status switched back and forth from one iteration to another. In testing, cycles

were rarely observed even for large problems that had many elements that are opening, sliding, or locked.

Because time stepping is used, typically the deformation equations are solved when the solution (the deformation at the end of the time step) is quite close to the initial guess (the deformation at the beginning of the time step). However, in Section 2.3.2.1, it is demonstrated that the method described in this chapter can be used for solving contact problems where the initial guess is not close to the solution.

2.2.3.8 Formation of New Tensile Fractures

The model has the ability to model the propagation of new tensile fractures, but it requires that the location of potential new tensile fractures be specified in advance. The potential new fractures are discretized prior to simulation. Before potential fracture elements become "real" elements (become "active"), they are considered "inactive," which means that they have zero transmissivity and cannot slide or open. Inactive elements are not included in any of the systems of equations. However, the stress state at inactive elements is updated constantly throughout the simulation. Figure 2-3, Figure 2-4, and Figure 2-5 show examples of fracture networks containing both natural and potentially forming fractures.

The process by which an element is activated is discussed in Section 2.2.3.8. When an element is activated, it is given an aperture equal to E_{hfres} (see Equations 2-15 and 2-16), set at 10 microns. Because the E_{hfres} is increased from zero to 10 microns, activation of an element does not strictly conserve mass. However, because E_{hfres} is small, the error is small relative to the total amount of fluid injected during stimulation. E_{hfres} could be made smaller, but in practice, elements with very small apertures can be problematic for the simulator. Once activated, an element is never deactivated.

2.2.3.9 Adaptive Time Stepping

With adaptive time stepping, the duration of each time step is varied in order to optimize efficiency and accuracy. Time steps are selected based on the maximum change in a variable δ_i^n, defined to measure how quickly stress is changing at each element. δ_i^n is

defined as the sum of the absolute value of the change in effective normal stress and the absolute value of the change in shear stress at each element i during the time step n. The duration of the next time step is selected using the method suggested by Grabowski et al. (1979):

$$dt^{n+1} = dt^n \min_i (\frac{(1+\omega)\eta_{t\,arg}}{\delta_i^n + \omega\eta_{t\,arg}}),$$

2-33

where η_{targ} is a user specified target for the maximum change in δ and ω is a factor that can be between zero and one (in this chapter, ω was set to one). If $\delta_i > 4.0\eta_{targ}$ for any element, the time step is discarded and repeated with a smaller value of dt.

Several secondary conditions are used to select time step duration. If convergence failure occurs in the shear stress residual equations, the flow/opening residual equations, or the overall iterative coupling, the time step duration is cut by 80% and repeated. The time step duration is sometimes adjusted so that the end of the time step coincides with the prespecified duration of the simulation or a prespecified adjustment in the wellbore boundary conditions (Section 2.2.10).

2.2.3.10   Wellbore Boundary Conditions

Wellbore boundary conditions can be specified by rate or pressure. For injection, the user specifies a maximum injection pressure, P_{injmax}, and a maximum injection rate, q_{injmax}. For production, the user specifies a maximum production rate, $q_{prodmax}$, along with a minimum production pressure, $P_{prodmin}$. A schedule of wellbore control parameters is specified by the user. At each time step, the simulator identifies which constraint should be applied such that the other is not violated and implements the appropriate boundary condition.

For constant rate boundary conditions, the source term s in Equation 2-24 is nonzero for elements connected to the wellbore. The specified rate is enforced such that it is equal to the sum of the source terms of all elements connected to the wellbore:

$$S = \sum_k s_{m,k} \, ,$$

2-34

where S is the specified injection/production rate (positive for injection) and k cycles through every element connected to the wellbore. Equation 2-34 is added to the system of flow equations, and P_{inj} is the corresponding unknown. The source term of each element connected to the wellbore, $s_{m,k}$ is:

$$s_{m,k} = \frac{T_{g,wk} \, (P_{inj} - P_k) \rho_{wk}}{\mu_{l,wk}} \, .$$

2-35

The geometric transmissibility between a fracture element and the wellbore, $T_{g,wk}$, is calculated from Equation 2-25 with the assumption that e_w is infinite (although obviously a wellbore does not literally have a hydraulic aperture). With a very large e_w, Equation 2-25 reduces to:

$$T_{g,wk} = 2he_k^3 /(12a_k) \, .$$

2-36

If a rate of zero is specified, the wellbore remains connected to the formation and there can be cross-flow between fractures through the wellbore. Pressure drop within the wellbore is assumed negligible. In this case, Equation 2-34 is still included in the flow equations, but S is set to zero.

Constant pressure boundary conditions are implemented by including an element in the flow equations with a very large (effectively infinite) volume and hydraulic aperture. Because the element has a very large volume, its pressure remains constant regardless of fluid flow in or out of the element.

2.2.4 Spatial Domain

2.2.4.1 Generation of the Discrete Fracture Network

The fracture network used by the simulator can be generated deterministically or stochastically. If specified deterministically, the user explicitly specifies the locations of the fractures (or the potentially forming fractures).

Simple techniques are used for stochastic fracture network generation. Fractures are generated sequentially with an accept/reject algorithm. The total number of fractures in the network is specified by the user. Before identifying the locations of any of the fractures, a population of lengths and orientations is chosen according to prespecified statistical distributions. The locations of the fractures are then determined in order from largest fracture to smallest. For each fracture, a candidate location is identified, and certain checks are performed before "accepting" the candidate location. If the checks are not satisfied, a new candidate location is selected, and the process is repeated until an acceptable location is found.

Candidate locations are chosen at random within a specified spatial domain. In order to avoid boundary effects, the candidate locations are located in a spatial domain significantly larger than the problem domain. After all the fractures have been generated, the network is cropped to the size of the problem domain.

Candidate fracture locations are accepted or rejected on the basis of several checks designed to avoid numerical difficulties associated with the use of the Displacement Discontinuity method (Shou and Crouch, 1995). As discussed in Section 2.2.5.6, low-angle fracture intersections cause numerical difficulties. To avoid this problem, fractures are not allowed to intersect (or come within one meter of intersecting) at an angle below a specified threshold (in Models B and C in this chapter, the threshold was 20°). In addition, fracture intersections are not allowed to be closer than one meter.

As discussed in Section 2.2.3.8, new tensile fractures can form, but the potential locations of these new fractures must be specified in advance. There are several simple algorithms that can be used to identify the potential locations of these new tensile fractures. In all cases, the potential new hydraulic fractures are assumed to be

perpendicular to the remote least principal stress. This is a simplification because, while newly formed fractures should form perpendicular to the least principal stress, deformations during stimulation cause stress perturbation that can rotate the principal stresses locally from its original orientation.

One way to locate the potential new hydraulic fractures is deterministically. To ensure compatibility with the accept/reject requirements for fracture intersections, deterministic potential fractures are located prior to stochastic generation of fractures. The deterministic technique can be useful if it is assumed that newly forming fractures will always be able to propagate across natural fractures. An example is shown in Figure 2-3. The network shown in Figure 2-3 was used in Model B (Section 2.3.3.1).
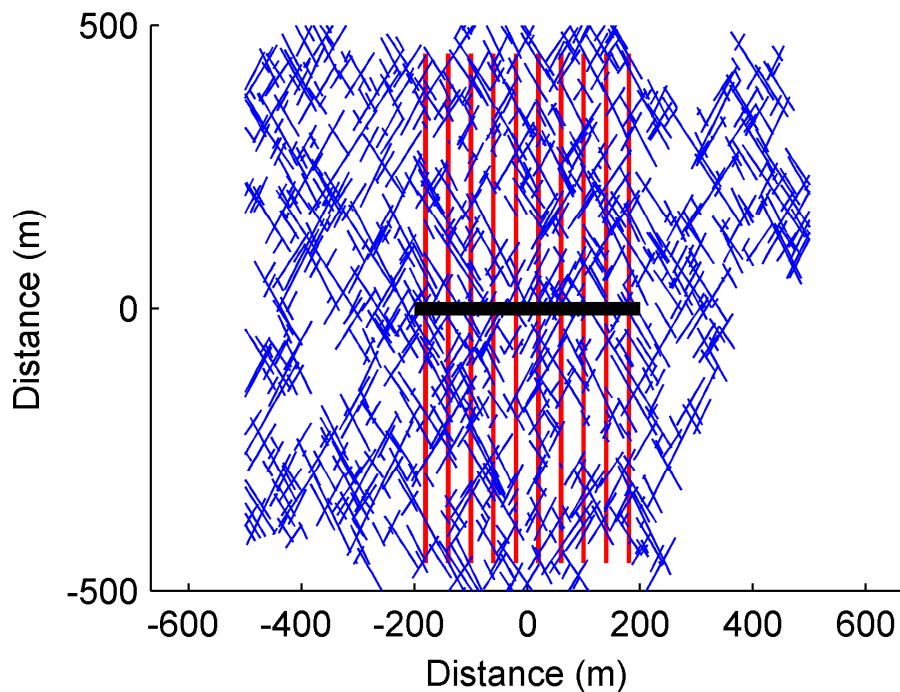
Figure 2-3: An example of a fracture network with prespecified deterministic potential hydraulic fractures. The black line is the (horizontal) wellbore; the blue lines are preexisting fractures, and the red lines are the potentially forming hydraulic fractures.

Two other algorithms are used for locating potential new tensile fractures. These algorithms are applied after the generation of the stochastic preexisting fracture network (rather than before, as with the deterministic method). These two algorithms can allow propagating fracture to terminate against natural fractures or propagate across natural

fractures. In the results shown in this chapter, the algorithms were used to create fracture networks where propagating fractures terminate against natural fractures.

One algorithm randomly selects a few locations along the wellbore to initiate potential new fractures, then propagates them away from the wellbore until they intersect preexisting fractures. Next, a few random locations along each of the intersected preexisting fractures are chosen, more potential fractures are initiated and propagated, and the process is repeated. A sample discretization using this method is shown in Figure 2-4. To avoid numerical difficulties, the newly formed fractures are not permitted to be closer than one meter from each other.
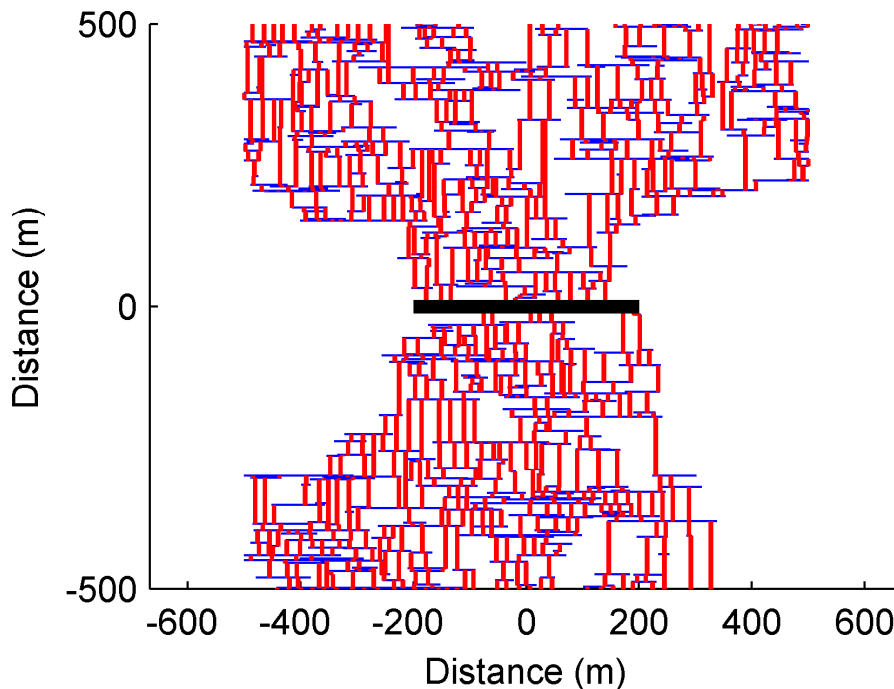
Figure 2-4: An example of a fracture network with potential hydraulic fractures. The black line is the wellbore; the blue lines are preexisting fractures, and the red lines are the potentially forming hydraulic fractures.

Another algorithm locates the potential new fractures off the tips of the preexisting fractures. These fractures are then propagated away from the wellbore until they reach a preexisting fracture. An example is shown in Figure 2-5. The network shown in Figure 2-5 is the network used for Model C in Section 2.3.3.2.
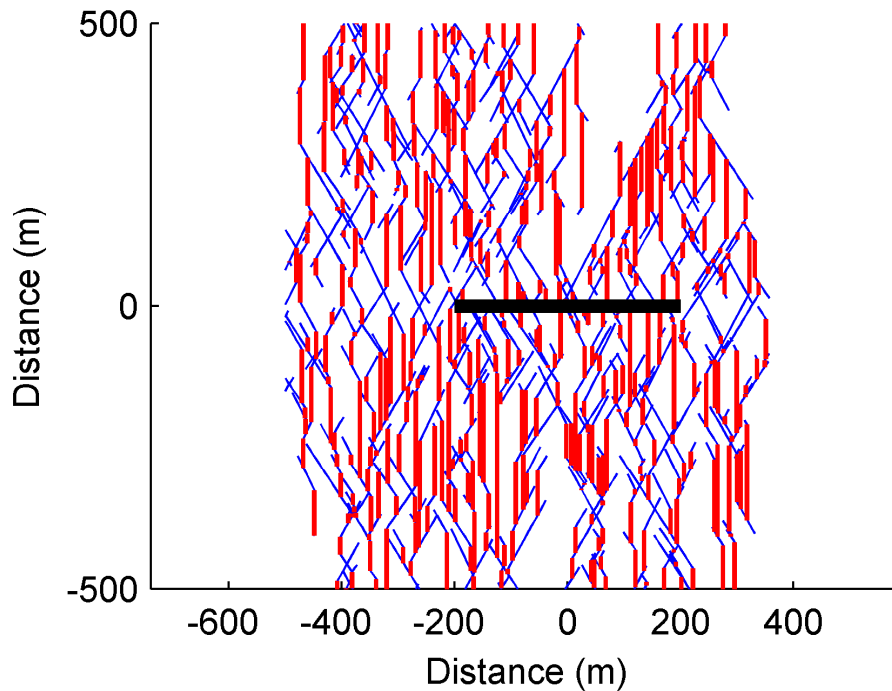
Figure 2-5: An example of a fracture network with potential hydraulic fractures. The black line is the wellbore; the blue lines are preexisting fractures, and the red lines are the potentially forming hydraulic fractures.

After all of the fractures have been generated, a breadth-first graph-search algorithm is used to identify which fractures are connected to the wellbore through a continuous pathway through preexisting or potential fractures. Because the matrix permeability is assumed to be zero, fractures that do not have a continuous pathway to the wellbore are hydraulically isolated from the injection. These fractures are omitted from the simulation.

2.2.4.2 Spatial Discretization

Because the matrix permeability is assumed to be negligible and mechanical deformation is calculated using the boundary element method, it is only necessary to discretize the fractures, not the area around the fractures. An example of a typical discretization is shown in Figure 2-6. Element size is not required to be constant.
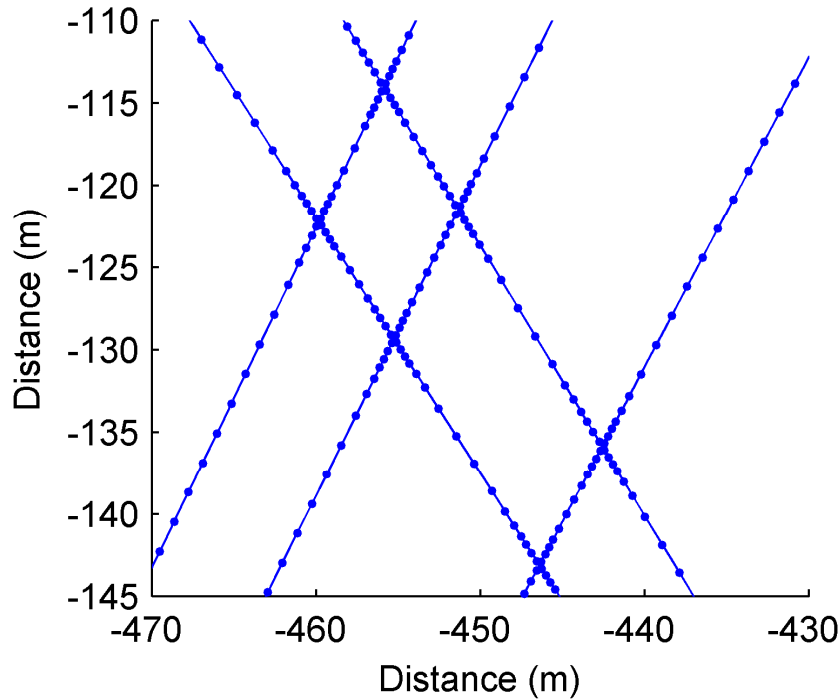
Figure 2-6: Example of a fracture network discretization. Each dot is located at the center of an element. Note the refinement around the fracture intersections.

The boundary element method of Shou and Crouch (1995) is inaccurate within a factor (less than one) of an element's half-length. To minimize inaccuracy, the discretization is refined when fractures are close together.

The discretization is performed in two parts. In the initial discretization, the fractures are discretized with a roughly uniform element half-length, a_{const}. In the second phase, the discretization is refined iteratively.

In the initial discretization, the algorithm starts at one end of each fracture and moves across it, generating one element at a time with a length of $2a_{const}$. Fracture intersections cannot occur in the middle of an element, and so an element is terminated if an intersection is reached or the end of the fracture is reached. Termination of elements at intersections or fracture endpoints results in elements that are not $2a_{const}$ long. If a newly created element has a half-length below a certain threshold, $0.5a_{const}$, it is combined with the previous element. An element is not combined with the previous element if the previous element is on the other side of an intersection or if there isn't a previous element because the new element is the first element on the fracture. If the endpoint of a fracture

is less than $0.1a_{const}$ from a fracture intersection, the end of the fracture is removed, leaving a "T" shaped intersection.

After generation of the initial discretization, an iterative algorithm is used for further refinement. During each iteration, two conditions are checked for each element, and if an element violates either condition, it is split in half. A minimum element half-length is set, a_{min}, below which an element is not split further. This process was repeated until no further elements are split.

The first condition enforces refinement around fracture intersections:

$$a_i < l_c + d_{ij}l_f, \hspace{4cm} \text{2-37}$$

where a_i is the half-length of element i, d_{ij} is the distance from the center of element i to intersection j, and l_c and l_f are constants. The second condition prevents elements from being too close together:

$$l_k a_i < D_{ij}, \hspace{4cm} \text{2-38}$$

where l_k was equal to a specified value, either l_s if elements i and j belong to the same fracture or l_o if i and j belong to different fractures. For elements of the same fracture, D_{ij} is the distance between the center of element j and the edge of element i. For elements of different fractures, D_{ij} is the smallest of three numbers: the distance between the center of element j and either (1) the center of element i or (2) either of the two endpoints of element i.

To avoid evaluating Equation 2-38 n^2 times every iteration, the spatial domain is divided into a grid, and Equation 2-38 is only evaluated between elements in neighboring gridblocks or in the same gridblock.

2.2.5 Special Simulation Topics

2.2.5.1 Efficient Matrix Multiplication

In the Shou and Crouch (1995) method, deformation at every element affects stress at every other element. As a result, updating stress requires multiplication of a dense matrix

of interaction coefficients -- a process that scales like n^2. As problem size grows, computation time and RAM requirements quickly become prohibitive.

Fortunately, approximate methods for efficient matrix multiplication are available. Two techniques are the fast multipole method (Morris and Blair, 2000) and hierarchical matrix decomposition (Rjasanow and Steinbach, 2007). The model uses Hmmvp, a publicly available implementation of hierarchical matrix decomposition and adaptive cross approximation (Bradley, 2012). Prior to running simulations, Hmmvp is used to perform matrix decomposition and approximation of the four matrices of interaction coefficients (Equations 2-19 to 2-22) for a given fracture network. The decomposition is stored and loaded into memory at the beginning of a simulation. Within the simulator, Hmmvp is used to perform the stress updating matrix multiplications. In Sections 2.3.5 and 2.4.5, it is demonstrated that Hmmvp drastically reduces the memory and computation requirements for matrix multiplication.

2.2.5.2 Crack Tip Regions

Special treatment is needed to model the progressive opening of both preexisting and newly forming fractures. As discussed in Section 2.2.3.8, the simulator is capable of modeling the propagation of new tensile fractures, but the locations of these fractures must be specified in advance. The simulator needs to have conditions to handle three situations: (1) the initiation of a new fracture (the activation of the first element on a newly forming fracture), (2) the extension of a newly forming fracture (the activation of subsequent elements on the newly forming fracture), and (3) the progressive opening of a preexisting fracture.

Initiation of new tensile fractures is handled in a very simple way. On each potentially forming hydraulic fracture, the (not yet activated) elements that are touching preexisting fractures or the wellbore are identified and labeled "initiation" elements. Initiation elements are "linked" to their adjoining elements on the neighboring fracture or the wellbore. At the end of each time step, a check is performed on all initiation elements to see if they should be activated. During the check, the fluid pressure of each initiation element is assumed to be equal to the fluid pressure that is highest among the elements that it is linked to. If the effective normal stress of an initiation element is less than zero

(tensile), the fracture is initiated. To avoid discretization dependence, all elements on the potentially forming fracture that are within one meter of the intersection (including the initiation element itself) are activated.

Once an element on a potentially forming hydraulic fracture has been activated, a second algorithm is used to extend the fracture. The stress intensity factor at a crack tip is estimated using the Displacement Discontinuity method according to the equation (Schultz, 1988):

$$K_I = \frac{G}{4\pi(1-\upsilon)} E_{open} \sqrt{\frac{2\pi}{a}} ,$$

2-39

where E_{open} is the opening of the crack tip element and a is its half-length. If the stress intensity factor reaches a critical threshold, $K_{I,crithf}$, then the fracture is allowed to propagate.

To propagate a fracture, a process zone is defined as the region of the newly forming fracture 2.0 m ahead of the crack tip. If the critical stress intensity factor is reached at the crack tip element, elements within the process zone are activated. For application of Equation 2-39, a crack tip element is permitted to be any element in the fracture that has been activated. It is not required to be the outermost active element.

A special treatment is also used to handle the propagation of opening along a preexisting fracture. In this case, only part of a preexisting fracture has opened. The location of the transition from open to closed on the fracture is considered an effective crack tip.

Without a special treatment, propagation of opening along a preexisting fracture could be unrealistically slow. In order for opening to propagate along a preexisting fracture, fluid must be able to flow from the open element at the effective crack tip into the adjacent closed element. Because geometric transmissibility between elements is calculated using a harmonic average (Equation 2-25), the rate of flow between a high transmissivity element and low transmissivity element is limited by the low transmissivity element. Because of this, the propagation of opening down a preexisting fracture is limited by the transmissivity of the closed elements ahead the effective

crack tip (without a special adjustment). This is not realistic because the crack tip should be able to propagate at a rate proportional to the (high) transmissivity of the open fracture behind the tip as fluid flows in behind it and progressively opens the crack. This is the same reason why a crack can propagate through very low permeability matrix: propagation depends on fluid flowing in behind the crack tip, not flowing ahead of the crack tip.

Opening induces tensile stresses ahead of the crack tip, but these stresses are unable to open the elements ahead of the effective crack tip because of a poroelastic response. Because of the low compressibility of water (relative to the fractures) and conservation of mass, effective normal stress of an element must be nearly constant unless there is fluid flow into or out of the element (otherwise the void aperture and resulting mass content of an element would change, from Equations 2-12 and 2-24). Because of this effect, the tensile stresses induced ahead of the crack tip produce a reduction in fluid pressure that allows the effective normal stress to remain nearly constant and prevents opening.

To correct for this problem, a special adjustment is used to increase element transmissivity ahead of effective crack tips. The stress intensity factor at an effective crack tip is calculated using Equation 2-39. If the stress intensity factor reaches a critical value, $K_{I,crit}$ (permitted to be different than $K_{I,crithf}$), then elements within 2.0 m of the effective crack tip (belonging to the same fracture) are placed in a process zone. The hydraulic aperture of the elements in the process zone is assigned a process zone hydraulic aperture, e_{proc} (equal to 106 microns), unless their hydraulic aperture is already higher than e_{proc}. The processes zone hydraulic aperture is high enough that fluid can rather quickly flow into the process zone.

As an aside, it is worth mentioning why a special adjustment is *not* needed for shear stimulation. In shear stimulation, transmissivity enhancement due to induced slip advances along a preexisting fracture. An effective shear crack tip can be defined at the boundary between where slip and transmissivity enhancement have taken place and where they have not. Shear stress concentration occurs ahead of the effective shear crack tip, just as tensile stress concentration occurs ahead of an effective opening crack tip. However, unlike for tensile stresses, there is not a poroelastic response that acts to

counteract the effect of the stress concentration. In this case, the induced shear stress can cause shear deformation and transmissivity enhancement ahead of effective crack tip without requiring any fluid to flow ahead of the crack tip, a process we refer to as crack-like shear stimulation (Sections 3.4.2.2 and 4.4.2).

2.2.5.3 Dynamic Friction Weakening

Seismicity occurs when friction weakens rapidly on a fault, resulting in a rapid release of shear stress through slip. The leading theory to describe friction evolution on a fault is rate and state friction, and it is widely used in earthquake modeling (Dieterich, 2007). In rate and state friction, the coefficient of friction changes over time as a function of sliding velocity and the past sliding history of the fracture. According to rate and state friction, the coefficient of friction is (Segall, 2010):

$$\mu_f = f_0 + a \ln \frac{v}{v_0} + b \ln \frac{\theta v_0}{d_c},$$ 2-40

where f_0 is a constant of order 0.6-1.0, a and b are constants of order 0.01, v_0 is a specified reference velocity, θ is a state variable that changes over time as friction evolves on the fracture, and d_c is a characteristic weakening distance on the order of microns (though in some applications, much larger values are used). In Chapter 4, a numerical approach is demonstrated that couples rate and state friction evolution, deformation, and fluid flow.

Coupling seismicity modeling with fluid flow is useful because in some cases seismicity is triggered by injection or other human activities (McGarr, 2002; Chapters 4 and 5). The model used in Chapter 4 is an earlier version of the model described in this chapter, and the model in this chapter retains the ability to do rate and state friction simulation (although that capability is not discussed).

Rate and state friction is significantly more intensive computationally than simulations using constant coefficient of friction. One reason rate and state friction models are so computationally intensive is that they are numerically unstable unless a very finely resolved spatial discretization is used (LaPusta, 2001). Another reason is that

rate and state friction requires a very large number of very short time steps in order to simulate seismic events accurately because frictional weakening is very non-linear.

In Chapter 4, explicit third-order Runge-Kutta time stepping was used. Sliding velocity was calculated by treating velocity as an unknown and calculating the velocity at each element to enforce the frictional equilibrium equation. This approach has significant difficulty when applied in settings where effective normal stress is very low. At low effective normal stress, small perturbations in shear stress can lead to large changes in sliding velocity, making accuracy challenging for explicit time stepping methods unless very small time steps are used. Possibly, implicit time stepping would perform better for settings with low normal stress, but that approach has not been tested.

As an alternative to rate and state friction, static/dynamic friction, was used to compute the results shown in this chapter. With static/dynamic friction, if the shear stress of an element exceeds the Coulomb failure criterion, Equation 2-8, then the element is considered to be sliding and its coefficient of friction is instantaneously lowered to a new dynamic value, μ_d. The sudden lowering of friction causes rapid sliding and can result in cascading sliding and weakening of friction on neighboring elements. The result is a process that mimics earthquake nucleation and propagation. Once the sliding velocity of a sliding element has gone below a certain threshold, friction is instantaneously restrengthened to its original static value.

When static/dynamic friction is used, checks are performed for frictional weakening and element status for all elements after every iteration in the shear stress subloop (see Section 2.2.3.7). Checks for friction restrengthening are performed at the end of each time step.

Static/dynamic friction has certain drawbacks, but it is a reasonable compromise between realism and efficiency. Static/dynamic friction is tested in Section 2.3.3.1 and discussed in Section 2.4.2.5. In Section 4.4.12, results from rate and state friction modeling were compared to static/dynamic friction modeling from McClure and Horne (2010b), and the results were qualitatively similar, with some differences that are described in the section.

In McClure and Horne (2010b), static/dynamic friction was used, but a radiation damping term was not used, and so all slip during a seismic event was effectively instantaneous. That was a rather problematic approach, and in the present version of the model, the inclusion of a radiation damping term prevents slip from occurring instantaneously (though weakening and restrengthening of friction is instantaneous).

Because static/dynamic friction allows a seismic event to nucleate at a single element (and friction weakens instantaneously), there is an inherent discretization-dependence to the results (also discussed in Section 4.1.3). Earthquake models with this property have been referred to as "inherently discrete" (Ben-Zion and Rice, 1993). In contrast, rate and state simulations that use an adequate spatial discretization require nucleation to occur on a cooperating patch of several elements, and these models are convergent to grid refinement.

A major assumption of the model in this chapter, quasistatic equilibrium, breaks down at very high slipping velocity, where dynamic stress transfer effects can play an important role. The radiation damping term is used to approximate the effects of dynamic stress transfer, but it is not necessarily accurate for calculations involving more than a single, planar fault (discussed by LaPusta, 2001). Full dynamic simulations could be used to solve the problems more accurately, but these are extremely computationally intensive and would not be feasible for large, complex fracture networks.

2.2.5.4 Alternative Methods for Modeling Friction

We have developed an alternative method for earthquake modeling that it intended to replicate results from rate and state friction, but with much better efficiency. The method has not been extensively tested, and because it remains a work in progress, results using the method are not given in this dissertation. However, the method is summarized in this section because it is a potential topic for future work.

An ideal method for modeling seismic events should be convergent to grid refinement, give a reasonably accurate answer with a coarse refinement, and give results similar to rate and state friction simulation. There are two particular problems that need to be overcome to make efficient earthquake simulation possible. Problem (1): crack tip

discretization error (with a coarse discretization) causes difficulty in modeling rupture propagation. Problem (2): groups of elements must be able to collectively interact to nucleate a rupture.

With crack tip discretization error (Problem 1), the issue is that the stress concentration at the crack tip is underestimated with a coarse discretization. With rate and state friction, friction weakening ahead of a rupture tip occurs because a concentration of stress causes displacement to occur ahead of the tip while the coefficient of friction is still high. If the concentration of stress ahead of the rupture tip is too weak because of inadequate discretization (the initiating rupture patch is discretized by one or a few elements), friction weakening may be artificially limited, and a seismic event may "fizzle out" shortly after nucleation.

The challenge of modeling rupture initiation (Problem 2) is that in order for results to be convergent to grid refinement, multiple elements must be able to cooperate to nucleate a single seismic event. With rate and state friction, there is a characteristic minimum patch size for nucleation of an earthquake (Segall, 2010). Therefore, with sufficient discretization refinement, nucleation patches are composed of a large number of elements. Any method where individual elements are able to nucleate ruptures will not be convergent to grid refinement.

Static/dynamic friction does not suffer the rupture initiation issue (Problem 2) because a single element is able to nucleate an event, regardless of element size. The problem is avoided because in static/dynamic friction the characteristic length scale of friction weakening is zero (an element does not have to displace over any distance in order to experience a drop in friction). However, as a consequence, the simulation results are discretization dependent.

A strategy called "RSQSim" has been proposed as an efficient method for modeling earthquakes (Dieterich, 1995; Dieterich and Richards-Dinger, 2010). In this strategy, a seismic event can nucleate from a single element. Semi-analytical treatments of state evolution are used to calculate the timing of earthquake nucleation. RSQSim requires that elements must be larger than the minimum nucleation patch size, and as a result it is not able to model multiple elements collectively nucleating (it does not solve Problem 2),

and as with static/dynamic friction, results are discretization dependent. Dieterich (1995) suggested handling the crack tip discretization problem (Problem 1) with a special multiplying factor applied to the elements adjacent to rupture tips. However, it is not clear whether this method is robust because it is effectively a heuristic tuning parameter. Because it is not theoretically derived, it is not clear whether it can be guaranteed to work in all cases. Ideally, it should be possible to derive the crack tip adjustment theoretically without needing to tune it using trial and error. Another issue is that it is unclear how RSQSim could be coupled with fluid flow.

In the following paragraphs, our proposed alternative method for efficient earthquake simulation is described.

The default setting for an element is "stuck." Stuck elements have zero sliding velocity. Stuck elements are converted to "sliding" elements if their shear stress exceeds their frictional resistance to slip according to the Coulomb law (Equation 2-8) with a constant, static coefficient of friction. Once converted to a sliding element, the element slides according to a velocity strengthening model, equivalent to the rate and state friction expression for friction (Equation 2-40) with the b coefficient set to zero.

A special condition is applied to sliding elements to determine if they should begin "nucleation." When an element is nucleating, a displacement weakening law is applied such that the coefficient of friction weakens linearly as a function of displacement over a specified displacement distance until it reaches a specified minimum value. Simultaneously, the velocity strengthening term continues to be used. This approach is equivalent to using the rate and state friction law (Equation 2-40) with a displacement weakening f_0 term and the b coefficient equal to zero.

It can be shown that during nucleation of a rupture using rate and state friction with the aging law for state evolution (Equation 4-9), friction evolution is equivalent to linear displacement weakening:

$$\frac{\partial \theta}{\partial t} = 1 - \frac{v\theta}{d_c} \sim -\frac{v\theta}{d_c} \Rightarrow \log(\theta) = \frac{-vt}{d_c} + C = \frac{-D}{d_c} + C \Rightarrow \frac{\partial \mu_f}{\partial D} = -\frac{b}{d_c},$$

where it has been assumed that during rupture, state is decreasing rapidly, and so $|v\theta/d_c|$ >> 1.0.

The minimum value of f_0 (the value at which friction no longer weakens with displacement) can be chosen so that it is equivalent to using a constant f_0 in the rate and state expression with a non-zero b parameter and with the state variable equal to its steady state value for sliding at 1.0 m/s. The steady state value for the state variable can be calculated for a given sliding velocity by setting the time derivative of state equal to zero in the aging law (Equation 4-9):

2-42

$$\frac{\partial \theta}{\partial t} = 1 - \frac{v_{ss}\theta_{ss}}{d_c} = 0 \Rightarrow \theta_{ss} = \frac{d_c}{v_{ss}}.$$

It is important to carefully select the condition to determine when an element should begin nucleation (begin to experience displacement weakening). If an element (or a patch of sliding elements) begins to experience displacement weakening, but the patch is smaller than the characteristic minimum patch size, then sliding will relieve shear stress faster than friction weakening induces slip, and a frictional instability (rapid weakening of friction) will not occur. Frictional instability requires that the weakening of friction occurs faster than sliding relieves shear stress. This principle is the basis of our nucleation condition.

The nucleation condition we propose is:

2-43

$$\frac{\partial |\tau|}{\partial D} < \frac{\partial \mu_f}{\partial D} \sigma_n'.$$

In Equation 2-43, the coefficient of friction derivative term on the right-hand side is a constant value because (by definition) weakening is linear with displacement. The left-hand side of Equation 2-43 is evaluated numerically for each element by determining the actual change in shear stress and displacement experienced by the element during the

time step. The shear stress change of an element is affected by its own sliding and also by the sliding of all other elements. If a patch of elements is sliding, the term on the left-hand side of Equation 2-43 is equivalent to the stiffness of the entire slipping patch. If a single element is sliding, it is equivalent to the stiffness of the single element. If Equation 2-43 is satisfied, then the slipping patch has become large enough (and its equivalent stiffness low enough) that the initiation of displacement weakening will lead to frictional instability and rapid acceleration of sliding velocity. Testing with well-resolved discretizations found that this method (successfully) nucleated events when slipping patches reached the same patch size as the full rate and state simulations. The method also worked well with coarse discretizations, even discretizations so coarse that a single element was larger than the minimum nucleation patch size.

A condition is needed for returning sliding elements to the "stuck" state. Recall that if an element is not "stuck," then it is sliding according to a velocity strengthening law (and may experience displacement weakening of friction if it has experience nucleation). If the sliding velocity of an element goes below a certain threshold, it is reset to "locked," and its sliding velocity returns to zero. Different thresholds are used for elements that have nucleated and elements that have not nucleated (the threshold is higher for the nucleated elements). If a nucleated element is returned to the "stuck" state, its coefficient of friction is returned to its initial value (the displacement weakening of friction is reset).

The crack tip discretization error problem is solved by applying a mechanism to enforce "nucleation" at the crack tip. Nucleation is enforced by reducing the f_0 to the minimum value it would reach due to the displacement weakening (which is a specified model parameter derived using Equation 2-42).

An appropriate condition is needed to determine when to enforce the crack tip adjustment. If nucleation is applied too readily, then ruptures will propagate further than they should. If nucleation is applied to sparingly, ruptures may not propagate far enough. The goal is that simulated ruptures with coarse discretizations will propagate the same distance as if full rate and state simulation were performed with a well resolved discretization. The crack tip adjustment should have no effect if a large number of elements are sliding (because the discretization is well resolved and no adjustment is

needed). It should also be possible to derive the adjustment in advance, rather than tuning it by trial and error.

It was found that a stress intensity factor approach worked as a method for determining when to apply nucleation at the crack tip. The stress intensity factor (also discussed in Section 2.2.5.2) may be calculated for mode II deformation using the Schultz (1988) method (Equation 2-39), with sliding displacement D replacing opening displacement E_{open}. With this method, nucleation is enforced at the crack tip if the stress intensity factor exceeds a specified mode II fracture toughness. It should be possible to derive the fracture toughness from rate and state parameters, but we have not yet done so. We found with trial and error that if an appropriate fracture toughness was used, then the distance of rupture propagation was insensitive to discretization refinement and consistent with a full rate and state simulation.

2.2.5.5 Adaptive Domain Adjustment

During some simulations, there are large regions of the spatial domain where stresses and fluid pressures change very slowly during all or some of the simulation. Depending on the specifics of the problem, fractures distant from the injector may experience virtually zero fluid flow and be in a stress state such that they are not close to either sliding or opening. Given this situation, there is an opportunity to reduce computational effort by not updating stresses at these elements during every time step and/or by not including them in the flow simulation equations. This strategy is referred to as adaptive domain adjustment. Adaptive domain adjustment is tested Sections 2.3.3.1 and 2.4.2.4.

Elements that are not deforming and experience virtually zero fluid flow are identified and placed in a *nochecklist*. All other elements are placed in a *checklist*. The stresses on elements in the *nochecklis*t are not updated during every time step. Cumulative deformations between *nochecklist* updates are tracked and at intervals the *nochecklist* elements are updated from the cumulative *checklist* deformations. Because linearly elastic deformations are path-independent, updating stresses periodically results in exactly the same final stresses as if they were updated frequently.

As an additional optimization, *nochecklist* elements are removed from the system of fluid flow equations. Removing the *nochecklist* elements from the fluid flow equations causes them to have effectively zero transmissivity.

An algorithm is used to sort elements into the *nochecklist*. To aid in categorization, a separate list called an *activelist* is kept. Once an element is placed in the *activelist*, it remains there for the duration of the simulation. Elements can be added to the *activelist* for the following reasons: connection to the wellbore, sliding residual greater than a specified negative value, *slidetol* (sliding occurs when sliding residual become positive), effective normal stress less than a specified positive value, *opentol* (opening occurs when normal stress becomes negative), or a perturbation from initial fluid pressure greater than 0.1 MPa. In Simulations B5 and B9 (the two simulations in this chapter that use adaptive domain adjustment), *opentol* was 4.0 and *slidetol* was -2.0. The entire problem domain is gridded into a 30x30 grid, and blocks containing an element in the *activelist* are identified as active blocks. All elements contained in an active block or a block surrounding the active blocks are placed in the *checklist*. All other elements are placed in the *nochecklist*. Overall, the algorithm leads to a region of *checklist* elements around the injector well that spreads out gradually over time as the region of stimulation grows.

2.2.5.6 Strain Penalty Method

Inaccuracy in the BEM calculations can occur when elements are in close proximity relative to their size (Crouch and Starfield, 1983). The best solution to this problem, described in Section 2.3.2, is to refine the discretization in locations where fractures are in close proximity. However, this strategy is not practical at low-angle fracture intersections, where neighboring fractures lie very close together over significant distances. Adequately discretizing these geometries requires a large number of extremely small elements, which is numerically undesirable in the fluid flow calculations. To avoid excessive discretization refinement, a minimum element size is specified in the discretization algorithm (Section 2.2.4.2). As discussed in Section 2.2.4.1, one strategy to avoid these difficulties is to avoid creating fracture networks that contain low-angle fracture intersections.

If low-angle intersections are included in a simulation, elements can interact in unstable ways. Displacements and stresses can grow extremely large, and displacement can form in strange, unrealistic patterns (see examples in Section 2.3.4). Not only are these behaviors unrealistic, in severe cases can cause simulations to be unusable. Some inaccuracy at low-angle fracture intersections is perhaps acceptable, but it is not acceptable for low-angle intersections to cause problems so severe that they prevent a simulation from continuing.

An algorithm, referred to as the strain penalty method, is used to minimize the effects of inaccuracies at low-angle fracture intersections. The algorithm identifies where large strains are beginning to develop and applies penalty stresses to prevent the strains from growing further. This approach could be considered a crude way to mimic rock failure, which is the process in nature that prevents extreme concentrations of stress and strain.

There is no theoretical basis for the strain penalty method. It is intended as a way to prevent catastrophic numerical error. It does not ensure that the solution is completely accurate. With discretization refinement, the region of inaccuracy can be limited to a small region very near the center of the intersection (Section 2.3.4), which minimizes error.

Perfect accuracy at intersections is probably a false goal because in reality, very complex deformations occur at fracture intersections that do not conform to the assumption of small strain, linearly elastic deformation made by the Shou and Crouch (1995) boundary element method. Therefore, numerical accuracy is overwhelmed by error from the model assumptions. This is not an issue unique to our model. Fracture intersections are very challenging for all numerical methods to describe, not just the boundary element method.

In most simulations in this chapter -- Models A, B, and C, the strain penalty method was not used (it was also not needed because low-angle intersections were not present in these networks). In Section 2.3.4, the strain penalty method was tested on Model D, which contains a very low-angle fracture intersection (Figure 2-33 to Figure 2-36).

At any location on a (zero-curvature) fracture, strain due to varying displacement discontinuity can be defined as:

2-44

$$\varepsilon_k = \frac{dD_k}{dx},$$

where k refers either normal, n, or shear, s, displacement discontinuity and x refers to the distance along the fracture. The derivatives for both modes of deformation are calculated using finite difference approximations at the boundaries between elements. A threshold strain, $\varepsilon_{k,lim}$, is set at each element boundary, and if the absolute value of strain at any element edge exceeds the threshold strain, a penalty stress is applied. The subscript k can refer to n, strain in normal displacement or s strain in shear displacement. After a penalty stress is applied, the limit $\varepsilon_{k,lim}$ at the interface is updated to be equal to the current value of ε_k.

The penalty stress is calculated according to:

2-45

$$\Delta\sigma_{k,strainadj} = (\varepsilon_k - \varepsilon_{k,\lim})\frac{G}{1-\nu}.$$

The penalty stress can be applied to both elements at the interface or only to one. The algorithm determines if the motion of each element in the preceding time step acted to increase or decrease the absolute value of the strain at the element interface. If only one element did, the full adjustment is applied to that element. If both did, the adjustment is divided between them proportionally based on their effect on the change in the strain.

The penalty stress is applied at the beginning of the subsequent time step. To prevent excessively large penalty strains from being applied during the subsequent time step, the adaptive time stepping equation, Equation 2-33 (Section 2.2.3.9), is applied with $\delta_{strainadj}$ defined as being equal to the largest absolute value of $\Delta\sigma_{k,strainadj}$, and $\eta_{targ,strainadj}$ defined to be a value equal to one tenth of η_{targ}. As with δ and η_{targ} (explained in Section 2.2.3.9), if the value of $\delta_{strainadj}$ exceeds $4\eta_{targ,strainadj}$, the time step is rejected and repeated with smaller value of dt.

2.2.5.7 Neglecting Stresses Induced by Deformation

A major purpose of the model in this chapter is to couple deformation with fluid flow. However for purposes of testing and comparison, it is useful to neglect the stresses

induced by deformation (Sections 2.3.3.1 and 2.4.2.6). To neglect stresses induced by deformation, all nondiagonal interaction coefficients in the boundary element matrices (Equations 2-19 to 2-22) are set equal to zero. In this case, when an element opens or slides, it affects its own stress, but not the stress at surrounding elements. This assumption has often been made in modeling of shear stimulation, apparently because it simplifies the design of the model significantly (Bruel, 1995; Bruel, 2007; Sausse et al., 2008; Dershowitz et al., 2010).

Neglecting the off-diagonal interaction coefficients causes element stiffness to be discretization dependent because in the Shou and Crouch (1995) method, self-interaction coefficients are a function of element size. To avoid discretization dependence when neglecting stress interaction, self-interaction coefficients are defined so that they are independent of element size. By treating a fracture as a single, constant displacement boundary element, the stiffness of a fracture, K_{frac}, can be calculated as (Crouch and Starfield, 1983):

$$K_{frac} = \frac{1}{\pi(1-\upsilon)}\frac{1}{a_{frac}},$$

2-46

where a_{frac} is the half-length of the fracture. The self-interaction coefficients of each element for effect of opening deformation on normal stress and shear deformation on shear stress are set to the fracture stiffness given by Equation 2-46. No adjustment is needed for the self-interaction coefficients that relate opening deformation to shear stress and shear deformation to normal stress because they are always zero.

2.3 Results

A variety of simulations were performed using four test models: Models A, B, C, and D. The simulations were designed to test the accuracy, convergence, and efficiency of the simulator and to test the effect of a variety of simulation options. In addition, tests were performed to evaluate the accuracy and scaling of Hmmvp for hierarchical matrix decomposition. Section 2.3.1 gives the details of the simulation settings. Other details of

the simulations and results are given in Sections 2.3.2, 2.3.3, 2.3.4, and 2.3.5.   All simulations were performed using a single processor in a dual quad-core (8 cores) Nehalem CPU running at 2.27 GHz with 24 GB memory as a part of the CEES-Cluster run by the Center for Computational Earth and Environmental Science at Stanford University.

2.3.1 Simulation and Discretization Details

The discretization settings for all models are given in Table 2-1. Models A1-A4 and D1 used constant element size discretizations, and A5, B, C, and D2 used variable element size discretizations.

Table 2-1: Discretization settings

Model	Total Elements	a_{const} (m)	l_c (m)	l_f	l_s	l_o	a_{min} (m)
A1	12	2.5	inf	0	0	0	-
A2	60	0.5	inf	0	0	0	-
A3	300	0.1	inf	0	0	0	-
A4	1500	0.02	inf	0	0	0	-
A5	48	1	0.3	0.3	0.4	2	0.2
B	52,748	5	0.3	0.3	0.4	2	0.2
C	22,912	5	0.3	0.3	0.4	2	0.2
D1	40	2.5	inf	0	0	0	-
D2	308	2.5	inf	0	0.3	2	0.1

Simulations performed with Model A are labeled A[X]-S[Y], where A[X] runs from A1 to A5, and S[Y] runs from S0 to S12. The [X] number refers to the discretization, and the [Y] refers to the particular settings used. Simulations performed with Model B are labeled B1-B9 (all use the same discretization), and the single simulation run with Model C is called C1. Simulations performed with Model D are labeled D[X]-DS[Y], where

D[*X*] could be D1 or D2 (referring to discretization), and DS[*Y*] could be DS1 or DS2 (referring to settings).

Table 2-2 gives the baseline settings that were the same in all simulations. For each group of simulations (A, B, C, and D), specific baseline settings are defined, given in Table 2-3. Settings for specific Model A and B simulations differ according to settings given in Table 2-4 and Table 2-5. Settings for DS1 and DS2 are identical except that DS2 uses the strain penalty method.

Table 2-2: Baseline settings for all simulations.

h	100 m
G	15 GPa
v	0.25
η	3 MPa/(m/s)
μ_f	0.6
$\sigma_{n,Eref}$	20 MPa
$\sigma_{n,eref}$	20 MPa
φ_{Edil}	0 °
φ_{edil}	2.5 °
$T_{hf,fac}$	10^{-9} m^2
$K_{I,crit}$ (Section 2.2.5.2)	1 MPa-m$^{1/2}$
$K_{I,crithf}$ (Section 2.2.5.2)	1 MPa-m$^{1/2}$
cstress (Section 2.2.3.3)	Turned off
Crack tip adjustment (Section 2.2.5.2)	Turned on
BEM method (Section 2.2.5.1)	Hmmvp
ε_{tol} (used by Hmmvp, Equation 2-50)	10^{-6}
Transmissivity updating	Implicit
Friction (Section 2.2.5.3)	Constant (no dynamic weakening)
Adaptive domain adjustment (Section 2.2.5.5)	Not used

Table 2-3: Model specific baseline settings.

	Model A	Model B	Model C	Model D
S_0	0 MPa	0.5 MPa	0.5 MPa	0.5 MPa
$S_{0, open}$	0 MPa	0.5 MPa	0.5 MPa	0.5 MPa
E_0	0.1 mm	.8 mm	0.5 mm	.5 mm
e_0	0.02 mm	0.03 mm	0.06 mm	0.02 mm
P_{init}	18 MPa	30 MPa	35 MPa	40 MPa
σ_{yy}	26 MPa	75 MPa	75 MPa	55 MPa
σ_{xx}	21 MPa	50 MPa	50 MPa	50 MPa
σ_{xy}	0 MPa	0 MPa	0 MPa	10 MPa
Duration of Simulation	Until $P = P_{inj}$ everywhere	2 hrs	2 hrs	Until $P = P_{inj}$ everywhere
P_{injmax}	20.25 MPa	70 MPa	70 MPa	60 MPa
q_{injmax}	none	50 kg/s	50 kg/s	100 kg/s
η_{targ}	0.05 MPa	0.5 MPa	0.5 MPa	0.05 MPa
$D_{e,eff,max}$	10 mm	5 mm	5 mm	5 mm
K_{hf}	Not used	0.01 MPa^{-1}	0.01 MPa^{-1}	Not used
mechtol (Section 2.2.3.5)	0.0003 MPa	0.003 MPa	0.003 MPa	.003 MPa
itertol (Section 2.2.3.1)	0.001 MPa	0.01 MPa	0.01 MPa	.01 MPa
Pseudo-3D adjustment (Section 2.2.3.2)	Not used	Used	Used	Used
New fractures (Section 2.2.3.8)	Not permitted	Not permitted	Permitted	Not permitted
Strain Penalty (Section 2.2.5.6)	Not used	Not used	Not used	Used with, $\varepsilon_{n,lim}$ and $\varepsilon_{s,lim}$ = .001

2.3.2 Model A: Small Test Problem

A small test problem (Model A, shown in Figure 2-7) was used to verify accuracy and convergence and to experiment with different numerical settings. Model A was designed to mimic the opening of splay fractures off a sliding, preexisting flaw (for examples from outcrops, see Pollard and Segall, 1983, and Mutlu and Pollard, 2008).

Constant pressure injection was performed at the center of the middle fracture until the fluid pressure everywhere in the model was equal to the injection pressure. The initial fluid pressure was low enough that none of the fractures were initially open or sliding.
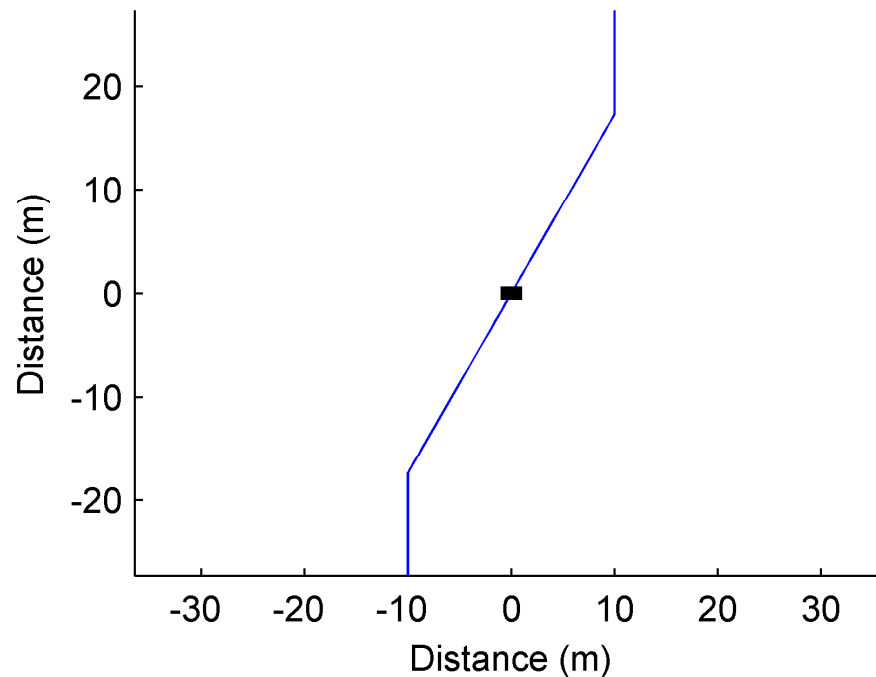
Figure 2-7: Model A. The blue lines represent preexisting fractures. The black line represents the wellbore.

In order to test the accuracy and convergence of the model's implementation of the Shou and Crouch (1995) Displacement Discontinuity method, the final displacement distributions were compared to results from an existing code, COMP2DD (Mutlu and Pollard, 2008), which implements the Crouch and Starfield (1983) Displacement Discontinuity method. There was not another code available that could be used for

comparison to test the accuracy of the time-dependent part of the calculation. Convergence of the time-dependent results was tested by refining the simulations in time and space and comparing results to the most highly refined solutions.

COMP2DD calculates fracture opening and sliding for given values of remote stress and fluid pressure. Unlike the model described in this chapter, COMP2DD performs the calculation in a single step; it does not take time steps. In COMP2DD, fluid pressure is assumed to be constant and equal to a value specified by the user. In our model, the fluid pressure changes over time and is variable spatially. To mimic COMP2DD using our model, constant pressure injection was performed until the fluid pressure in every element was the same as the fluid pressure specified in the COMP2DD calculations. Because the final fluid pressures were the same, the final displacements were expected to be the same as long as the results from the model are path-independent.

The results from the model are not necessarily path-independent, but path-dependence does not appear to have played a role in the particular problem used for the code comparison because, as will be shown, the COMP2DD solution was identical to the solution from the model. Stresses caused by opening and sliding are path-independent because deformation is assumed to be elastic. However, determination of the amount of fracture sliding is not path-independent because sliding against friction is not a reversible process: if friction is reduced on a fracture, the fracture will slide, but if friction is subsequently reapplied, the fracture will not slide back to its initial position.

Because elements can be open, sliding, or stationary, COMP2DD does not know ahead of time which boundary conditions to apply (for further discussion, see Section 2.2.3.7). COMP2DD uses a linear complementarity algorithm to handle this issue. Mutlu and Pollard (2008) demonstrated how complementarity has efficiency and accuracy advantages compared to penalty and Lagrange multiplier methods.

In total, 18 simulations were run. Simulations were named according to the both the discretization (A1-A5) and settings (S0-S12): A1-S3, A2-S3, A3-S3, A4-S3, A5-S3, A4-S0, A5-S1, A5-S2, A5-S3, A5-S4, A5-S5, A4-S6, A4-S7, A3-S8, A3-S9, A3-S10, A3-S11, and A3-S12.

The baseline settings used for the simulations are given in Section 2.3.1. Table 2-4 gives specific settings for individual simulations. If not stated explicitly in Table 2-4, the settings used in each simulation were the same as the baseline settings given in Table 2-2 and Table 2-3. Models A1-A4 had constant element size with increasing level of refinement. Model A5 had a nonuniform discretization with slightly fewer total elements than A2 (Section 2.3.1).

Table 2-4: Deviations from baseline settings for Simulations S0-S12.

S0	*Direct BEM (Hmmvp not used) (Section 2.2.5.1)*
S1	$\eta_{targ} = 0.00125$ *MPa (Section 2.2.3.9)*
S2	$\eta_{targ} = 0.0125$ *MPa (Section 2.2.3.9)*
S3	
S4	$\eta_{targ} = 0.5$ *MPa (Section 2.2.3.9)*
S5	$\eta_{targ} = 4$ *MPa (Section 2.2.3.9)*
S6	*Direct solution (Section 2.3.2.1), mechtol = .0001 (Section 2.2.3.5), itertol = .0002 (Section 2.2.3.1)*
S7	*Direct solution (Section 2.3.2.1) and uses direct BEM (not Hmmvp), (Sections 2.2.5.1), mechtol = .0001 (Section 2.2.3.5), itertol = .0002 (Section 2.2.3.1)*
S8	$E_0 = 0.01$ *mm (Section 2.2.1)*
S9	*cstress option (Section 2.2.3.3) and $E_0 = 0.01$ mm (Section 2.2.1)*
S10	*cstress option (Section 2.2.3.3) and $E_0 = 0.1$ mm (Section 2.2.1)*
S11	*cstress option (Section 2.2.3.3) and $E_0 = 1$ mm (Section 2.2.1)*
S12	*cstress option (Section 2.2.3.3) and $E_0 = 10$ mm (Section 2.2.1)*

COMP2DD was used to solve the problem with Model A4, the most finely resolved discretization (Section 2.3.1). The constant displacement method used by COMP2DD (Crouch and Starfield, 1983) is lower order than the quadratic method used in the

simulator (Shou and Starfield, 1995), and so for the same discretization, COMP2DD should be less accurate. However, the accuracy of the simulator is limited by the convergence criteria used in the iterative solvers (Sections 2.2.3.1, 2.2.3.4, and 2.2.3.5). Therefore, the COMP2DD solution should not be considered an "exact" solution because its results may be of comparable order of accuracy as the most precise results from the model. To demonstrate the accuracy of the model, it is sufficient to show that with refinement the results converge to an answer that is very close to the COMP2DD result.

The COMP2DD result was compared to results from Simulations A1-S3, A2-S3, A3-S3, A4-S3, and A5-S3. Figure 2-8 and Figure 2-9 show the final opening and sliding distributions from the simulations and COMP2DD.
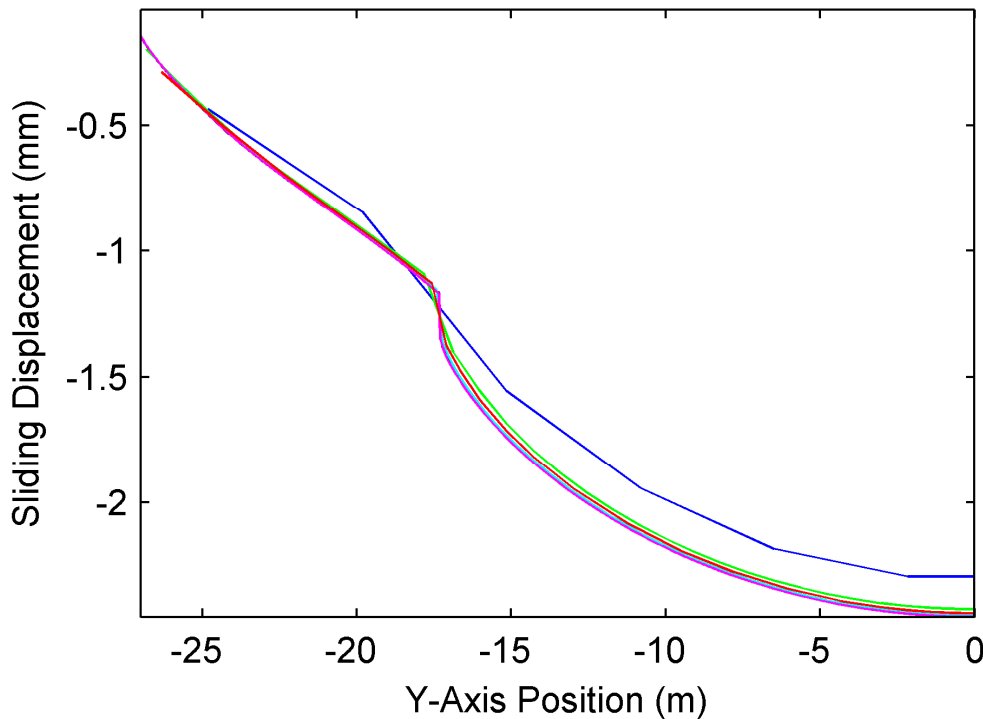
Figure 2-8: Final sliding distribution along a section of Model A for COMP2DD (black), A1-S3 (blue), A2-S3 (green), A3-S3 (cyan), A4-S3 (maroon), and A5-S3 (red). The COMP2DD and A4-S3 lines coincide.
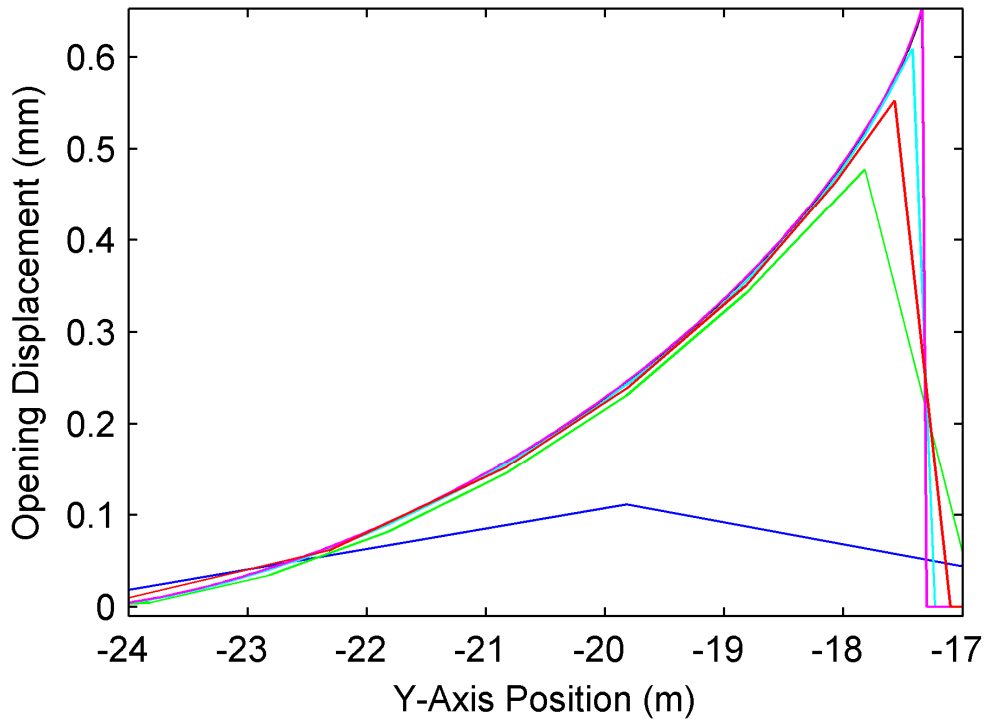
Figure 2-9: Final opening distribution along a section of Model A for COMP2DD (black), A1-S3 (blue), A2-S3 (green), A3-S3 (cyan), A4-S3 (maroon), and A5-S3 (red). The COMP2DD and A4-S3 lines coincide.

The relative difference, e_j, between the results from COMP2DD and from the model was quantified by comparing the final values of opening and sliding at different points along the fracture. The comparison points were at the center of each element in the discretization. When comparing results, the term "relative difference" is used instead of "error" because the COMP2DD solution is not an exact solution. Because the A5 discretization was nonuniform, the element centers of the COMP2DD solution (which used the A4 discretization) and the A5 discretization did not coincide. For comparison to the A5 solutions, COMP2DD values were linearly interpolated to the A4 grid. Relative difference was calculated according to the expression:

$$e_j = \sqrt{\sum_i^{N_j} [(((D_i^0 - D_i^j)/|D^0|_{max})^2 + ((E_i^0 - E_i^j)/|E^0|_{max})^2)/(2N_j)]}, \qquad \text{2-47}$$

where j refers to the particular result being compared (A1-S1 to A5-S1), i refers to a particular nodal point on the discretization, the superscript ^{0} refers to the COMP2DD

solution (interpolated to the grid of j in the case of A5-S1), N_j refers to the total number of elements in grid j, D refers to shear displacement, and E refers to opening displacement. The values $|D^0|_{max}$ and $|E^0|_{max}$ refer to the largest absolute values of D and E in the COMP2DD solution, about 0.65 mm for opening and about 2.45 mm for sliding, and are used to normalize the results.

The relative differences and computation times for A4-S0, A1-S3, A2-S3, A3-S3, A4-S3, and A5-S3 are shown in Figure 2-10.
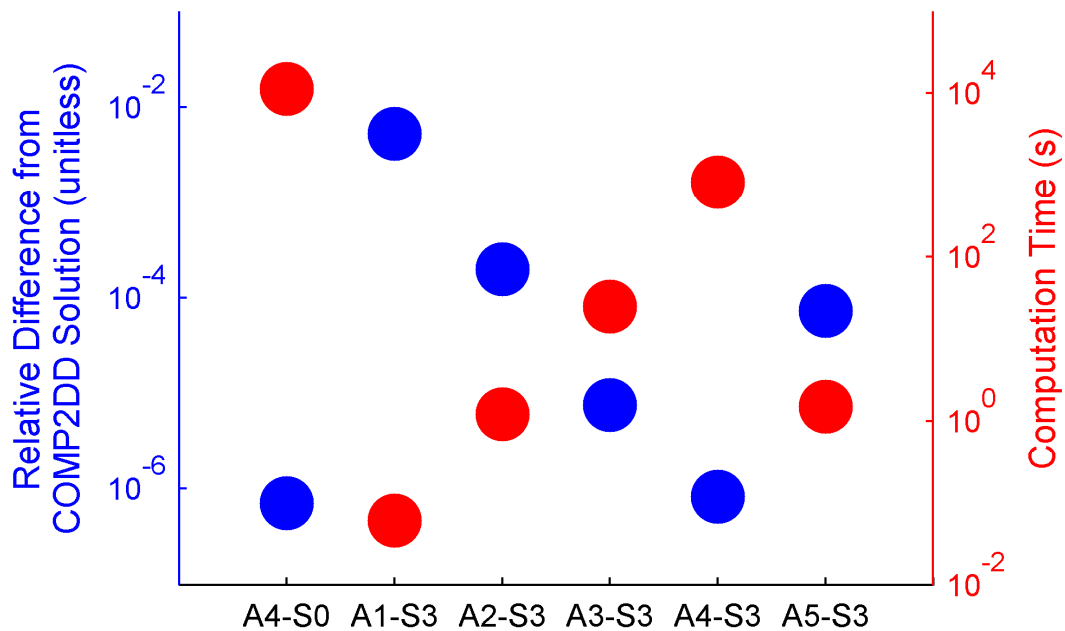
Figure 2-10: Computation time (red) and relative difference (blue) from COMP2DD for Simulations A4-S0, A1-S3, A2-S3, A3-S3, A4-S3, and A5-S3. Relative difference was calculated according to Equation 2-47 on the basis of final fracture deformation and normalized by reference values.

To identify the effect of spatial discretization on accuracy of the time-dependent results, flow rate over time was compared for different spatial discretizations (using the same temporal discretization factor η_{targ}). Figure 2-11 is a plot of injection rate versus time for Simulations A1-S3, A2-S3, A3-S3, A4-S3, and A5-S3.
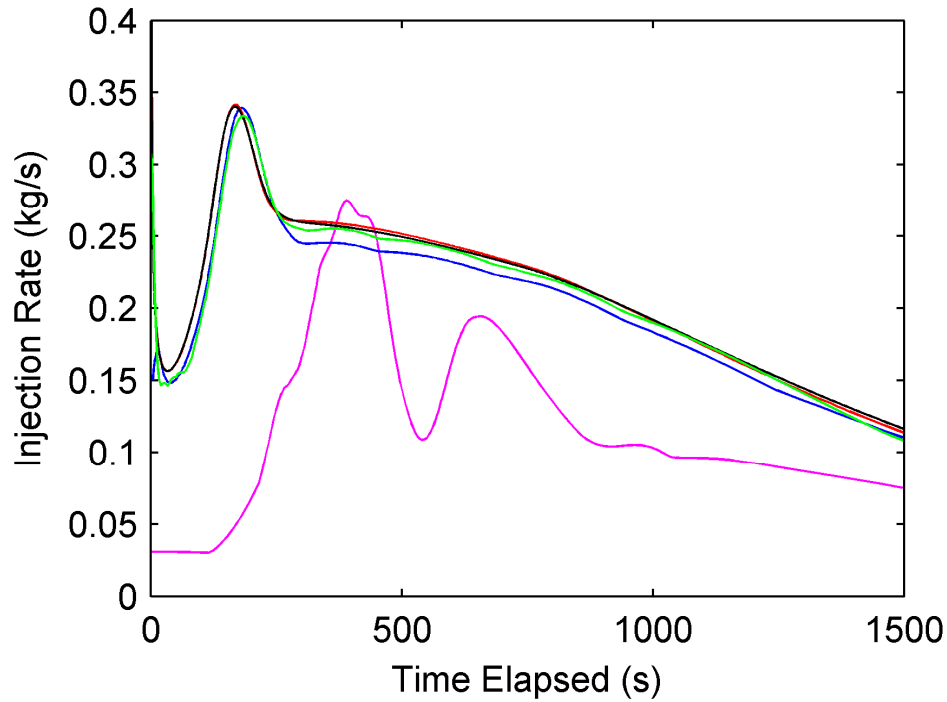
Figure 2-11: Injection rate versus time for Simulations A1-S3 (maroon), A2-S3 (blue), A3-S3 (red), A4-S3 (black), and A5-S3 (green).

The relative difference for different discretizations was calculated by comparing the various solutions to the most finely refined solution, A4-S3. Values of flow rate were interpolated onto a temporal discretization spaced one second apart for the first 5000 seconds of the simulation. Relative difference in flow rate was calculated according to:

$$e_j = \sqrt{\frac{1}{N} \sum_i^N (Q_i^0 - Q_i^j)^2} \ , \qquad \text{2-48}$$

where the superscript ^{0} refers to Simulation A4-S3, Q is the injection rate, and N refers to the 5000 points in time where Q was sampled. Relative difference and computation time are shown in Figure 2-12.
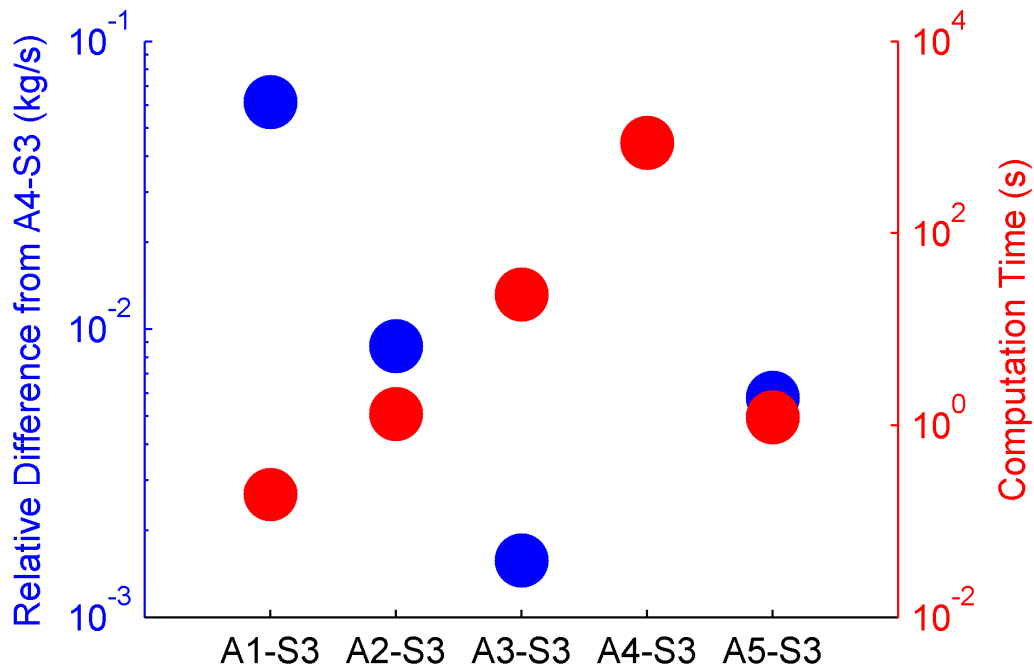
Figure 2-12: Computation time (red) and relative difference (blue) in flow rate versus time for Simulations A1-S3, A2-S3, A3-S3, A4-S3, and A5-S3. Relative difference calculated according to Equation 2-48 on the basis of injection rate versus time.

To isolate the effect of temporal discretization, simulation settings S1-S5 were used with Model A5. The simulations were identical except that they used different values of η_{targ}. Relative difference was calculated by comparing the flow rate over time between the various simulations and Simulation A5-S1, which used the smallest η_{targ}. Because Model A5 was only moderately well refined spatially, all solutions had some error, regardless of temporal discretization. Figure 2-13 shows plots of injection rate versus time for the various simulations. Figure 2-14 shows the relative differences (compared to A5-S1) and the computation times for the various simulations.
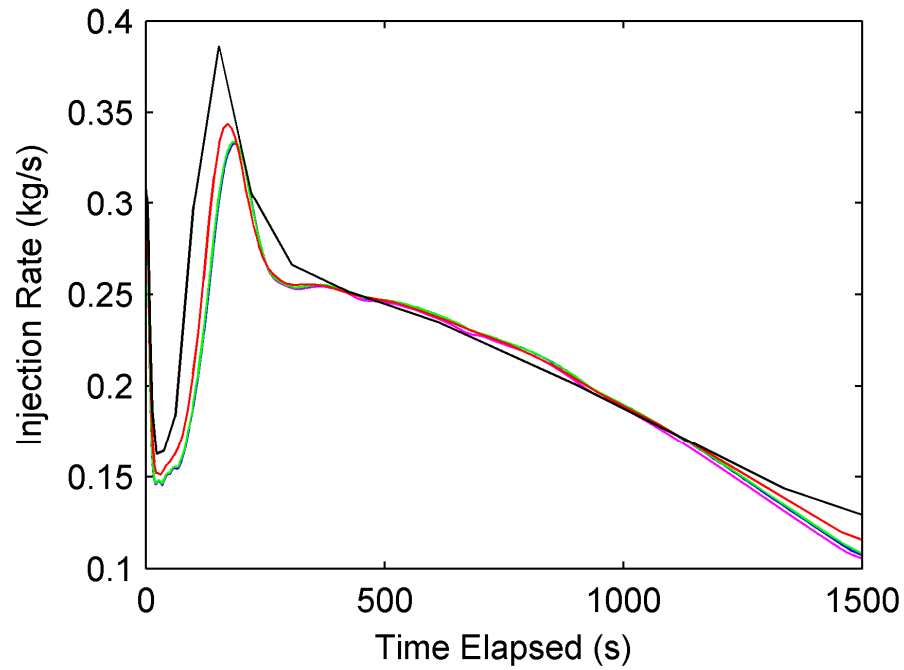
Figure 2-13: Injection rate versus time for A5-S1 (maroon), A5-S2 (blue), A5-S3 (green), A5-S4 (red), and A5-S5 (black).
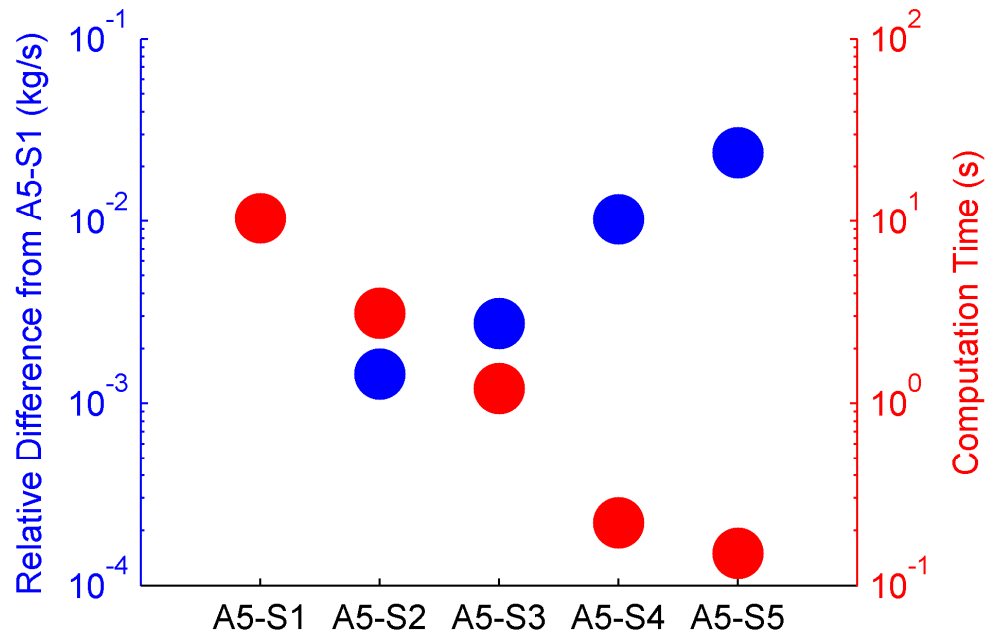
Figure 2-14: Computation time (red) and relative difference (blue) from A5-S1 for Simulations A5-(S1-S5). Relative difference calculated according to Equation 2-48 on the basis of injection rate versus time.

2.3.2.1 Solving Directly for the Final Deformations

It is possible to modify the model to directly solve for the final fracture displacements in a single step (what COMP2DD does) instead of using time steps. This approach could be useful if the objective of the calculation is to determine the final displacement field, and the intermediate displacements are not of interest. Because the model was not designed to be used in this way, it is necessary to use several unusual settings. In order to maintain constant fluid pressure as the fractures deform, the fluid compressibility is made extremely large (effectively infinite) and the transmissivity is set to zero. The fluid flow and normal stress subloop convergence criteria are modified to depend only on the residual of the stress equations and not the mass balance equations. Finally, the radiation damping coefficient, η, is set to zero. With these settings, the problem can be solved in a single "time step" (the duration of the time step has no effect on the solution), and yields the same solution as COMP2DD.

Two simulations using discretization A4 were run with the direct solution method, S6 and S7. S6 used Hmmvp for approximate matrix multiplication, and S7 used the direct BEM (see Section 2.2.5.1). A comparison of the results is given in Figure 2-15. Two different complementarity algorithms implemented in COMP2DD were used, Lemke (Ravindran, 1972) and SOCCP (Hayashi et al., 2005).
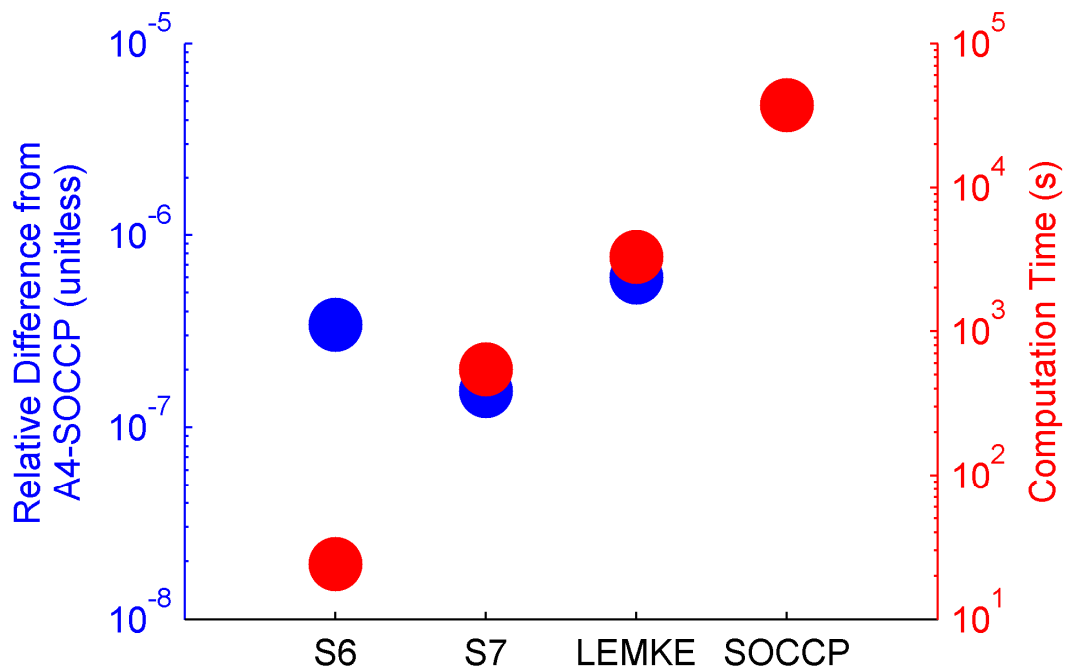
Figure 2-15: Computation time (red) and relative difference (blue) from A4-SOCCP for A4-S6, A4-S7, and A4-LEMKE, and computation time for A4-SOCCP. Relative difference calculated according to Equation 2-47 on the basis of final fracture deformation and normalized by reference values.

2.3.2.2 Testing the Effect of *cstress*

Simulations A3-S9, A3-S10, A3-S11, and A3-S12 were performed with the *cstress* option (Section 2.2.3.3). In S9-S12, different values for E_0 were used. The simulations using S9-S12 can be compared to Simulation A3-S8, which was identical to A3-S9 but did not use the *cstress* option.

With the *cstress* option activated, stresses induced by the normal deformation of closed fractures are not neglected. Fractures with larger values of E_0 contain a greater volume of fluid and experience greater normal deformation (and induce greater stresses) for the same perturbation in fluid pressure. The final displacements of the simulations are shown in Figure 2-16 and Figure 2-17.
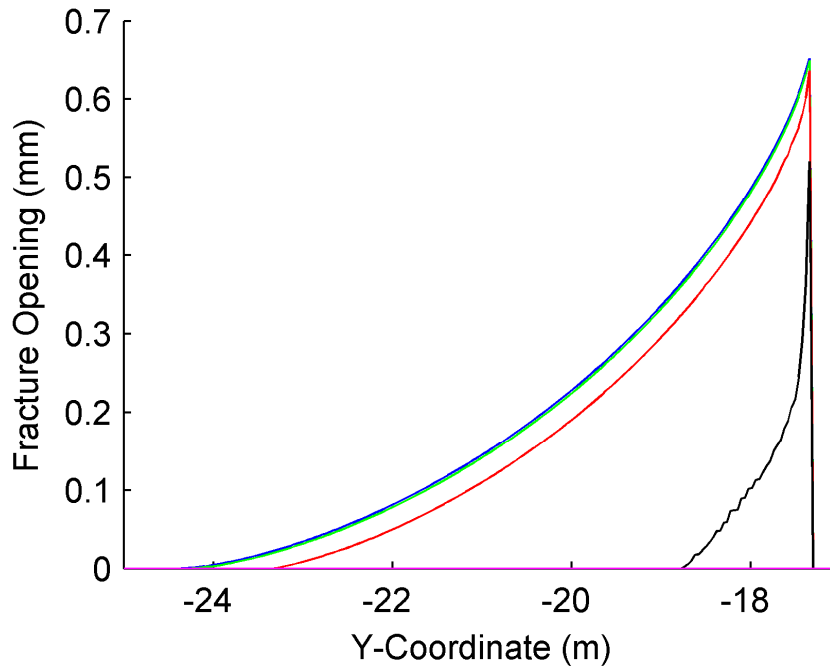
Figure 2-16: Final opening distribution along a section of Model A for A3-S8 (blue), A3-S9 (green), A3-S10 (red), A3-S11 (black), and A3-S12 (maroon). Models A3-S8 and A3-S9 coincide.
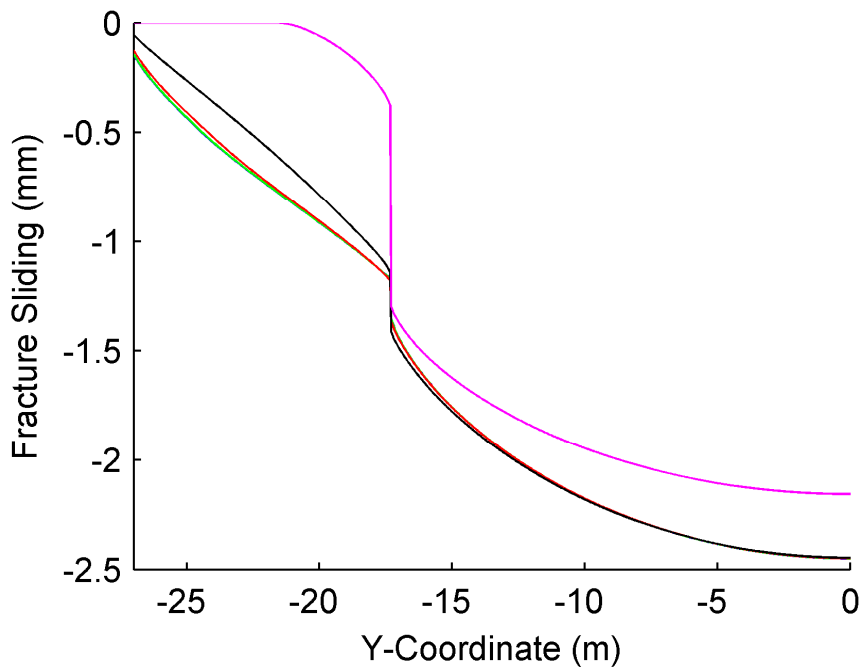
Figure 2-17: Final sliding distribution along a section of Model A for A3-S8 (blue), A3-S9 (green), A3-S10 (red), A3-S11 (black), and A3-S12 (maroon). Models A3-S8 and A3-S9 coincide.

2.3.3 Models B and C: Large Test Problems

Several simulations were performed on large fracture networks, Models B and C. Model B was designed to demonstrate shear stimulation. In shear stimulation, injection enhances transmissivity by inducing slip on preexisting fractures (Section 3.1.1). Model C was designed to demonstrate mixed mode propagation -- where injection causes shear and opening of preexisting fractures as well as propagation of new opening mode fractures (Section 3.1.1). The discretization settings used for Models B and C are given in Section 2.3.1. Models B and C are shown in Figure 2-1 and Figure 2-5.

In the Model B and C simulations, injection was carried out for two hours at a constant injection rate. The simulation was stopped at the end of two hours. The post-injection redistribution of fluid pressure was not included in the simulation.

During the Model B simulations, the fluid pressure exceeded the least principal stress, a condition that should have led to the propagation of new tensile fractures. However, "potentially forming fractures" were not specified in the fracture network, and so new fractures were not able to form. This unrealistic model behavior is acceptable for the purposes of this chapter, because the simulations in this chapter are intended only to test the accuracy and convergence of the numerical simulator. Even though there was not any propagation of new fractures, opening was able to occur on preexisting fractures.

2.3.3.1 Model B: Large Test Problem of Shear Stimulation

Nine simulations were performed with Model B, B1-B9, and one simulation, Simulation C1, was performed with Model C. The objective of these simulations was to test the effect of simulation options on the results and efficiency of the model.

The baseline settings for all simulations are given in Table 2-3. The baseline settings for all Model B simulations are given in Table 2-4. The deviations from baseline for each individual simulation B1-B9 are given in Table 2-5.

Table 2-5: Deviations from baseline settings for Simulations B1-B9.

B1	$\eta_{targ} = 0.05$
B2	$\eta_{targ} = 0.2$
B3	
B4	$\eta_{targ} = 4.0$
B5	Adaptive domain adjustment (Section 2.2.5.5)
B6	Dynamic friction weakening with $\mu_d = 0.5$ (Section 2.2.5.3)
B7	No stress transfer (Section 2.2.5.7)
B8	cstress, explicit transmissivity updating (Section 2.2.3.3)
B9	Same as B8, also with adaptive domain adjustment (Sections 2.2.3.3 and 2.2.5.5)

The objective of Simulations B1-B4 was to test the efficiency and accuracy of simulations with various values of η_{targ}. This parameter affects how many time steps are taken during the simulation (Section 2.2.3.9). Figure 2-18 and Figure 2-19 show the final shear displacement (proportional to color) and opening (proportional to thickness, but exaggerated scale) for Simulations B1 and B4, the most and least temporally resolved simulations. The fracture opening and sliding distributions for B2 and B3 are not shown because they appear visually identical to Figure 2-18.
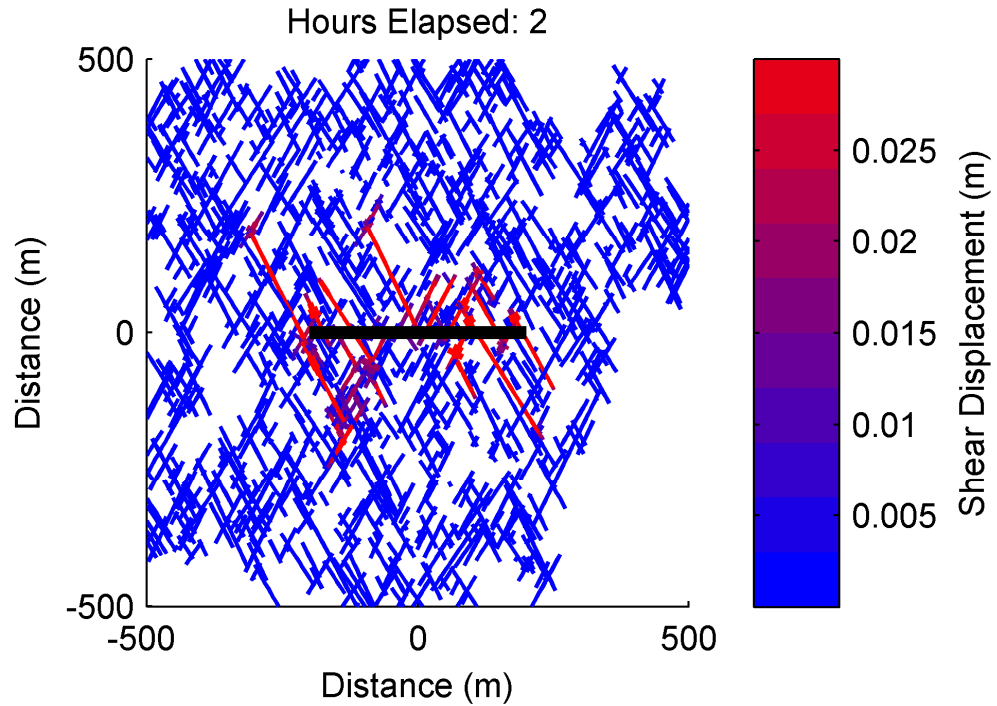
Figure 2-18: Final fracture shear displacement and opening (thickness is proportional to opening) of Simulation B1, the most highly temporally-resolved simulation.
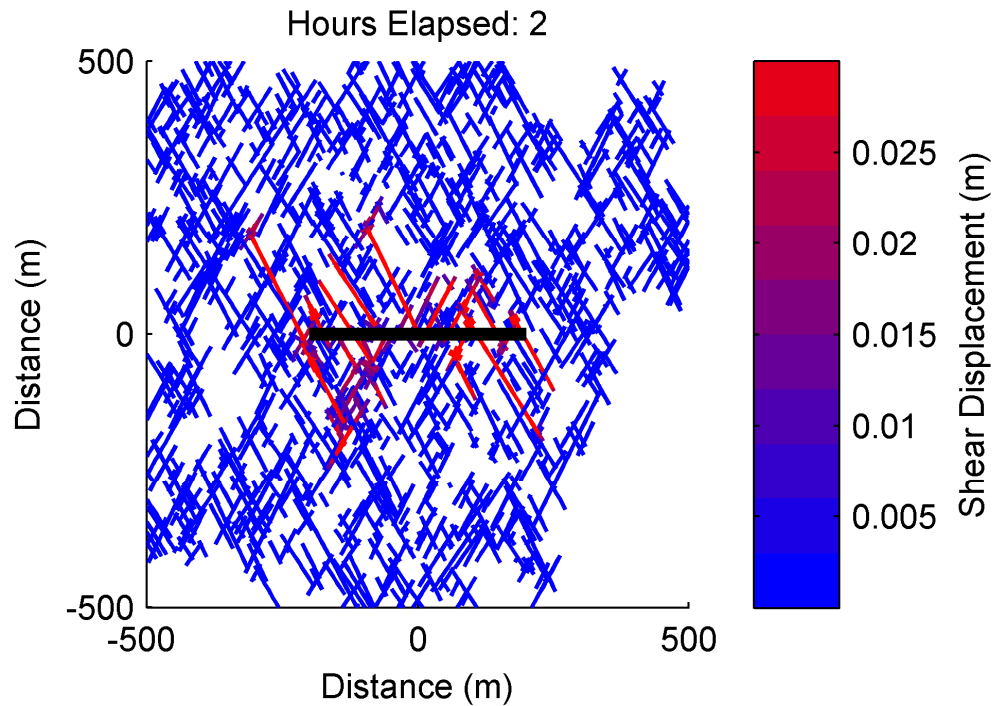
Figure 2-19: Final fracture shear displacement and opening (thickness is proportional to opening) of Simulation B4, the most poorly temporally-resolved simulation.

The relative difference in sliding displacement between Models B1 and Models B2-B5, B8 and B9 is shown in Figure 2-20. Model B5 used the same value of η_{targ} as B3 but used adaptive domain adjustment (Section 2.2.5.5). Models B8 and B9 used *cstress* (Section 2.2.3.3), and Model B9 also used adaptive domain adjustment. Relative difference in sliding displacement was calculated according to:

$$e_j = \sqrt{\frac{1}{M}\sum_i^M ((D_i^0 - D_i^j))^2} \; ,$$

2-49

where *D* refers to the sliding displacement, ^{0} refers to the result from Simulation B1, *i* refers to a particular element, *j* refers to the particular simulation, $|D^0|_{avg}$ is a scaling displacement, and *M* refers to the number of comparison points. The comparison points were the elements from Simulation B1 that had a sliding displacement with magnitude greater than 1.0 mm. The average absolute value of the displacements at the comparison points was 2.27 cm.
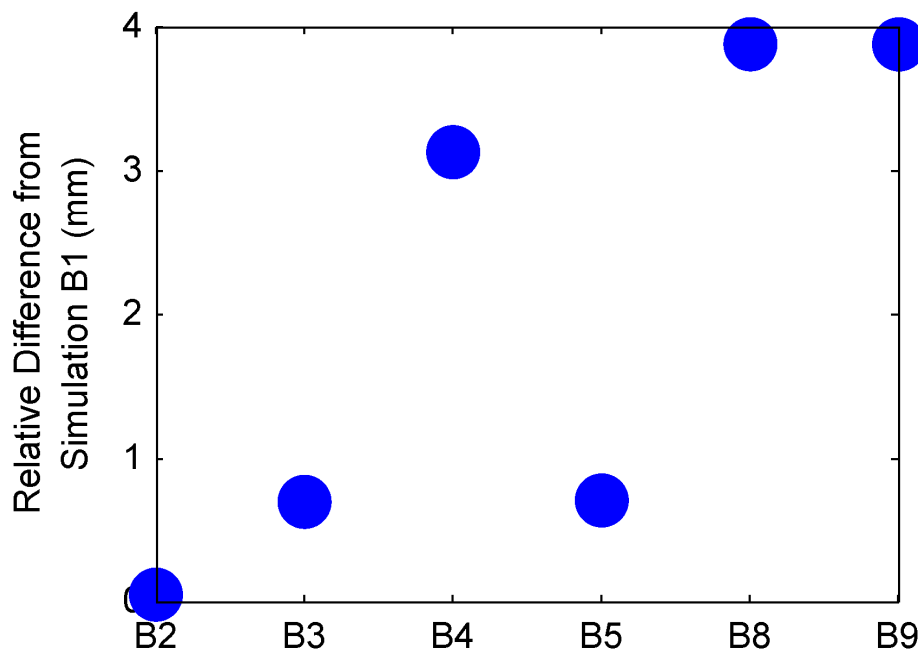
Figure 2-20: Relative difference between sliding displacement in Simulations B2-B5, B8 and B9 compared to Simulation B1. Relative difference calculated according to Equation 2-49.

Model B6 used dynamic friction weakening (Section 2.2.5.3). Model B7 neglected all stress transfer -- allowing elements to deform in response to changes in fluid pressure, but not updating stresses on surrounding elements due to those deformations (Section 2.2.5.7). Model B8 used the *cstress* option (Section 2.2.3.3). Model B9 used the *cstress* option and adaptive domain adjustment (Section 2.2.3.3 and 2.2.5.5).

The final sliding and opening distributions of Models B6-B8 are shown in Figure 2-21 to Figure 2-23. The sliding and opening distribution for Model B9 is not shown because it appears visually identical to the sliding and opening distribution for Model B8, shown in Figure 2-23.
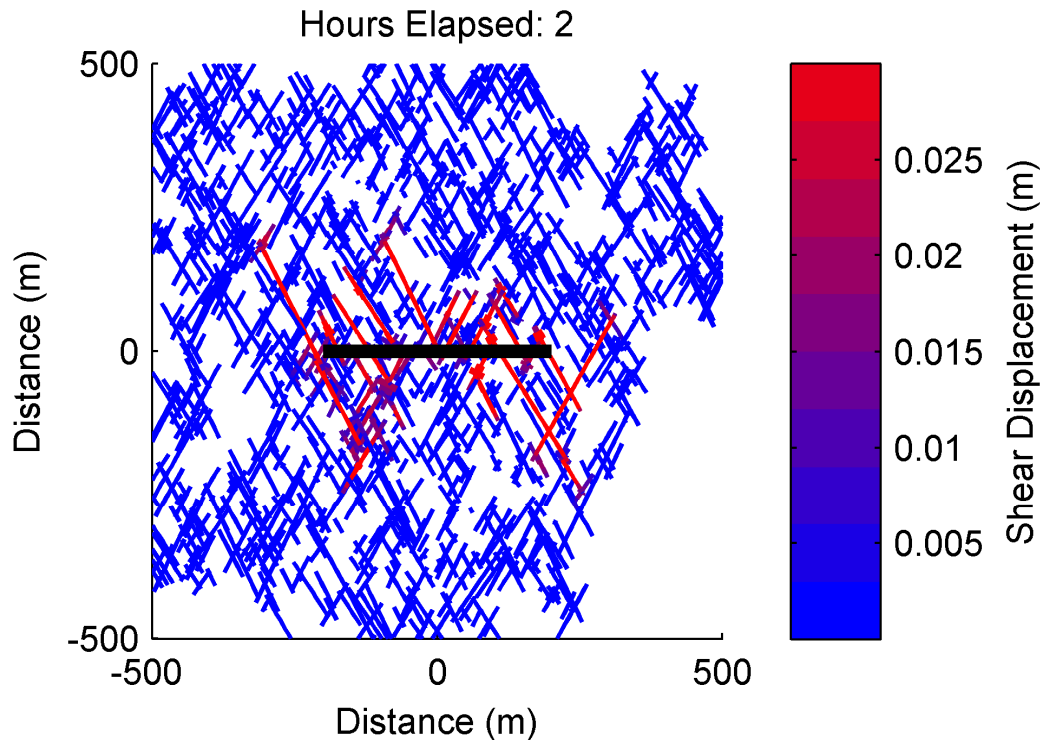
Figure 2-21: Final fracture shear displacement and opening (thickness is proportional to opening) of Simulation B6, which used dynamic friction weakening.
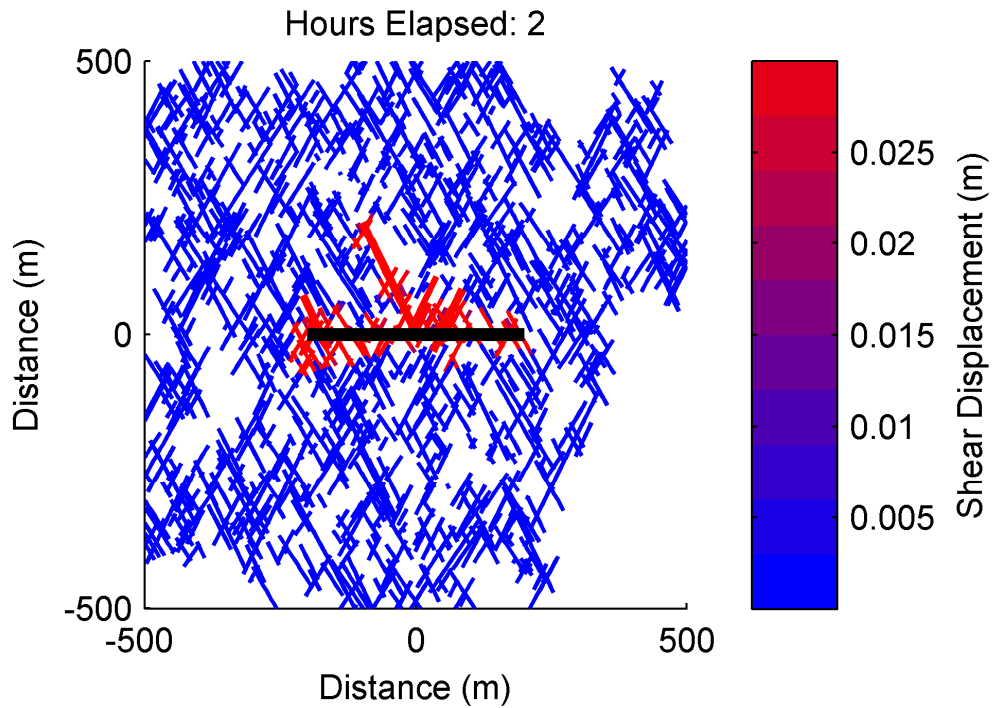
Figure 2-22: Final fracture shear displacement and opening (thickness is proportional to opening) of Simulation B7, which neglected stresses induced by deformation of fracture elements.
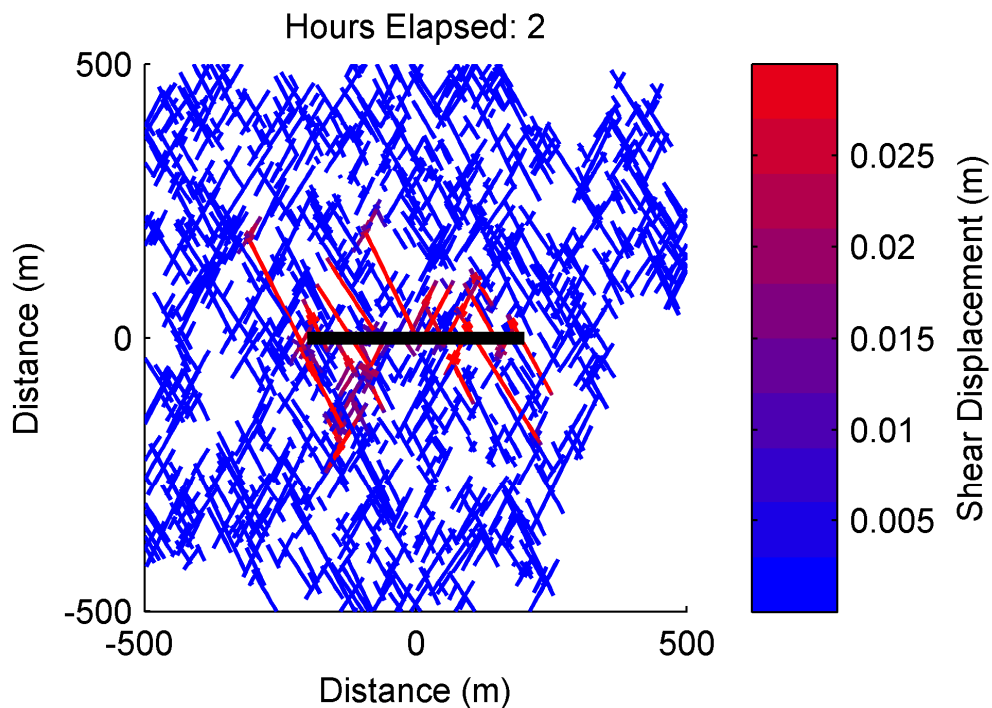
Figure 2-23: Final fracture shear displacement and opening (thickness is proportional to opening) of Simulation B8, which used the *cstress* option.

In Simulation B6, dynamic friction weakening caused seismic events to occur. By definition, a seismic event occurred whenever the sliding velocity of the fastest sliding element in the model was above a certain threshold, 5 mm/s. When the fastest sliding element in the model had a velocity below 5 mm/s, by definition, the seismic event ended. The simulator tracked the total cumulative slip that took place at velocity greater than 5 mm/s during each seismic event, D_{cum}. After the seismic event ended, the seismic moment of the event, M_0, was calculated (Hanks and Kanamori, 1979):

$$M_0 = G \int D_{cum} dA, \qquad \text{2-50}$$

where A is fracture surface area. The moment was correlated to a moment magnitude, M_w, according to (Hanks and Kanamori, 1979):

$$M_w = \frac{\log_{10} M_0}{1.5} - 6.06, \qquad \text{2-51}$$

where M_0 is expressed in Newton-meters.

Typical seismic event durations were 0.001 - 0.01s for the smaller events and as long as 0.2 s for the largest events. Figure 2-24 shows a plot of event magnitude versus time for Simulation B6.
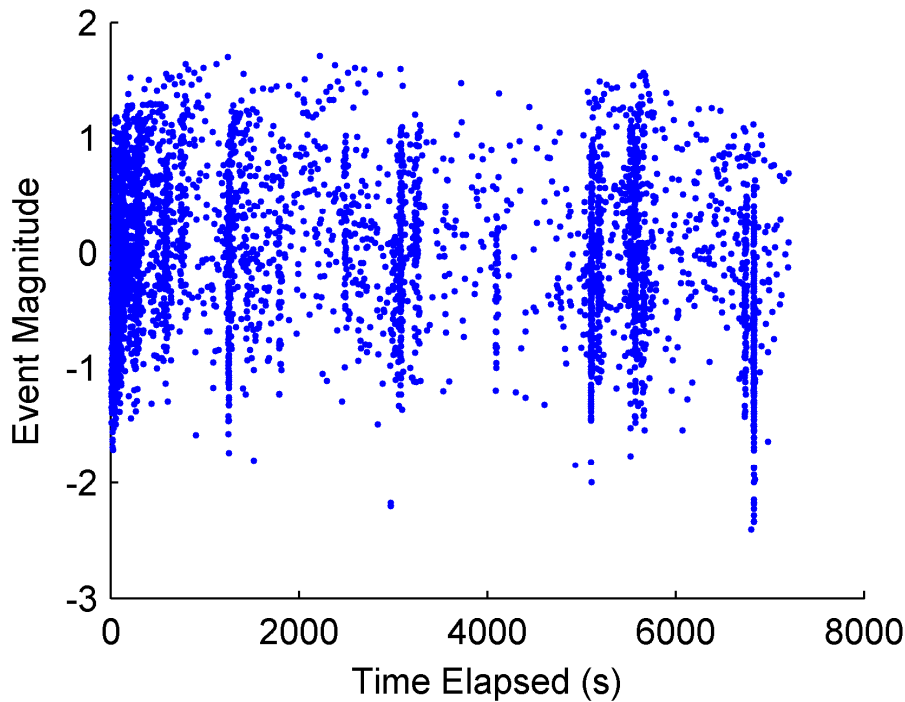
Figure 2-24: Seismic event magnitude versus time for Simulation B6. Magnitude calculated according to Equation 2-51.

Figure 2-25 shows the magnitude-frequency distribution during Simulation B6. The trend in Figure 2-25 is curving, and so we conclude that it does not replicate a Gutenberg-Richter magnitude frequency distribution. Parameters could probably have been tuned to force the magnitude-frequency distribution to be linear, but this would have been a model overfit, not a meaningful model result.

Seismic events were usually confined to a single fracture, and so the magnitude-frequency distribution for larger events was controlled by the fracture size distribution. The smallest events occurred on a single element, and so the magnitude-frequency distribution for small events was controlled by the distribution of element sizes. The magnitude-frequency distribution in the intermediate range was affected by the tendency for slip on a small number of fractures to cascade into larger slip events and the tendency for larger cascades to stop propagating.
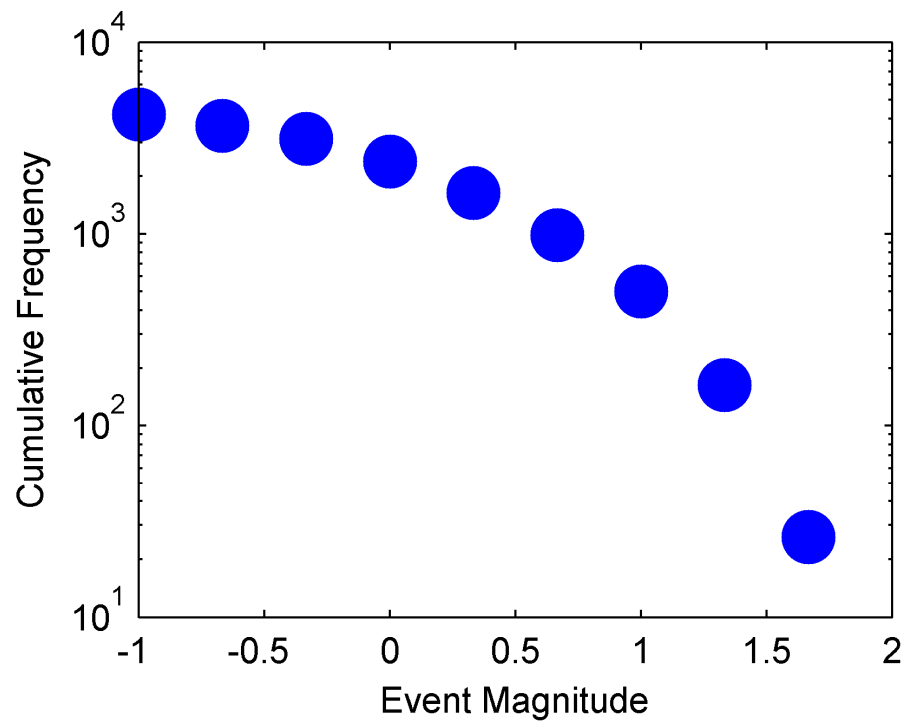
Figure 2-25: Magnitude-frequency distribution during Simulation B6.

Figure 2-26 shows the location of the event hypocenters during Simulation B6. To approximate the effect of relocation error, the hypocenters were relocated randomly within a circle with radius of 30 m from the actual hypocenter. For each seismic event, the hypocenter was defined as the first location where sliding velocity increased above 5 mm/s.
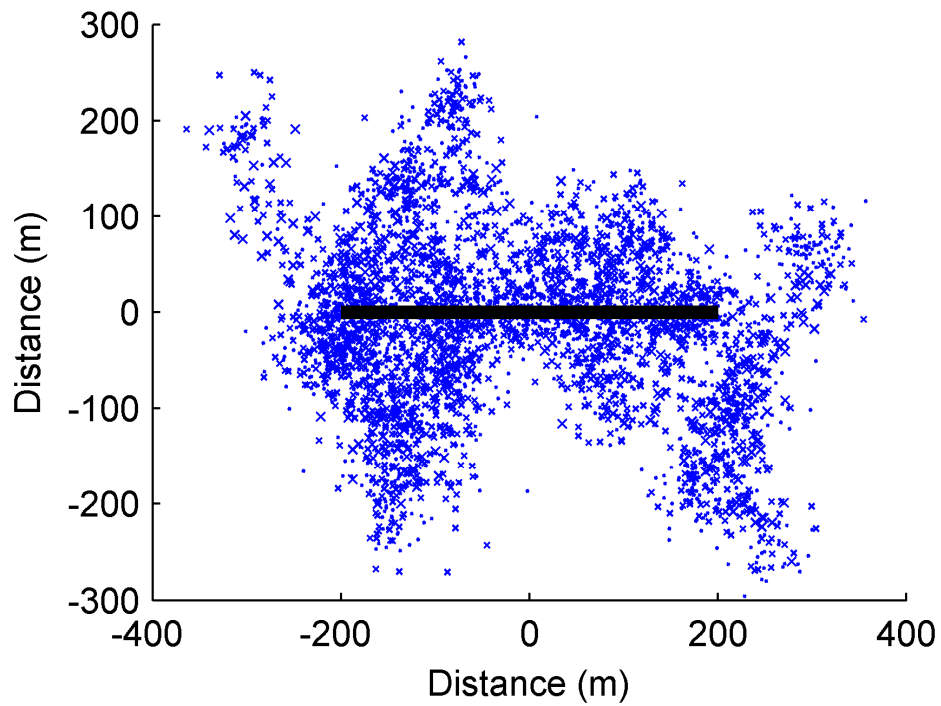
Figure 2-26: Seismic event hypocenters (with adjustment to approximate the effect of relocation error) for Simulation B6. Larger symbols represent larger magnitude events.

Figure 2-27 shows the total computer run-time and total number of time steps taken during Simulations B1-B9. Figure 2-28 shows the average computer run-time per time step taken during Simulations B1-B9.
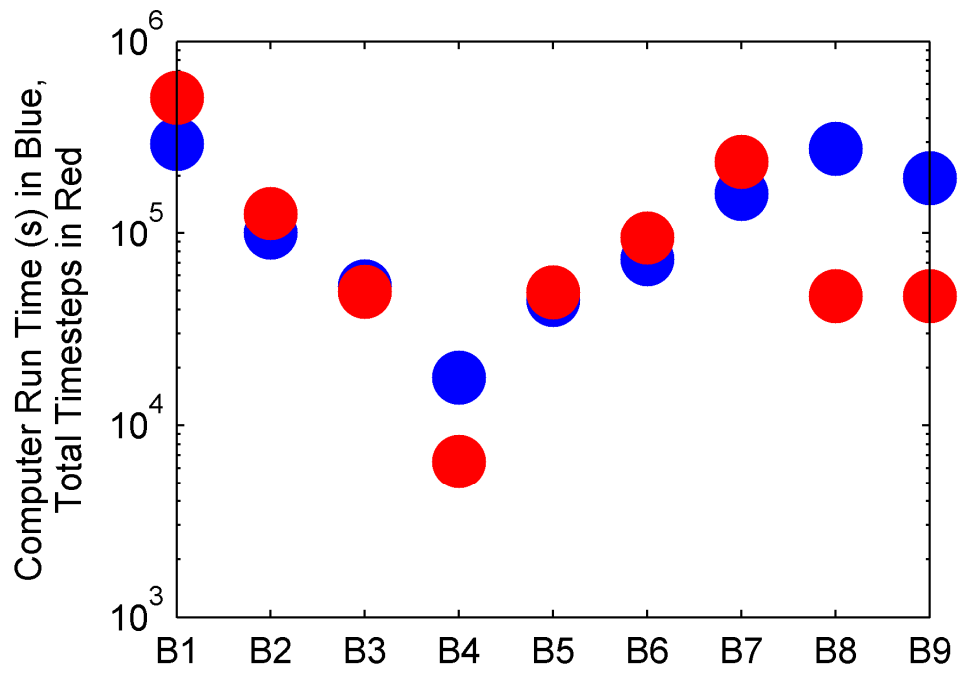
Figure 2-27: Computer run-time (blue) and total number of time steps (red) for Simulations B1-B9.
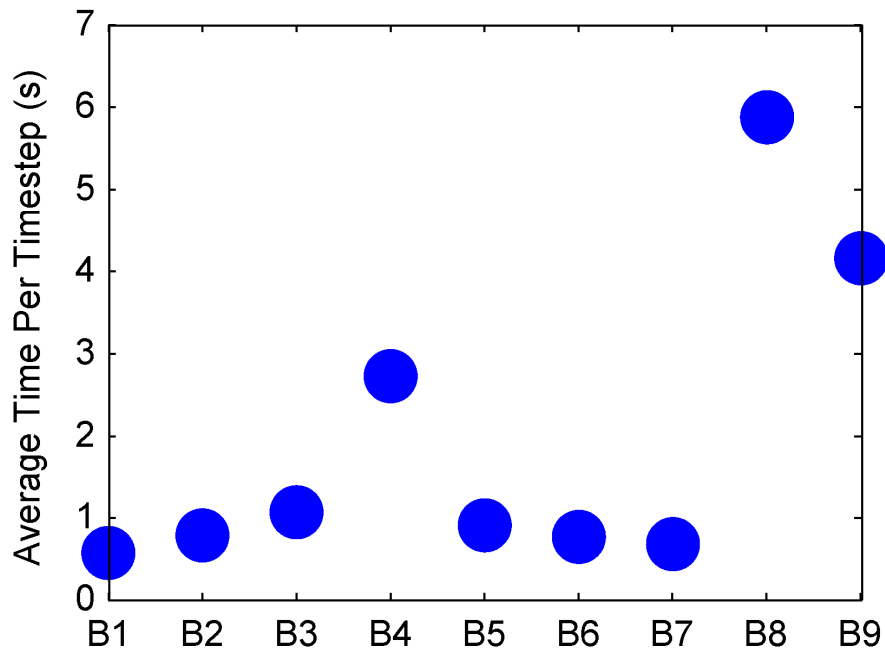
Figure 2-28: Average computer run-time per time step for Simulations B1-B9.

Figure 2-29 shows a plot of total time steps performed versus computer run-time for Simulations B3, B5, B8, and B9. Simulations B8 and B9 used the *cstress* option, and B3 and B5 did not. B3 and B5 are identical except that the latter used adaptive domain adjustment. B8 and B9 are identical except that B9 used adaptive domain adjustment.
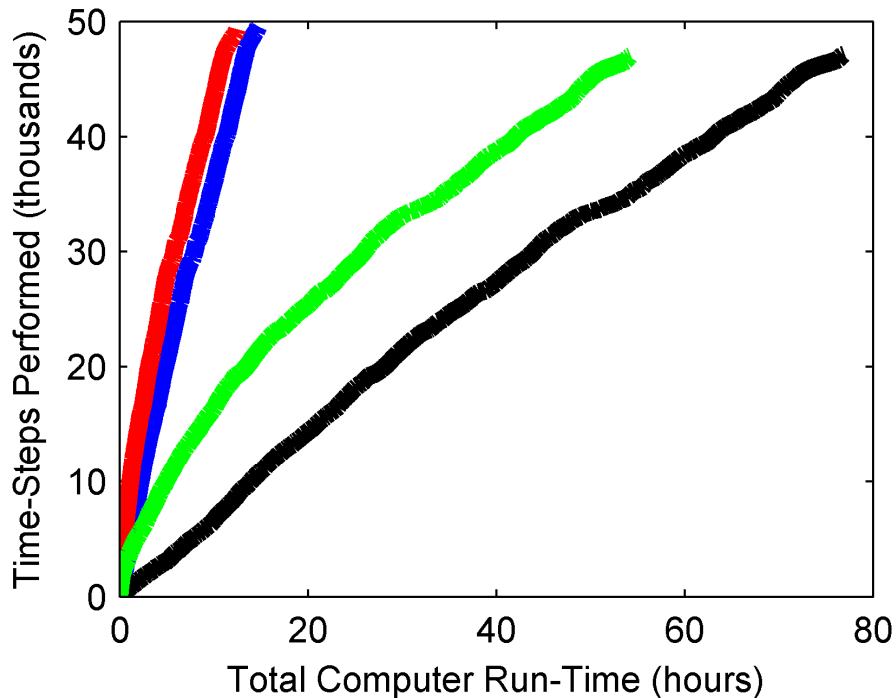
Figure 2-29: Total number of time steps performed versus run-time for Simulations B3 (blue), B5 (red), B8 (black), and B9 (green)

Figure 2-30 shows injection pressure versus time for Simulations B1-B4. Figure 2-31 shows injection pressure versus time for Simulations B6-B8. In all simulations, injection pressure was constant at 50 kg/s for the entire simulations (except a brief period at the initiation of injection).
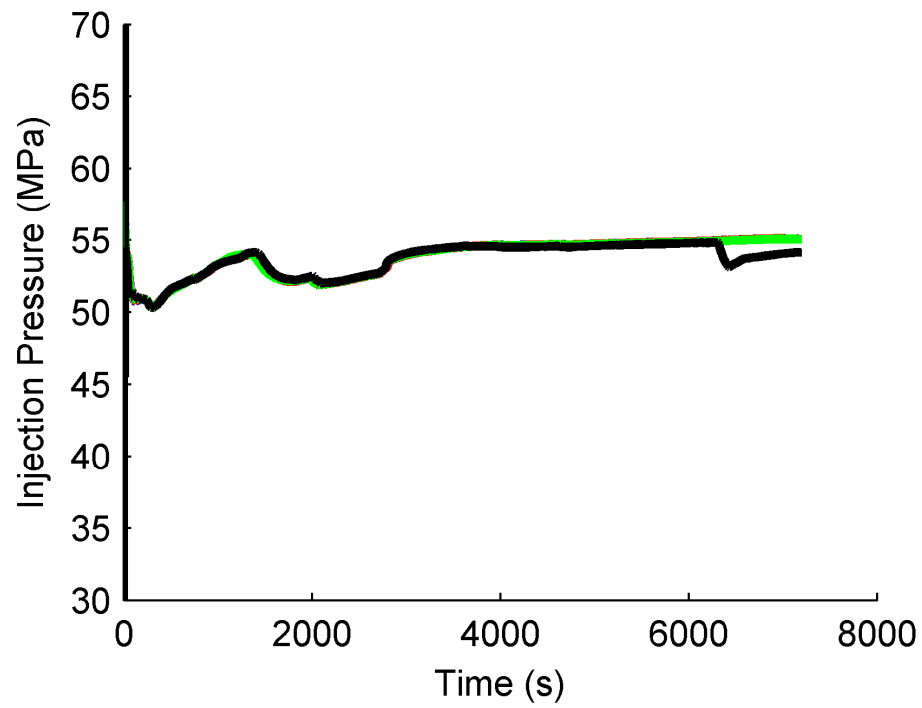
Figure 2-30: Injection pressure versus time for Simulations B1 (blue), B2 (red), B3 (green), and B4 (black).
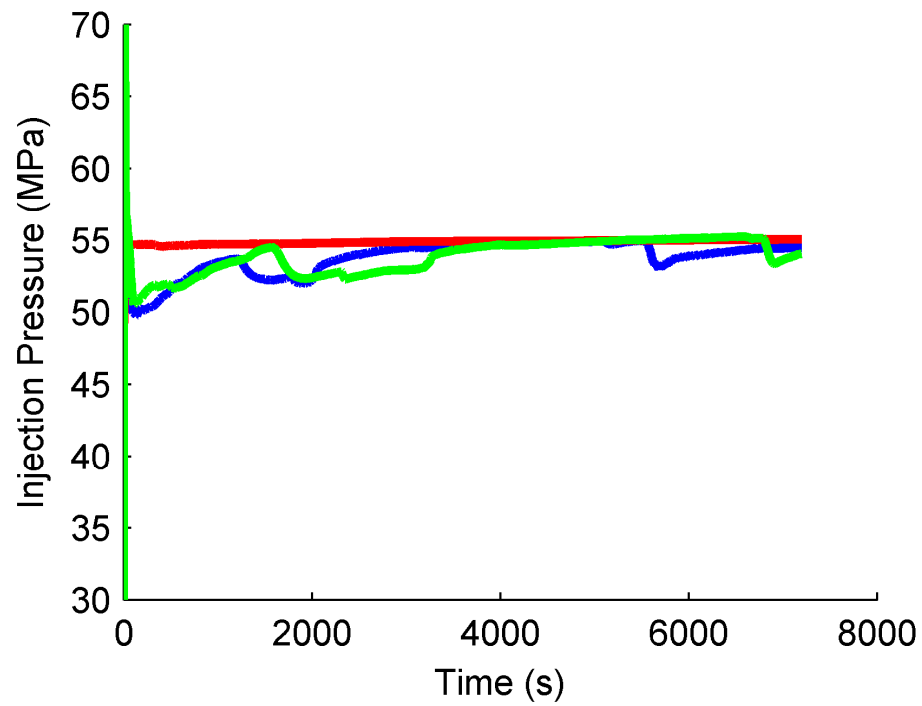
Figure 2-31: Injection pressure versus time for Simulations B6 (blue), B7 (red), and B8 (green).

2.3.3.2 Model C: Large Test Problem of Mixed-Mode Stimulation

Simulation C1 was performed as an example of mixed-mechanism hydraulic fracturing. In Simulation C1, propagation of new opening mode fractures occurred (Section 2.2.3.8), in contrast to the simulations using Models A, B, and D, in which no new fractures formed. Figure 2-5 shows a realization of both the potentially forming and the preexisting fractures in Model C. Settings for Simulation C1 are given in Section 2.3.1. Figure 2-32 shows the final transmissivity and opening distribution for Simulation C1. The computer run-time was 15,992 s (about four hours) and 15,574 time steps were taken.
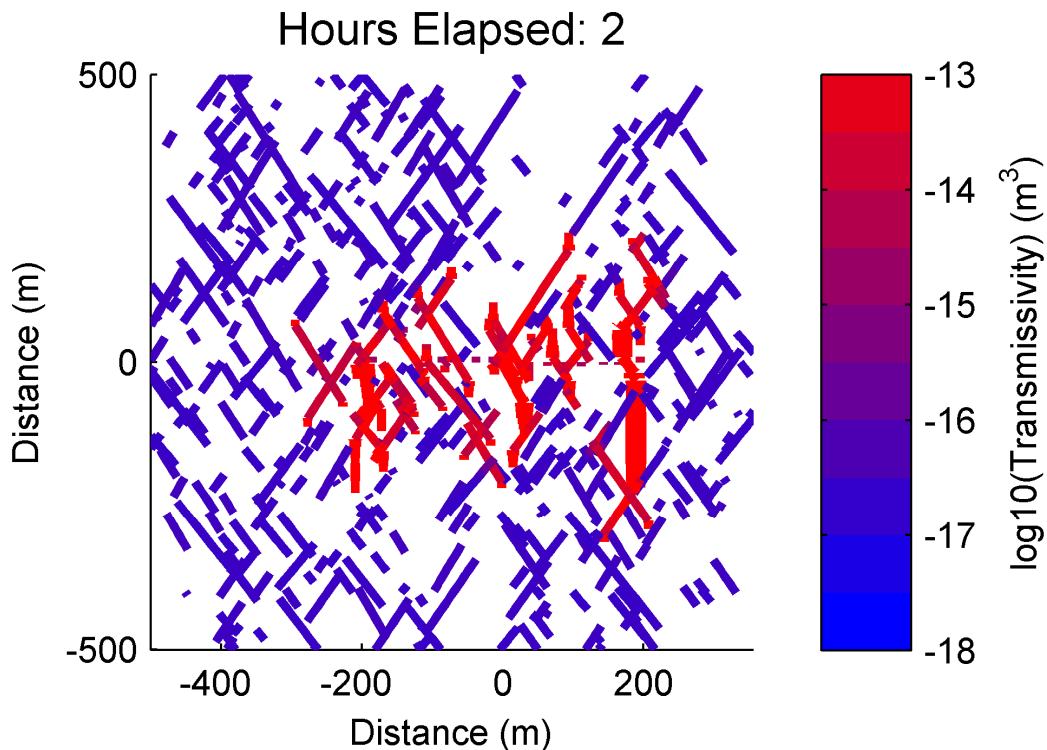
Figure 2-32: Final transmissivity and opening distribution (thickness is proportional to opening, but not to scale) for Simulation C1.

2.3.4 Model D: Testing the Strain Penalty Method

Four simulations using Model D were performed to test the strain penalty method described in Section 2.2.5.6. Two discretizations were used, D1 and D2, (described in Section 2.3.1), and two settings files were used, DS1 and DS2. The settings used in DS1

and DS2 are given in Section 2.3.1. DS1 and DS2 were identical except that the strain penalty method was used in the latter and not the former. Discretization D1 was coarsely refined. D2 was significantly refined, especially around the intersection.

Figure 2-33 to Figure 2-36 shows the final shear displacement and opening distributions for the four simulations, D1-DS1, D1-DS2, D2-DS1, and D2-DS2.
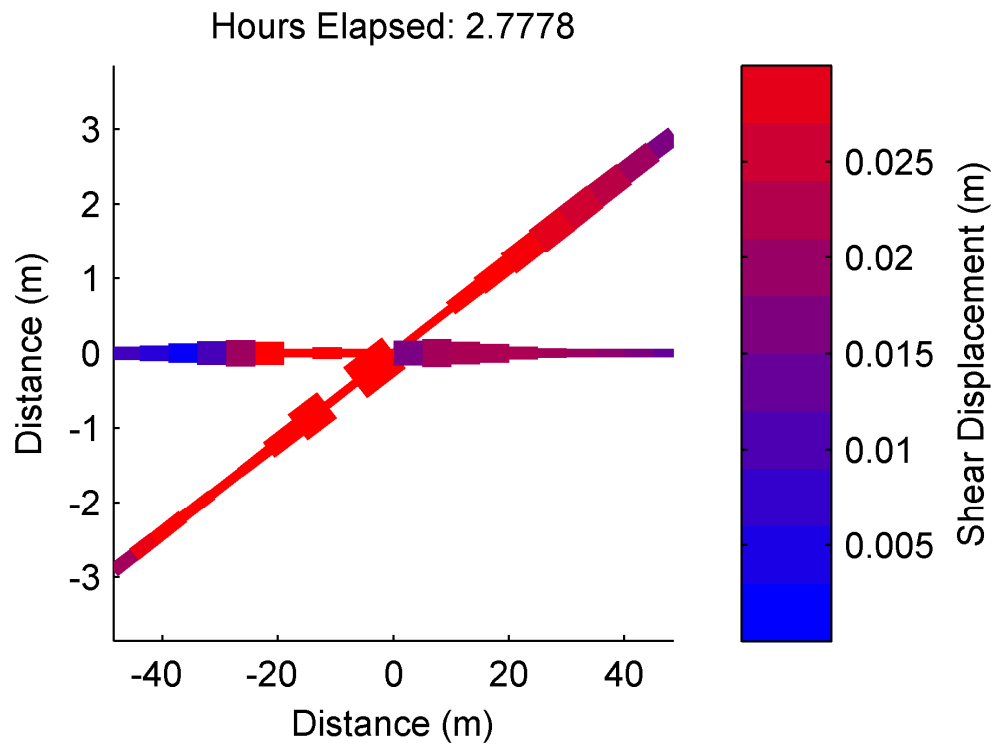
Figure 2-33: Final shear displacement and opening displacement (thickness is proportional to opening, but not to scale) for Simulation D1-DS1. Note that the x-axis scale and the y-axis scale are different.
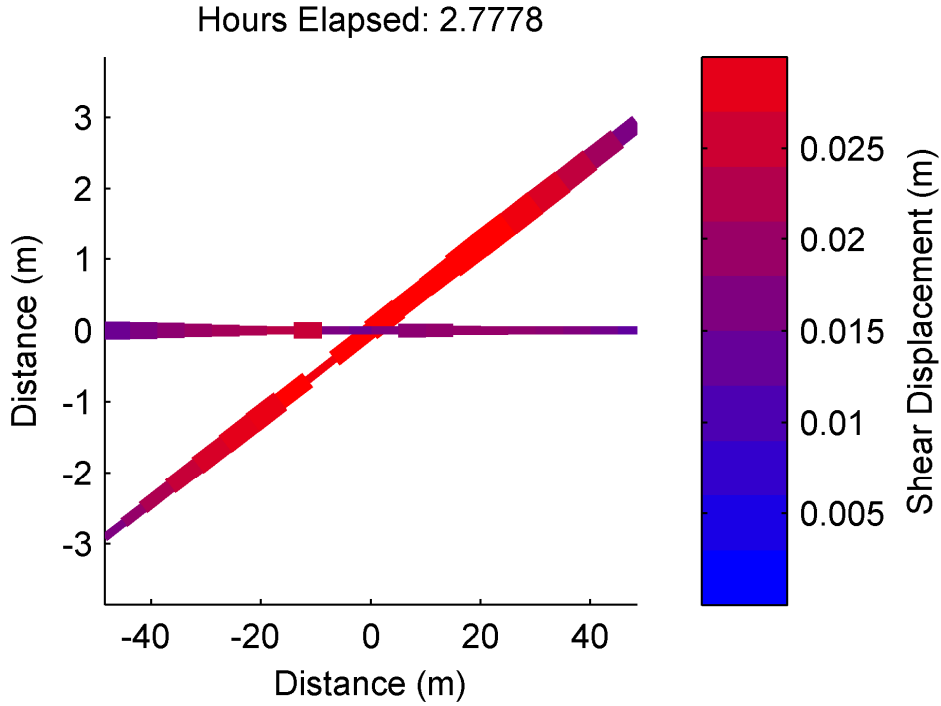
Figure 2-34: Final shear displacement and opening displacement (thickness is proportional to opening, but not to scale) for Simulation D1-DS2. Note that the x-axis scale and the y-axis scale are different.
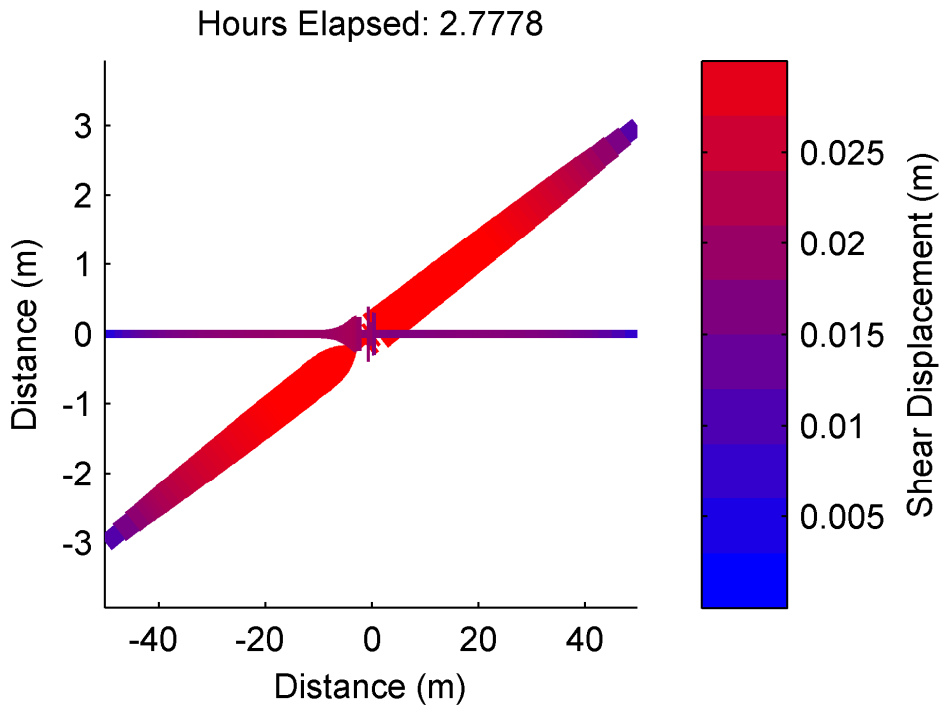
Figure 2-35: Final shear displacement and opening displacement (thickness is proportional to opening, but not to scale) for Simulation D2-DS1. Note that the x-axis scale and the y-axis scale are different.
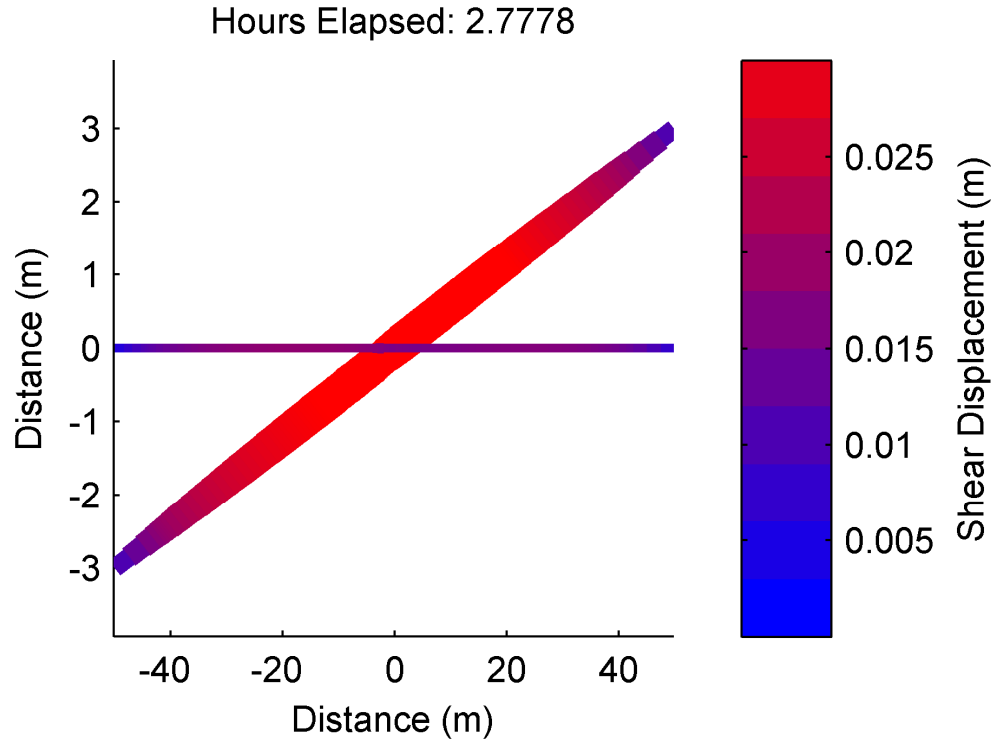
Figure 2-36: Final shear displacement and opening displacement (thickness is proportional to opening, but not to scale) for Simulation D2-DS2. Note that the x-axis scale and the y-axis scale are different.

2.3.5 Hierarchical Matrix Decomposition

A variety of tests were performed to measure the accuracy and compression Hmmvp, the BEM approximation code (Bradley, 2012). Plots of floating point operations (FLOPs) per matrix multiplication versus problem size were created for two cases: increasing discretization refinement for a given fracture network and increasing fracture network size for a given degree of discretization refinement. FLOPs per matrix multiplication is defined as being the number of additions and multiplications required to update both the normal and shear stress of all elements in a model due to normal and shear displacements of all elements. For n elements, a direct matrix multiplication would require $8n^2$ FLOPs. FLOPs per matrix multiplication is a close proxy for the memory required to store the interaction coefficients of the matrix decompositions.

In Hmmvp, a relative tolerance ε_{tol} of 10^{-6} was specified, such that:

$$\frac{\| \, B\Delta D - B_h \Delta D \, \|_2}{\| \, B \, \|_F \| \, \Delta D \, \|_2} \leq \varepsilon_{tol} \, ,$$

<div align="right">2-52</div>

where B represents one of the full matrices of interaction coefficients, and B_h represents the Hmmvp matrix approximation (Bradley, 2012). The subscript F reflects the Frobenius norm of a matrix and the subscript 2 reflects the Euclidian norm of a vector. Frobenius and Euclidian norms are defined as the square root of the sum of squares of all values in a matrix or vector, respectively. Testing on a variety of fracture networks with randomly generated displacement vectors demonstrated that the relative error, e_{hmat}, never exceeded 0.001, where:

$$e_{hmat} = \frac{\| \, B\Delta D - B_h \Delta D \, \|_2}{\| \, B\Delta D \, \|_2} \, .$$

<div align="right">2-53</div>

To test increasing refinement on a given fracture network, the fracture network shown in Figure 2-37 was used. The network contains 237 fractures. A variety of discretizations were created using different values for l_s, l_o, l_f, l_c, and minimum element size. Table 2-6 gives the settings used for each discretization and the total number of elements in each discretization. Each discretization was decomposed using Hmmvp. Figure 2-38 shows the number of FLOPS required to perform a matrix multiplication with Hmmvp method and with direct multiplication.
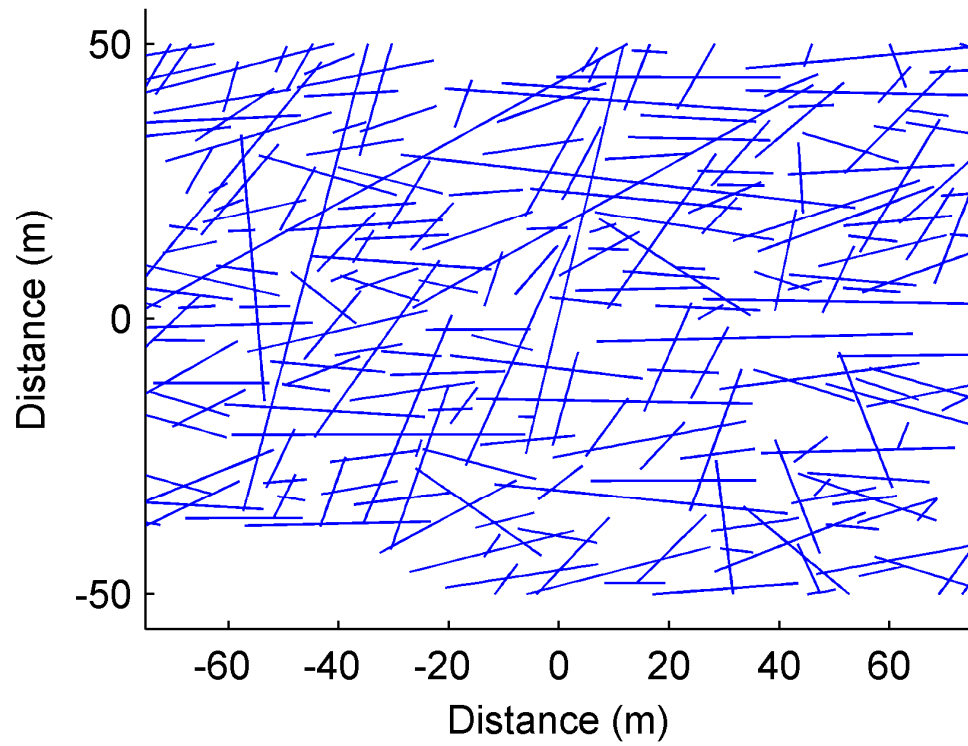
Figure 2-37: Fracture network used for discretization comparison at different levels of refinement.

Table 2-6: Settings used for the discretizations in Figure 2-38.

N	l_s	l_o	l_c (m)	l_f	a_{min}
872	0	0	inf	0.7	0.4
3966	0	0.5	0.5	0.7	0.4
4646	0.1	2	0.5	0.7	0.4
6352	0.2	2	0.5	0.7	0.4
15872	0.4	4	0.5	0.7	0.1
64192	0.6	4	0.5	0.7	0.05
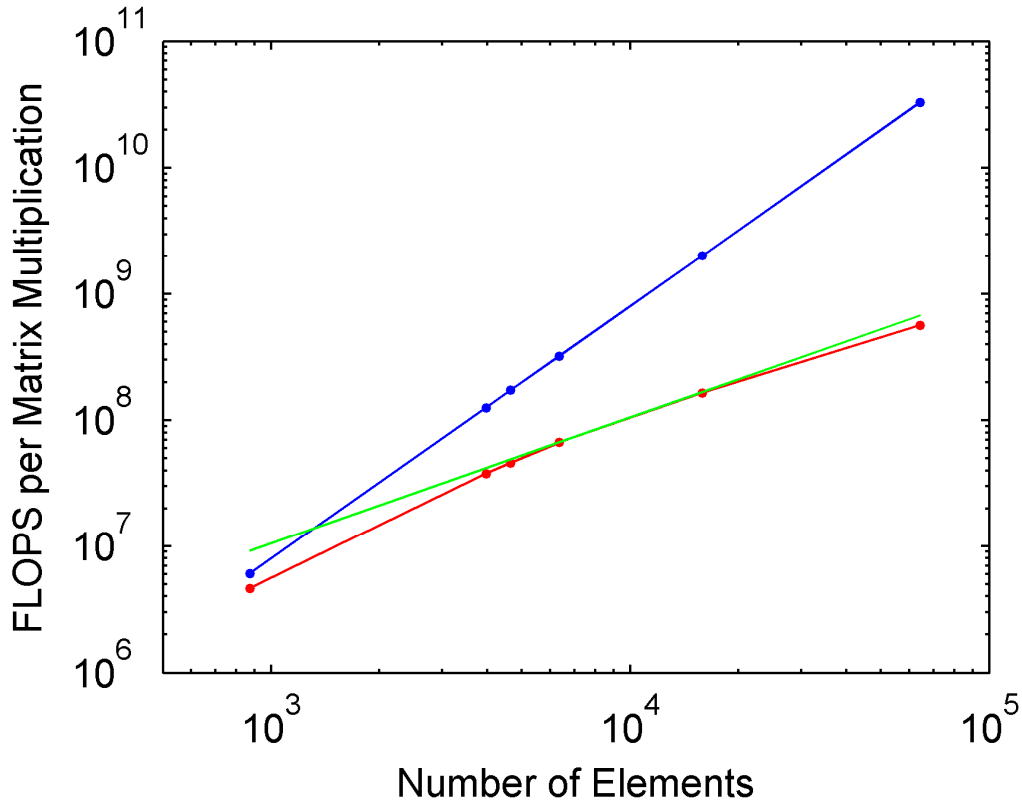
Figure 2-38: Comparison of FLOPS/multiplication for different levels of refinement on the fracture network shown in Figure 2-37. Shown in blue is the full matrix multiplication. The Hmmvp result is shown in red. The green line is linear with a slope of one and is shown for reference.

Next, a scaling comparison was performed for different sized fracture networks using the same level of discretization. A large network was generated with 6000 fractures and then different subsets of the network were used. Figure 2-39 shows the full fracture network with black rectangles showing the subdivisions of the network that were used for comparison. The discretizations were created using $l_s = 0.4$, $l_o = 4.0$, $l_f = 0.7$, $l_c = 0.5$ m, and a_{min} equal to 0.1 m. Figure 2-40 shows the number of FLOPS for a matrix multiplication using each discretization.
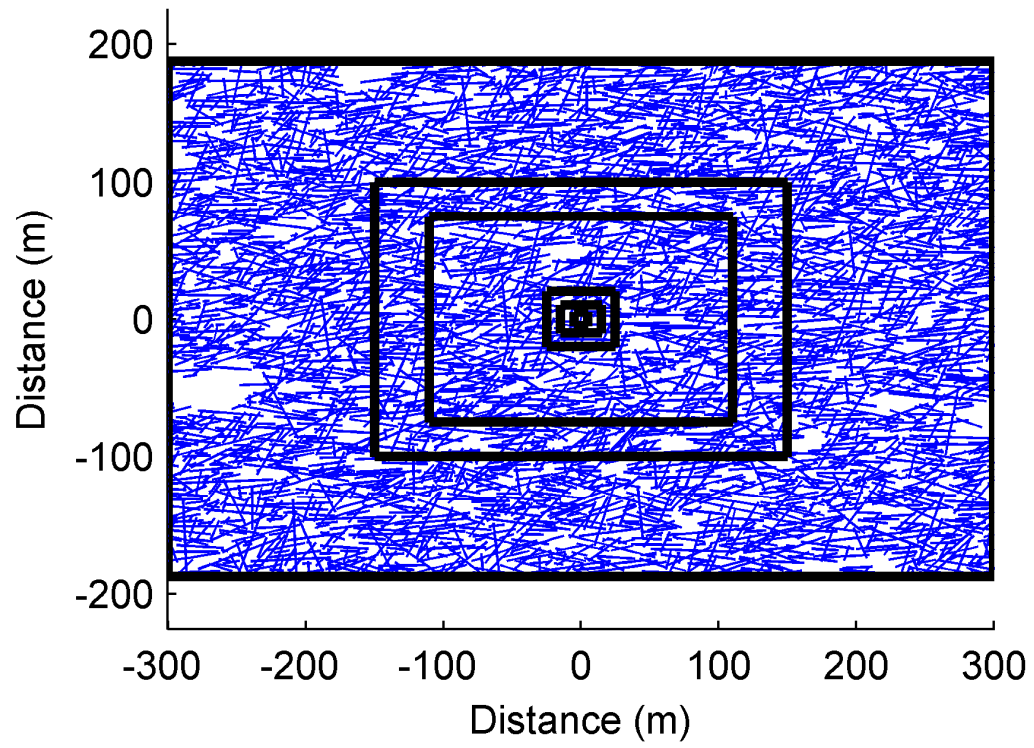
Figure 2-39: Fracture network used the test matrix approximation scaling for a variety of network sizes. Black boxes show the boundaries of each fracture network.
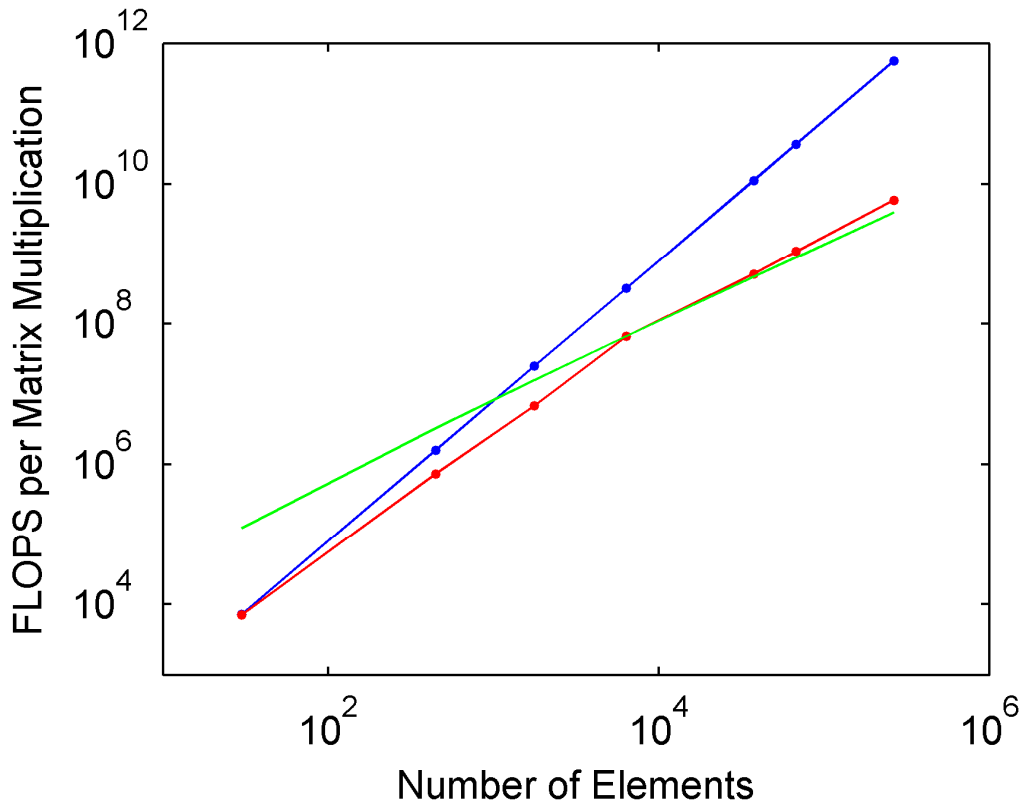
Figure 2-40: Comparison of FLOPS/multiplication for the same discretization refinement on different sized fracture networks shown in Figure 2-39. The full matrix multiplication is shown in blue. The Hmmvp result is shown in red. The green line scales like $n\log(n)$ and is shown for reference.

The amount of time required to generate the matrix decompositions does not affect the efficiency of the simulator because the decompositions are performed once, prior to simulation. However, the decompositions must be efficient enough that they can be performed in a practical duration of time. Figure 2-41 shows the amount of time required to perform the decompositions discussed in this section.
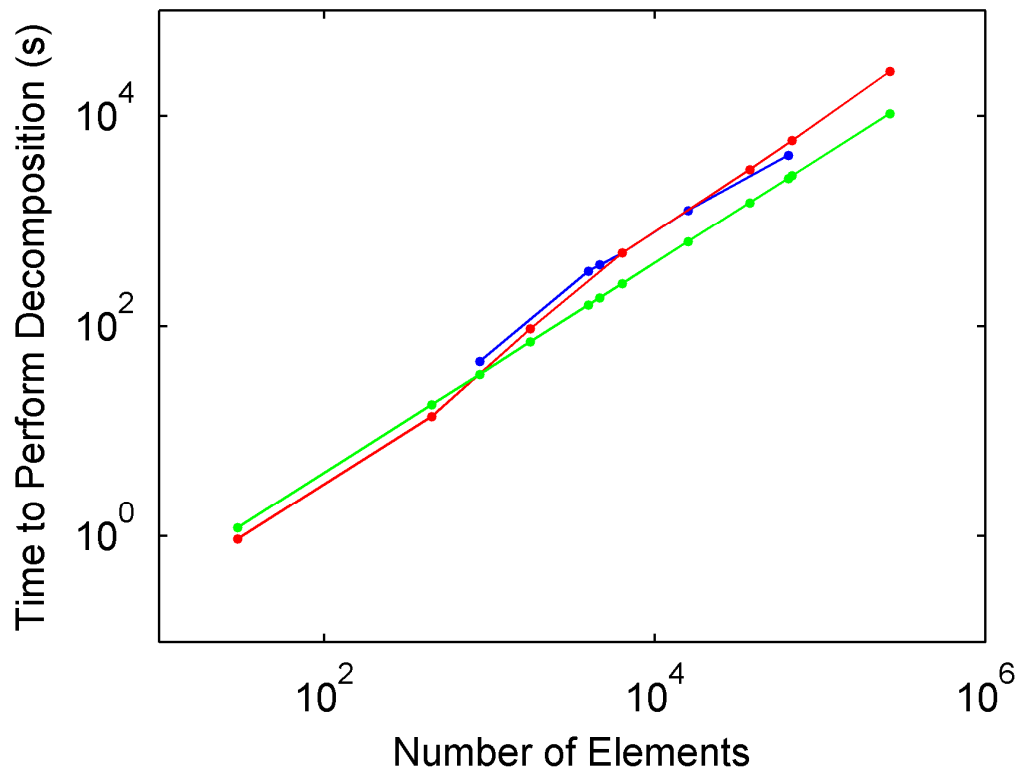
Figure 2-41: Amount of time required by Hmmvp to calculate the matrix decompositions. The red line shows the networks of variable sizes shown in Figure 2-39. The blue line shows the results for the variable refinements shown in Figure 2-37. The green line is linear with a slope of one and is shown for reference.

2.4 Discussion

2.4.1 Model A

2.4.1.1 General Description of Results

In the Model A simulations, injection was performed at constant pressure (less than the least principal stress) into the center of the fracture shown in Figure 2-7. The simulations ended when the entire system has reached the injection pressure. As in all simulations, matrix permeability was assumed negligible, so fluid did not leak off from the fractures.

Injection reduced the effective normal stress in the fractures, inducing slip on the central fracture. The neighboring fractures did not initially bear shear stress because they were perpendicular to the least principal stress, but the slip of the central fracture induced shear stress on the neighboring fractures and caused them to slip (Figure 2-8). Slip of the central fracture also induced tensile stress on the neighboring fractures and caused them to partially open, even though the fluid pressure remained below the remote least principal stress (Figure 2-9).

The behavior of the injection rate with time was rather complex (Figure 2-11). Typical for constant pressure injection, the injection rate began high (because there was a large pressure difference between injection pressure and initial pressure) and declined rapidly. The decline in injection rate was reversed as slip began to occur and transmissivity increased around the wellbore. After a period of increase, the injection rate began to fall again as the progressive increase in transmissivity was unable to maintain the flow rate. The spreading of transmissivity enhancement was delayed as the pressure perturbation reached the edges of the central fracture. At around 250 seconds, the neighboring fractures began to open and slip, increasing their transmissivity and slowing (but not reversing) the decrease in injection rate. Subsequently, injection rate entered a period of gradual decline as the pressure of the entire system slowly approached the injection pressure.

2.4.1.2 Effect of Spatial and Temporal Discretization

The effect of spatial and temporal discretization on simulation results is shown in Figure 2-8 to Figure 2-14. The results were convergent to discretization refinement in both time and space.

Models A1-A4 used constant element size discretizations of increasing refinement. Model A5 used a variable size discretization with significant refinement near the wellbore and fracture intersections. Simulation settings S1-S5 included a variety of values of η_{targ}, the main parameter that controls time step duration.

Figure 2-8 and Figure 2-9 show the final sliding and opening displacements of the simulations with different spatial discretizations (and the COMP2DD result). Other than

Model A1, which used the coarsest discretization, results appear quite similar to the most highly refined results. Figure 2-10 shows a calculation of the difference between the various simulations and the COMP2DD result. It shows that the COMP2DD result was virtually identical to the result from Model A4-S3, which used the same discretization. Comparison between A4-S0 and A4-S3 indicates that results with direct BEM multiplication were virtually identical to results with Hmmvp. Figure 2-10 shows that the results were convergent to discretization refinement.

Figure 2-8, Figure 2-9, and Figure 2-10 give some insight into the coarsest discretization that can be reasonably used. Results from A1 were clearly unacceptable, but results from A2 and A5 were reasonably close to the more spatially refined simulations. Comparing between A2 and A5, A5 was modestly more accurate even though it had fewer elements than A2. Evidently, the strategy of refining the discretization around the fracture intersections is better than using a constant element size.

Figure 2-11 and Figure 2-12 show the effect of the spatial discretization on the flow rate history. The A1 simulation was extremely different from the others. The results for A2, A3, and A5 all matched the result from A4 reasonably closely, and A3 was the closest match. A5 was significantly closer to the A4 result than A2 after about 250 seconds. Overall, every discretization except A1 performed reasonably well in matching the most highly resolved simulation, A4. The A5 simulation was the best compromise between efficiency and accuracy, evidently because it used refinement near the wellbore and fracture intersections.

Figure 2-13 and Figure 2-14 show the effect of time step duration on results. Simulations settings S1-S5 were used with Model A5. The same spatial discretization was used because these simulations were designed to test the effect of temporal discretization. Simulation A5-S1 used an exceptionally small value for η_{targ} and for comparison purposes was assumed to be the most accurate solution. Figure 2-13 shows that A5-S5 was the only result that was extremely different from A5-S1. Simulation A5-S4 showed some difference from the benchmark, and A5-S2 and A5-S3 were very similar to A5-S4. Figure 2-14 shows that the results were convergent to refinement.

The degree of discretization refinement in a simulation must be balanced against efficiency. If the objective of a simulation is to obtain a highly accurate result, a more refined simulation may be required. However, in subsurface modeling, error is usually unavoidable because of poor or incomplete information about the subsurface and simplifying assumptions about the physical processes taking place. Because error due to uncertainty is already high, there little benefit to driving numerical error to nearly zero. Practically, accepting a modest numerical error is justified, especially if a problem is so complex it cannot be solved otherwise. Model A is very simple, and so efficiency was not a major concern, but in larger models, efficiency is critically important. Simulation results with Model A5 were reasonably similar to results from Model A4, yet were roughly 1000 times more efficient (Figure 2-10 and Figure 2-12). For this reason, Model A5 was chosen as the best compromise between efficiency and accuracy, and discretization settings similar to A5 were used with Models B and C. For temporal refinement, S3 or S4 were probably the best compromise between efficiency and accuracy (η_{targ} equal to 0.5 MPa and 0.05 MPa, respectively).

2.4.1.3 Solving Directly for Final Deformations

In simulations A4-S6 and A4-S7, the final deformations of the fractures were calculated in a single step (Section 2.3.2.1). This simulation strategy could be useful if the deformations between the initial and final state were not considered important. In effect, the direct calculation method solves the same contact problem as COMP2DD (Mutlu and Pollard, 2008).

Figure 2-16 and Figure 2-17 show that the final displacements from A4-S6 and A4-S7 were virtually identical to the results from COMP2DD (relative error less than 10^{-6}), and the calculations were much more efficient. Comparison between A4-S6 and A4-S7 shows that the direct BEM yielded virtually the same result as Hmmvp, yet the results using Hmmvp were much more efficient.

Simulation A4-S6 (which used Hmmvp) reached virtually the same answer as COMP2DD and was 135 times faster than the Lemke algorithm and 1550 times faster than the SOCCP algorithm (Figure 2-15). The time comparisons between COMP2DD and Simulation A4-S6 are not completely equivalent because COMP2DD is a Matlab

code and the simulator is written in C++. Typically, Matlab codes have worse performance than C++ code (except for functions that are vectorized in Matlab). Nevertheless, the difference in efficiency cannot be completely explained by the difference between Matlab and C++.

The direct solution method should have excellent scaling with problem size because the computation time is dominated by the matrix multiplications associated with updating stresses, and with Hmmvp, this step scales like n or $n\log(n)$ (Sections 2.3.5 and 2.4.5). Because the model does not ever require assembly of the dense matrix of interaction coefficients (it only requires storage of the highly compressed heirarchical matrix form of the interaction matrices), the RAM requirements are much lower. Therefore, the model could be used to solve extremely large contact problems that would not be feasible for algorithms that require assembly and solution of the full, dense matrix of interaction coefficients.

It is likely that if the model had been more specifically tailored to be used as a direct solution algorithm, the calculation could have been done even more efficiently. The fluid flow equations, while altered to have no effect on the solution, remained in the fluid flow/normal stress system of equations (Section 2.3.2.1), creating unnecessary computational effort. Possibly, the solution could have been made more efficient if full coupling, rather than iterative coupling, had been used.

As discussed in Section 2.2.3.8, it was found that the enforcement of inequality constraints on fracture displacements could lead to convergence failure in the shear stress residual equations for very complex, dense, or poorly discretized fracture systems. Possibly, convergence could be an issue for problems in which a direct solution is attempted because the initial guess may not be close to the final solution. To improve robustness, a sparser iteration matrix could be used (Section 2.2.3.8). A diagonal iteration matrix is the least efficient, but most robust choice. Another alternative would be to apply the stresses gradually over several steps and perform several calculations. An equivalent strategy would be to apply the stresses abruptly, but use time stepping with an artificially large value of the radiation damping coefficient (or equivalently, use a normal

radiation damping coefficient but enforce very short time steps), which would force the deformations to occur gradually over several time steps.

2.4.1.4 Effect of *cstress*

The effect of the *cstress* option was tested by Simulations A3-(S9-S12). Simulation A3-S9 can be compared to A3-S8, which was identical except that A3-S8 did not use the *cstress* option. The final opening and sliding displacements from these simulations are shown in Figure 2-17 and Figure 2-18.

Results from A3-S8 and A3-S9 were virtually identical. The value of E_0 in these simulations was very small, and so the closed fractures experienced very little normal deformation and induced little normal stress. As E_0 was increased, from S9 to S12, the normal displacements of the closed fractures became greater, and the induced normal stresses became increasingly significant. As induced normal stresses became greater, the induced opening and sliding of the elements decreased, shown in Figure 2-17 and Figure 2-18.

These results demonstrate that for small values of E_0 consistent with cracks, the *cstress* option has a limited effect. For larger values of E_0, consistent with faults or fracture zones, the *cstress* option could have a major impact on results. However, these results are probably not realistic (Section 2.2.3.3) because the Shou and Crouch (1995) Displacement Discontinuity method is probably not appropriate for larger values of E_0. The Shou and Crouch (1995) method is intended to describe the opening of cracks, not the poroelastic swelling of fault zones. Future work is needed to replace the Shou and Crouch (1995) kernal with a boundary element method designed for swelling of porous fault zones.

2.4.2 Model B

Simulations were performed with Model B to test simulations options on a large, relatively complex fracture network. Model B contained 52,748 elements and 1080 fractures. Each simulation involved injection at constant rate for two hours (in simulation

time), involved thousands to hundreds of thousands of time steps, and required hours to days of computation time on a single processor.

The fracture network and simulation parameters were not calibrated to match any particular location. Nevertheless, the results could be used to draw some interesting insights about shear stimulation.

2.4.2.1 General Description of Results

The results from Model B demonstrate pure shear stimulation -- transmissivity enhancement was from induced slip on preexisting fractures. Injection pressure was consistently above 50 MPa, the least principal stress (Figure 2-30), but it was specified as a model parameter that new fractures could not form (Section 2.3.3). As a result, all injected fluid was contained in preexisting fractures, some of which opened as the fluid pressure exceeded their normal stress. The injection pressure was quite variable with time as evolution of transmissivity sometimes caused drops in injection pressure (Figure 2-30).

All fractures in the model were well oriented to slip in the preexisting stress state, yet not all fractures close to the wellbore slipped (Figure 2-18). This occurred because of the way that shear stimulation progresses through the network and because of stress shadowing.

The process of crack-like shear stimulation (described in Sections 3.4.2.2 and 4.4.2) is very efficient at propagating transmissivity enhancement down a single, linear fracture. Ahead of an effective shear crack tip (the boundary of where slip has occurred), there is a shear stress concentration that can induce slip and permeability enhancement (even if fluid pressure perturbation has not yet reached this point). Therefore, once slip begins to occur on a fracture, it tends to relatively rapidly advance down the entire fracture.

Episodic propagation of shear stimulation down faults can be seen in Figure 2-24, which shows the timing and magnitude of seismic events from Simulation B6. There were periods of relatively intense seismicity. Each period of seismic intensity corresponded to the progressive advancement of fluid pressure, slip and transmissivity enhancement down a particular fracture. The effects were evident in the plot of injection

pressure. For example, there was a period of intense seismicity at around 5500 seconds (Figure 2-24) as slip and transmissivity enhancement advanced down a newly stimulating fracture. At the same time, injection pressure dropped (Figure 2-31). There was a similar, smaller drop in injection pressure that corresponded with a period of intense seismicity around 5000 seconds (Figure 2-24 and Figure 2-31).

In contrast to propagation of slip down a fracture, the initiation of slip on a fracture is (typically) not aided by induced stresses. Most commonly, initiation of slip requires fluid pressure to diffuse into the (unstimulated) fracture, which is a process that is rate-limited by the initial transmissivity of the fracture (Section 3.4.2.2).

When fractures slip, they relieve shear stress along their sides, inhibiting neighboring, parallel fractures from also slipping, a process referred to as stress shadowing. In the simulations, the spatial range of the perturbation was limited by the height of the formation, 100 m, because the Olson (2004) correction was used (Section 2.2.3.2). Stress interaction was manifested in other ways. Fracture opening occurred in the extensional quadrants of slipping fractures (Figure 2-18) due to induced reductions in normal stress.

These effects explain why many apparently well oriented fractures did not slip. The most optimally oriented fractures intersecting the wellbore slipped earliest. Once they began to slip, the shear stimulation process allowed stimulation to propagate along them quite rapidly. The fractures that slipped first caused stress shadows that prevented or delayed the neighboring fractures from slipping.

The final distribution of transmissivity was relatively extensive spatially, spreading 200 m from the wellbore. Yet most connections to the wellbore were relatively isolated from each other. There were not necessarily direct flow pathways between neighboring stimulated fractures. This is a realistic result for flow in fracture networks in low permeability matrix and a direct consequence of the use of discrete fracture network modeling and the inclusion of stresses induced by fracture deformation.

2.4.2.2 Effect of Temporal Discretization Refinement

Simulations B1-B4 tested the performance and accuracy of the model at various values of η_{targ}, the parameter that determines time step duration (Section 2.2.3.9). Figure

2-18 and Figure 2-19 show the final sliding and opening displacements for Simulations B1 and B4, the most and least temporally resolved simulations. With visual inspection, small differences can be observed (most notably, there is an entire fracture that slipped in Simulation B4 that did not slip in B1), but the results were generally rather similar. Plots of the final displacements for B2 and B3 are not shown because they are visually indistinguishable from the results from B1 in Figure 2-18.

From these results, it can be concluded that the value of η_{targ} in Simulation B4 was too large, but the value for η_{targ} in B2 and B3 was sufficient for reasonably accurate results. Figure 2-20 demonstrates that results the results were convergent to temporal refinement. The behavior of injection pressure with time was visually identical for Simulations B1-B3. Simulation B4 was similar, but a major difference was that there was a drop in injection pressure near the end of the simulation that did not occur in Simulations B1-B3 (Figure 2-30). The drop in injection pressure occurred when shear stimulation rapidly propagated a particular large fracture. This fracture was stimulated in Simulation B4 but not in Simulations B1, B2, and B3 (Figure 2-18 and Figure 2-19), and so the drop in injection pressure did not occur in those simulations.

Run-time and number of iterations increased significantly as η_{targ} decreased (Figure 2-27). With larger η_{targ}, average time step duration increased, and so the iterative coupling scheme required more iterations between the shear stress residual equations and the flow/normal stress residual simulations (see Section 2.2.3.1). As a result, the simulations with larger η_{targ} took fewer time steps but had greater run-time per time step (Figure 2-28).

2.4.2.3 Effect of *cstress*

Simulations B8 and B9 tested the *cstress* option with an E_0 equal to 0.8 mm. Testing of *cstress* with Model A3-(S9-S12) suggested that with E_0 equal to 0.8 mm, the *cstress* option would probably have a moderate effect on the results. For example, Simulation A3-S11, which used E_0 equal to 1 mm, was significantly affected by the *cstress* option (Figure 2-16 and Figure 2-17).

From visual inspection, the plot of final slip and opening for Simulation B8 (Figure 2-23) appears reasonably similar to the result from Simulation B1 (Figure 2-18). *cstress* may have had less effect in Model B because the fractures were significantly larger than in Model A. Because fracture stiffness decreases with length, less stress is induced on a fracture of greater length for the same normal displacement. Figure 2-20 shows that within the stimulated fractures, the Euclidean norm (scaled for problem size) of the difference in sliding displacement between Simulation B8 and B1 was roughly 4 mm. This difference is fairly significant because the average sliding displacement in the stimulated region was about 2.3 cm.

The number of time steps performed during B8 simulations was almost identical to the number performed in B3 (which used the same η_{targ}), but the simulation run-time was 5.2 times greater. Computation time per time step was roughly 5.9 s for B8 and 0.8 s for B3. The additional simulation time was needed for two reasons. With the *cstress* option, updating the stresses caused by deformation of the closed elements requires multiplication by the matrix of interaction coefficients (using Hmmvp). Second, the iteration matrix in the flow/normal stress system of equations is significantly larger and requires more time to solve (Equation 2-30).

2.4.2.4 Effect of Adaptive Domain Adjustment

Simulations B5 and B9 used adaptive domain adjustment. These simulations can be compared to B3 and B8, which were otherwise identical to B5 and B9 but did not use adaptive domain adjustment. The reduction in computation time achieved by the adaptive domain adjustment was around 15% for the simulations not using *cstress* and about 30% for the simulations using *cstress* (Figure 2-27 and Figure 2-29). The simulation results using adaptive domain adjusment were virtually identical to the simulations not using adapative domain adjustment.

From Figure 2-29, it can be seen that at early time the simulations using adaptive domain adjustment were significantly more efficient, but after the early stages of the simulation, the advantage had disappeared. It was expected that the efficiency gain would only occur early in the simulation beacuse as pressure perturbation and simulation

spread from the injector well, the number of elements included in the *checklist* increased until it included all elements.

2.4.2.5 Dynamic Friction Weakening

Simulation B6 was performed to test the effect of dynamic friction weakening (Section 2.4.3). Seismic event magnitudes spanned a range between -2.5 and 2.0 (Figure 2-24). The minimum magnitude was determined by the minimum element size in the model. Because slip was typically confined to a single fracture during a seismic event, the maximum magnitude was limited by the largest fracture in the model.

Due to the Crack-like Shear Stimulation mechanism (Section 3.4.2.2). There were periods of relatively intense seismicity separated by periods of relatively mild seismicity (Figure 2-24). The periods of greater activity occurred as slip and transmissivity enhancement propagated down a fracture for the first time. Once a fracture began to slip, transmissivity enhancement and fluid pressure were able to propagate down the fracture relatively quickly because slips induced shear stress along the fracture, which encouraged slip and transmissivity enhancement (Sections 3.4.2.2 and 4.4.2).

Figure 2-26 shows the locations of the hypocenters with an adjustment to simulate the effect of relocation error. The relocation causes the hypocenters to form a volumetric cloud. However, Figure 2-21 shows the final slip distribution (with transmissivity enhancement closely correlated to slip), and it demonstrates that the actual fracture network is relatively sparse, widely spaced, and poorly connected. This result is consistent with results from EGS, for example, where production logs sometimes demonstrate a wide spacing of flowing fractures yet microseismic relocations appear volumetric (Michelet and Toksöz, 2007).

The results indicate the peril of attempting to infer fracture geometry from the shape of a microseismic cloud. Without knowing the actual locations of stimulated fractures (Figure 2-21), an observer might infer from Figure 26 that there is a long fracture oriented in the direction of the y-axis at the location x = -150 m. Figure 2-26 shows that no such fracture exists.

Simulation B6 was slightly more efficient per time step than Simulation B3, which used the same η_{targ}. Simulation B6 used significantly more time steps than Simulation B3 because a large number of short time steps were needed to simulate the rapid slip during seismic events.

2.4.2.6 Neglecting Stress Interaction

In Simulation B7, neglecting stress interaction between fractures caused the stimulated fracture geometry to be completely different (Figure 2-22). Stress interaction is rarely included in models of large, complex fracture networks (Section 1.2), but this example demonstrates how profoundly stress interaction affects simulation results. There are many effects from stress interaction, but one of the most important is helping the region of transmissivity enhancement spread (a process referred to as crack-like shear stimulation that is described in detail in the Sections 3.4.2.2 and 4.4.2). Induced shear stresses help stimulation propagate along fractures. Without that effect, the stimulated region (in shear stimulation) can only grow as rapidly as flow can occur into elements at initial transmissivity, a process that can be very slow if initial transmissivity is low. If the region of transmissivity enhancement grows too slowly to accommodate the injected fluid, fluid pressure is forced to rise, causing opening.

In Simulation B7, new fractures were not permitted to form (Section 2.3.3), but preexisting fractures were permitted to open. The thickness of the stimulated fractures in Figure 2-22 indicates that these fractures have opened significantly. The crack tip region adjustment (Section 2.4.2) was not deactivated in Simulation B7, and this process turned out to be the primary way that the region of stimulation was able to grow. Figure 2-31 shows that the injection pressure during Simulation B7 was almost constant at around 55 MPa. This was the injection pressure at which the natural fractures were able to open, enabling the crack tip adjustment to be activated.

2.4.3 Model C

Model C is an example of mixed-mechanism propagation, where stimulation progresses through both propagation of new fractures and opening and sliding of preexisting fractures (Section 3.1.1). Mixed mechanism propagation is most commonly proposed as an explanation for gas shale stimulations (Gale et al., 2007; Weng et al., 2011). The natural fracture network was not percolating -- there were no continuous pathways through the reservoir contained only in the natural fractures However, continuous, long distance pathways for flow were able to develop because of the formation of new fractures (Figure 2-32). This is an important point of distinction between pure shear stimulation and mixed-mechanism propagation. Shear stimulation requires percolation of the natural fracture network while mixed-mechanism propagation does not (Section 3.4.8). In Chapter 3, there is much more analysis and discussion of mixed-mechanism propagation.

Model C demonstrated that the model is capable of performing efficiently for mixed-mechanism stimulations. Model C ran significantly faster and used fewer time steps than Model B3, which used the same value for η_{targ}. However, Model C had fewer than half as many elements as Model B3 (Section 2.3.1).

2.4.4 Model D

The Model D simulations were performed to test the efficacy of the strain penalty factor and to investigate model behavior at low-angle fracture intersections. In the two simulations without the strain penalty factor, there were unrealistic numerical artifacts, with rapid oscillation between large and small opening between elements (Figure 2-33 and Figure 2-35).

Comparison between D1-DS1 and D2-DS1 shows that discretization refinement reduces numerical artifacts at low-angle intersections, but it cannot eliminate then completely. In D2-DS1, the region of numerical artifacts is smaller, localized in the immediate vicinity of the intersection, while in D1-DS1, numerical artifacts are present a significant distance from the intersection.

Numerical artifacts such as oscillations in fracture opening are not present in the simulations that used the strain penalty method, D1-DS2 and D2-DS2 (Figure 2-34 and Figure 2-36). In D2-DS2, modest penalty stresses applied very near the intersection prevented numerical oscillations without having a major effect on the overall results. In D1-DS2, penalty stresses prevented numerical oscillations, but comparison to D2-DS2 shows that the results were affected significantly. These results show that while the penalty stress method prevents numerical artifacts, it also causes inaccuracy. D2-DS2 shows that the inaccuracy caused by the penalty method can be limited to a very small region if the discretization is reasonably refined around the intersection.

2.4.5 Hierarchical Matrix Decomposition

Hmmvp demonstrated exceptional performance and scaling for matrix multiplication. For progressive refinement of a fracture network, Hmmvp had linear scaling with problem size (Figure 2-38). For constant level of refinement and increasing problem size, Hmmvp had $n\log(n)$ scaling with problem size (Figure 2-40). For creation of the matrix approximation, Hmmvp had linear scaling (Figure 2-41).

Tests of Hmmvp with the simulator demonstrated its accuracy and efficiency. The settings for Simulations A4-S0 and A4-S3 were identical except that A4-S0 used direct matrix multiplication instead of Hmmvp. The results were virtually identical, yet A4-S0 required roughly ten times more computation time (Figure 2-10). A similar comparison was made between Simulations A4-S6 and A4-S7, and in this case, the simulation using Hmmvp was 23 times more efficient. The A4-S6 and A4-S7 simulation results were virtually identical (Figure 2-15). Because FLOPs per multiplication achieved by Hmmvp grows much more slowly with size than direct matrix multiplication, the efficiency gain grows as the problem size increases.

2.4.6 Extension of the Model to Three Dimensions

The model described in this chapter could be extended to three-dimensional modeling. Stress calculations would be identical except that a different boundary element method would be used to calculate interaction coefficients. In the fluid flow

equations, three-dimensionality would only change the calculation of the geometric transmissibility term. A few specific details would be changed, such as changing the way that the stress intensity factors are calculated (Section 2.2.5.2). Changes would also be required for discretization and visualization of results.

There are several physical issues specific to three-dimensional models that could be challenging to handle due to their inherent complexity. For example, a propagating mode I fracture subjected to mode III loading may form an en echelon array of smaller fractures (Pollard et al., 1982).

The main challenge of three-dimensional simulations is that they would require a greater number of elements. Because our model only requires discretization of the fractures, the number of elements would be much smaller than if volumetric discretization was required (such as with finite element). Because the Model B simulations ran in hours or days on a single computer, parallelization would be necessary for simulating substantially larger problems. Fortunately, there is no major theoretical obstacle to parallelization. The matrix multiplication aspect of the problem would be trivial to parallelize and has excellent scaling with problem size. Solving the iteration matrix system in the flow/normal stress subloop could be done with standard parallel solvers for sparse systems.

2.5 Conclusions

The modeling methodology described and demonstrated in this chapter is capable of efficient and accurate simulation of fluid flow, deformation, seismicity, and transmissivity evolution in large two-dimensional discrete fracture networks. Appropriate stress boundary conditions and constraints on displacements are applied on elements depending on whether they are open, sliding, or stationary. Results are convergent to grid refinement, and discretization settings required for acceptable accuracy were identified. A variety of techniques that enable efficiency and realistic model behavior -- such as adaptive domain adjustment, crack trip region adjustment, and the strain penalty method -- have been developed and tested. The model can be used for

direct solution of fracture contact problems in a way that has minimal memory requirement, excellent efficiency, and desirable scaling with problem size.

Test results demonstrated the critical importance of including stresses induced by deformation in modeling of stimulation. These stresses directly impact the mechanism of stimulation propagation and the properties of the resulting fracture network.

The primary limitations of the model are that it is two-dimensional and that it requires the paths of newly forming tensile fractures to be specified in advance. There is no theoretical reason why these limitations could not be resolved in future work.

The model can be used to explore the behavior of hydraulic stimulation in settings where preexisting fractures play an important role. The model can be used to describe pure shear stimulation, mixed-mechanism stimulation, or purely opening-mode propagation of tensile fractures.

Chapter 3

3 Conceptual Models of Stimulation

This chapter describes the investigation of the mechanisms of stimulation during hydraulic fracturing in low matrix permeability settings such as gas shale or Enhanced Geothermal Systems (EGS). Four stimulation mechanisms were identified that encompass the variety of conceptual models that are used in the EGS and gas shale literature: pure opening mode (POM), pure shear stimulation (PSS), mixed-mechanism stimulation (MMS), and primary fracturing with shear stimulation leakoff (PFSSL). Identification of stimulation mechanism has direct application in stimulation modeling, stimulation optimization, and formation evaluation. Numerical simulations representative of the four stimulation mechanisms were performed using a hydraulic fracturing model that couples fluid flow, stresses induced by fracture deformation, and transmissivity evolution in two-dimensional discrete fracture networks that contain as many as thousands of fractures. The behavior of the models was studied to determine the overall properties of the different stimulation mechanisms. Based on the simulation results, practical methods of diagnosing stimulation mechanism were developed. These diagnostic methods include interpretation of the downhole fluid pressure during injection, shut-in, and production, microseismicity, and wellbore image logs. A "Tendency for Shear Stimulation" (TSS) test was designed as a practical, direct way to interrogate formation properties and help identify stimulation mechanism in the field. Potential

pitfalls for estimating least principal stress were identified. A variety of geological factors that may affect the stimulation mechanism were summarized. Mechanisms that could cause reduced fluid recovery were demonstrated. A mechanism referred to as "Crack-like Shear Stimulation" (CSS) was identified as controlling the rate at which shear stimulation progresses along a fracture. Even thought the PSS mechanism is commonly assumed in geothermal energy, there is substantial reason to suspect that MMS may be a better conceptual model in many EGS projects.

3.1 Introduction

The classical conceptual model of hydraulic fracturing is that one or several wing-shaped, opening mode fractures propagate away from the wellbore (Khristianovic and Zheltov, 1955; Perkins and Kern, 1961; Geertsma and de Klerk, 1969; Nordgren, 1972). This conceptual model is still used in hydraulic fracturing design and modeling in conventional settings (Economides and Nolte, 2000; Meyer and Associates, Inc., 2011; Adachi et al., 2007). However, the classical conceptual model neglects the effect of preexisting fractures, which play a critical role in low matrix permeability settings such as EGS or gas shale.

Evidence of the role of preexisting fractures comes from a variety of sources. In EGS projects in crystalline rock, wellbore observations demonstrate that during and after stimulation, fluid exits from the wellbore from preexisting fractures, not from newly formed tensile fractures. For example, this has been observed at projects in Fenton Hill, New Mexico, USA (Brown, 1989), Rosemanowes, UK (Moore and Pearson, 1989, section 3.4.3), Ogachi, Japan (Ito, 2003), Soultz-sous-Forêts, France (Evans, Genter, and Sausse, 2005; Dezayes et al. 2010), and Cooper Basin, Australia (Baisch et al., 2009).

In gas shale, the word "complexity" is often used to express the idea that formation productivity is generated by both the propagation of new fractures and induced opening and shear of preexisting fractures (Fisher et al., 2004; Bowker, 2007; Gale et al., 2007; Cipolla et al., 2008; King, 2010). The complex fracture network conceptual model for gas shale is based on wide fairways of microseismicity (Warpinski et al., 2005),

laboratory experiments (Blanton, 1982; Renshaw and Pollard, 1995; Gale and Holder, 2008; Gu et al., 2011), direct observation from mine-backs and coring across induced fractures in settings other than gas shale (Warpinski and Teufel, 1987; Warpinski et al., 1993; Mahrer, 1999; Jeffrey et al., 2009), correlation of productive zones to natural fracture density (Ketter et al., 2006; Mullen et al., 2010; Moos et al., 2011), and calculations demonstrating that large stimulated fracture surface areas are needed to explain the high cumulative recoveries achieved in low matrix permeability formations (Mayerhofer et al., 2010; Fan et al., 2010; Cipolla et al., 2010).

In both EGS and gas shale, microseismicity is apparently generated by the process of induced slip on preexisting fractures. In EGS, induced seismicity can sometimes be strong enough to be felt at the surface, indicating that slip surfaces during a single event can be as high as tens of thousands of m^2 (Majer et al., 2007). In gas shale, microseismicity is much lower magnitude, and substantial evidence suggests that most slip is aseismic (Zoback et al., 2012).

Although it is well established that preexisting fractures play an important role in EGS and gas shale, the details are not fully understood. Permeability generation and fluid storage may occur in new opening-mode fractures or in preexisting fractures that either open or fail in shear. Each of these processes may play a greater role in some settings than in others and may occur to different degrees in different parts of the same reservoir. The way that different modes of deformation interact to generate permeability can be categorized in different ways, which we refer to as the "stimulation mechanism" or the "conceptual model."

In this work, four conceptual models for stimulation mechanism were investigated (described in detail in Section 3.1.1): (1) pure opening mode propagation of new fractures, referred to as POM (Pure Opening Mode), (2) pure shear mode deformation of preexisting fractures, referred to as PSS (Pure Shear Stimulation), (3) opening mode propagation of primary fractures with leakoff into a surrounding zone of shear stimulation of preexisting fractures, referred to as PFSSL (Primary Fractures with Shear Stimulation Leakoff) and (4) mixed propagation of new opening mode fractures and

shear and opening of preexisting fractures, referred to as MMS (Mixed-Mechanism Stimulation).

We do not intend to propose a general classification scheme for stimulation mechanism. These four mechanisms do not include every possible conceptual model (for example, Zhai and Sharma, 2005). In some cases, conceptual models might be best described as intermediate between the different mechanisms. It is also possible that different mechanisms could take place simultaneously in different parts of the reservoir during a single stimulation. Despite some limitations, these concepts are presented because they are useful for conceptualizing and modeling hydraulic stimulation.

Here, we use the term "complexity" to refer to fracture network that has a large number of distinct fractures participating in flow. Complexity is a property that is distinct from stimulation mechanism. Hypothetically, any of the four mechanisms described in this chapter could occur in a "simple" or a "complex" way. For example, the PSS mechanism would be considered simple if shear stimulation was localized to a few large, planar fault zones (shown later in Simulation B). PSS would be considered complex if shear stimulation occurred in a volumetric, distributed network of smaller fractures (shown later in Simulation H). Complex stimulation in settings with high matrix permeability is unfavorable because of excessive fluid leakoff. Low stress anisotropy contributes to greater fracture complexity by allowing a variety of fractures orientations to be able to open or shear at similar fluid pressure (Delaney et al., 1986; Olson and Pollard, 1989; Doe and Boyce, 1989).

Categorizing and identifying stimulation mechanisms could be useful for a variety of modeling and engineering purposes (Section 3.1.2). In a computational model, stimulation mechanism is a fundamental assumption that directly affects both results and the design of the model itself. In formation evaluation, variations in stimulation mechanism could help explain differences in productivity between wells and stages. In stimulation design, operational parameters could be optimized for each mechanism.

The four conceptual models described in this chapter represent different ideas about the physical mechanisms causing enhancement of formation productivity. Stimulations

are designed to encourage the physical processes causing stimulation, and so different hypotheses about mechanism will lead to different stimulation designs.

Based on modeling results in this chapter and a review of the literature, a variety of geological conditions that may affect stimulation mechanism were identified (Section 3.1.3). However, modeling and analysis have not progressed to the point where these factors can be integrated unambiguously into a prediction of mechanism prior to stimulation. Predicting mechanism in advance is particularly difficult because stimulation mechanism is often not well established even after stimulation has been performed.

As noted by Starfield and Cundall (1988), when modeling systems with limited data, problems can be ill-posed and validation can be difficult or impossible. For example, stimulation models commonly perform validation by matching injection pressure, flow rate, and/or spatial and temporal distribution of microseismicity (Bruel, 2007; Palmer et al., 2007; Cipolla et al., 2011). However, these validations are nonunique, and a great variety of potential models, using a variety of underlying assumptions, could be constructed to match the limited available data. Drilling, coring, and/or logging a well through a newly fractured volume of rock in an EGS or gas shale reservoir (for example, through a region of high microseismic density) would allow direct observation of stimulation mechanism. However, this sort of data collection would be expensive and is very rarely done (two examples where this has been done are Warpinski et al., 1993 and Fast et al., 1994, from tight gas sand and Opal-A diatomite, respectively).

Diagnostic methodologies are needed that can identify stimulation mechanism using data that can be collected routinely during and after stimulation. The ability to diagnose mechanism would enable validation of numerical models and lead to the development of methodologies that could be used to predict mechanism in advance.

In this study, computational modeling was used to investigate the properties of the stimulation mechanisms in order to identify methodologies that could be used practically to identify mechanism. A variety of simulations were performed that were designed to be representative of the various mechanisms of stimulation (Sections 3.2 and 3.3). The overall behavior of these simulations is discussed in Sections 3.4.1 to 3.4.4.

Methodologies to diagnose stimulation mechanism are summarized in Section 3.4.11. Diagnostic methodologies include identifying the relationship between downhole fluid pressure and the least principal stress, σ_3, during injection, shut-in, and production (Sections 3.4.5 and 3.4.6) and a proposed test called a Tendency for Shear Stimulation test (TSS), that would directly measure the formations ability to shear stimulate (Section 3.4.8). Microseismicity hypocenter relocations can be used in TSS tests and for identification of shear stimulation propagating along large faults (Section 3.4.9). Because of the importance of accurate estimation of σ_3 for the results of this chapter, a variety of pitfalls are discussed that could cause inaccurate estimation of σ_3 (Section 3.4.7). Two different mechanisms were identified for poor fluid recovery (in addition to leakoff into the matrix): leakoff into the natural fracture network and snapoff, where fracture closure causes isolation of open fractures away from the wellbore (Section 3.4.6). A physical process, referred to as crack-like shear stimulation (CSS) was identified as the mechanism by which shear stimulation propagates along a fracture (Section 3.4.2.2). The CSS process was observed in simulation results throughout this dissertation and is important in determining the rate at which shear stimulation propagates through a formation (Sections 2.4.2.5, 3.4.2.2, and 4.4.2).

The numerical model used in this chapter is described in complete detail in Chapter 2 and is summarized in Section 3.2.1. The model simulates fluid flow, deformation, permeability evolution, and fracture propagation in complex discrete fracture networks involving up to several thousand fractures. The model assumes single-phase, isothermal flow of liquid water, negligible matrix permeability, and small strain deformation in a homogeneous, isotropic, infinite, linearly elastic medium. The model was designed specifically for simulation of hydraulic stimulation in low matrix permeability settings where preexisting fractures play an important role.

In this research, we sought to follow the methodology described by Starfield and Cundall (1988), who said that "the purpose of modelling data-limited problems is to gain understanding and to explore potential trade-offs and alternatives, rather than make absolute predictions." They suggested an iterative strategy for studying data-limited systems. In this strategy, models are used to identify insightful new ways to obtain or interpret data. Subsequent gathering of new data leads to improved models, and so on.

Here, modeling was used to identify data collection and analysis that could be used to determine stimulation mechanism, which would in turn lead to improved design of stimulation models.

A significant amount of terminology is defined in this chapter, and so Table 3-1 is provided as a reference to help keep track.

Table 3-1: Summary of terminology used in Chapter 3.

Terminology	Description	Description in Text
POM	Pure Opening Mode	Section 3.1.1
PSS	Pure Shear Stimulation	Section 3.1.1
PFSSL	Primary Fracturing with Shear Stimulation Leakoff	Section 3.1.1
MMS	Mixed mechanism stimulation	Section 3.1.1
CSS	Crack-like shear stimulation	Section 3.4.2.2
ECSS	Episodic crack-like shear stimulation	Section 3.4.2.2
SCSS	Smooth crack-like shear stimulation	Section 3.4.2.2
TSS	Tendency to Shear Stimulation	Section 3.4.8
Simulation A	Prototype of POM	Section 3.2.2
Simulation B	Prototype of PSS	Section 3.2.2
Simulation C	Simulation B with low initial transmissivity	Section 3.2.2
Simulation D	Simulation B with low fracture storativity	Section 3.2.2
Simulation E	Prototype of MMS	Section 3.2.2
Simulation F	Prototype of PFSSL	Section 3.2.2
Simulation G	TSS test in a non-percolating network	Section 3.2.2
Simulation H	TSS test in a percolating network	Section 3.2.2
Simulation I	Step rate test with fracture properties similar to Simulation B	Section 3.2.2
Injection Schedule S1	Injection at three different rates, shut-in, then production	Section 3.2.2
Injection Schedule S2	Injection at constant pressure less than minimum principal stress	Section 3.2.2
Injection Schedule S3	Step rate test injection schedule	Section 3.2.2

Fracture Network F1	Only potentially forming fractures	Figure 3-3
Fracture Network F2	A few spatially extensive faults and long, continuous potentially forming fractures	Figure 3-4
Fracture Network F3	Non-percolating natural network with lots of potentially forming fractures that terminate against natural fractures	Figure 3-5
Fracture Network F4	Percolating, dense network of intermediate length fractures with long, continuous potentially forming fractures	Figure 3-6
Fracture Network F5	Non-percolating natural network with a high density of short fractures	Figure 3-7

3.1.1 Mechanisms of Stimulation

The four stimulation mechanisms investigated in this research are: Pure Opening Mode, POM, Pure Shear Stimulation, PSS, Primary Fracture with Shear Stimulation Leakoff, PFSSL, and Mixed-Mechanism Stimulation, MMS (Figure 3-1).
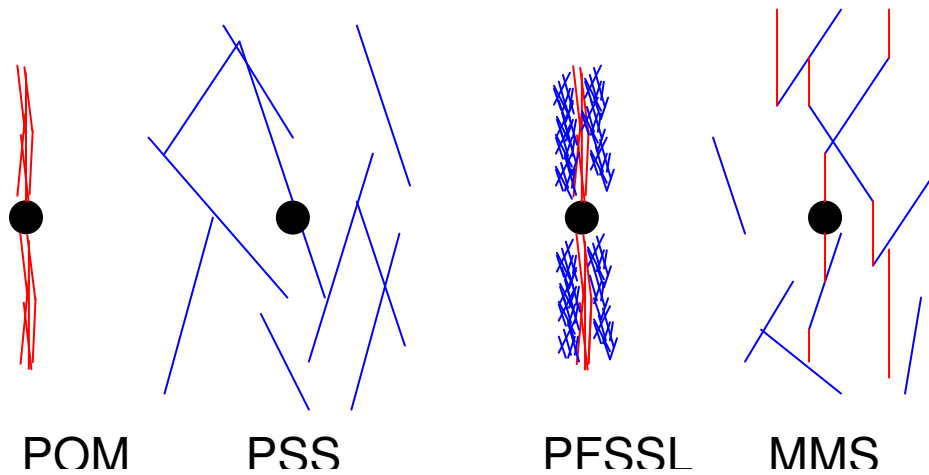
Figure 3-1: Reservoir scale schematics of stimulation mechanism. Blue lines represent preexisting fractures that experience enhanced transmissivity due to opening or slip. Red lines represent newly formed tensile fractures. Black dots represent the wellbore.

In the POM mechanism, fracturing occurs through the propagation of new, opening mode fractures. The classical conceptual model of hydraulic fracturing is POM stimulation in which fractures form in large planar features (Khristianovic and Zheltov, 1955; Perkins and Kern, 1961; Geertsma and de Klerk, 1969; Nordgren, 1972). This

conceptual model is still used widely in modern hydraulic fracturing design (Economides and Nolte, 2000; Adachi et al., 2007; Meyer and Associates, Inc., 2011). According to our definition of POM stimulation, the fractures do not have to form large planar features (which is an idealization of actual fractures geometries, see Warpinski et al., 1993 and response by Nolte, 1993; Mahrer, 1999), but it is necessary that continuous paths through the reservoir traverse almost entirely through newly formed, opening-mode fractures. To satisfy our definition of POM, permeability enhancement due to slip on preexisting fractures must be minor or nonexistent. The POM model is appropriate for reservoirs where natural fractures have little impact on either the propagation of newly forming fractures or the overall process of permeability enhancement.

In the PSS mechanism, injected fluid induces slip on preexisting fractures, increasing their transmissivity. In general, the fluid pressure needed to induce slip on preexisting fractures can be above or below the minimum principal stress (typically below) and is dependent on the local stress state and fracture orientation (Murphy and Fehler, 1986; Pine and Batchelor, 1984). If injection pressure is above the least principal stress, opening of new or preexisting fractures may occur. This may happen during the PSS mechanism, but in order to be categorized as PSS, the effect of fracture opening on fluid flow and stimulation must be minor relative to the effect of shear stimulation.

The PSS mechanism is the most widely accepted conceptual model in EGS, where it is referred to as shear stimulation or hydroshearing (Pine and Batchelor, 1984; Murphy and Fehler, 1986; Evans, 2005; Kohl and Mégel, 2007; Bruel, 2007; Dezayes et al., 2010; Ito, 2003; Ito and Hayashi, 2003; Tester, 2007, Cladouhos et al., 2011). The PSS mechanism is not found in the gas shale literature because in gas shale it is always assumed that newly forming fractures propagate through the reservoir. The PSS mechanism is only possible in lithologies where slip causes an increase in permeability (Esaki et al., 1999; Lutz et al., 2010).

In the PFSSL mechanism, as in the POM mechanism, opening mode fractures propagate continuously through the reservoir without major disruption due to preexisting fractures. In the PFSSL mechanism, unlike the POM mechanism, shear stimulation takes place during or after the propagation of the new fractures. Fluid leaks off from the

primary fractures (the continuous, propagating opening mode fractures) into a surrounding region of shear stimulation.

In gas shale, the PFSSL mechanism is often used because the high fracture surface area of the secondary region could explain the high productivity of wells after stimulation. The PFSSL mechanism has been used in gas shale stimulation modeling by Warpinski et al. (2001), Palmer et al. (2007), Rogers et al. (2010), Nagel et al. (2011), and Roussel and Sharma (2011). The primary fractures (the large, continuous opening mode fractures) are typically modeled with the same techniques used in classical hydraulic fracturing.

In the MMS mechanism, opening mode fractures propagating through the formation tend to terminate at preexisting fractures. Preexisting fractures may open or slide, and new opening mode fractures may initiate from preexisting fractures. A key characteristic of the MMS mechanism is that continuous flow pathways through the reservoir pass through both new and preexisting fractures.

The MMS mechanism does not necessarily imply a complex fracture network. However, in gas shale, the process of branching through fracture termination and reinitiation is often used to explain the fracture complexity believed to exist in the reservoir based on the typically high well productivity (Gale et al., 2007; Bowker, 2007; Warpinski et al., 2009; Cramer, 2008). The MMS mechanism has been used in gas shale stimulation modeling by Damjanac et al. (2010), Weng et al. (2011), and Wu et al. (2012). The MMS mechanism is not prominent in the EGS literature, but as discussed in Section 3.4.6, Brown (1989) and Brown et al. (2012) argued that the MMS mechanism took place at the Fenton Hill EGS project.

3.1.2 Practical Consequences of Stimulation Mechanism

Engineers' assumptions about stimulation mechanism have a variety of practically important consequences. Stimulations mechanism affects analysis of well performance data to identify optimal design, design decisions based on physical intuition, formation evaluation, and stimulation modeling.

Some studies of gas shale stimulation technique have used large data sets to seek correlations between wellbore performance and various operational and geological parameters (Lehman and Shelley, 2010). A problem with this approach is that optimal stimulation strategy may depend on geological parameters that are not the same for every well. Studies may not be successful if they lump every well in a play into a single data set. A sophisticated statistical analysis may attempt to derive more complex relationships between geological parameters, operational parameters, and performance. But even the best statistical methods may not be able to distinguish the full character of complex relationships. Also, statistical methods remain limited by the imagination of the user. Critical data that could be used for stimulation optimization (for example, wellbore image logs) may not be gathered or may not be included in the statistical analysis. A better understanding of mechanism could alert engineers to the relationships that they might expect to find in datasets (assisting in the design of statistical studies) and help engineers decide what data might be useful to collect.

Just as importantly, understanding of mechanism could assist engineers extrapolate performance to settings where data has not yet been gathered. Ideas about mechanism could help predict stimulation performance in new geological settings and to predict the performance of new stimulation techniques that have not yet been tried.

From the point of view of stimulation design, different strategies may be attempted depending on the physical process that is believed to be causing good performance. Perhaps with PFSSL, maximizing the length of the "primary" fracture may be viewed as the best way to maximize stimulated fracture surface area. Perhaps with MMS, fracture branching due to termination at natural fractures may be viewed as key to creating an effective stimulation. Decisions such as injection rate and timing of proppant may be very different depending on whether engineers are trying to maximize branching (assuming MMS) or maximize fracture length (assuming PFSSL).

From the point of view of formation evaluation, engineers expecting PSS or PFSSL may seek out formations with abundant fractures that are well oriented to slip in the local stress state. High anisotropy of stress may be seen as a positive, because it would tend to cause higher shear stress on natural fractures. In contrast, if engineers expect MMS,

lower stress anisotropy may be seen as a positive because it would encourage fracture branching.

From the point of view of modeling, it is clear that accurate ideas about mechanism are critical. Models may be developed with great care and sophistication, but if they do not describe the correct physical processes, they will have limited usefulness. Nonuniqueness allows a variety of models to match the limited data, leading to a sense of confidence in numerical modeling results that may not be well founded.

3.1.3 Effect of Geological Parameters on Stimulation Mechanism

In this section, the effects of certain geological parameters on stimulation mechanism are summarized. This discussion is based on review and interpretation of the literature and on results in this chapter. Interpretation of these various geological parameters to determine stimulation mechanism may sometimes be ambiguous, which is why a major purpose of this research is to identify ways that stimulation mechanism could be identified in the field (after stimulation) without relying on interpretation of geological parameters. Nevertheless, understanding of the effect of geological parameters is useful. Future studies could use geological characterization to predict stimulation mechanism and then use diagnostic methodologies to validate or refute the predictions. With increasing experience, methodologies to predict stimulation mechanism will grow more robust. Table 3-5 in Section 3.4.11 summarizes the methodologies that could be used to diagnose mechanism after stimulation has been performed.

The geological parameters discussed in this section are: storativity of natural fractures, transmissivity of natural fractures before and after induced shear, stress state, natural fracture density and orientation, percolation of the stimulated natural fractures network, termination of propagating new tensile fractures at preexisting fractures, and the difference in tensile strength between intact rock and natural fractures. In keeping with the focus of this chapter, low matrix permeability and low initial fracture transmissivity are assumed.

Table 3-2 summarizes key points about how these factors may affect the tendency for a particular mechanism to occur.

Table 3-2: Effect of geological conditions (columns) on stimulation mechanism (rows).

	High natural fracture storativity	*Percolation of natural fractures*	*Frequent termination of propagating fractures against natural fractures*	*Initial fracture transmissivity*	*Closed, stimulated fracture transmissivity*	*Natural fractures well oriented for slip and that increase transmissivity with slip*
POM			*Discourages*			*Discourages*
PSS	*Required, unless fractures are very closely spaced*	*Required*		*Must be adequate*	*Must be adequate to prevent pressure buildup*	*Required*
PFSSL		*Encourages*	*Discourages*	*Must be adequate*		*Required*
MMS			*Encourages*			

Geological parameters that encourage frequent fracture termination (the fourth column of Table 3-2) are (1) low stress anisotropy (causing a similarity in the normal stress between propagating new fractures and the natural fractures being intersected), (2) abundant fractures oriented at a low angle to the direction perpendicular to the least principal stress (so that propagating fractures tend to intersect natural fractures at low angles), and (3) weak fracture infilling (Section 3.1.3.3).

3.1.3.1 Requirements for Shear Stimulation

Several geological conditions must be present for shear stimulation to occur (in either the PSS, MMS, or PFSSL mechanisms). The two basic requirements are that there must be natural fractures that are well oriented to slip in the local stress state (Murphy and Fehler, 1986), and slip on those fractures must permanently increase transmissivity (Lee and Cho, 2002; Esaki et al., 1999; Lutz et al., 2010).

A requirement for effective shear stimulation in the PSS and PFSSL mechanisms is percolation of the stimulated natural fracture network. In the context of fracture

networks, percolation refers to the presence of continuous flow paths through the network (Berkowitz, 1995). If a natural fracture network does not percolate, then fluid cannot flow significant distances through the reservoir unless new fractures are formed (because we assume matrix permeability and initial fracture transmissivity are low). If the natural fracture network does not percolate, pressure will build up and lead to propagation of new, opening mode fractures. The PFSSL mechanism could happen only to a limited extent without percolation. In the PFSSL mechanism without percolation, the secondary region of shear stimulation would be localized near to the primary tensile fractures. Percolation is not required for the MMS mechanism.

For a given fracture size distribution, there is a fracture density percolation threshold at which the reservoir transitions abruptly between percolation and nonpercolation. For the same number of fractures intersecting a wellbore, a greater number of smaller fractures will be less likely to percolate than a smaller number of larger fractures (demonstrated in Section 3.4.8). Unfortunately, fracture size is not well constrained from wellbore image logs, and predicting percolation is challenging. Another complication is that only fractures that experience shear stimulation (the fractures that are well oriented to slip in the local stress state and experience increased transmissivity due to slip) contribute to percolation of the stimulated network.

3.1.3.2 Requirements for the PSS Mechanism

A characteristic of the PSS mechanism is that the (stimulated) natural fracture network must have the capacity to accept fluid at the rate that it is injected. If the natural fracture network cannot do so, even if injection causes shear stimulation of some natural fractures, injection pressure will build up and fluid will eventually be diverted into new, opening mode tensile fractures that propagate through the formation.

If fractures are able to open (the fracture walls come out of contact), void aperture can be as large as centimeters. But for truly crack-like, closed fractures, void aperture is typically on the order of hundreds of microns (Barton et al., 1985; Esaki et al, 1999; Chen et al., 2000; Lee and Cho, 2002). To contain large volumes of injected fluid, closed, crack-like fractures must either be extremely densely spaced or occupy an unrealistically large areal extent (discussed in Section 3.4.2.3 and Chapter 6). In EGS, natural fractures

are often closely spaced, but flowing fractures tend to be rather widely spaced (Richards et al., 1994; Ito and Kaieda, 2002; page 533 of Brown et al., 2012; Miyairi and Sorimachi, 1996; Wyborn et al., 2005; Baria et al., 2004; Evans, Genter, and Sausse, 2005; Dezayes et al., 2010). As a result, the PSS mechanism may be difficult in settings where fractures are only crack-like fractures. In gas shale, we are not aware of studies that have directly observed the spacing of flowing natural fractures.

In some geological settings, "closed fractures" are not crack-like and can have significant storativity. For example, at the EGS project at Soultz, there are fault zones with thickness of meters that have elevated permeability and porosity (Genter and Traineau, 1996; Genter et al., 2000; Chapter 5). An alternative, more speculative, explanation for fluid storage in closed fractures is that nonlinear fracture geometry may cause macroscopic opening when fractures shear (Dieterich and Smith, 2010; Griffith et al., 2010; Kaven et al., 2012; Ritz and Pollard, 2012), leading to significant storativity. Most of the time in gas shale and EGS, natural fractures are mineralized completely shut prior to stimulation (Gale et al., 2007; Fan et al., 2010).

Another requirement related to fluid storage is that the "stimulated region" must be able to grow fast enough to contain the injected fluid. The stimulated region can be defined as the region of the reservoir where fluid pressure is elevated and slip and transmissivity enhancement have occurred. If the stimulated region cannot grow fast enough to contain all of the injected fluid, pressure will build up, which could lead to tensile fracturing. The rate of growth of the stimulated region is affected by the initial fracture transmissivity, the stimulated fracture transmissivity, and the natural fracture network complexity (Section 3.4.2.2).

Another requirement for shear stimulation to prevent tensile fracturing is that the stimulated transmissivity must be adequate. Even if the fractures in the stimulated region have high storativity and the stimulated region is able to grow relatively quickly, fluid pressure will build up excessively if the transmissivity of the stimulated region is too low (McClure and Horne, 2012).

3.1.3.3 Fracture Termination

A key differentiating factor between the MMS and PFSSL mechanisms is whether propagating fractures terminate at natural fractures (and subsequently divert and branch) or whether they propagate across natural fractures. If crossing consistently occurs, then newly forming fractures will be able to form continuous pathways through the reservoir, leading to the PFSSL mechanism.

The idea that fracture termination can occur during hydraulic stimulation is supported by laboratory experiments (Blanton, 1982; Renshaw and Pollard, 1995; Zhou et al., 2008; Gu et al., 2011), mine-back experiments (Warpinski and Teufel, 1987; Warpinski et al., 1993; Mahrer, 1999; Jeffrey et al., 2009), and many computational investigations, including Dahi-Taleghani and Olson (2009), Gu and Weng (2010), Keshavarzi and Mohammadi (2012), and Fu et al. (2012).

Fractures can be terminated by inducing either opening or slip of the intersected fracture. The consensus in the literature is that fracture arrest is encouraged by a low angle of approach, close proximity of the normal stress resolved on the propagating fracture and the natural fracture, weak infilling for natural fractures, and low net pressure (defined as the amount fluid pressure exceeds σ_3). It is also possible for a propagating fracture to both open and cross a preexisting fracture (Gu et al., 2011).

Net pressure can be increased by high fluid viscosity and proppant, which is probably why fracture "complexity" has been observed to be increased in slickwater fracturing treatments (Cipolla et al., 2008). A more viscous fluid may reduce the likelihood of diversion due to opening of preexisting fractures by increasing pressure drop in the preexisting fracture (Zoback et al., 1977).

Within the MMS mechanism, there is competition between the opening of new, propagating fractures, and the opening of preexisting fractures. Once a preexisting fracture is opened, new tensile fractures may initiate off of it and begin to propagate. This would be favorable because the newly forming fractures can be oriented perpendicular to the least principal stress, and typically preexisting fractures are not oriented perpendicular to the least principal stress (though they could be). However, to initiate a new fracture, the tensile strength of intact rock must be overcome, which may

be significantly greater than the tensile strength of the mineralized joints (Gale and Holder, 2008). The influence of tensile strength on fracture initiation was demonstrated by Brown (1989), who reported that at the Fenton Hill EGS project in granite, injection was performed at 15 MPa above the minimum principal stress, causing opening of preexisting fractures, but tensile fractures did not form at the wellbore.

The effect of fracture termination against natural fractures may be somewhat different between two-dimensional models and three-dimensional models. Considering the three-dimensional problem, a natural fracture may not span the entire height of a formation, in which case the full height of a propagating vertical fracture would not terminate against it. The consequences of partial termination for the overall propagation of hydraulic fractures are complex, and we are not aware of a study that has addressed this issue.

Because of the possibility of partial termination, it seems that interference from natural fractures may be somewhat less effective at preventing propagation of large, continuous fractures in three-dimensional models. On the other hand, growing hydraulic fractures in three dimensions face resistance from propagation in the vertical direction, and this is a process that does not occur in two-dimensional models (which assume that newly formed fractures span the entire formation thickness).

3.2 Methodology

3.2.1 Details of the Stimulation Model

Basic details of the stimulation model used in this work are reviewed in this section. The model is described fully in Chapter 2. The simulator couples fluid-flow, fracture deformation, and permeability evolution in two-dimensional discrete fracture networks. The simulations are isothermal, assume matrix permeability is negligible, and assume small strain deformation in a linearly elastic, isotropic, homogeneous, infinite medium. The Displacement Discontinuity method (Shou and Crouch, 1995), a boundary element method, is used to calculate stresses induced by deformation. Because of these

assumptions, it is only necessary to discretize the fractures themselves, not the area around the fractures.

A simulation is initialized with a realization of the preexisting fracture network (which can be specified deterministically or stochastically). The model allows newly forming fractures to initiate and propagate. A major limitation of the model is that the location and orientation of these newly forming fractures must be specified in advance. In practice, a large number of "potentially forming" new fractures can be specified in the model. As the simulation progresses, some potentially forming fractures may become actual fractures, but many or most may never form. Because the location of the potentially forming fractures must be specified in advance, they are assumed to be linear. A more realistic treatment would permit the fracture orientations to curve.

An example of a discrete fracture network model is shown in Figure 3-2. The blue lines represent preexisting fractures and the red lines represent "potentially forming" new fractures. The simulations are two-dimensional. Because they are two-dimensional, they could be considered either vertical strike-slip faults or normal faults viewed in cross-section, but it is most natural to consider them vertical strike-slip faults.
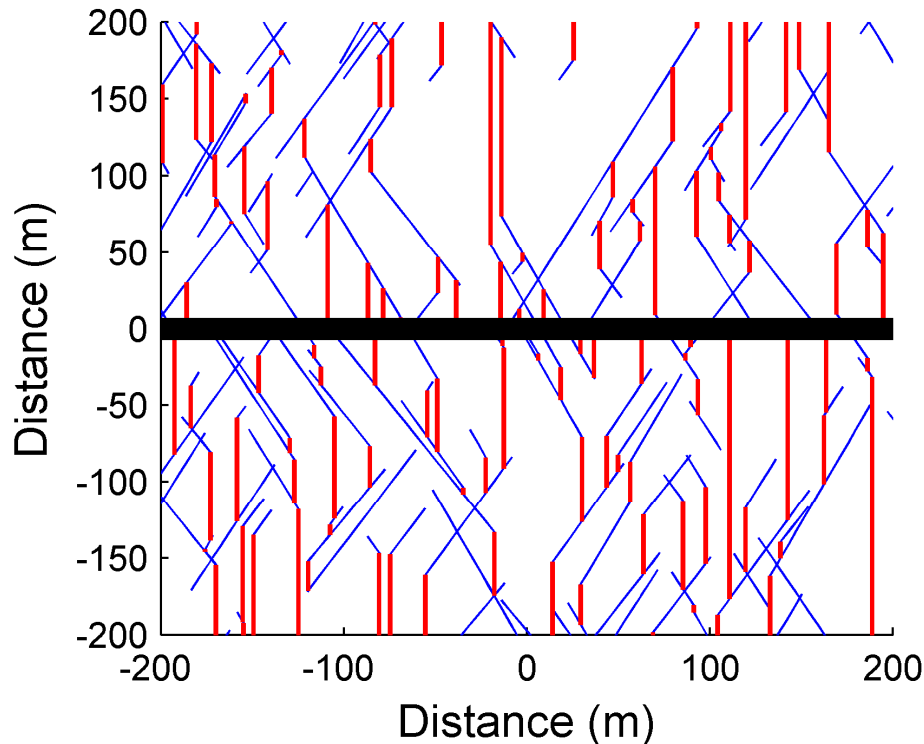
Figure 3-2: An example of a DFN model. The black line represents the wellbore. The blue lines represent preexisting fractures. The red lines represent fractures that could potentially form during the simulation.

The simulations are isothermal, single-phase liquid water, and proppant is not included. The unsteady-state fluid mass balance equation in a fracture is (adapted from Aziz and Settari, 1979):

$$\frac{\partial(\rho E)}{\partial t} = \nabla \cdot (q_{flux}e) + s_a ,$$

<div align="right">3-1</div>

where s_a is a source term (mass per time for a unit of area of the fracture), t is time, E is void aperture (the pore volume per unit area of the fracture), ρ is fluid density, q_{flux} is mass flux (mass flow rate per cross-sectional area of flow), and e is the hydraulic aperture (the effective aperture for flow in the fracture).

Void aperture is used to refer to the fluid storage of the fracture and hydraulic aperture is used to refer to the ability for the fracture to transmit fluid. These apertures are permitted to be different.

Darcy flow is assumed, in which mass flux in a direction x_i is (Aziz and Settari, 1979):

$$q_{flux,i} = \frac{k\rho}{\mu_l} \frac{\partial P}{\partial x_i} = \frac{e^2 \rho}{12\mu_l} \frac{\partial P}{\partial x_i},$$
3-2

where P is fluid pressure, μ_l is fluid viscosity, k is permeability, and the cubic law for fracture permeability has been used (Jaeger et al., 2007). The cross-sectional area of flow in a one-dimensional fracture in a two-dimensional area is $e{\times}h$, where h is the out of plane dimension of the fracture (equivalent to height in our simulations, assuming the model shows strike-slip faults in plan view). Overall, the ability to flow water through a crack is proportional to the transmissivity, T, which for a crack is defined as $k{\times}e$, or $e^3/12$ (Jaeger et al., 2007).

A "closed" fracture bears compressive (defined as positive) normal stress, and the fracture walls are in contact. A closed fracture becomes "open" when the fluid pressure reaches the normal stress, and the fracture walls come out of contact.

Relationships are used to relate effective normal stress and cumulative shear displacement to void and hydraulic aperture. These relationships are chosen so that there is not any discontinuity in aperture as elements transition between open and closed. The aperture of a closed fracture is defined as (Willis-Richards et al., 1996; Rahman et al., 2002; Kohl and Mégel, 2007):

$$E = \frac{E_0}{1 + 9\sigma_n' / \sigma_{n,Eref}} + D_{E,eff} \tan \frac{\phi_{Edil}}{1 + 9\sigma_n' / \sigma_{n,Eref}},$$
3-3

where E_0, $\sigma_{n,Eref}$, and φ_{Edil} are specified constants. $D_{E,eff}$ is defined as equal to D if $D <$ $D_{E,eff,max}$, and equal to $D_{E,eff,max}$ otherwise. The constants are allowed to be different for hydraulic aperture, e, and void aperture E. Nonzero φ_{Edil} corresponds to pore volume dilation with slip, and non-zero φ_{edil} corresponds to transmissivity enhancement with slip. σ_n' is the effective normal stress, defined as (Jaeger et al., 2007; Segall, 2010):

$$\sigma_n' = \sigma_n - P,$$
3-4

where compressive stresses are taken to be positive.

The void and hydraulic apertures of an open preexisting fracture are defined as:

$$E = E_0 + D_{E,eff} \tan \phi_{Edil} + E_{open}, \qquad \text{3-5}$$

$$e = e_0 + D_{e,eff} \tan \phi_{edil} + E_{open}, \qquad \text{3-6}$$

where E_{open} is the physical separation between the fracture walls (which is a primary unknown that is calculated during the simulations, Section 2.2.3.4).

The hydraulic and void apertures of newly formed fractures are treated differently than preexisting fractures. A value E_{hfres} is defined as the residual aperture of a newly formed fracture. Hydraulic aperture, e, is set equal to void aperture, E. The aperture of an open, newly formed fracture is:

$$E = E_{hfres} + E_{open}, \qquad \text{3-7}$$

and the aperture of a closed, newly formed fracture is:

$$E = E_{hfres} \exp(-\sigma_n K_{hf}), \qquad \text{3-8}$$

where K_{hf} is a specified stiffness for closed hydraulic fracture elements. When a new fracture forms or propagates, it must be open (because it is forming due to propagation as a tensile fracture), but it might close later if the fluid pressure or stress state changes. The transmissivity of a newly formed fracture element is defined as:

$$T = T_{hf,fac} E_{hfres}, \qquad \text{3-9}$$

and if open, transmissivity is defined as:

$$T = T_{hf,fac} E_{hfres} + (E_{open})^3 / 12, \qquad \text{3-10}$$

where $T_{hf,fac}$ is a specified constant. This treatment of transmissivity for newly forming fractures allows them to be assigned a relatively high residual transmissivity. High residual transmissivity for newly formed fractures may be desirable as a very simple way of approximating the effect of proppant in newly formed fractures, which would tend to cause higher residual transmissivity after closure (Fredd et al., 2001).

Mechanical equilibrium is enforced on the fractures using conditions for shear and normal stress of open and closed fractures. For a closed fracture, the Coulomb failure criterion with a radiation damping term is used (Jaeger et al., 2007; Segall, 2010):

$$| \tau - \eta v | = \mu_f \sigma_n' + S_0, \qquad \text{3-11}$$

where τ is shear stress, η is the radiation damping coefficient, v is sliding velocity of the fracture, μ_f is the coefficient of friction (assumed to be constant in this chapter), and S_0 is fracture cohesion. The radiation damping term approximates the effect of inertia at high slipping velocities (Rice, 1993; Segall, 2010). For fractures with shear stress less than the frictional resistance to slip, shear deformation is assumed to be negligible. If shear stress exceeds the frictional resistance to slip, fracture shear deformations are calculated so that equality in Equation 3-11 is enforced.

Force balance requires that the fluid pressure of open fractures must be equal to their normal stress. It is assumed that the fluid inside open fractures cannot support shear stress (Crouch and Starfield, 1983). These stress conditions are stated:

$$\sigma_n' = 0, \qquad \text{3-12}$$

$$\tau - \eta v = 0. \qquad \text{3-13}$$

Shear and normal deformations are calculated to enforce equality of Equations 3-12 and 3-13. As discussed in Section 2.2.3.5, a small cohesion term is added to Equation 3-13 for numerical convenience. If the absolute value of the shear stress is less than the cohesion term, sliding velocity is assumed to be zero (non-sliding fractures have infinite shear stiffness).

The finite volume method is used to calculate fluid flow. The implicit Euler method is used to discretize time. Stresses induced by deformation are calculated according to the boundary element method of Shou and Crouch (1995), which assumes that fractures open or shear in a linearly elastic, infinite, homogeneous medium in plane strain. The Olson (2004) adjustment is used to account for the effect of finite fracture height (so that the calculations are not plane strain). The formation height is assumed to be 100 m.

Stresses induced by normal displacements of closed fractures are neglected (this issue is discussed in Section 2.2.3.3). The dense matrices arising from the use of the Displacement Discontinuity method are approximated very accurately and efficiently using Hmmvp (Bradley, 2012) a publicly available code that performs hierarchical matrix approximation combined with adaptive cross-approximation (Rjasanow and Steinbach, 2007). The fractures in the DFN are discretized using variable element size, with greater refinement near intersections and where fractures are in close proximity.

At every time step, Equations 3-1, 3-11, 3-12, and 3-13 are solved with fluid pressure, void aperture, and shear deformation as unknowns. The problem is solved with fully implicit time stepping. Iterative coupling is used to couple shear deformations with fluid flow and opening deformations. Constraints are applied to prevent backward sliding against the direction of shear stress and interpenetration of fracture walls.

Propagation of new fractures is handled by using a stress intensity factor approach. A stress intensity factor is also calculated to model progressive opening along a preexisting fracture (Section 2.2.5.2). Stress intensity factors, (defined for mode I deformation as K_I), are parameters that measure the degree of stress concentration at a crack tip. A crack tip propagates when its stress intensity factor reaches the fracture toughness (K_{Ic} for mode I deformation), a material property. For a single fracture oriented perpendicular to the minimum principal stress, σ_3, under uniform pressure in plane strain, the stress intensity factor is (Rooke and Cartwright, 1976):

$$K_I = (P - \sigma_3)\sqrt{\pi a},$$

3-14

where a is the half-length of the fracture. In our simulator, stress intensity factor is calculated using the method of Schultz (1988). Newly forming fractures do not curve (because we prespecify their paths as being linear), and so it is not necessary to calculate a mode II stress intensity factor.

3.2.2 Details of the Simulations

Nine simulations (Simulations A-I) were performed of a single stage hydraulic fracturing treatment in a horizontal well under a variety of conditions. The simulations

were two-dimensional, and should be interpreted as showing strike-slip faulting in plan view in which each fracture is confined to and fully penetrates a layer of finite thickness. The nine simulations used different realizations of the fracture network and different geological parameters such as stress state and fracture properties. The purpose of each simulation was to represent a particular process or to investigate a particular aspect of stimulation. The simulation names, discretization names, and injection schedule names are summarized in Table 3-1.

In Simulations A, B, C, D, E, and F, injection schedule S1 was used. In S1, injection was performed for one hour at 30 kg/s, one hour for 60 kg/s, and one hour at 90 kg/s (Figure 3-9). Then the wellbore was shut in for one week (Figure 3-10), followed by production at 30 kg/s until downhole pressure reached 30 MPa (at bottom-hole conditions), and then production was continued at constant downhole pressure of 30 MPa (Figure 3-11). Production was continued for 24 hours, and then the simulation was ended. Simulations G and H used injection schedule S2. In injection schedule S2, injection was performed at constant pressure, 48 MPa, for one week. In Simulation D, injection schedule S1 was used, but the simulation was terminated after only a few minutes of simulation. In Simulation I, injection schedule S3 was used. In this schedule, a step rate test was simulated in which injection was initiated at 3 kg/s and increased by 3 kg/s every thirty minutes. This was continued for a total of five hours, finishing with a final injection rate of 30 kg/s (Figure 3-30).

Table 3-3 gives the settings that were common to all simulations. Table 3-4 gives specific simulation settings used for each simulation. An additional model specific setting, not given in Table 3-4, is that the flow between the wellbore and natural fractures was not permitted in Simulation F, only flow between the wellbore and newly formed tensile fractures. This approximated injection out of perforated casing.

Table 3-3: Simulation settings used in all simulations. For definition of terms that are not described in this chapter, see Chapter 2. Variables are also defined in Table 7-1.

h	100 m	η	3 MPa/(m/s)
G	15 GPa	μ_f	0.6
u_p	0.25	$\sigma_{n,Eref}$	20 MPa
η_{targ}	0.5 MPa	$\sigma_{n,eref}$	20 MPa
S_0	0.5 MPa	φ_{Edil}	0 °
$S_{0,\,open}$	0.5 MPa	φ_{edil}	2.5 °
K_{hf}	0.01 MPa^{-1}	$T_{hf,fac}$	10^{-9} m^2
$K_{I,crit}$	1.0 MPa-m$^{1/2}$	Strain Penalty Method	Not used
$K_{I,crithf}$	3.0 MPa-m$^{1/2}$	cstress	Turned off
P_{init}	35 MPa	Adaptive domain adjustment	Not used
σ_{xx}	50 MPa	BEM method	Hmmvp
σ_{xy}	0	ε_{tol}	10^{-6}
mechtol	.003 MPa	Transmissivity updating	Implicit
itertol	0.01 MPa	Friction	Constant coefficient of friction
Pseudo-3D adjustment (Olson, 2004)	Used		

Table 3-4: Differences in settings between Simulations A-H.

	A	B	C	D	E	F	G	H	I
E_0	-	5 cm	5 cm	0.5 mm	0.5 mm	0.2 mm	0.2 mm	0.2 mm	5 cm
e_0	-	0.2 mm	0.01 mm	0.5 mm	0.02 mm	0.03 mm	0.03 mm	0.03 mm	0.2 mm
$D_{e,eff,max}$	-	2 cm	2 cm	2 cm	1 mm	1 mm	1 mm	1 mm	2 cm
σ_{yy}	75 MPa	75 MPa	75 MPa	75 MPa	55 MPa	75 MPa	75 MPa	75 MPa	75 MPa
Injection Schedule	S1	S1	S1	S1	S1	S1	S2	S2	S3
Fracture Network	F1	F2	F2	F2	F3	F4	F5	F4	F2

The nine simulations used five different realizations (Networks F1-F5) of the preexisting and potentially forming fractures. Networks F1-F5 are shown from Figure 3-3 to Figure 3-7. In Figure 3-3 to Figure 3-7, the black line is the wellbore, blue lines are preexisting fractures, and red lines are fractures that could potentially form during the simulation. Only some of the potentially forming fracture elements (the red lines) actually become active during a simulation.
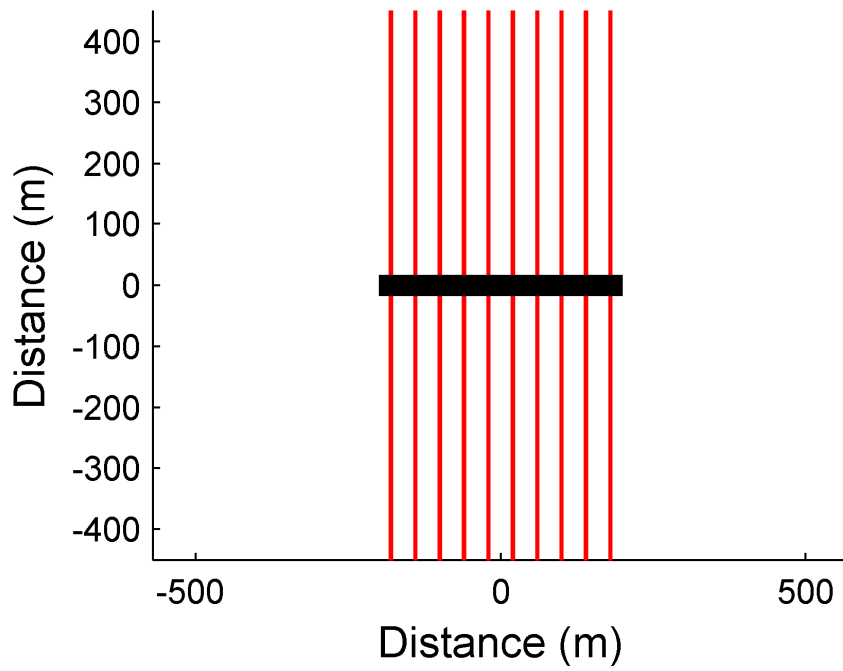
Figure 3-3: Fracture network F1. The black line is the wellbore (parallel to the x-axis). The red lines are potentially forming hydraulic fractures.
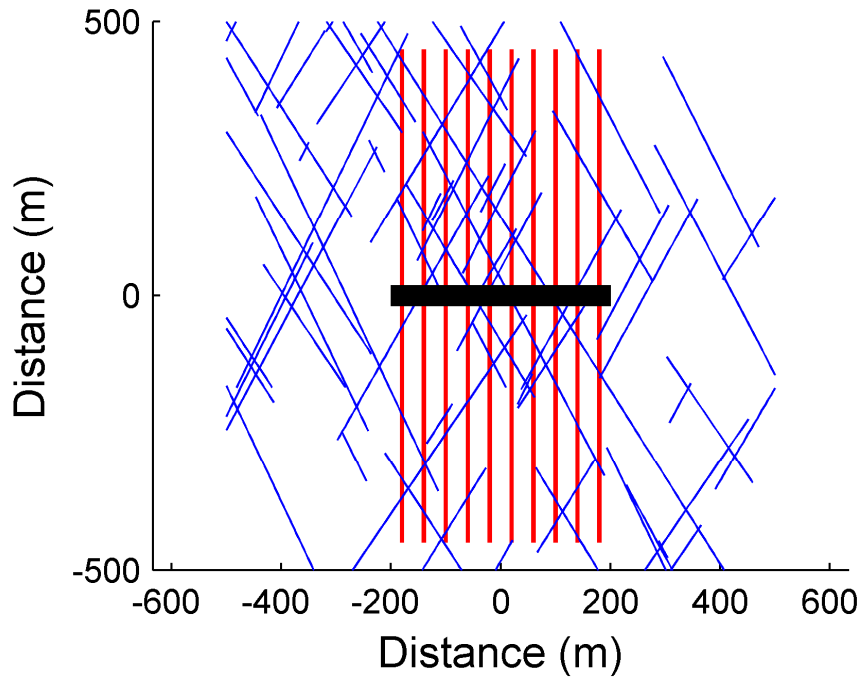
Figure 3-4: Fracture network F2. The black line is the wellbore (parallel to the x-axis). The red lines are potentially forming hydraulic fractures, and the blue lines are preexisting fractures.
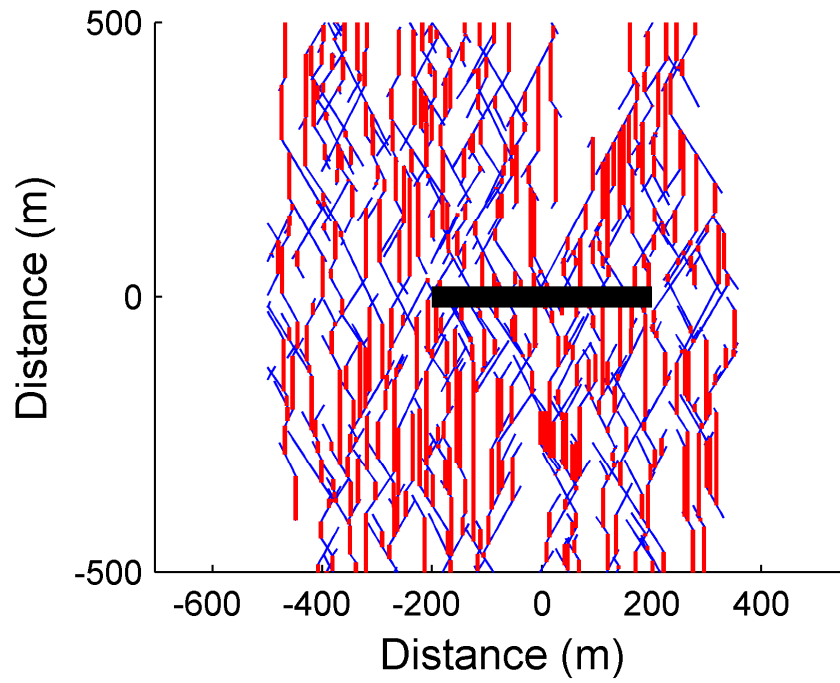
Figure 3-5: Fracture network F3. The black line is the wellbore (parallel to the x-axis). The red lines are potentially forming hydraulic fractures, and the blue lines are preexisting fractures.
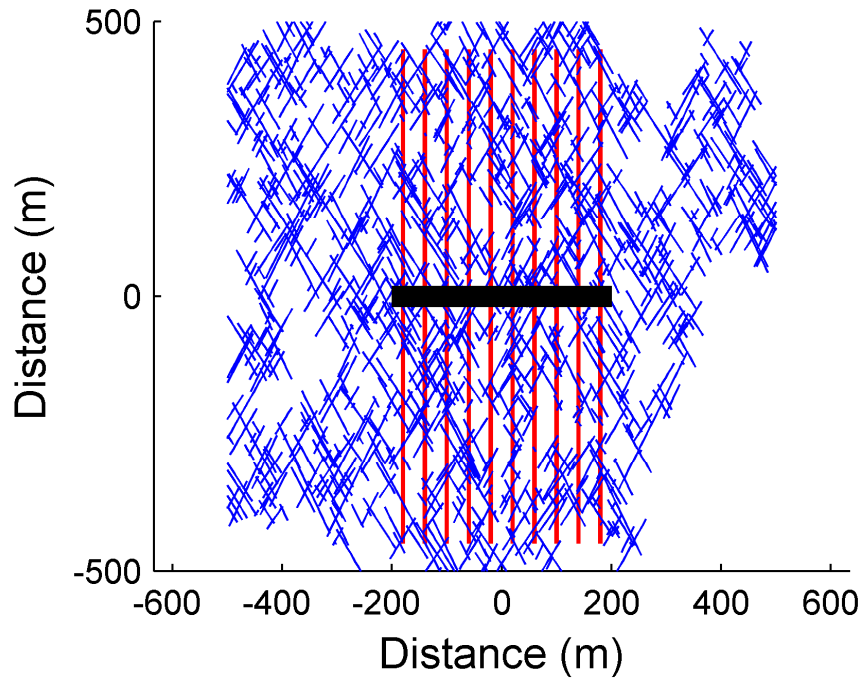
Figure 3-6: Fracture network F4. The black line is the wellbore (parallel to the x-axis). The red lines are potentially forming hydraulic fractures, and the blue lines are preexisting fractures.
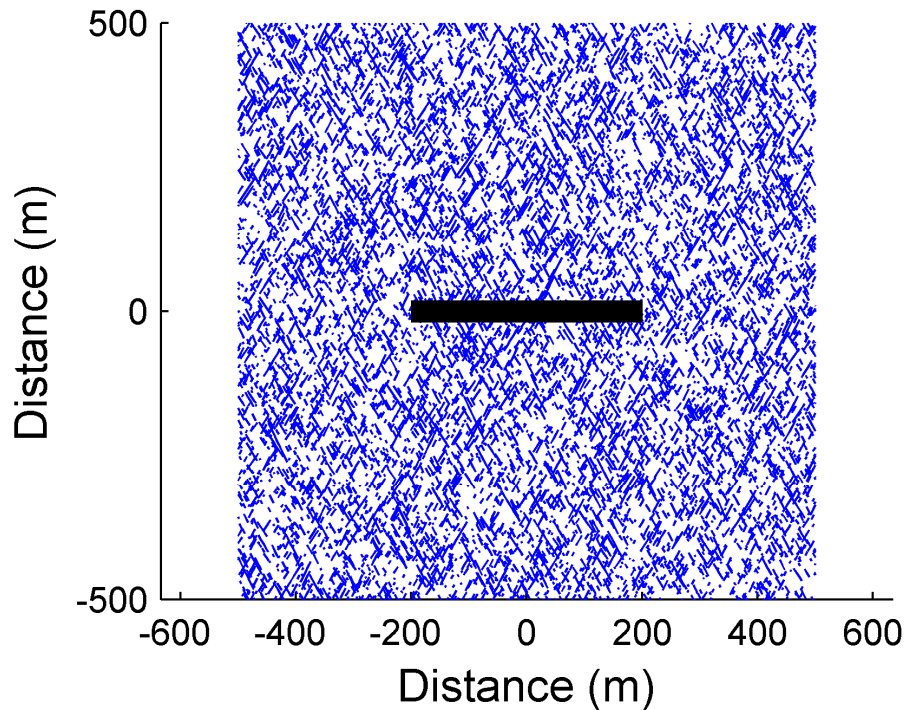
Figure 3-7: Fracture network F5. The black line is the wellbore (parallel to the x-axis). The blue lines are preexisting fractures.

Simulations were designed to investigate a particular process. Simulation A (Network F1) involved propagation of new, opening mode fractures, a prototype for the POM mechanism. Simulations B, C, D and I (using Network F2) were designed to investigate the PSS mechanism under different conditions. Simulation E (Network F3) was representative of the MMS mechanism, with a large number of potentially forming fractures terminating against preexisting fractures. Simulation F (Network F4) was representative of the PFSSL mechanism, with large, continuous, newly forming fractures propagating through a dense network of natural fractures. Simulations G and H (Networks F4 and F5) demonstrated the effect of fracture percolation on the PSS mechanism.

3.3 Results

Results from Simulations A, B, C, D, E, F, G, H, and I can be seen from Figure 3-8 to Figure 3-30. The final distributions of transmissivity, and/or bottom hole pressure and

flow rate versus time during injection, shut-in, and/or production are shown. For brevity, all four possible figures are not shown for all simulations. In plots of fracture networks, fracture thickness is proportional to void aperture, but thickness is exaggerated (not to scale) for ease of view.
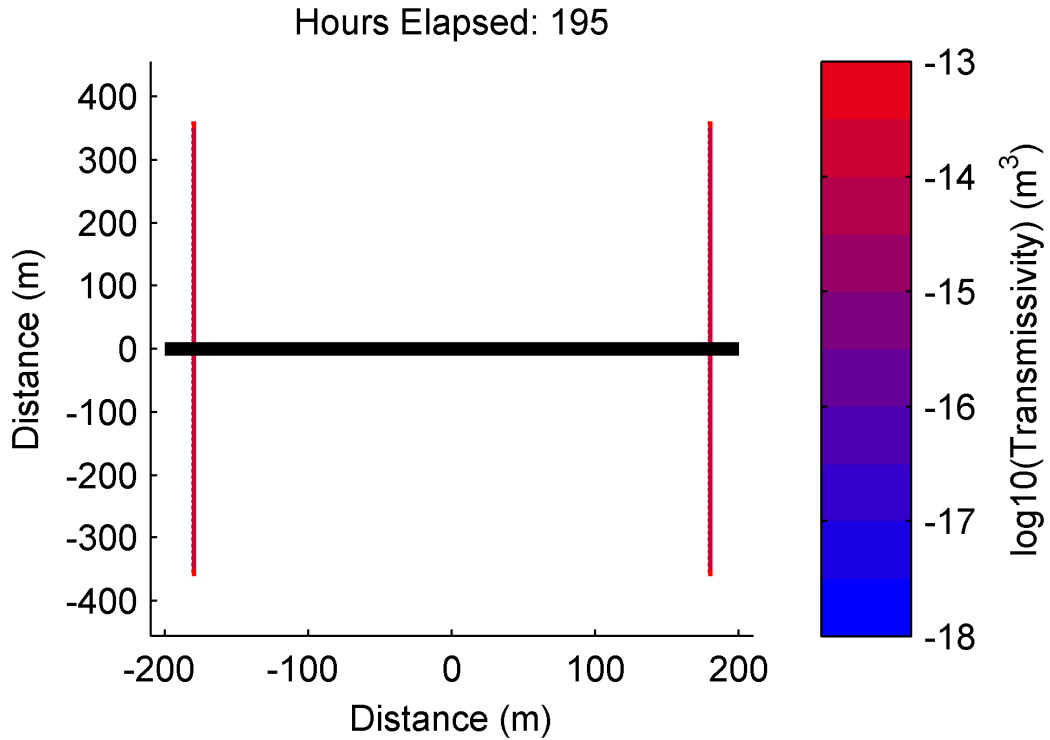
Figure 3-8: Final transmissivity distribution for Simulation A (fracture network F1, σ_{xx} = 50 MPa, and σ_{yy} = 75 MPa). Line thickness is proportional to void aperture but not to scale. Simulation A is a prototype for POM. The black line represents the wellbore (parallel to the x-axis).
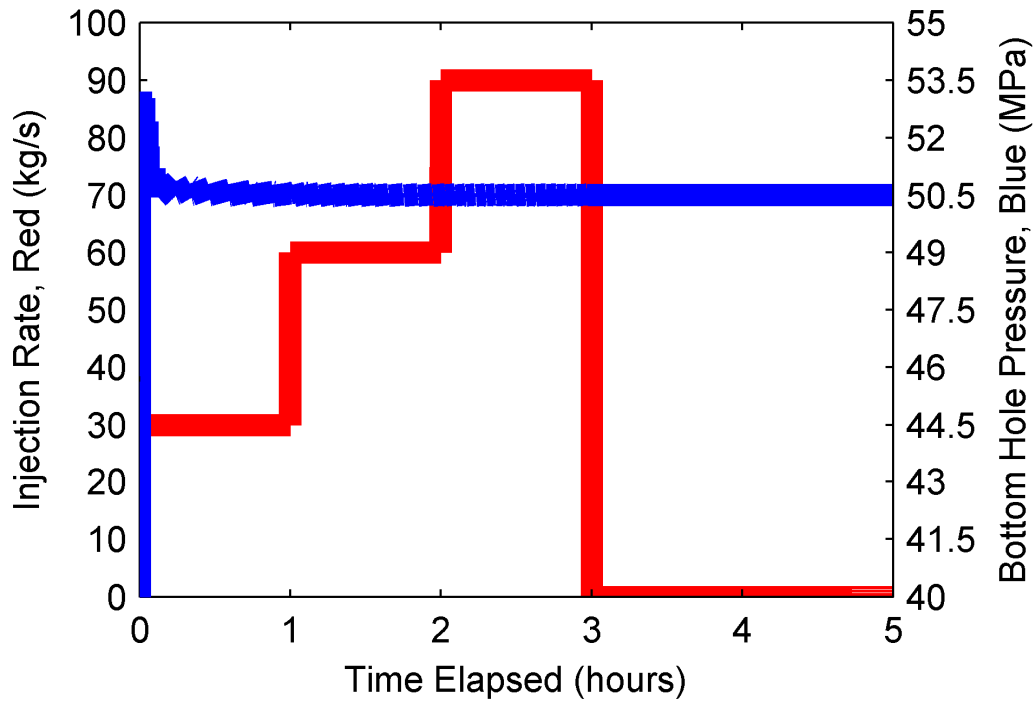
Figure 3-9: Bottom hole pressure and flow rate during injection for Simulation A.
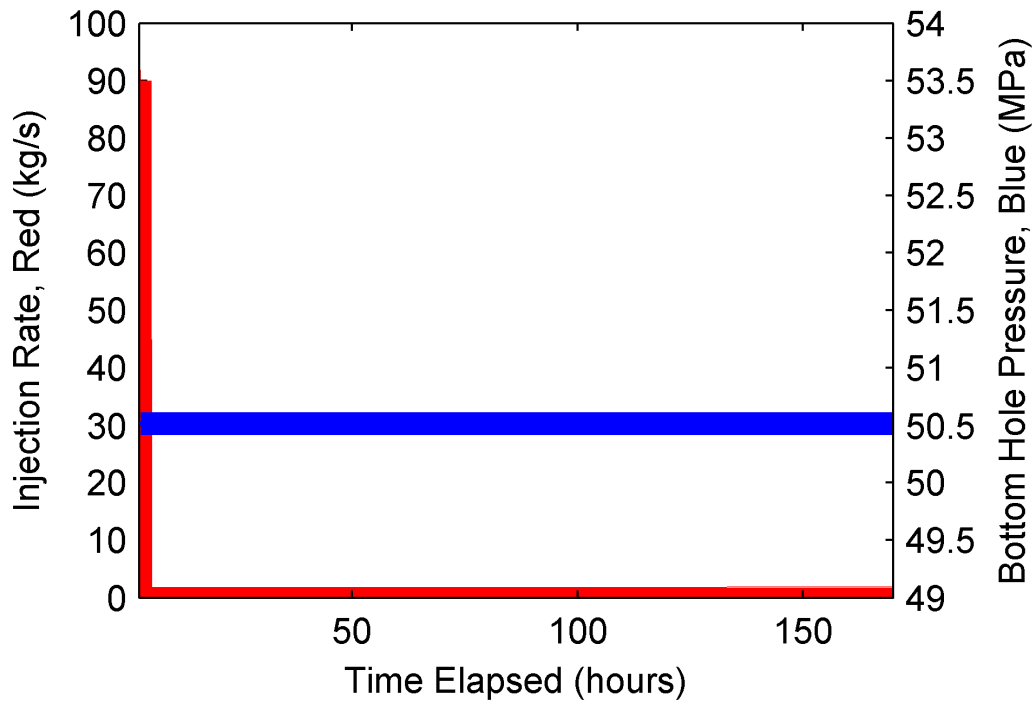
Figure 3-10: Bottom hole pressure and flow rate during shut-in for Simulation A.
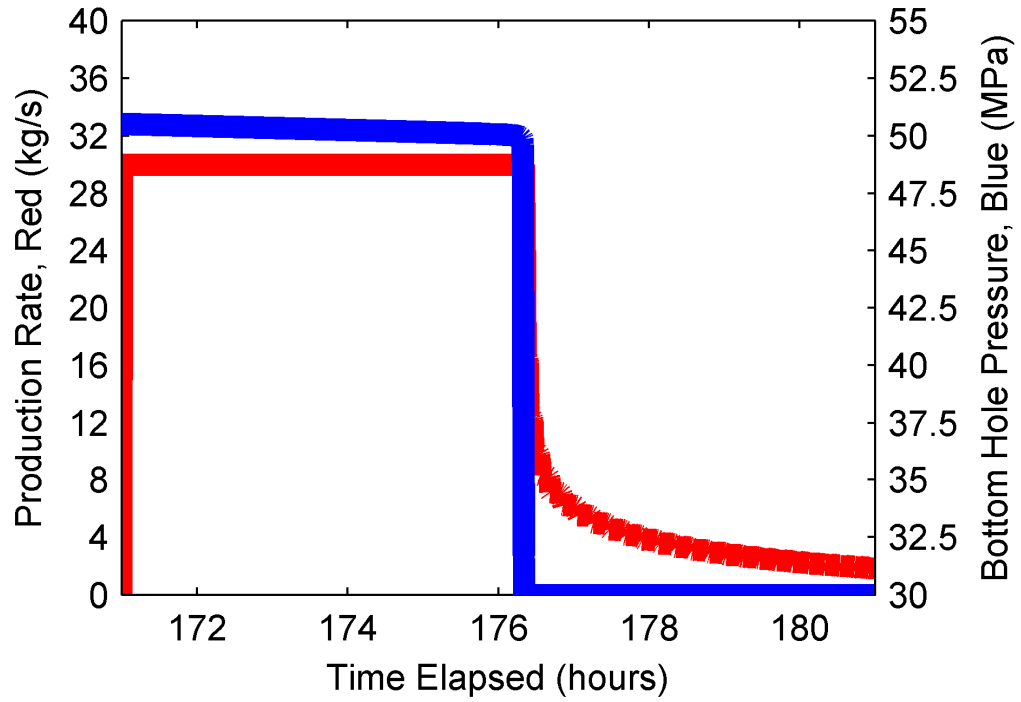
Figure 3-11: Bottom hole pressure and flow rate during production for Simulation A.
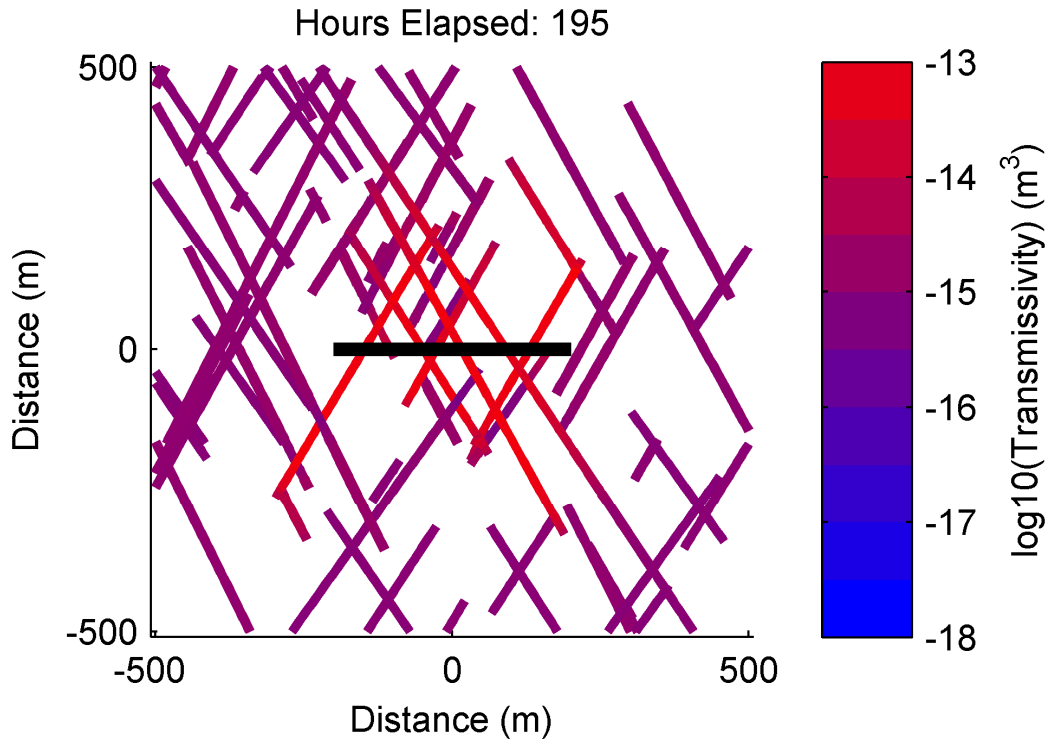
Figure 3-12: Final transmissivity distribution for Simulation B (fracture network F2, σ_{xx} = 50 MPa, and σ_{yy} = 75 MPa). Line thickness is proportional to void aperture but not to scale. Simulation B is a prototype for PSS. The black line represents the wellbore (parallel to the x-axis).
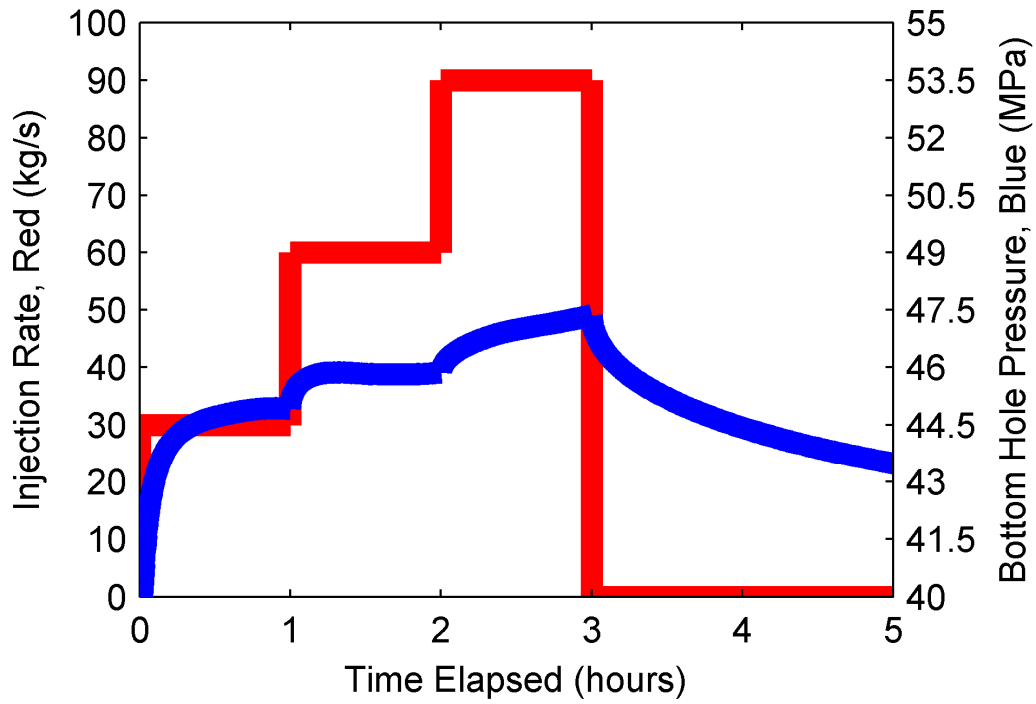
Figure 3-13: Bottom hole pressure and flow rate during injection for Simulation B.
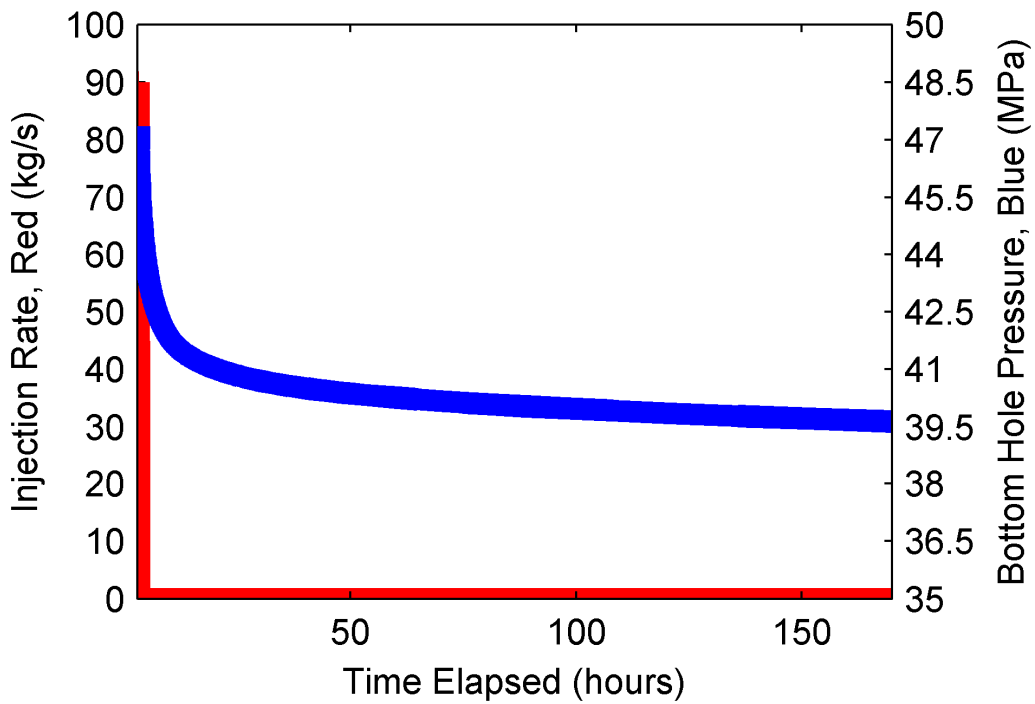
Figure 3-14: Bottom hole pressure and flow rate during shut-in for Simulation B.
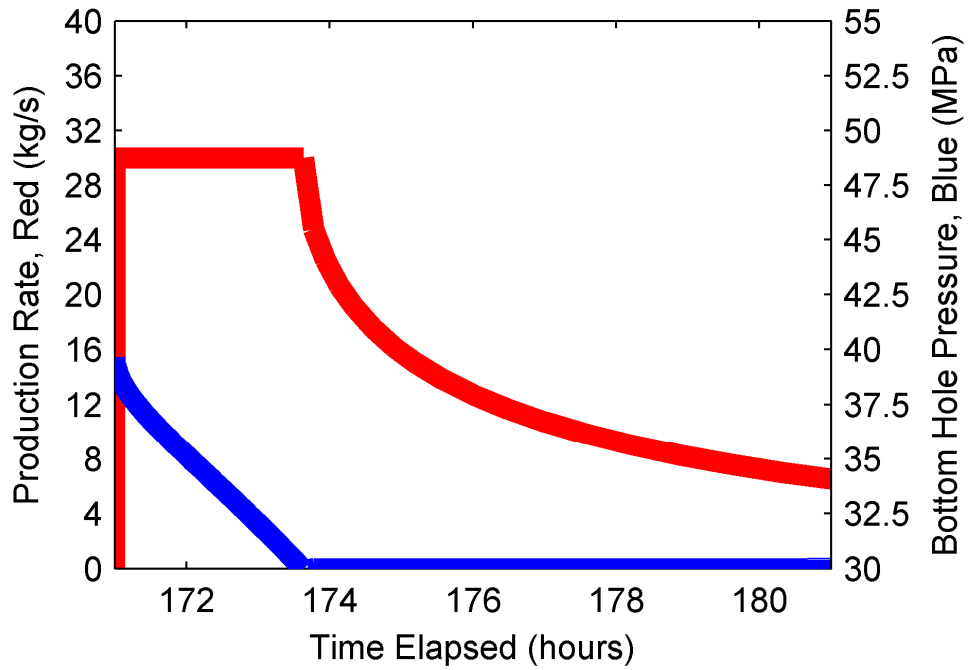
Figure 3-15: Bottom hole pressure and flow rate during production for Simulation B.
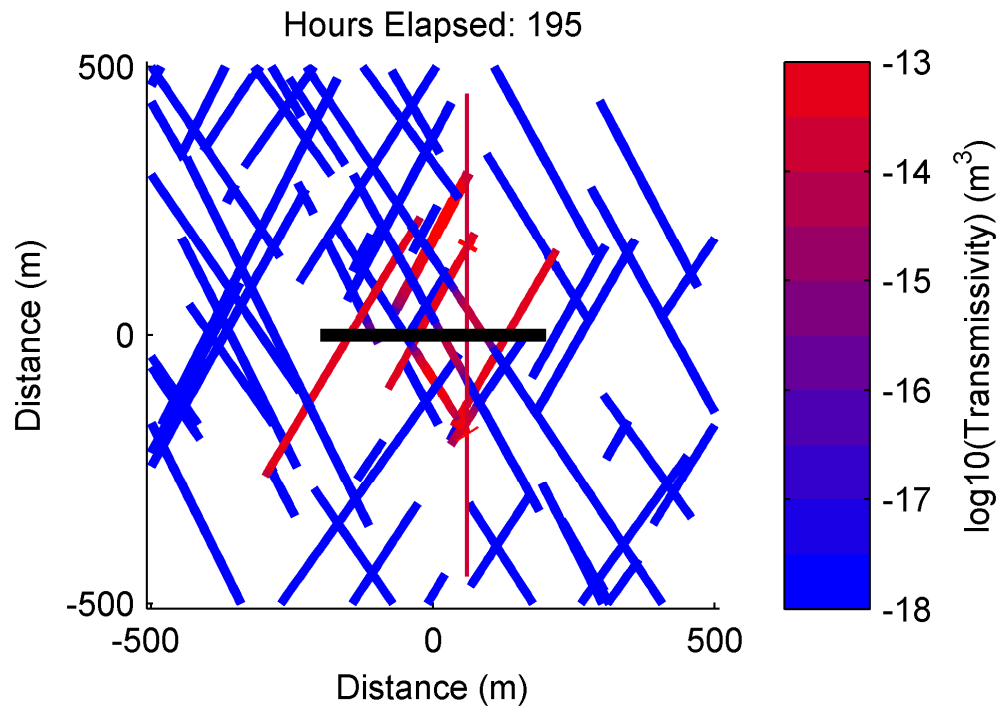
Figure 3-16: Final transmissivity distribution for Simulation C (fracture network F2, σ_{xx} = 50 MPa, and σ_{yy} = 75 MPa). Line thickness is proportional to void aperture but not to scale. Simulation C is similar to Simulation B but has lower e_0. The black line represents the wellbore (parallel to the x-axis).
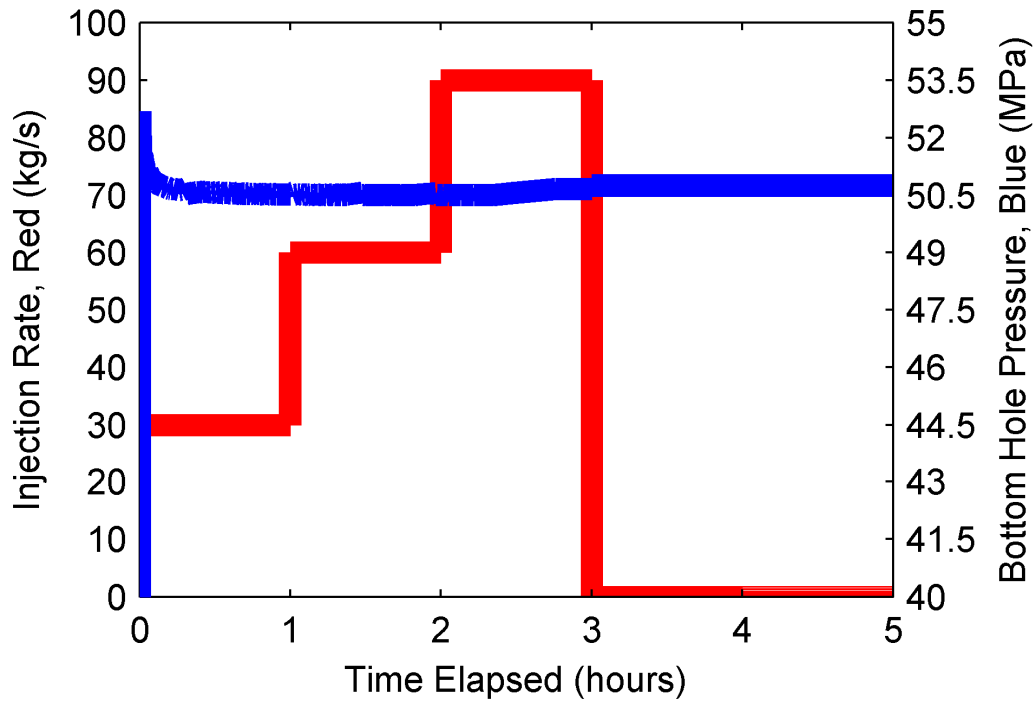
Figure 3-17: Bottom hole pressure and flow rate during injection for Simulation C.
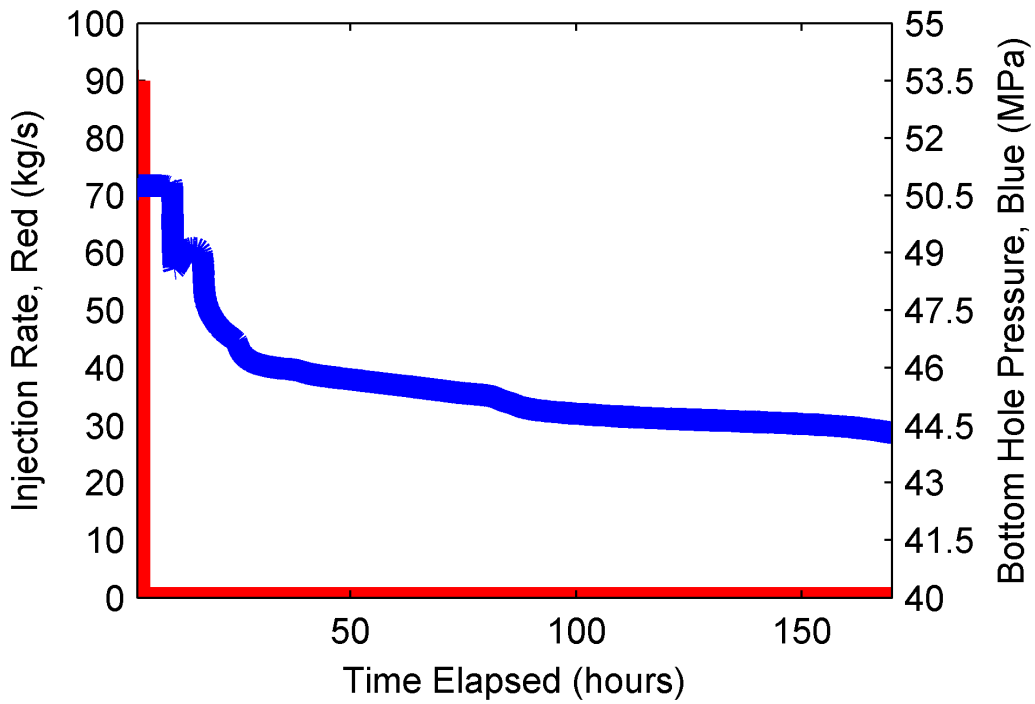
Figure 3-18: Bottom hole pressure and flow rate during shut-in for Simulation C.
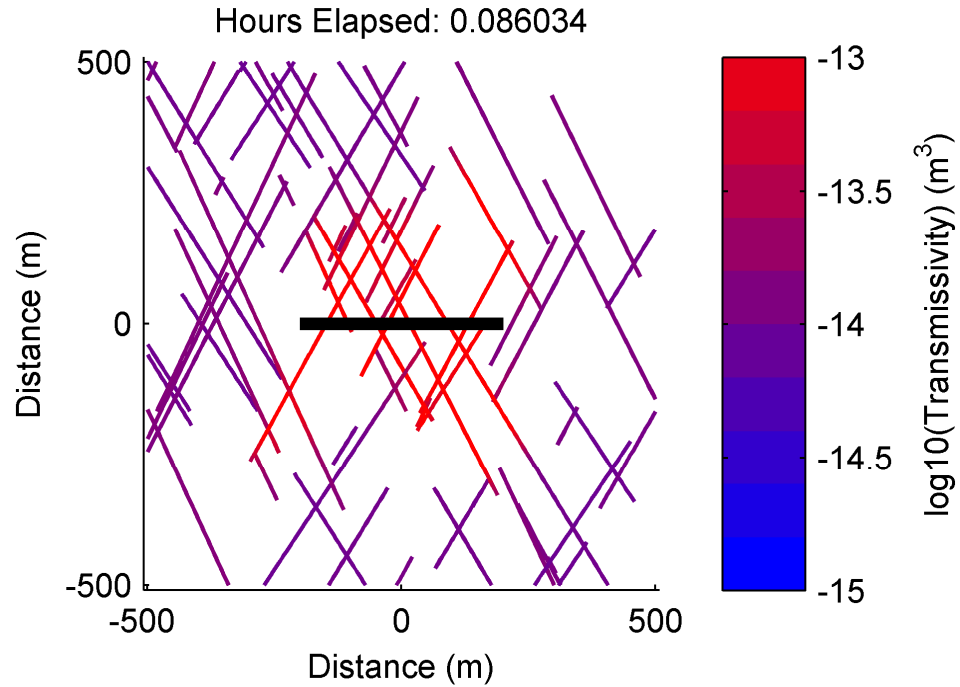
Figure 3-19: Final transmissivity distribution for Simulation D (fracture network F2, σ_{xx} = 50 MPa, and σ_{yy} = 75 MPa). Line thickness is proportional to void aperture but not to scale. Simulation D is similar to Simulation B but has lower E_0. The colorbar in this figure uses a different scale than in other maps of transmissivity given in this chapter. The black line represents the wellbore (parallel to the x-axis).
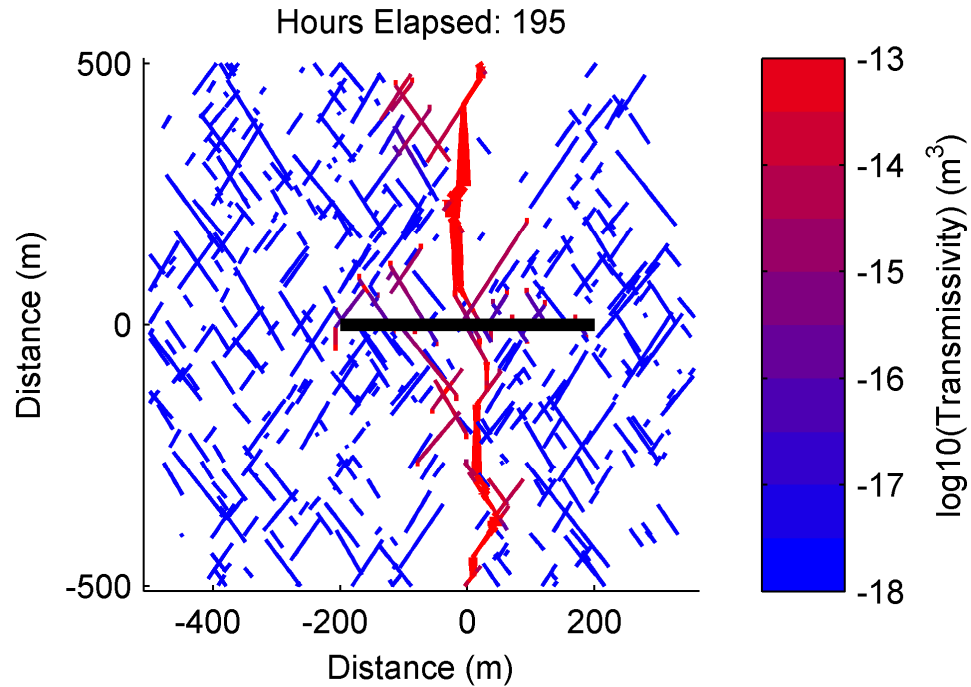
Figure 3-20: Final transmissivity distribution for Simulation E (fracture network F3, σ_{xx} = 50 MPa, and σ_{yy} = 55 MPa). Line thickness is proportional to void aperture but not to scale. Simulation E is a prototype for MMS. The black line represents the wellbore (parallel to the x-axis).
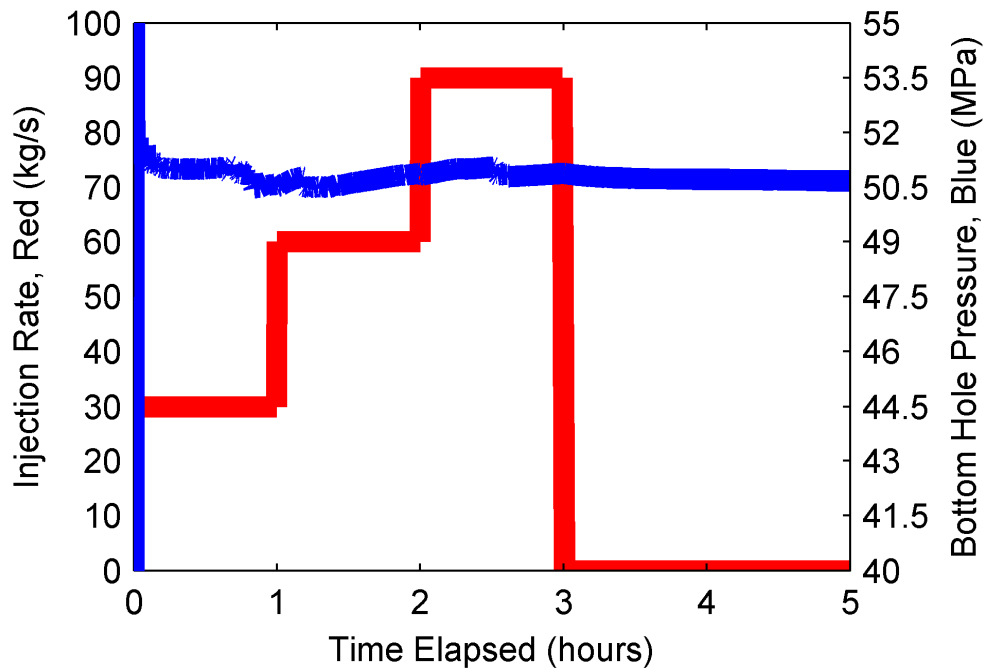
Figure 3-21: Bottom hole pressure and flow rate during injection for Simulation E.
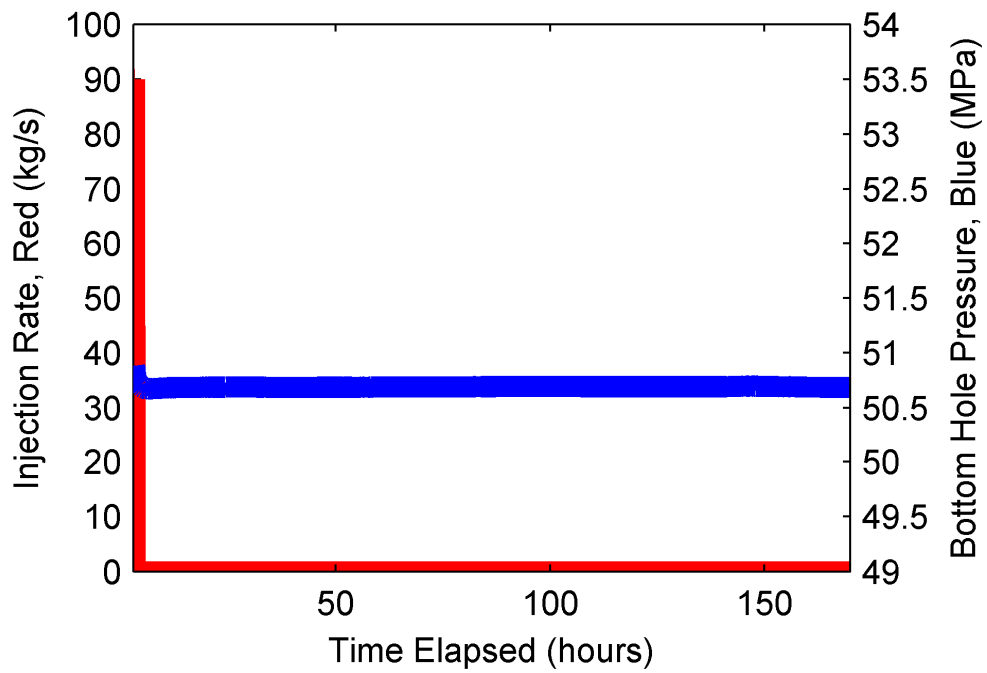
Figure 3-22: Bottom hole pressure and flow rate during shut-in for Simulation E.
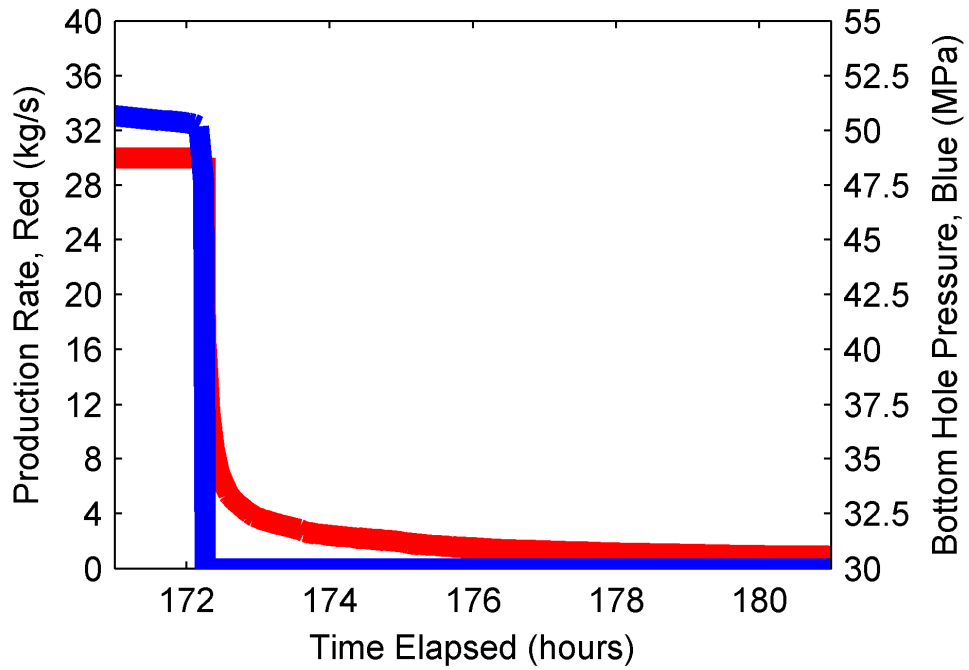
Figure 3-23: Bottom hole pressure and flow rate during production for Simulation E.
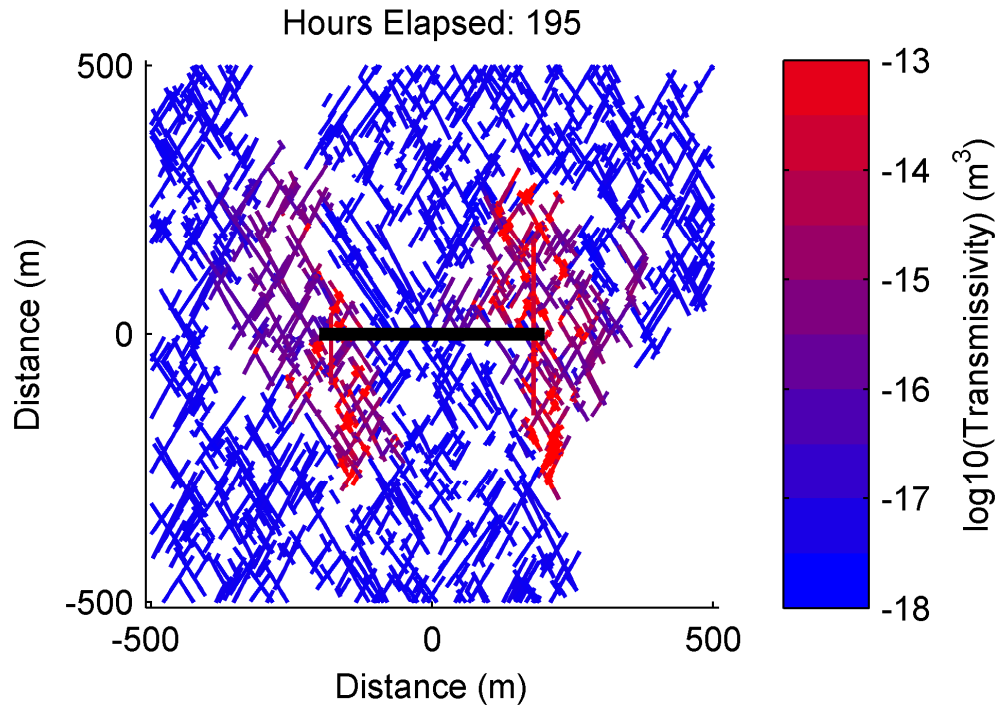
Figure 3-24: Final transmissivity distribution for Simulation F (fracture network F4, σ_{xx} = 50 MPa, and σ_{yy} = 75 MPa). Line thickness is proportional to void aperture but not to scale. Simulation F is a prototype for PFSSL. The black line represents the wellbore (parallel to the x-axis).
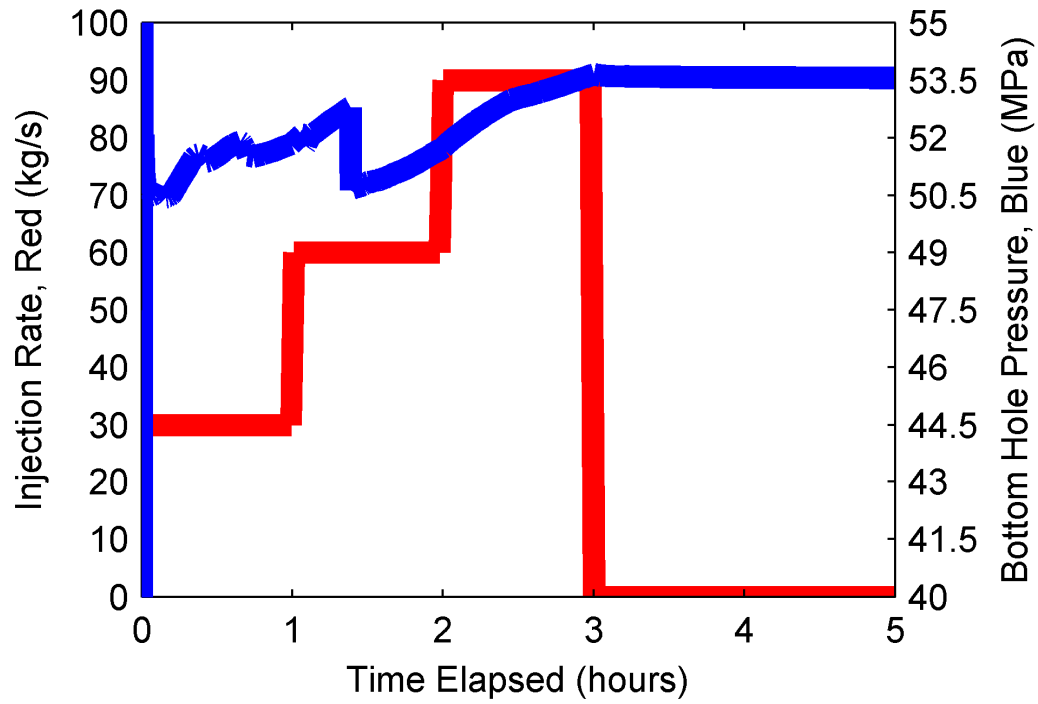
Figure 3-25: Bottom hole pressure and flow rate during injection for Simulation F.
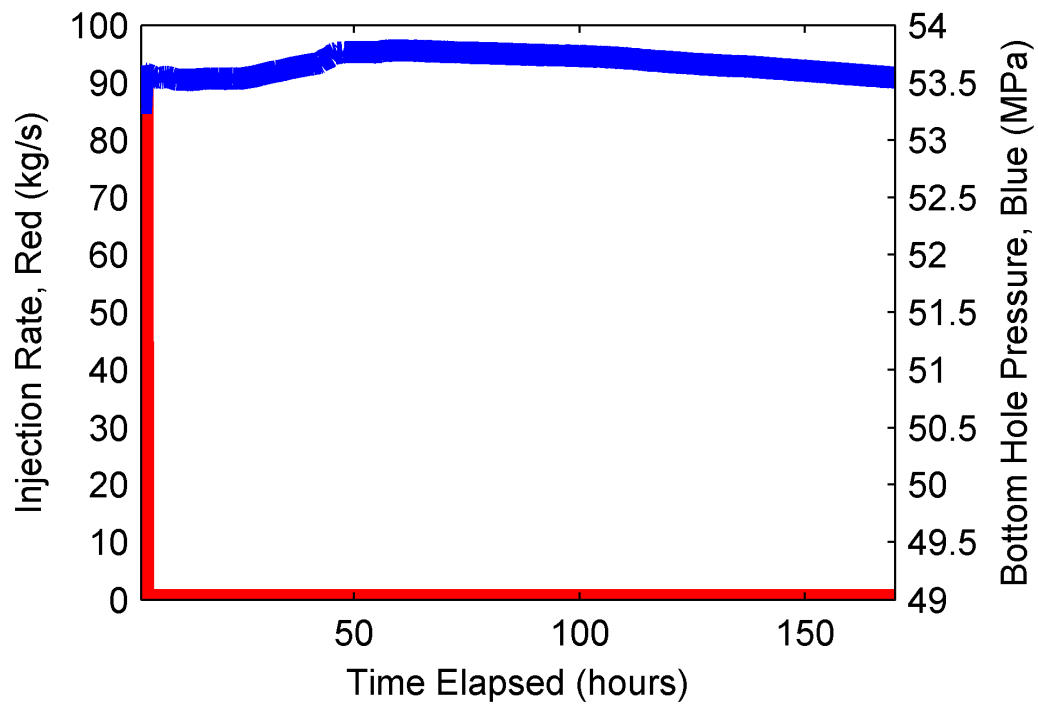
Figure 3-26: Bottom hole pressure and flow rate during shut-in for Simulation F.
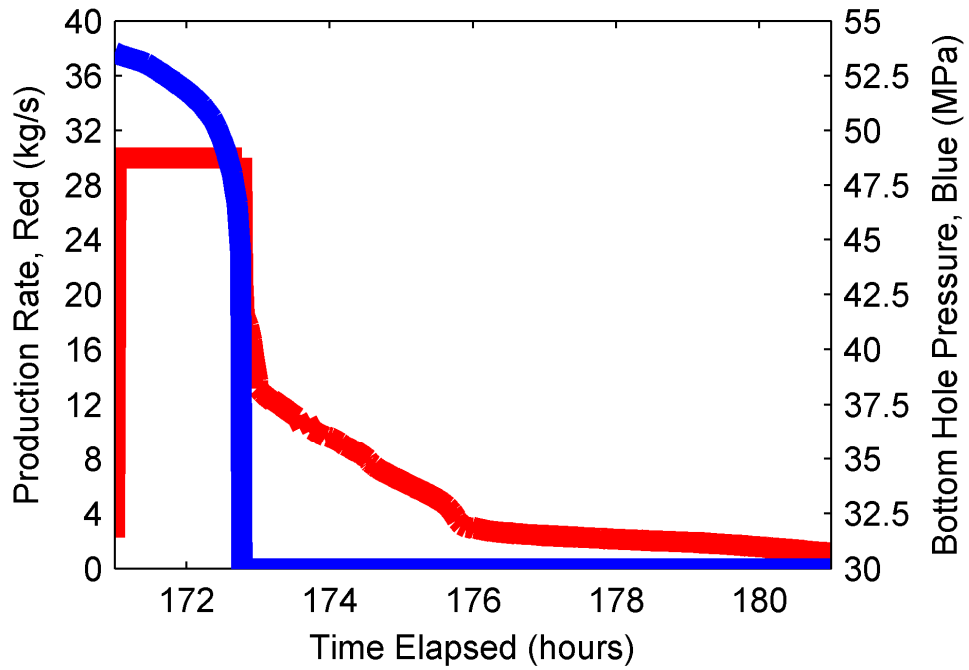
Figure 3-27: Bottom hole pressure and flow rate during production for Simulation F.
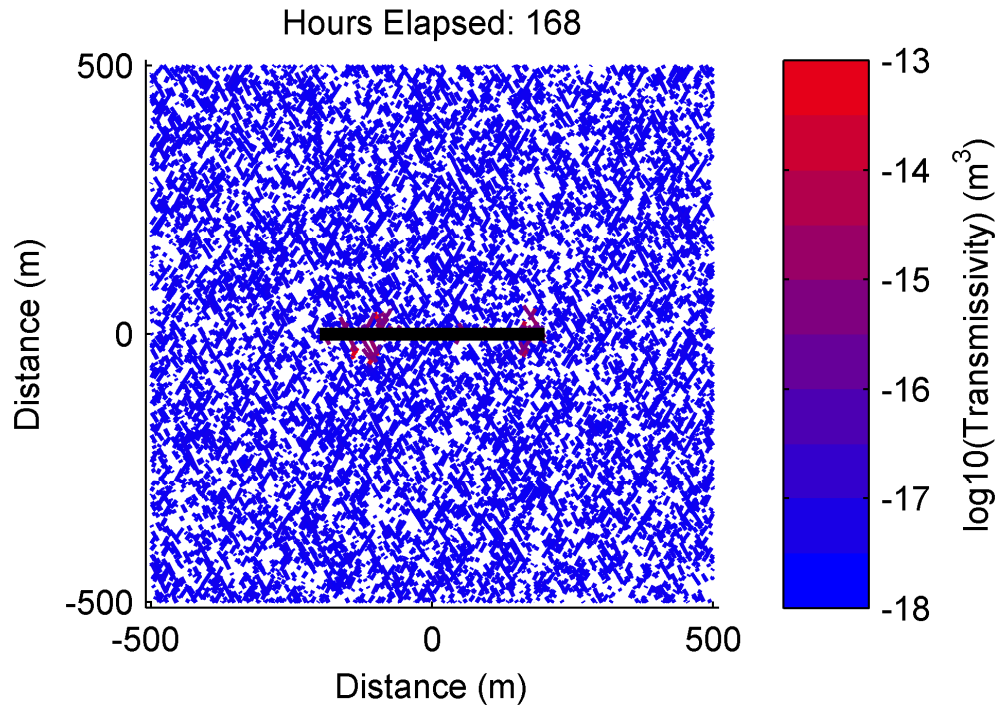
Figure 3-28: Final transmissivity distribution for Simulation G (fracture network F5, σ_{xx} = 50 MPa, and σ_{yy} = 75 MPa). Line thickness is proportional to void aperture but not to scale. Simulation G demonstrates the percolation requirement for PSS. The black line represents the wellbore (parallel to the x-axis).
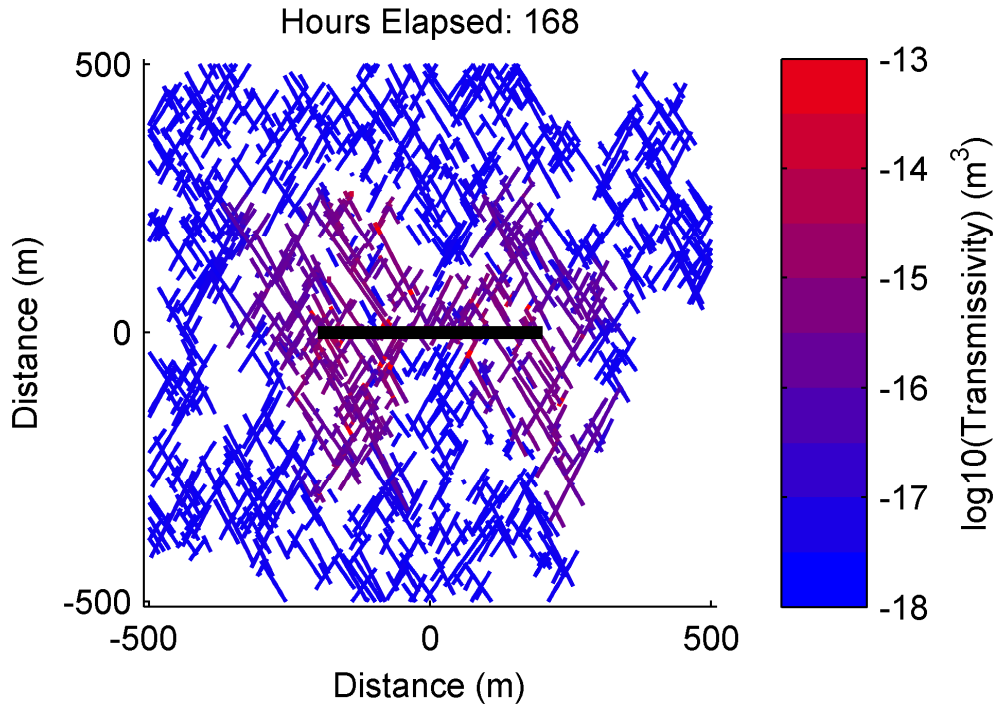
Figure 3-29: Final transmissivity distribution for Simulation H (fracture network F4, σ_{xx} = 50 MPa, and σ_{yy} = 75 MPa). Line thickness is proportional to void aperture but not to scale. The black line represents the wellbore (parallel to the x-axis).
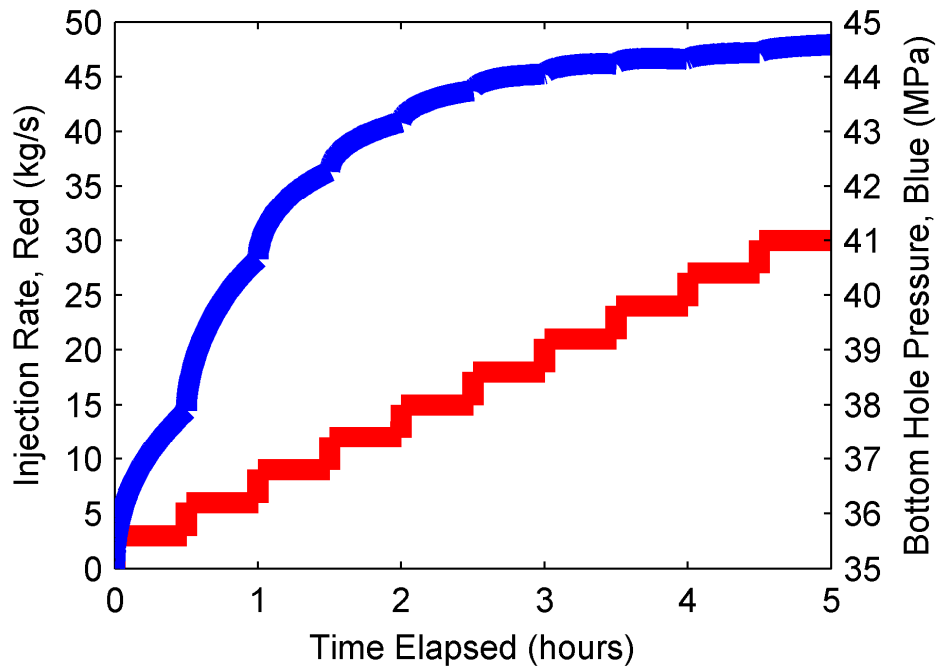
Figure 3-30: Bottom hole pressure and flow rate during injection for Simulation I.

3.4 Discussion

3.4.1 Pure Opening Mode Fracturing

Simulation A (Figure 3-8) is an end-member case of POM, toughness dominated fracture propagation with no fluid leakoff (Detournay, 2004). The fracturing in Simulation A was toughness dominated because fluid pressure along the fractures was almost constant due to the high transmissivity of the open fractures and the low viscosity of the injection fluid, liquid water. A propagating fracture would not be toughness dominated if pressure drop along the fracture was not negligible (perhaps due to proppant or fluid additives).

In most oil and gas applications, fluid leakoff is not negligible. However, negligible fluid leakoff is a reasonable assumption for very low matrix permeability settings such as gas shale or EGS unless leakoff occurs into the natural fracture network (as in the PFSSL mechanism, see Section 3.4.4). As discussed in Section 3.4.7, fluid trapping due to the MMS mechanism may be erroneously interpreted as leakoff (Brown et al., 2012, page 74).

As the fractures propagated, the stress intensity factor at the tips was roughly equal to the fracture toughness. Whenever the stress intensity factor reached the fracture toughness, the fracture propagated. In the toughness dominated regime, longer fractures require lower fluid pressure to propagate (due to Equation 3-14), and so they propagate preferentially over shorter fractures. Pressure drop along the fractures would tend to favor propagation of shorter fractures (in a regime that is not purely toughness dominated), but in Simulation A, pressure drop along the fractures was negligible. If the model calculation had been plane strain, the injection pressure would have approached σ_3 as the fracture continued to grow because holding K_I constant in Equation 3-14 leads to a smaller P as a increases in size. However the calculation was not plane strain because the Olson (2004) adjustment was used. As a result, the injection pressure stabilized at a value above σ_3 because the stress concentration at the crack tips was limited by the formation height (100 m, Table 3-3).

Ten fractures initiated at the wellbore, but only two propagated a significant distance into the formation (Figure 3-8). The initial configuration of ten propagating fractures was a metastable state. Because of the preferential propagation of longer fractures, if any fracture became longer than the others, it would be able to propagate at a lower injection pressure, inhibiting propagation of the other fractures. Any perturbation to the system that allowed one fracture to become longer than the others would lead to runaway propagation of that fracture with no further growth by the others. Subcritical crack growth (Olson, 2004) is a process that could conceivably allow shorter fractures to grow, but this process was not included in the model.

In Simulation A, localization of stimulation occurred due to stress interaction. Two fractures propagated (instead of one) because the problem was symmetrical. These two fractures were located at the ends of the wellbore. When the fractures opened, they induced compressive stress on the neighboring fractures, increasing the fluid pressure needed for propagation. This stress shadowing effect was weakest on the two outermost fractures because they had fewer neighbors, and so after an initial period, they become slightly longer than the others and were able to preferentially propagate.

Following shut-in, the fluid pressure remained constant until production was initiated a week later (Figure 3-10 and Figure 3-11). This occurred because there was zero leakoff from the fractures and there was very little pressure redistribution within the fractures following shut-in because pressure drop along the fractures was negligible.

During production, fluid pressure dropped gradually and linearly with time as the fractures drained in a tank-like fashion (Figure 3-11). After about five hours and twenty minutes of production, the sections of the fractures nearest the wellbore closed, creating a bottleneck in transmissivity and rapidly dropping the bottom hole pressure, BHP, to 30 MPa, the specified minimum BHP. Production rate dropped abruptly and then continued to decline rapidly as the remainder of the fractures closed. Fluid recovery was 89% when the production rate dropped and was close to 100% at the end of the simulation.

3.4.2 Pure Shear Stimulation

Simulations B-D were designed to investigate shear stimulation under different conditions. Simulation B is a prototype of Pure Shear Stimulation (Figure 3-12). In Simulation C, shear stimulation occurred, but low initial permeability caused a new opening mode fracture to form (Figure 3-16). In Simulation D, low fracture void aperture caused unrealistically rapid spreading of pressure perturbation (Figure 3-19).

In Simulations B and C, the natural fractures had E_0 equal to 5 cm (Table 3-4). This very high void aperture was used to represent thick, porous fault zones, which are found at many EGS projects (Section 4.1.4 and Chapter 5). In Simulation D, the natural fracture E_0 was 0.5 mm and was intended to represent crack-like fractures.

3.4.2.1 Prototype of Shear Stimulation

Simulation B is a prototype for the PSS mechanism. Injection pressure was always below σ_3 (Figure 3-13) and there was no propagation of new, opening mode fractures (Figure 3-12). Increased fluid pressure triggered slip on the natural fractures, and they experienced increased transmissivity (Figure 3-12). After shut-in, fluid pressure continued to leak off into the natural fracture network (which had a reasonably high initial transmissivity), and shear stimulation continued to spread. The BHP declined gradually during shut-in (Figure 3-14). During production, injection pressure declined gradually, and when production switched to constant pressure, rate declined gradually.

3.4.2.2 Initial Transmissivity and Crack-like Shear Stimulation

In Simulation C, shear stimulation did not occur at the beginning of the simulation because the initial transmissivity of the natural fractures was too low. Simulation C was intended to represent a setting where there are large faults capable of being stimulated with very low initial transmissivity. This might happen, for example, if the faults were initially mineralized shut, and induced slip broke up the mineralization. In Simulation C, fluid was confined almost entirely to a single, newly formed hydraulic fracture for the entire three hours of injection and roughly six and half hours after shut-in. Figure 3-31 shows the transmissivity distribution in the network 9.568 hours after the beginning of

the simulation (injection ended after three hours). It can be seen that that very little flow/transmissivity enhancement had occurred in the natural fractures at that point.

After about 2.4 hours of injection, the propagating fracture reached its specified maximum size of 450 m and was not permitted by the model to grow further. This model artifact could have been avoided by using a larger problem domain (or a larger fracture toughness), and led to the gradual, slight increase in injection pressure that can be observed during the end of the injection period in Figure 3-17.
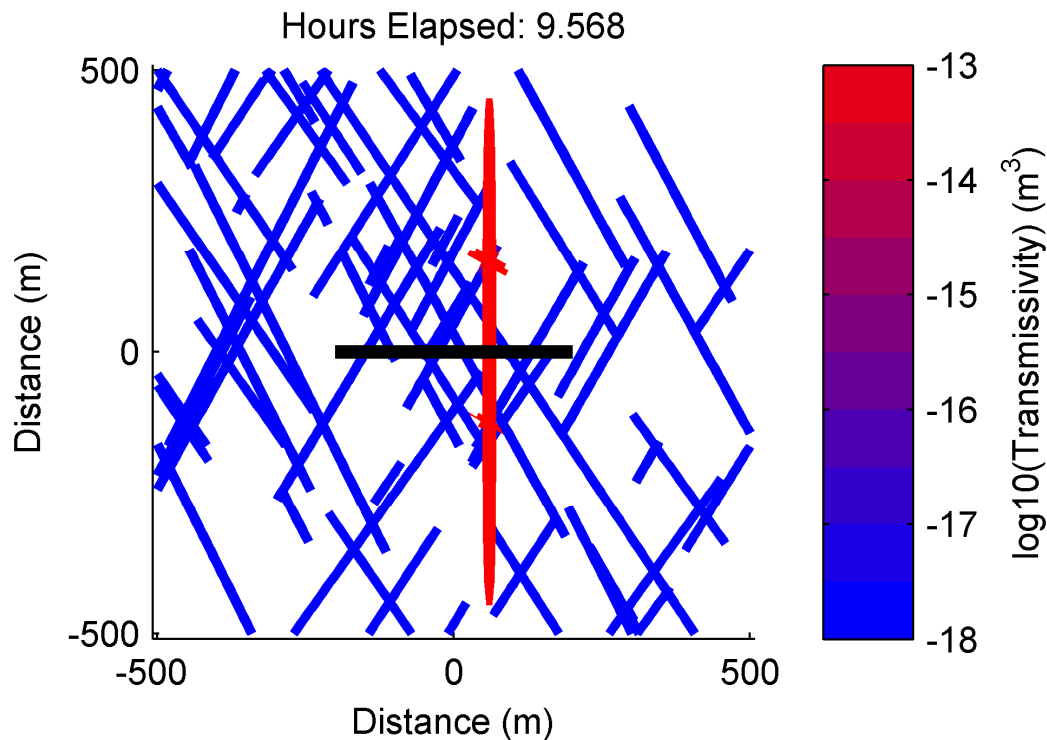
Figure 3-31: Transmissivity distribution during Simulation C after 9.568 hours.

The propagation of shear stimulation during the shut-in period of Simulation C occurred in a series of brief episodes of rapid propagation. Figure 3-32 shows the transmissivity distribution in the fracture network 10.1385 hours after the start of the simulation, just 34.2 minutes after the transmissivity distribution shown in Figure 3-31. Strikingly, pressure, slip, and transmissivity enhancement propagated a significant distance down two of the fractures during this 39 minute period, even though there had been virtually zero fluid flow in any of the preexisting fractures for the previous nine and a half hours.
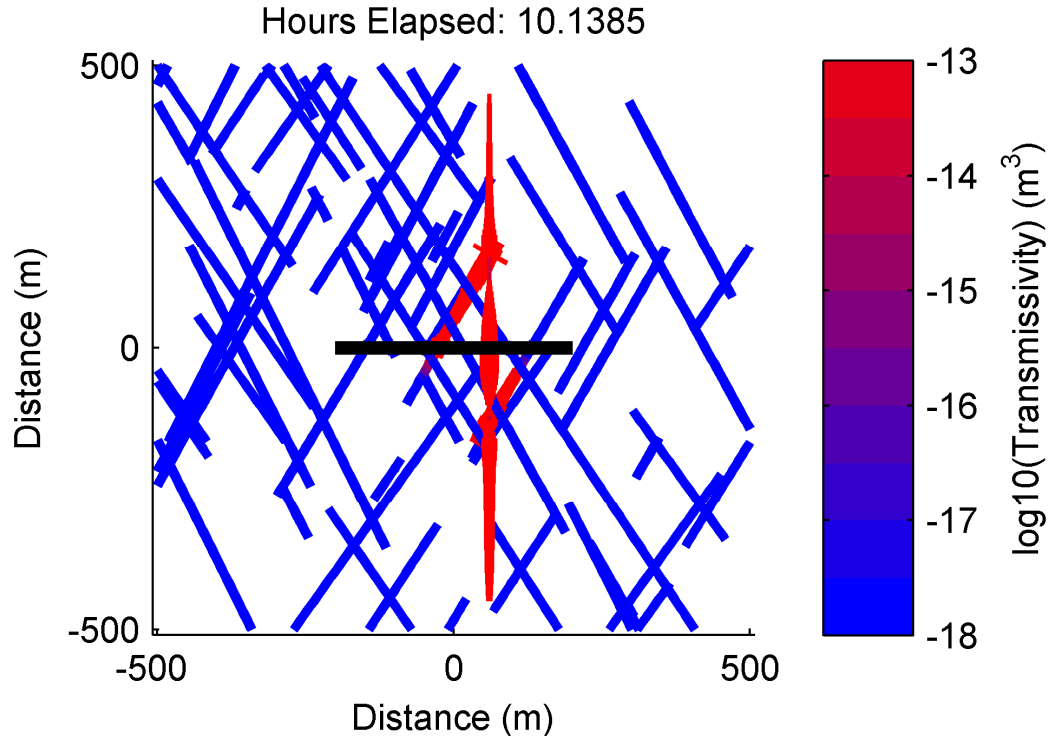
Figure 3-32: Transmissivity distribution during Simulation C after 10.1385 hours.

Episodic propagation of shear stimulation occurred because shear stimulation involves two different processes that can occur at different rates: (1) initiation of slip on a fracture and (2) propagation of slip along a fracture.

We refer to the process of shear stimulation propagating down a fracture as crack-like shear stimulation (CSS). If slip is aseismic (due to constant or gradually changing friction), as in the simulations in this chapter, CSS occurs smoothly in a process we refer to as smooth crack-like shear stimulation (SCSS). In contrast, if slip is seismic (due to abrupt frictional weakening), then CSS occurs episodically, in a process we refer to as ECSS (Section 4.4.2). For ECSS, the word "episodic" refers to propagation along an individual fracture. However, for both the ECSS and SCSS mechanisms, episodic propagation of shear stimulation can occur in a network of fractures because of the two different processes that occur at different rates: propagation of stimulation along an individual fracture and initiation of stimulation on a fracture (Section 3.4.2.2).

The CSS mechanism occurs because of the interaction between deformation, induced stresses, fluid flow, and transmissivity enhancement. When a patch of a fracture slips,

shear stress is reduced on that patch but increases on the rest of the fracture surrounding it (Crouch and Starfield, 1983, page 83). The boundary between where the fracture has slipped and where it has not slipped forms an effective crack tip, and a concentration of shear stress develops. If the concentration of shear stress is strong enough, slip can be induced ahead of the crack tip even if perturbation in fluid pressure lags behind. When slip occurs on a patch of fracture (ahead of the effective crack tip) for the first time, transmissivity increases, and fluid is able to flow rapidly into the newly slipped patch, causing slip, transmissivity enhancement, and further advance of the effective crack tip. The rate of propagation may be insensitive to the initial transmissivity because it depends on the rate of fluid flow to the effective crack tip, which occurs at the "stimulated" transmissivity, not the initial transmissivity. As long as slip is aseismic, this process happens smoothly. The process is referred to as "crack-like" because it involves propagation of displacement along an individual fracture, and an effective "crack-tip" forms (and creates stress concentration) at the boundary between where deformation has occurred and where it has not occurred. This process is analogous to the propagation of an opening mode tensile fracture in a very low matrix permeability medium, which occurs at a rate insensitive to the permeability of the medium ahead of the crack tip.

Figure 3-33 demonstrates the SCSS mechanism. Figure 3-33 shows displacement, pressure, shear stress, friction, and transmissivity along one of the fractures in Figure 3-32. Because of stresses induced by slip along the fracture, the front of shear displacement and transmissivity enhancement was ahead of the front of fluid pressure. As fluid pressure followed behind the displacement front (at a transmissivity much greater than the initial transmissivity), further slip was triggered, inducing shear stress, and allowing the displacement front to continue to advance. Extreme concentration of shear stress was not possible at the effective crack tip because the shear stress could not exceed the frictional resistance to slip. Instead, a zone of distributed shear deformation developed. Ahead of the displacement front, where displacement had not yet occurred, frictional strength remained greater than shear stress.
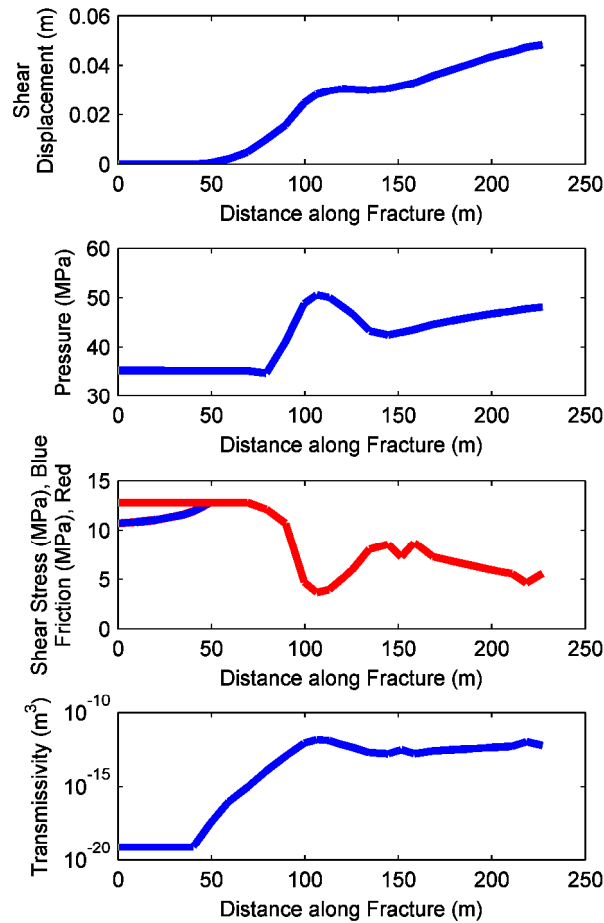
Figure 3-33: An example of the SCSS mechanism. Shear displacement, fluid pressure, shear stress, frictional strength (coefficient of friction multiplied by effective normal stress), and transmissivity along a fracture near an effective crack tip. These results were taken from Simulation C after 10.1385 hours, as seen in Figure 3-32. The left hand side of the fracture shown in this figure is located at about (-80,-100) and the positive direction in "distance along the fracture" moves to the upper right in Figure 3-32. The fracture intersects the wellbore at "distance along the fracture" equal to about 105 m.

Under most conditions, induced stresses cannot cause the first patch on a fracture to slip, and fluid flow into the unstimulated fracture is required. This process is dependent on the initial transmissivity, which could potentially be quite low. Therefore, this process could be much slower than propagation of stimulation along a fracture.

Under some circumstances, stresses from one fracture could induce slip on an adjacent fracture. The details of this interaction would depend on the relative orientations and locations of the fractures and the magnitude of their slip. This type of stress transfer

assisted propagation would be less efficient than the CSS mechanism because induced stresses directly ahead of a crack tip are stronger than induced stresses in other orientations.

Deformation of one fracture may lower the normal stress of a neighboring fracture. However, as discussed in Section 2.2.5.2, in undrained conditions (the instantaneous response), effective normal stress must be nearly constant on a fracture due to conservation of mass and the low compliance of liquid water. Therefore, a reduction in normal stress must be matched by a reduction in fluid pressure. Eventually, fluid recovers as fluid flows into the region of lower pressure (lowering effective normal stress and potentially causing slip), but if the initial fracture transmissivity is low, this process may take a significant amount of time.

In practice, one strategy to enable shear stimulation and avoid tensile fracturing in settings with low initial fracture transmissivity (such as Simulation C) would be to inject at a low rate and pressure prior to the main stimulation in order to raise the fluid pressure in the low transmissivity fractures near the wellbore (and bring them closer to initiating slip). A similar strategy would be to vary injection rate over time in order to maintain fluid pressure below the least principal stress, similar to the TSS test described in Section 3.4.8.

Shapiro et al. (1999) proposed that the rate of microseismicity during shear stimulation is related only to the initial hydraulic diffusivity (see definition of diffusivity in Section 3.4.2.3). However, this technique to estimate initial hydraulic diffusivity could be problematic if the CSS mechanism controls the spreading of stimulation. The CSS mechanism allows stimulation to propagate at a rate insensitive to the initial diffusivity.

A direct coupling between transmissivity and pressure is another process that could cause stimulation to propagate at a rate much faster than would be suggested by the initial hydraulic diffusivity. Rice (1992) analyzed this process in the context a buoyant fluid leaking up a fault and found that coupling of transmissivity and pressure could lead to solitary waves of pressure as the fluid leaked upward. Shapiro and Dinske (2009) discussed how this process could complicate the process of trying to infer information about formation diffusivity from the spreading of seismicity.

The CSS mechanism is a distinctly different mechanism than direct coupling of pressure with fracture transmissivity (the process described by Rice (1992) and Shapiro and Dinske (2009)). The similarity is that in both cases, fluid pressure increase causes transmissivity enhancement. However, in the CSS mechanism, this coupling is indirect, with pressure causing slip, which causes increase in transmissivity.

The most important difference is that the CSS mechanism does not occur until slip has been initiated on a fracture (by flow at the initial diffusivity). Therefore, the CSS mechanism on a particular fault occurs with some delay, causing episodic propagation in a fracture network. With direct coupling of transmissivity to pressure, stimulation can initiate on a fracture and cross from one fracture to another without delay, resulting in non-episodic propagation a fracture network.

3.4.2.3 Shear Stimulation and Void Aperture

In Simulation D, the low void aperture (hundreds of microns) of the fractures (compared to the Simulations B and C) caused exceptionally rapid spreading of stimulation. Figure 3-19 shows that after only five minutes, stimulation had propagated hundreds of meters from the wellbore.

The rapid spreading occurred because of the high hydraulic diffusivity, D_{dif}. In groundwater hydrology terminology, hydraulic diffusivity is defined as the ratio of hydraulic conductivity to specific water capacity (Hillel, 1971). If it is assumed that e is equal to E, that aperture increases $E/12$ per MPa change in fluid pressure, and fluid viscosity is 10^{-9} MPa-s (the viscosity of water at room temperature), then hydraulic diffusivity can be calculated:

$$D_{dif} = \frac{(e^3 h\rho)/(12\mu_l)}{\rho h(\partial E/\partial P)} = \frac{e^3/12}{\mu_l e/12} = 10^9 e^2 .$$

3-15

From Equation 3-15, if e is equal to 100 microns, D_{dif} is equal to 10 m^2/s. If e is equal to 500 microns, D_{dif} is equal to 250 m^2/s. Penetration depth of diffusive processes scales like $2(tD_{dif})^{1/2}$. These diffusivities imply penetrations depths after one hour of 190 m and 949 m.

If rapid spreading of stimulation occurred in practice, it would be observed from rapid spreading of microseismicity. However, microseismicity migrating hundreds of meters in 5-6 minutes has not ever been observed, as far as we are aware. This is important because the values for E_0 and e_0 used in Simulation D, 0.5 mm for both, were roughly consistent with laboratory observations of fracture parameters (Barton et al., 1985; Lee and Cho, 2002; Esaki et al., 1999).

Hydraulic diffusivity could be made lower by using either a lower hydraulic aperture or a larger void aperture. However, if hydraulic aperture is too small, fluid pressure will build up, and tensile fracturing will result.

The issue can alternatively be considered from point of view of pore volume. If void aperture is low, it will require a huge fracture surface area to store the injected fluid. Huge fracture surface area could be possible if the spatial extent of stimulation was very large (which is not realistic) or if the fractures storing the fluid were very closely spaced. Yet wellbore observations in EGS projects typically indicate that flowing fracture are widely spaced (spacing of 20-100 m) (Richards et al., 1994; Ito and Kaieda, 2002; page 533 of Brown et al., 2012; Miyairi and Sorimachi, 1996; Wyborn et al., 2005; Baria et al., 2004; Evans, Genter, and Sausse, 2005; Dezayes et al., 2010).

This is a major problem because PSS is the main conceptual model in the EGS literature, yet it is common for EGS to be performed in places with low matrix permeability and only crack-like fractures. For example, in Chapter 5, nine historical EGS projects were reviewed and no evidence of fractures with mechanical aperture larger than a few millimeters was found at five of the projects.

We offer two hypotheses to explain how PSS could be possible in geological settings with very low matrix permeability and crack-like fractures. One possibility is that thin, crack-like features actually have greater effective void aperture than laboratory experiments suggest, perhaps due to macroscopic opening that occurs when nonlinear fractures shear (Dieterich and Smith, 2009; Griffith et al., 2010; Kaven et al., 2012; Ritz and Pollard, 2012). Another possibility is that a significant volume of fluid leaks off into the more abundant, but apparently sealed, natural fractures in the formation. However, it

is difficult to imagine that a huge volume of fluid could leakoff into the natural fracture network given that wellbore logs indicate that flowing fractures are widely spaced.

A final possibility is that while PSS is believed to occur at many projects, in reality, fracture opening occurs (the walls come out of contact). With fracture opening, void aperture of crack-like fractures could be millimeters to centimeters and provide very significant storativity. If fracture opening occurs, then fluid pressure must be in excess of σ_3, and newly formed fractures may propagate through the formation. The possibility of fracture opening and propagation is rarely considered in the EGS literature (as discussed in Section 3.4.6, Brown, 1989, is an exception), probably because newly formed tensile fractures are not typically observed along the wellbore. However, it is possible that new fractures could initiate off of opened natural fractures away from the wellbore (perhaps exploiting the concentration of tensile stress that would be caused by slip of the natural fracture prior to opening). The lack of new fractures at the wellbore could be a consequence of the high tensile strength of the rock in typical geothermal projects.

3.4.3 Mixed Mechanism

Simulation E was an example of the MMS mechanism (Figure 3-20). Most stimulation was concentrated in a single large region of opening mode tensile fracturing oriented roughly parallel to the y-axis and near the center of the x-axis. This region had fully formed by the end of injection (Figure 3-34).
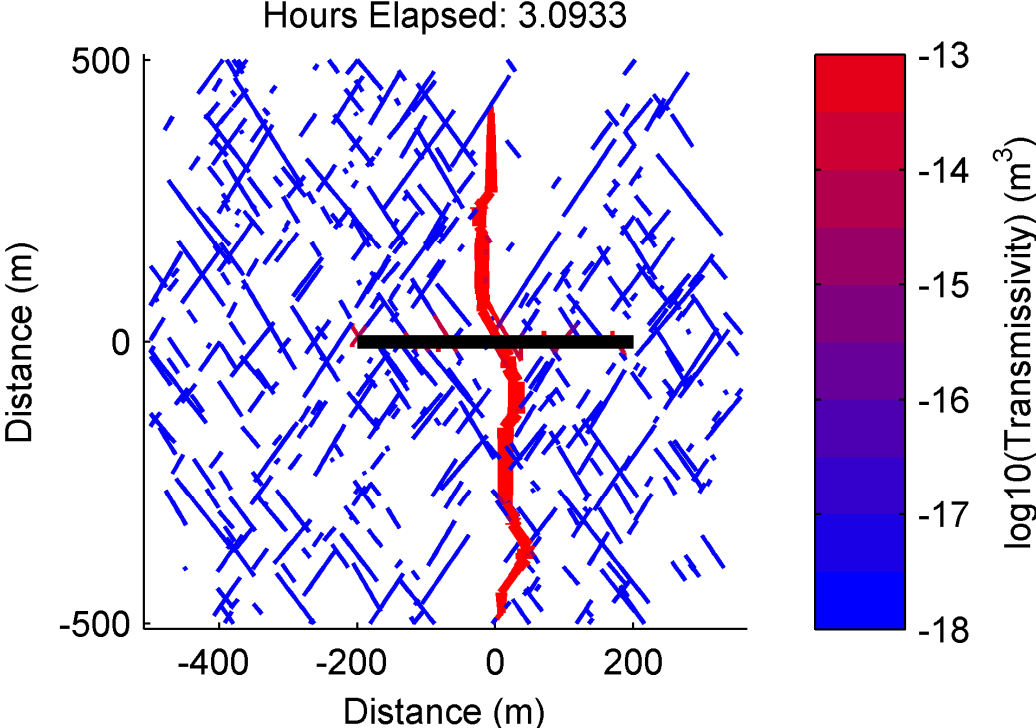
Figure 3-34: Transmissivity distribution shortly after the end of injection for Simulation E.

During shut-in, some spreading of stimulation occurred, primarily through leakoff and stimulation in the natural fractures (Figure 3-20 and Figure 3-34). Stimulation could not travel too far without being accompanied by tensile fracturing because the natural fracture network was not percolating.

The nature of the fracturing in the central region of opening mode fracturing in Simulation E was very different than in Simulations A, C, or F. In Simulation E, continuous flow paths through the central fracture region passed through both newly formed fractures and preexisting fractures (Figure 3-20). In Simulations A, C, and F, newly formed tensile fractures propagated continuously through the reservoir without interruption (Figure 3-8, Figure 3-16, and Figure 3-24). Some of the consequences of this difference are discussed more in Section 3.4.6.

During injection, fluid pressure was modestly above the least principal stress, and during shut-in, fluid pressure was almost constant, with very little pressure decline. Production was maintained at 30 kg/s for roughly an hour before production pressure and

rate dropped dramatically. Roughly one sixth of the injected fluid had been recovered when the drop in injection rate occurred.

3.4.4 Primary Fractures with Shear Stimulation Leakoff

Simulation F was an example of the PFSSL mechanism (Figure 3-24). Two opening mode tensile fractures (of a possible ten) propagated through the formation and bled fluid off into a shear stimulating region. The two fractures that formed were in the same location as the fractures that formed during Simulation A, but the fractures were significantly shorter and wider. The largest fracture opening during Simulation F occurred at the end of injection (Figure 3-35) and was about 3 cm (this was the greatest fracture opening that occurred in any of the simulations). Shorter and wider fractures could be caused by greater fracture toughness, yet the fracture toughness was the same in Simulation F, 3.0 MPa-m$^{1/2}$, as during all other simulations.

The greater apparent fracture toughness occurred because of heterogeneity in stress caused by deformation of the natural fractures. As fluid leaked off into the natural fractures, the natural fractures slipped and/or opened, changing the stress around them. These stress perturbations were felt at the tips of the propagating fractures and could either encourage or hinder propagation. When they encouraged propagation, the fracture advanced rapidly, but when they hindered propagation, the crack tip stopped advancing, causing fluid pressure to build up, opening the fracture wider and potentially allowing other fractures to propagate. This effect was clearly evident after about 1.25 hours of injection, when the injection pressure, which had been steadily building up during injection, abruptly dropped. Prior to this, only the fracture on the left had propagated a significant distance into the formation. The abrupt drop in injection pressure corresponded to the initiation and propagation of the fracture on the right.

The high apparent fracture toughness may have been exaggerated somewhat by our model because fractures were only allowed to follow a few, prespecified paths. If fractures had the ability to initiate anywhere and to propagate in any direction, there would be more opportunities for fractures to follow the "path of least resistance," and barriers to propagation would have less effect.

After injection stopped, stimulation continued to spread through the formation. Little additional propagation of new fractures occurred, but the surrounding region of shear stimulation grew very significantly during shut-in. Figure 3-35 shows the distribution of fracture transmissivity shortly after shut-in. It can be compared to Figure 3-24, which shows the distribution of transmissivity at the end of the simulation.
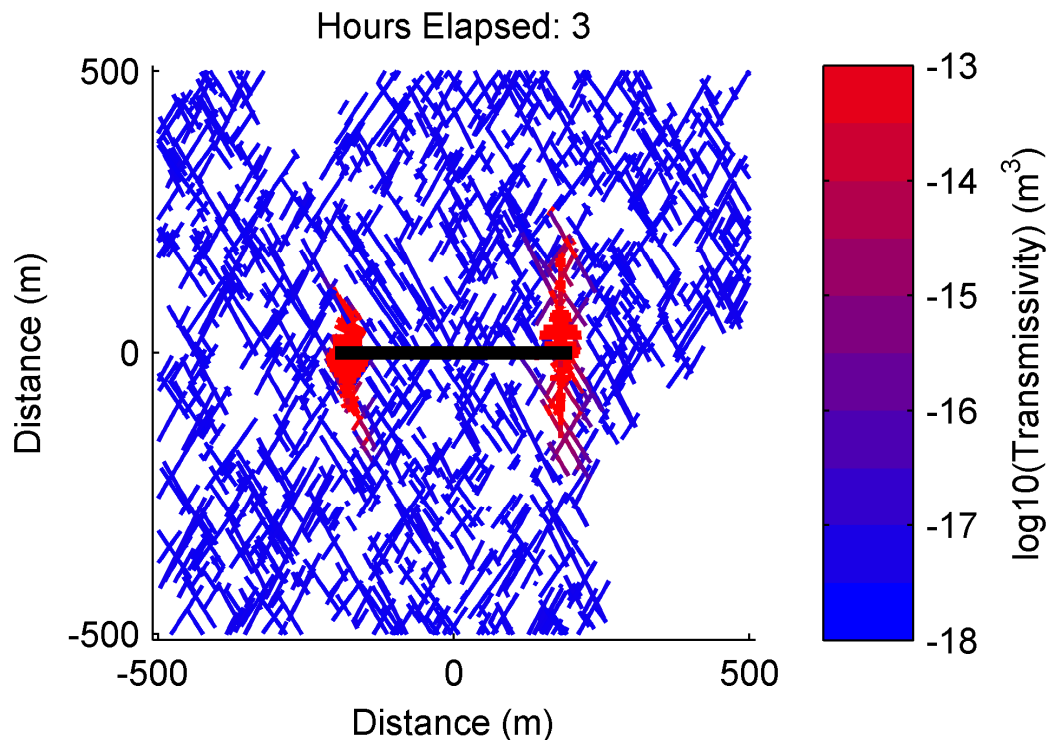
Figure 3-35: Transmissivity distribution at the end of injection for Simulation F.

The exact timing and spatial extent of the spreading of shear stimulation depended on the particular choices made for the void and hydraulic apertures of the natural fractures. Shear stimulation was relatively limited during the injection period because the initial fracture transmissivity in Simulation F was relatively low. The relatively low value of initial transmissivity was chosen intentionally. In designing this study, several simulations with different values for e_0 were performed until a simulation was found that demonstrated the PFSSL mechanism. If e_0 was too high, leakoff from the propagating fractures was so significant that little propagation of new fractures occurred, and the simulation was essentially PSS. On the other hand, if initial fracture transmissivity was too low, then shear stimulation was very limited because fluid was prevented from ever entering into the natural fractures, and the simulation was essentially POM. Overall,

PFSSL only occurred in simulations within a fairly narrow range of values for e_0. This observation suggests that PFSSL may be less likely to occur in reality, because it could only take place within a relatively narrow set of geological conditions. However, because our model did not allow new fractures to form anywhere and forced propagating fractures to travel in a straight line, it may have been artificially difficult for the PFSSL mechanism to occur.

The significant growth of the shear stimulation region during shut-in suggests that with the PFSSL mechanism, it may be useful to delay producing fluid back to the surface following stimulation. As long as the well remains shut-in, the formation is pressurized, and fluid has more time to seep into low transmissivity fractures and cause slip. However, longer shut-in periods will lead to greater water loss.

The BHP during shut-in increased for a few days, an unusual result (Figure 3-26). Typically, fluid pressure would be expected to spread out and dissipate during shut-in. In fact, fluid did flow away from the wellbore after shut-in, but paradoxically, the spreading of fluid into the formation increased the BHP slightly. Apparently, the spreading of fluid pressure triggered slip on the preexisting fractures, and the stresses induced by these deformations caused a slight net increase in compressive stress on the two primary fractures in Simulation F, increasing the BHP.

Production at 30 kg/s was performed with modest pressure drop until BHP reached about 50 MPa, the least principal stress, and then injection rate and pressure dropped dramatically.

3.4.5 Bottom Hole Pressure During Injection and Shut-in

The behavior of the bottom hole pressure during injection and shut-in was diagnostic of stimulation mechanism. In general, a fracture opens (the fracture walls come out of contact) when the fluid pressure exceeds its normal stress. Presumably, proppant (which was not included in the model) can only be contained in fractures that have opened. Depending on fracture orientation, normal stress can be no less than the least principal stress. Therefore, if BHP is below the least principal stress, it can be concluded that fractures are not open in the reservoir, except for regions where deformation has caused

localized reduction in stress (such as wing cracks off a shearing fracture, see Section 2.3.2).

If BHP during injection never exceeds the least principal stress (but stimulation is taking place) then the mechanism of stimulation must be PSS (as in Simulation B, Figure 3-13). On the other hand, if injection pressure exceeds the least principal stress, PSS probably should probably not be ruled out. It is conceivable that some limited propagation of new tensile fractures could take place (with fluid pressure above the least principal stress), but that shear stimulation could still be the dominant mechanism of permeability creation. However, in this case, fluid pressure should drop below the least principal stress soon after shut-in as the open, newly formed fractures leak off into the natural fractures.

Pressure decline during shut-in was diagnostic for whether fractures in the formation remained open. In hydraulic fracturing with reasonable matrix permeability, fractures typically close soon after shut-in because fluid leaks off into the formation. However if matrix permeability is negligible, fluid can only leak off into the natural fracture network. In Simulation C, where the natural fractures had significant ability to store fluid, leakoff from the newly formed fracture was significant, and during shut-in, the newly formed fracture closed and the fluid pressure dropped below the least principal stress. The closure of the newly formed fracture manifested as an abrupt, large drop in BHP (made more abrupt by the CSS mechanism) that occurred hours after shut-in (Figure 3-18). Prior to that drop, BHP had been almost constant during shut-in.

In Simulations A, E, and F, BHP remained above the least principal stress during shut-in (Figure 3-10, Figure 3-22, and Figure 3-26). In Simulation A, there were no natural fractures and so there was zero leakoff. In Simulations E and F, some fluid was able to leak off from the open fractures. However, the void aperture of the natural fractures, specified by E_0, was much lower in Simulations E and F than in Simulation C. As a result, the volume of water that leaked off was not great enough to empty the newly formed fractures, allow them to close, and allow fluid pressure to drop below σ_3.

To summarize, fluid pressure above σ_3 during injection indicates that fracture opening is taking place in the formation. If BHP is less than σ_3 during injection, then fracture

opening is not taking place and the mechanism of stimulation is PSS. During shut-in, BHP above σ_3 indicates that some fractures remain open in the formation. Fractures opened by injection can only close if they are drained by fluid leakoff, and so if BHP drops below σ_3 during shut-in, the natural fracture network has sufficient storativity to contain all the injected fluid.

3.4.6 Production Behavior

In some cases, fracture closure occurred during production as fluid was drained out of open fractures. Closure was apparent in the behavior of production rate and pressure. When closure happened, fracture transmissivity dropped abruptly. Fractures oriented perpendicular to the least principal stress would tend to close at a fluid pressure near σ_3, but fractures of other orientations could close at higher fluid pressures. Fracture closure would only be expected to occur if injection was performed at a pressure greater than the least principal stress. Otherwise, significant fracture opening would not occur during injection.

Abrupt drops in production rate occurred during Simulations A, E, and F, indicating fracture closure (Figure 3-11, Figure 3-23, and Figure 3-27). In Simulation C, fracture closure occurred during shut-in (Figure 3-18). These simulations can be compared to Simulation B, where fracture closure did not occur, and there were not any abrupt drops in production rate (Figure 3-15).

Fluid recovery prior to fracture closure was extremely high in Simulation A (Figure 3-11), and between 25-50% in Simulations E and F (Figure 3-23 and Figure 3-27). Careful investigation demonstrates that the causes of limited fluid recovery in Simulations E and F were different. In Simulation F, a significant amount of fluid leaked off into the natural fracture network surrounding the newly formed fractures (Figure 3-24). However, in Simulation E, the natural fracture network was less dense (Figure 3-20), and leakoff into these fractures was volumetrically less significant. Limited recovery in Simulation E occurred because of localized fracture closure around the wellbore, which could be referred to as "snapoff" (Figure 3-36). Snapoff can occur if

continuous paths through open fractures in the reservoir pass through both new and preexisting fractures.

In Simulation E, there were abundant open, preexisting fractures that were not oriented perpendicular to the least principal stress. When production began, they closed at a fluid pressure greater than the least principal stress. When the natural fractures near the wellbore closed, they created a bottleneck in transmissivity, trapping a large amount of fluid in open fractures away from the wellbore. Over weeks or years, the transmissivity of the closed fractures would be great enough to drain water (or hydrocarbons) from the most distant, open fractures (although relative permeability effects would also come into play). But the fluid was essentially trapped for production on the time-scale of hours.

Figure 3-36 shows a close-up of the fractures near the wellbore at the end of Simulation E. These fractures have transmissivity in the range of 10^{-15} m^3, which is not tiny, but is not high enough to sustain large flow rates. The closing natural fractures created bottlenecks in flow that trapped in open fractures away from the wellbore.
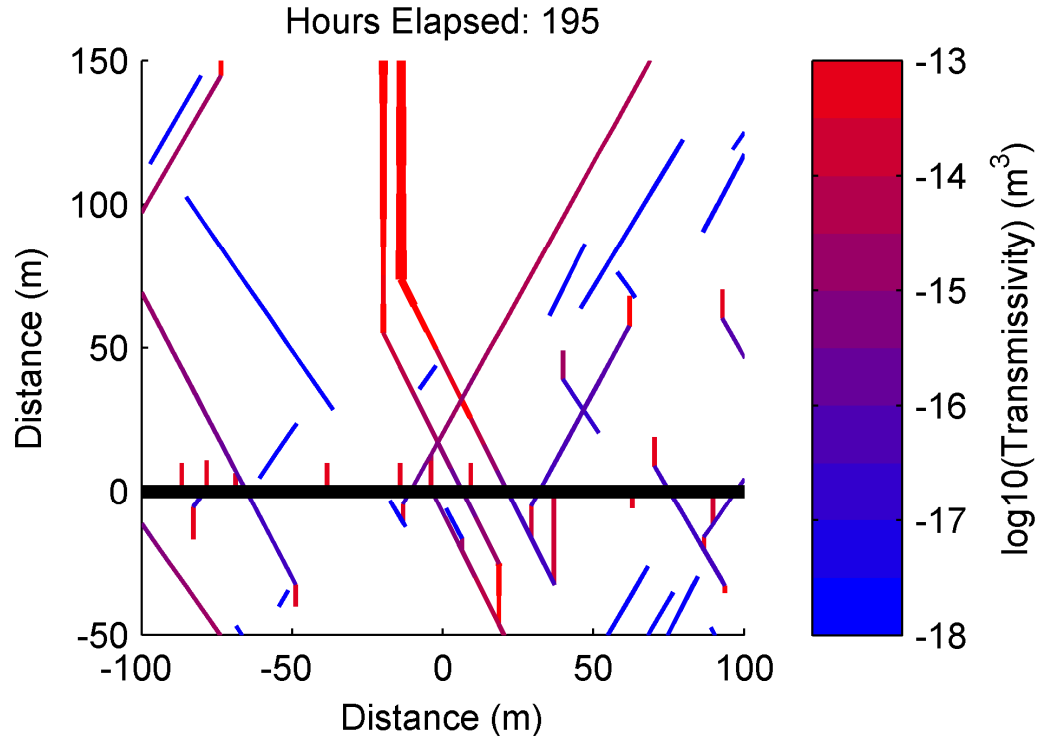
Figure 3-36: Transmissivity distribution at the end of injection for Simulation E. The figure is zoomed in to show closure of natural fractures near the wellbore. Newly formed fractures away from the wellbore remain open (line thickness is proportional to aperture, and the open fractures are thicker).

The fluid trapping mechanism that occurred in Simulation E was hypothesized to have occurred at the Fenton Hill EGS project (Brown, 1989; Brown et al., 2012). Brown et al. (2012) explained how engineers at Fenton Hill were perplexed by poor fluid recovery following mini-frac tests. In these tests, packers were used to isolate a zone of the wellbore, and then tens or hundreds of m^3 of fluid were injected. The fluid was believed to be flowing into a large, natural fracture intersecting the wellbore. Fluid recovery was expected to be high because the granite matrix had exceptionally low permeability. Three alternative hypotheses for the poor fluid recovery were (1) leakoff into the matrix, (2) leakoff into natural fractures, and (3) trapping of fluid due to closure of the natural fracture near the wellbore. To distinguish between the three hypotheses, a mini-frac test was performed with proppant. In this case, almost complete recovery of fluid was achieved. This was taken as evidence that the fluid recovery was due to snapoff. The proppant held the natural fracture open near the wellbore, preventing closure and trapping (Brown et al., 2012, page 74). Proppant would not have prevented leakoff into the matrix or into natural fractures. As described by Brown (1989), snapoff

could occur at fluid pressure significantly above the least principal stress if the natural fractures are poorly oriented to open in the local stress state.

It might be argued that if fluid pressure exceeds the least principal stress, then new tensile fractures should form at the wellbore and propagate through the formation. If this happened, snapoff could still occur if these propagating fractures terminated against natural fractures and were forced to reinitiate elsewhere on the natural fracture.

In rock with high tensile strength, it may not be reasonable to assume that natural fractures always form at the wellbore when fluid pressure exceeds the least principal stress. According to Brown et al. (2012, page 73), newly formed fractures were never observed along the wellbores at the Fenton Hill EGS project despite extensive injection at pressure well above the least principal stress. Brown et al. (2012, page 73) attributed the lack of new fractures at the wellbore to the high tensile strength (relative to typical sedimentary rocks) of the granite at the Fenton Hill project (which would be typical EGS, but not gas shale). The lack of new tensile fractures at the wellbore does not rule out that they may have formed off opened natural fractures further into the formation (in fact, it is probable).

Zoback et al. (1977) performed laboratory experiments in which hydraulic fracturing was attempted in rock samples with preexisting fracture that were not oriented perpendicular to the least principal stress. They found that in some cases the preexisting fracture opened before a new tensile fracture could form.

Baumgärtner and Zoback (1989) described a series of mini-frac tests that were performed at various intervals in crystalline rock in a thrust faulting regime. They reported breakdown pressures well above both the minimum principal stress (vertical) and the minimum horizontal stress (the intermediate principal stress). They reported that during some tests, equipment limitations prevented new tensile fractures from being initiated, despite fluid pressure well above the minimum principal stress.

To summarize, we identify two mechanisms that could cause limited fluid recovery, leakoff of fluid to natural fractures and trapping due to closure of natural fractures. As suggested by Brown (1989), the snapoff mechanism could take place with a fluid pressure well above the least principal stress (depending on the degree of stress

anisotropy and the orientation of the closing natural fractures). With the PFSSL mechanism, fracture closure may be observed in the pressure history, but only at the least principal stress. In contrast, fracture closure could occur at fluid pressures greater than the least principal stress in the MMS mechanism.

Identification of fracture closure can rule out the PSS mechanism, because the PSS mechanism requires that little or zero fracture opening can occur. Fracture closure at pressure well above the least principal stress is a strong indication of the MMS mechanism.

A distribution of fracture orientations exists in the subsurface, and orientation affects an individual fracture's closure stress. However fracture orientations in a particular location tend to be clustered into certain sets, and so all fractures in a particular set may be expected to close within a relatively narrow range of fluid pressure.

The effect of fracture closure may have been exaggerated in Simulations E and F because in these simulations the stimulated, closed fracture transmissivity was rather low. With a higher closed fracture transmissivity, fracture closure would not cause such an abrupt and dramatic decrease in production rate/pressure. Therefore, in practice, fracture closure may not manifest as such a large, immediate drop in production pressure. However, it would be expected to cause a discontinuity in the derivative of pressure with time, which could be identified in a pressure history.

Proppant, which is used in gas shale but very rarely in EGS, could complicate attempts to identify fracture closure. With proppant, the transmissivity of unstimulated fractures should be much higher than without proppant (Fredd et al., 2001), and an abrupt drop in transmissivity may not occur with closure.

If a modest amount of proppant is used, as is most common in gas shale, then the stimulated volume may be divided into two sections: the propped region and the unpropped region. Fracture closure in the unpropped region may be identified in the pressure history after the fractures in the propped region have all closed. Perhaps, closure in the propped region could be identified if the propped transmissivity was not high enough to prevent a significant discontinuity in transmissivity with closure.

3.4.7 Estimation of the Least Principal Stress

In this section, several pitfalls are summarized that could lead to inaccurate estimation of σ_3. Accurate estimation of σ_3 is important to the diagnostic methodologies described in this chapter because they often depend on identifying the relationship between fluid pressure and σ_3.

Closure pressure, P_c, is defined as the fluid pressure at which "fracture closure" occurs, and is sometimes taken to be an average value of σ_3 in the interval where hydraulic fracturing is taking place (Gulrajani and Nolte, 2000). However, closure pressure may not be equal to σ_3 if fractures are opened that are not perpendicular to the least principal stress.

As discussed in Section 3.4.6, Brown (1989) pointed out that if injection causes opening of preexisting fractures at the wellbore rather than creation of new opening mode fractures at the wellbore, the observed P_c may be greater than σ_3 (even if new fractures perpendicular to the minimum principal stress form off the preexisting fractures and propagate through the formation).

Baumgärtner and Zoback (1983) did a series of fracturing tests in crystalline rock that demonstrate that closure pressure is not necessarily equal to the least principal stress. In the tests, packers were used to isolate sections of the wellbore and fracturing was attempted at various intervals. The minimum principal stress was vertical. The initial shut-in pressure (ISIP) was interpreted from the time history of the wellbore pressure and defined as the pressure at which fracture closure appeared to occur. Because of the concentration of stress around the vertical wellbore, new tensile fractures sometimes formed axially along the wellbore, perpendicular to the minimum horizontal stress (the intermediate principal stress). Evidently, as these fractures propagated into the formation, they tended to rotate to be perpendicular to the minimum principal stress (which was vertical). When injection ended, fluid bled out of the vertical fractures near the wellbore into the horizontal fractures that formed away from the wellbore. The ISIP was identified from inflections in the wellbore pressure with time. The highest closure pressure was the closure pressure of the vertical fractures (at the minimum horizontal stress, σ_2), not the closure pressure of the horizontal fractures away from the wellbore

(which would be σ_3). Because of this, Baumgärtner and Zoback (1983) interpreted the ISIP in these cases to be equal to the minimum horizontal stress, σ_2, not the minimum principal stress.

The interpretation that the closure pressure was above σ_3 could be independently confirmed because the vertical principal stress can be found by integrating the density of the overlying rock. For example, Figure 3 in Baumgärtner and Zoback (1983) shows that the ISIP (wellhead) during a test at depth of 837 m was around 19 MPa. Hydrostatic head was around 8.37 MPa, and so the minimum horizontal stress (the sum of hydrostatic head and ISIP at the wellhead) was 27.4 MPa (given in Figure 2 of Baumgärtner and Zoback, 1983). The average rock density was given as 2.61 g/cm^3, which would give a value of σ_v equal to 21.85 MPa at 837 m (Figure 2 in the paper gives a value of 21.3 MPa). Clearly, in this case, ISIP was significantly greater than σ_3. In both Brown (1989) and Baumgärtner and Zoback (1983), ISIP was much greater than the least principal stress because the fractures connecting to the wellbore were not perpendicular to the least principal stress.

Another potential issue is that ISIP may not be equal to closure pressure. In settings with high matrix permeability or significant leakoff to the natural fracture network, fluid flows out of the newly formed tensile fractures after the end of injection, allowing them to close. However, if leakoff is limited, fracture closure may not occur with shut-in (as in Simulations A, E, and F).

If fracture closure does not occur shortly after shut-in, the error in setting ISIP equal to the least principal stress depends on the effective fracture toughness. For typical laboratory derived fracture toughness, fractures of significant size can propagate with fluid pressure only slightly above σ_3. For example, for a value of a equal to 20 m and K_I equal to 3.0 MPa-m$^{1/2}$, Equation 3-14 predicts that a fracture would propagate at fluid pressure only 0.38 MPa above the least principal stress. If the fracture propagation pressure is only slightly greater than the least principal stress, ISIP will be close to σ_3 (assuming closure is related to optimally oriented fractures) even if fracture closure does not occur with shut-in.

However, non-ideal fracture propagation, fracture termination at preexisting fractures, or stress heterogeneity may cause effective fracture toughness to be greater than the laboratory derived values (Shlyapobersky, 1985). For example, in Simulation F, ISIP was around 3.5 MPa greater than the least principal stress (Figure 3-25). In this case, the ISIP could be significantly higher than the least principal stress if the fracture remains open after shut-in.

Sometimes, the decline in pressure after shut-in is interpreted to infer to closure pressure, but such methods typically require the assumption of significant fluid leakoff into the matrix and simple, planar fracture geometry (Nolte, 1979; Gulrajani and Nolte, 2000), assumptions that do not necessarily hold in EGS or gas shale.

The initiation of shear stimulation could be mistaken for the initiation of tensile fracturing and lead to underestimation of the least principal stress. This was also proposed by Couzens-Schultz and Chan (2010), who gave two field examples of leakoff tests that they hypothesized had given incorrect values for σ_3. This process was also discussed by McClure and Horne (2010b) and is discussed in Section 4.4.6.

Step rate tests are sometimes used to identify σ_3. In step rate tests, injection rate is increased in steps. The theory is that when BHP reaches σ_3, tensile fracturing will be initiated and injection pressure will demonstrate a near insensitivity to further increases in rate. In fact, this behavior can be seen in Simulations A, C, E, and F. However, near insensitivity of injection pressure to injection rate could be plausibly explained by the process of shear stimulation alone, without requiring new fractures to propagate through the formation, or for fluid pressure to reach σ_3 (also discussed in Section 4.4.6). During Simulation B, the injection pressure was modestly insensitive to increases in injection rate. Injection at 30 kg/s caused an increase in fluid pressure from 35 MPa to around 45 MPa. Subsequent doubling and tripling of the injection rate caused increases in fluid pressure of only a few MPa.

Simulation I was performed to demonstrate the effect of shear stimulation in a step rate test. Simulation I used an identical fracture network as Simulation B, but used a different injection schedule. A plot of injection rate versus the bottom hole pressure at the end of the injection period is shown in Figure 3-37. From Figure 3-37, a standard

step rate test interpretation would be that σ_3 was around 43 MPa. In fact, σ_3 was 50 MPa in Simulation I.
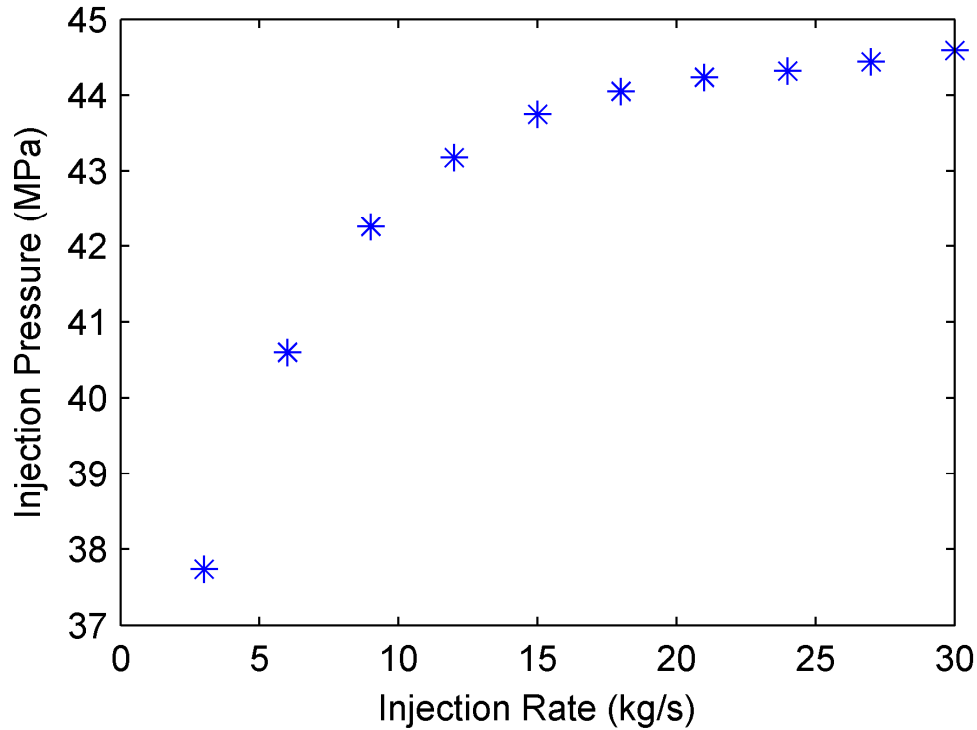
Figure 3-37: Bottom hole pressure during injection versus rate during Simulation I. The plot shows the initiation of shear stimulation at around 43 MPa, a behavior that could be mistaken for tensile fracturing at σ_3.

Sometimes, identification of a "Leakoff Point" (Gaarenstroom et al., 1993) is used to identify σ_3. In this method, an abrupt decrease in the rate of injection pressure increase with time signals the initiation of tensile fracturing at σ_3. However, the initiation of shear stimulation could create an apparent leakoff point that would be misinterpreted.

As discussed in Section 6.1.2, shear stimulation is probably the reason why the down hole pressure during the stimulation of GPK2 at Soultz was significantly below the least principal stress as estimated by Valley and Evans (2007) (which itself may be an underestimation of the least principal stress, see Section 4.4.6), yet the injection pressure become almost insensitive to increases in injection rate (Weidler et al., 2002).

To summarize, many standard methods for estimation of σ_3 rely on assumptions that may not be valid in settings other than simple, POM stimulation. Shear stimulation may create pressure behavior that appears similar to tensile fracturing (causing an

underestimation of σ_3 with step rate tests and leakoff tests). Poorly oriented fractures in the MMS mechanism can cause "closure pressure" (equivalent to ISIP) to be significantly greater than σ_3 (causing overestimation of σ_3). ISIP may be greater than σ_3 if fracture closure does not happen immediately after shut-in and the effective fracture toughness is high.

3.4.8 Testing a Formation's Tendency for Shear Stimulation

Whether a formation is capable of being shear stimulated is an important factor in determining mechanism. In this chapter, the ability of a formation to be shear stimulated is referred to as TSS, or Tendency for Shear Stimulation. TSS is important because if a formation cannot be effectively shear stimulated, the PSS and PFSSL mechanisms are impossible. If a formation has high TSS, the PFSSL and PSS mechanisms are more likely, though the MMS mechanism cannot not be ruled out.

The TSS test is needed to resolve the ambiguity of interpretation between MSS and PFSSL. These mechanisms may have similar microseismic signatures (Section 3.4.9), and it is unclear how pressure transients could be used to differentiate. The TSS test is an unambiguous technique to differentiate between the two mechanisms.

TSS depends on several factors, including whether fracture slip couples to an increase in transmissivity, whether there are fractures that are well oriented to slip in the local stress state, whether the initial fracture transmissivity is high enough (to allow slip to initiate, as in Simulation C), and whether the network of shear stimulating fractures percolates. As discussed in Section 3.1.3, percolation refers to the presence of continuous fracture pathways for flow through the reservoir.

One way to determine TSS would be to measure the various parameters that affect it, and then attempt to integrate those measurements into an assessment of TSS. However, these parameters may not always be known with high precision.

As an alternative, we propose that TSS could be measured directly in a "TSS test." A TSS test would be performed by injecting at a BHP below the least principal stress into an uncased section of wellbore that has sufficient length to access a significant number of

natural fractures.   The injection pressure would be maintained relatively close to σ_3 without exceeding it.   As long as fluid pressure was below σ_3, PSS would be the only possible mechanism of stimulation, which is important to ensure that there is no ambiguity of interpretation.

During a TSS test, microseismic monitoring could be used to estimate the distance of deformation and transmissivity enhancement from the wellbore. Well injectivity would be measured prior to the TSS test and after the TSS test.   Limited spreading of microseismicity and/or limited increase in injectivity would indicate that the formation has low TSS.

Due to cost and the requirement that the section of the wellbore must be uncased, it would not be feasible to perform TSS tests routinely.   However, as a part of a large drilling program, it would be reasonable to perform TSS tests in a small number of wells and apply the results in the rest of the field.   Methodologies to predict TSS based on geological conditions and geophysical measurements could be validated using TSS tests.

Simulations G and H were examples of TSS tests.   Simulations G and H were identical, except that they used different fracture networks, F5 and F4. Networks F4 and F5 would appear similar on a wellbore image log because they had identical statistical distributions of orientation and an equal number of fractures intersected the wellbore in both networks.   The difference between the two networks was that F5 had a shorter average fracture size (and more total fractures) and was not percolating.

Injection was performed at constant pressure (below σ_3) for one week. Figure 3-28 and Figure 3-29 show the final distributions of transmissivity. Figure 3-42 and Figure 3-43 show approximations of the microseismicity maps that would have resulted from these stimulations (the microseismicity maps are explained in Section 3.4.9).

The shear stimulation spread much further in Simulation H, and consequently the fracture network had a much greater TSS. In Simulation G, the TSS test unambiguously showed that the PSS and PFSSL mechanisms could not be effective at stimulating the reservoir. If a conventional hydraulic stimulation was subsequently performed and a high flow rate resulted, the MMS mechanism could be positively identified.

As a caveat for microseismic interpretation, it is important to keep in mind that in some settings, such as gas shale, the vast majority of fracture deformation is aseismic (Zoback et al., 2012), and the precise mechanism of microseismicity generation is not fully understood. In these settings, it is possible that variations of formation properties could lead to variations in the tendency for deformation to cause microseismicity. Therefore, limited spreading of microseismicity in a formation might be a consequence of aseismic slip, rather than lack of stimulation. In this case, measurement of well injectivity/productivity before and after the TSS test would be the most important ways to measure the outcome of the TSS test.

3.4.9 Microseismicity

In this section, it is shown how relocations of microseismicity have some usefulness for identifying mechanism but that their value is limited to a few specific applications. The simulator used in this chapter has the ability to directly model seismicity by including abrupt weakening of friction on individual fractures (Section 2.2.5.3 and Chapter 4). However, in this chapter, the coefficient of friction was assumed constant, and so slip in the simulations was aseismic. Because direct seismicity simulations were not performed, a simple correlation was used in this section to extract maps of microseismicity hypocenters from the results of the simulations. The objective of this process was to extract approximate maps of what the microseismic data might look like for the various simulations. Microseismicity hypocenter maps were created from Simulations A, B, E, F, G, and H.

At the end of a simulation, elements were identified that had either opened or slipped during the stimulation. Each element that had opened or slipped was randomly assigned a certain number of microseismic events according to the Poisson distribution, with a specified average number of events per length of fracture. The events were located at the center of the element, and then normally distributed random error was added to approximate the effect of relocation error.

Microseismicity maps for Simulations A, B, E, F, G, and H are shown from Figure 3-38 to Figure 3-43.
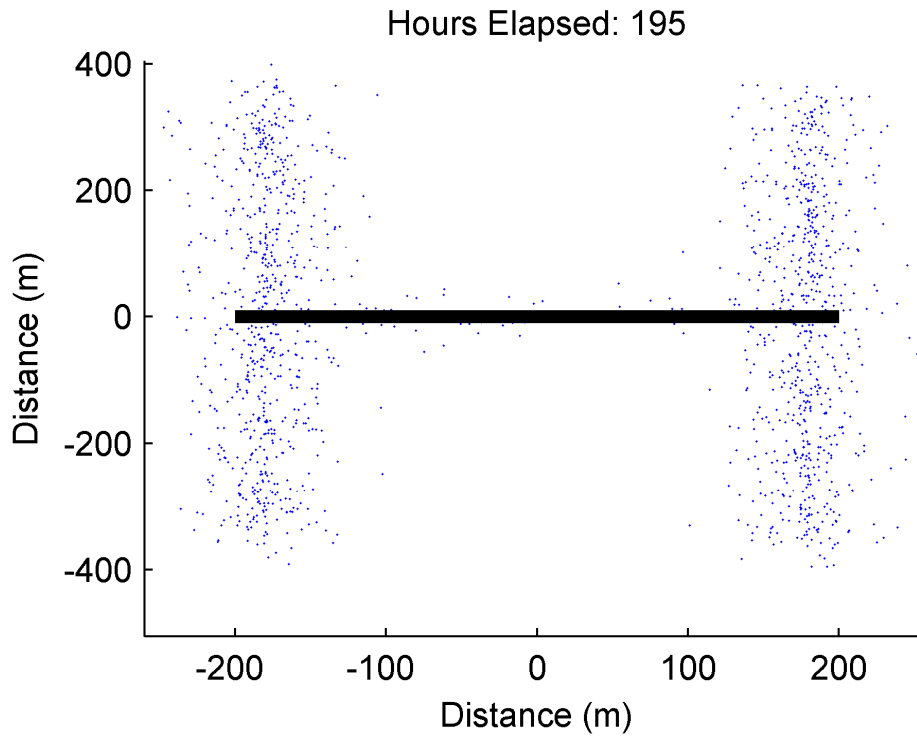
Figure 3-38: Simulated microseismicity hypocenter map for Simulation A. Microseismicity was not directly simulated because the coefficient of friction was assumed constant (Section 3.2.1). The simulated microseismic maps were generated using a simple correlation.
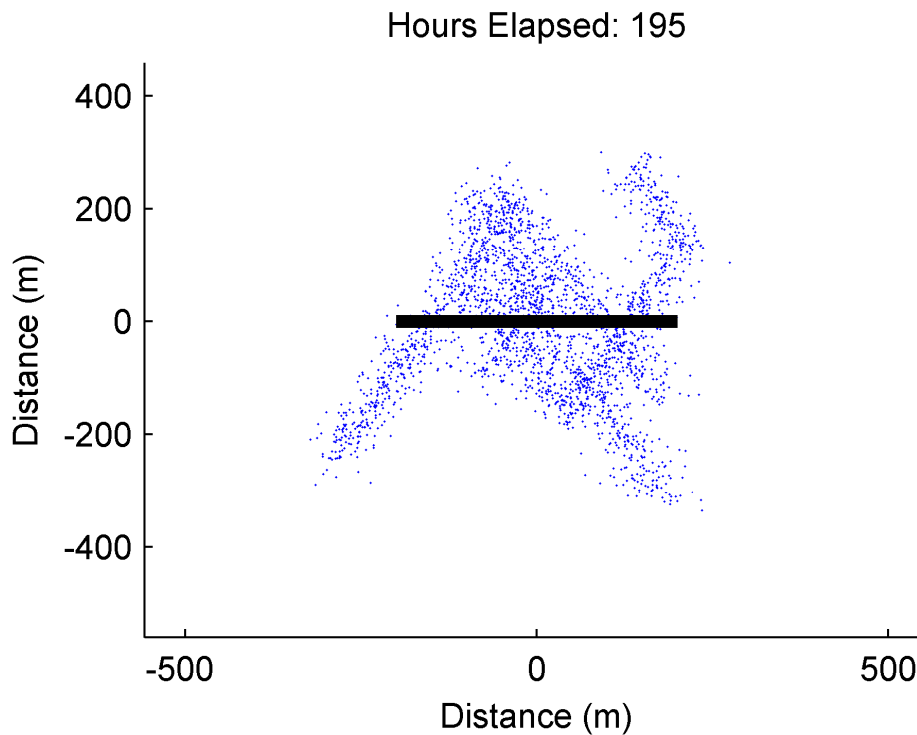
Figure 3-39: Simulated microseismicity hypocenter map for Simulation B. Microseismicity was not directly simulated because the coefficient of friction was assumed constant (Section 3.2.1). The simulated microseismic maps were generated using a simple correlation.
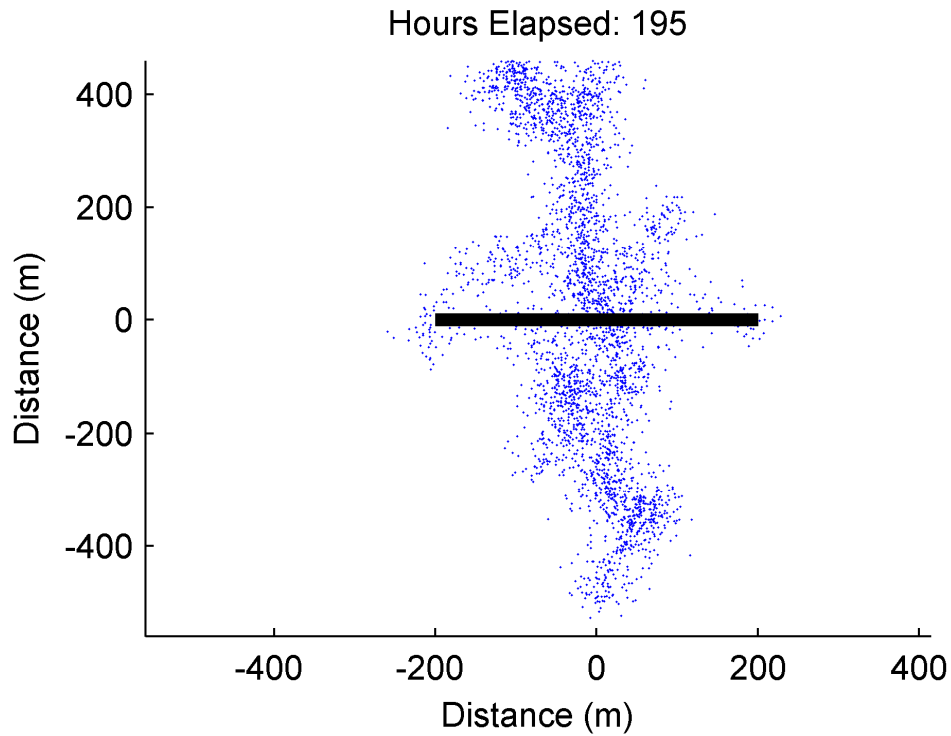
Figure 3-40: Simulated microseismicity hypocenter map for Simulation E. Microseismicity was not directly simulated because the coefficient of friction was assumed constant (Section 3.2.1). The simulated microseismic maps were generated using a simple correlation.
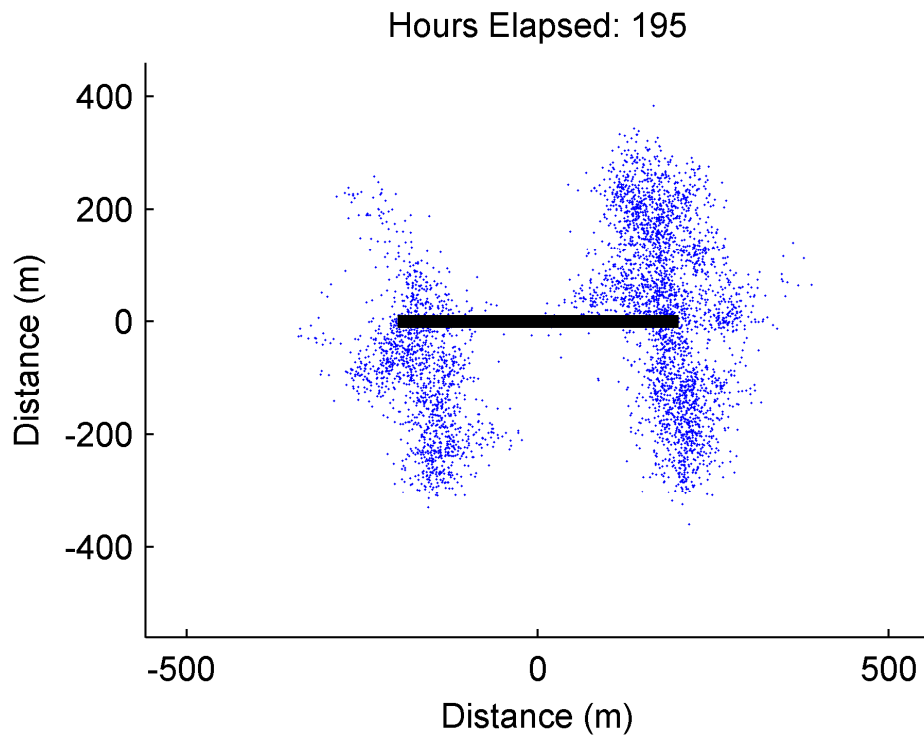
Figure 3-41: Simulated microseismicity hypocenter map for Simulation F. Microseismicity was not directly simulated because the coefficient of friction was assumed constant (Section 3.2.1). The simulated microseismic maps were generated using a simple correlation.
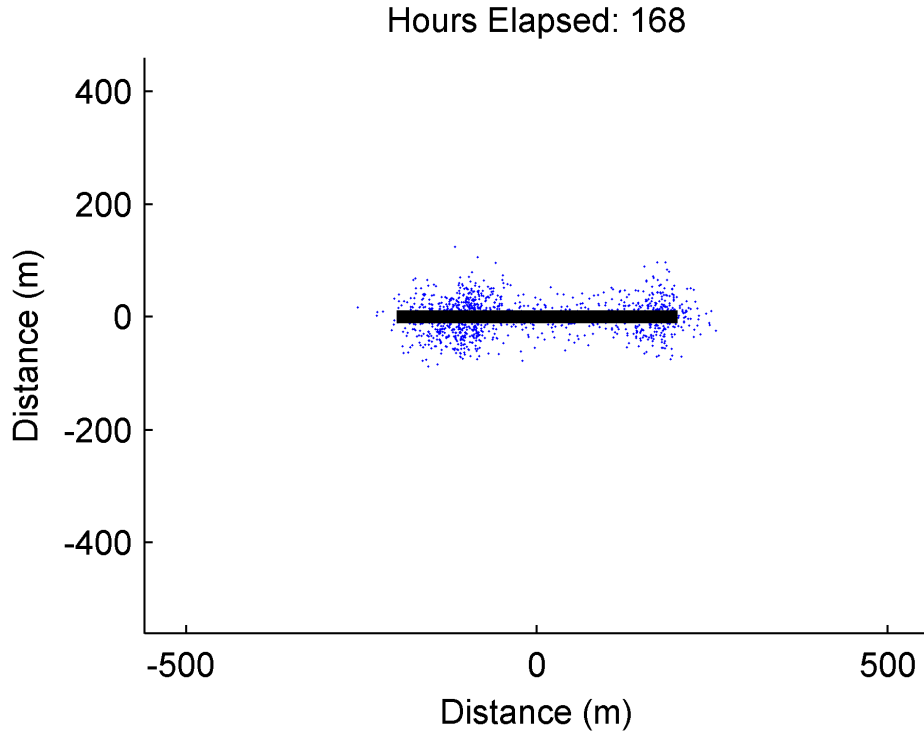
Figure 3-42: Simulated microseismicity hypocenter map for Simulation G. Microseismicity was not directly simulated because the coefficient of friction was assumed constant (Section 3.2.1). The simulated microseismic maps were generated using a simple correlation.
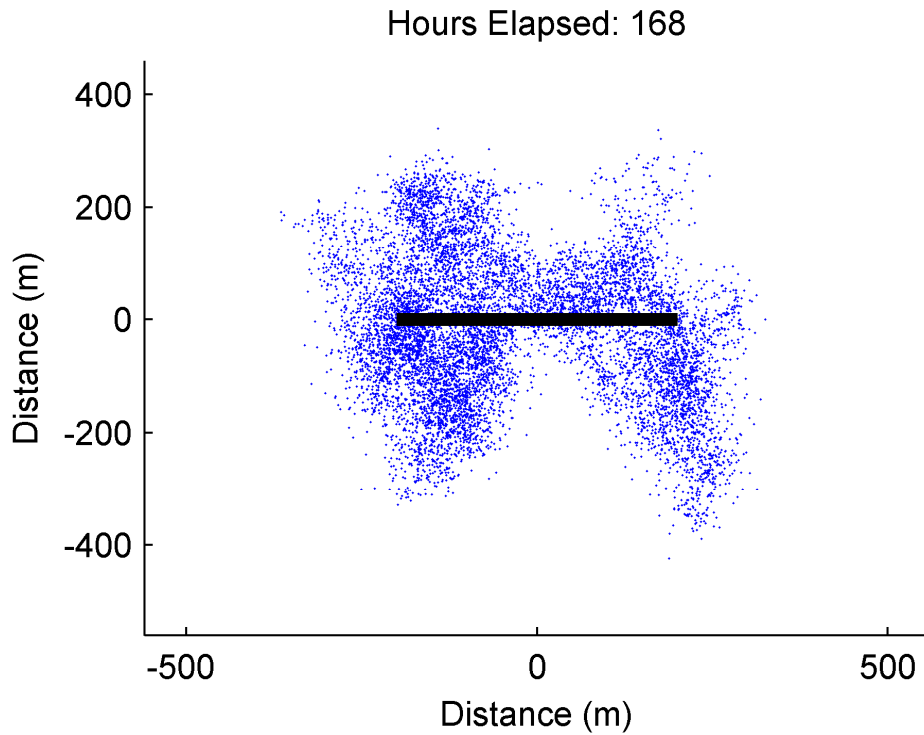
Figure 3-43: Simulated microseismicity hypocenter map for Simulation H. Microseismicity was not directly simulated because the coefficient of friction was assumed constant (Section 3.2.1). The simulated microseismic maps were generated using a simple correlation.

The microseismicity maps for Simulations A, E, and F appear to show large clouds of microseismicity propagating away from the wellbore in a direction perpendicular to the least principal stress. These maps could not be used to distinguish between the POM, MMS, and PFSSL mechanisms.

The microseismicity map for Simulation B looks significantly different, with large linear features that are clearly not oriented in the direction of the least principal stress. Microseismicity relocations like this could be used to identify induced slip on large faults (a field example is described in Downie et al, 2010). This suggests that PSS may be distinguishable from microseismic relocations. However, the microseismic map from Simulation H, another example of PSS, is significantly more ambiguous, and could be consistent with any mechanism. Furthermore, a large fault may be reactivated by injection, but this would not rule out that propagation of new fractures occurred during the stimulation.

Comparison between Figure 3-42 and Figure 3-43 shows that microseismic relocations could be useful for TSS tests.

3.4.10   Wellbore Logs

Wellbore image logs and spinner logs run before and after stimulation could be useful in diagnosing mechanism. The advantage of well logs is that they directly observe fracturing and fluid flow in the subsurface.

One application of wellbore image logs is to determine whether preexisting fractures intersecting the wellbore are only cracks or are thicker damage zones (Genter et al., 1997). Sections 3.4.2.3 and 3.1.3.2 discuss how the storativity of fractures affects stimulation mechanism. The PSS mechanism requires that all injected fluid must be stored in closed fractures and is more likely if there are thick fault zones present.

Wellbore image logs can also be used to observe directly whether new opening mode fractures formed at the wellbore during stimulation. A complication is that drilling induced tensile fractures may form locally at the wellbore but not propagate into the formation. If flow is distributed into a large tensile fracture propagating away from the

wellbore, spinner logs should indicate that outflow from the wellbore is distributed along the length of the newly formed axial fracture, not localized to preexisting fractures. If newly formed tensile fractures are not observed at the wellbore, then the POM and PFSSL mechanisms can be ruled out. If newly formed tensile fractures are observed and spinner logs indicate that flow is distributed (indicating that the newly formed tensile fractures at the wellbore are propagating into the formation), then the PSS mechanism can be ruled out.

Wellbore image logs (or better still, cores) could be especially useful if the fracture stimulation from one well reached a neighboring well. For example, a well could be drilled through the seismic cloud formed by the stimulation of another well. Even better, two wells could be drilled in close proximity and logged with spinner logs and image logs prior to stimulation. Then, one of the wells could be stimulated, and under the right conditions, the neighboring well would be in the region of fracture stimulation (which could be confirmed from microseismicity). Spinner and image logs could then be rerun in both wells. The distribution of newly formed fractures and stimulated natural fractures in the neighboring well would be very useful for identifying the mechanism of stimulation because it would be a direct observation of the fracturing process away from the injection well. If newly formed fractures were observed at the neighboring well, the PSS mechanism could be ruled out. If one large fracture was observed, and several surrounding preexisting fractures had enhanced transmissivity, then the PFSSL mechanism could be identified. If the stimulation was distributed across a significant length of the wellbore in both new and preexisting fractures, then the MMS mechanism could be identified. If newly formed fractures were not observed at the neighboring well, then the PSS mechanism could be considered more likely, but not ruled out because new fractures may have formed closer to the injection well.

3.4.11   Summary of Methods to Diagnose Stimulation Mechanism

Table 3-5 shows a summary of the various observations that could be used to diagnose stimulation mechanism. Observations can be used to either identify or rule out various hypotheses.

Table 3-5: Reservoir scale observations that are diagnostic of stimulation mechanism.

	POM	PSS	MMS	PFSSL
Injection pressure less than σ_3 (Section 3.4.5)	No	Yes*	No	No
Fracture closure pressure much greater than σ_3 (Section 3.4.6)	No	No	Yes	No
Low TSS (Section 3.4.8)		No		Discourages
High TSS (Section 3.4.8)	No			
No newly formed tensile fractures at the wellbore (if wellbore is uncased) (Section 3.4.10)	No			No
*If $P_{inj} > \sigma_3$, then PSS should be ruled out unless BHP relatively quickly drops below σ_3 during shut-in. **Various wellbore observations at neighboring wells could potentially be used to identify mechanism, as discussed in Section 3.4.10				

If injection pressure is below σ_3 during stimulation, PSS is the only possible mechanism. If injection pressure is above σ_3, PSS may still be the mechanism if tensile fracturing plays a minor role. However, if fluid pressure remains above σ_3 during shut-in, then fractures remain open in the formation, implying that fracture opening has played a hydraulically significant role, and PSS should be ruled out (Section 3.4.5).

If injection pressure is above σ_3 during stimulation, then it should be assumed that fracture opening (either new or preexisting fractures) is occurring in the formation (Section 3.4.5). If injection pressure remains above σ_3 during shut-in, fractures remain

open in the formation. If injection pressure drops below σ_3 during shut-in, fractures have closed in the formation, which implies that the natural fracture network has sufficient storativity to contain all injected fluid. In that case, the natural fracture network must either contain thick, porous fault zones, closely spaced cracks, or cracks that somehow have an elevated storativity above their typical laboratory values (Section 3.4.6).

If fluid pressure remains above σ_3 during shut-in, fracture closure may be identified during production. Fracture closure would manifest itself as an abrupt drop in transmissivity of the closing fractures and would lead to a rapid drop in production rate and/or pressure (though not necessarily as abrupt as in the simulations in this chapter).

In the MMS mechanism, natural fractures open, and depending on their orientation in the stress state, they may close at a pressure well above the least principal stress (the Brown, 1989 mechanism). If this was identified, it should be taken as a clear indication of the MMS mechanism. Newly formed fractures are expected to form perpendicular to the least principal stress, and so in a setting where only newly formed fractures are open, fracture closure would be expected at fluid pressure close to the least principal stress. Closure of newly formed fractures could be observed for the MMS, POM, or PFSSL mechanisms (Section 3.4.6).

A Tendency for Shear Stimulation (TSS) test could be used to distinguish between POM, MMS, and PFSSL mechanisms. If a formation has high TSS, then the POM mechanism is not possible because by definition POM occurs when there is negligible shear stimulation. If a formation has low TSS, the PFSSL mechanism could be possible but it would have limited effectiveness. The MMS mechanism can be effective with high or low TSS (Section 3.4.8).

If TSS is high, either the MMS and PFSSL mechanisms are possible. In either case, if TSS is high, then a significant amount of fluid leakoff from open fractures into a surrounding shear stimulating zone would be expected. The difference between MMS and PFSSL in this case would be the continuity of the opening mode tensile fractures. The PFSSL mechanism would involve formation of large, continuous tensile fractures. The MMS mechanism would involve formation of flow pathways that alternate between natural and newly formed fractures. An MMS tensile fracturing mechanism with

significant leakoff into a shear stimulation zone might be considered almost a hybrid MMS-PFSSL mechanism. We have not identified a diagnostic method that could distinguish between MMS and PFSSL with high TSS (Section 3.4.8).

Low fluid recovery is consistent with the PSS, PFSSL, and MMS mechanisms (assuming initial formation permeability is very low). In any of these mechanisms, low fluid recovery could be caused by leakoff into a shear stimulated natural fracture region. In MMS, snapoff due to fracture closure is an additional possible cause of low fluid recovery (Section 3.4.6). The POM mechanism is not consistent with low fluid recovery (as long as initial formation permeability is very low).

If a wellbore is uncased, then wellbore image logs can be used following stimulation. If newly formed tensile fractures are not visible on the wellbore, then fluid must have excited the wellbore from natural fractures, and the POM and PFSSL mechanisms can be ruled out (Section 3.4.10).

All four mechanisms are capable of leading to clouds of microseismicity that are oriented roughly in the direction perpendicular to the least principal stress. However, if large lineaments in microseismicity are identified in a direction that is not perpendicular to the least principal stress, this may indicate that slip is being induced on large faults. Microseismicity can also be helpful in the interpretation of a TSS test (Section 3.4.9).

The POM mechanism is typically presumed not involve complex fracture network propagation. Therefore, information that suggests significant fracture network complexity might be taken as evidence that the POM is not taking place. Such evidence could include high well productivity in gas shale, or a wide fairway of microseismicity (relative to relocation error).

3.5 Conclusions

Four mechanisms for hydraulic stimulation have been described: pure opening mode (POM), pure shear stimulation (PSS), mixed-mechanism stimulation (MMS), and primary fracturing with shear stimulation leakoff (PFSSL). These mechanisms are not intended to cover all possible mechanism and should be considered limiting cases.

Nevertheless, these concepts are useful in describing and modeling the processes taking place during hydraulic stimulation.

A review of literature was performed to identify geological parameters that may affect stimulation mechanism (Section 3.1.3). Computational models were created that were representative of the four stimulation mechanisms (Sections 3.2.2 and 3.3).

Results confirmed that in a toughness dominated propagation regime in POM, localization of stimulation takes place into one or two fractures (Section 3.4.1). For shear stimulation, it was shown that if initial transmissivity is too low, shear stimulation will be delayed or prevented (Section 3.4.2.2). It was shown that the assumption that fluid is stored in closed cracks (with aperture of hundreds of microns) leads to unusual results related to fluid storage. Either the fractures must be very closely spaced, occupy a very large spatial extent, or have low transmissivity (Section 3.4.2.3). An alternative possibility is that fracture storativity could be supplied by fracture opening. This could explain how fluid is contained in settings with very thin cracks and very low matrix permeability (Sections 3.4.2.3 and 3.4.3), but it would rule out the PSS mechanism.

The crack-like shear stimulation mechanism (CSS) was identified as a process that allows shear stimulation to progress along a fracture at a rate insensitive to the initial fracture transmissivity. The overall rate of shear stimulation propagation depends on the two processes: fluid flow into fractures at the initial transmissivity (to initiate slip on each fracture for the first time) and CSS propagation of stimulation along the fracture once slip has been initiated.

The Brown (1989) snapoff mechanism for fluid trapping was demonstrated as an explanation for poor fluid recovery. Another cause for poor fluid recovery was found to be leakoff into natural fractures (Section 3.4.6).

It was found that the PFSSL mechanism can only take place within a rather narrow range of natural fracture transmissivity. However, this result requires more study because it may have been a result of model limitations that restrict the freedom of newly forming fractures to initiate and propagate in any direction (Section 3.4.4).

A variety of techniques for identifying stimulation mechanism were proposed (summarized in Section 3.4.11). The PSS mechanism can be diagnosed if the injection pressure remains below σ_3 during injection. In contrast, if fluid pressure remains above σ_3 during shut-in, fractures remain open in the reservoir, indicating the POM, MMS, or PFSSL mechanisms (Sections 3.4.5 and 3.4.6).

A Tendency for Shear Stimulation (TSS) test was proposed as a way to directly measure whether shear stimulation is possible in a formation. With low TSS, the PSS mechanism can be ruled out, and the PFSSL mechanism is unfavorable. With high TSS, the POM mechanism can be ruled out (Section 3.4.8). Wellbore image log observations after stimulation could be used to identify if newly formed tensile fractures have formed at the wellbore. If they have not, the POM and PFSSL mechanisms can be ruled out (Section 3.4.11). Wellbore image logs through the zone of stimulation are rarely available, but if they were, they would be extremely valuable for identifying mechanism (Section 3.4.11).

Microseismic relocations were shown to be useful for TSS tests and for identifying shear stimulation along large faults that are not oriented perpendicular to the least principal stress. However, microseismic relocations could not distinguish between most mechanisms because all lead to a roughly planar region of microseismicity oriented perpendicular to the least principal stress (Section 3.4.9).

It was discussed how low matrix permeability and shear stimulation could lead to errors in estimating the least principal stress. The initiation of shear stimulation could be mistaken for the initiation of tensile fracturing in step rate tests and in identification of a leakoff point (also discussed in McClure and Horne, 2010b; Section 4.4.6; and Couzens-Schultz and Chan, 2010). If fracture closure does not take place immediately at shut-in (due to low matrix permeability) and there is a high effective fracture toughness, the ISIP will be above the least principal stress. As described by Brown (1989), in the MMS mechanism, fracture closure pressure could be greater than the least principal stress (Section 3.4.7) if poorly oriented natural fractures are opened by fluid injection.

PSS is generally assumed to be the predominant mechanism in EGS (Section 3.1.1). However, there are several specific geological conditions that must be in place for PSS to

occur (Sections 3.1.3, 3.4.2.2, and 3.4.2.3). Therefore, it cannot be assumed in advance that stimulation will occur through the PSS mechanism. If newly formed fractures are not observed in the wellbore following stimulation, the mechanism could be PSS or MMS.

Determining the correct conceptual model for hydraulic stimulation is critical for stimulation modeling, optimization, and reservoir evaluation. This chapter describes four hypotheses for stimulation mechanism and describes how they may be determined in practice. At a given site, establishing the correct conceptual model should be considered a fundamental requirement for successful application of modeling and reservoir engineering.

Chapter 4

4 Investigation of Injection-Induced Seismicity using a Coupled Fluid Flow and Rate/State Friction Model

This chapter describes a numerical investigation of seismicity induced by injection into a single isolated fracture. Injection into a single isolated fracture is a simple analog for hydraulic stimulation in certain EGS projects: settings where water is injected into large scale fracture zones in low matrix permeability rock. A model was developed and used that couples (1) fluid flow, (2) rate and state friction, (3) coupling of slip, fluid pressure, and transmissivity, and (4) mechanical stress interaction between fracture elements. The interaction of these processes causes stimulation to propagate according to a mechanism we refer to as episodic crack-like shear stimulation (ECSS). The results suggest that shear stimulation could propagate at a rate insensitive to the initial fracture transmissivity (also discussed in Section 3.4.2.2). Results suggest that the initiation of shear stimulation could be mistaken for tensile fracturing, causing an underestimation of the minimum principal stress (also discussed in Section 3.4.7). We investigated the effect of injection pressure on induced seismicity. For injection at constant pressure, there was

not a significant dependence of maximum event magnitude on injection pressure, but there were more relatively large events for higher injection pressure. Decreasing injection pressure over time significantly reduced the maximum event magnitude. Significant seismicity occurred after shut-in, which was consistent with observations from EGS stimulations. Production of fluid from the well immediately after injection inhibited shut-in seismic events. The results of the model in this study were found to be broadly consistent with results from prior work using a simpler treatment of friction that we refer to as static/dynamic. We investigated the effect of shear-induced pore volume dilation and the rate and state characteristic length scale, d_c. Shear-induced pore dilation resulted in a larger number of lower magnitude events. A larger value of d_c caused slip to occur aseismically.

4.1 Introduction

4.1.1 Overview

An important challenge for the deployment of EGS is that shear stimulation sometimes causes low magnitude seismic events that can be felt at the surface (Majer et al., 2007). Induced seismicity threatens public acceptance of EGS, and the possibility of triggering a truly damaging seismic event, while seemingly remote, deserves careful consideration. In 2005 one of the largest seismic events ever associated with an EGS project, a magnitude 3.4, occurred following the hydraulic stimulation of an EGS well in Basel, Switzerland. As a result the project was suspended and eventually cancelled (Häring et al., 2007; Majer et al., 2007). Events strong enough to be felt at the surface have occurred during stimulations at several other EGS projects, including at Soultz-sous-Forêts, France, magnitude 2.9, and Cooper Basin, Australia, magnitude 3.7 (Majer et al., 2007).

There is a practical need for credible shear stimulation modeling, because shear stimulation directly impacts induced seismicity, well productivity, and the long term temperature decline of the system. Shear stimulation and induced seismicity modeling

have applications in areas outside of EGS, including gas shale hydraulic fracturing and carbon dioxide sequestration.

Shear stimulation models typically include (1) stochastic or deterministic generation of a preexisting fracture network, (2) simulation of fluid flow in the network, and (3) modeling of induced slip (Willis-Richards et al., 1996; Rahman et al., 2002; Ghassemi and Tarasovs, 2006; Kohl and Mégel, 2007; Bruel, 2007; Baisch et al., 2010; Rachez and Gentier, 2010; Deng et al., 2011).

Significant issues remain in the development of shear stimulation modeling. The complexity of the physical processes taking place and the uncertainty and incompleteness of the data forces modelers to make significant simplifying assumptions. Two physical phenomena that are frequently subject to simplifying assumptions are fracture friction and stresses induced by fracture slip. A more detailed discussion of these topics can be found in Section 4.1.3

A goal of the shear stimulation modeling described in this chapter was to focus on realistic treatment of friction and induced stresses. Rate and state theory was used to describe fracture friction. Rate and state friction is based on laboratory observations of rock friction and has been successful in describing a variety of earthquake phenomena (Dieterich, 2007; Segall, 2010). Stress interaction was calculated using the Crouch and Starfield (1983) boundary element method which assumes that the rock material is homogenous, isotropic, and linearly elastic. These assumptions are reasonable for EGS reservoirs that are located in fractured granite.

Injection into a single, isolated, one-dimensional fracture was modeled. The problem geometry was simple, but it was a reasonable analog for injection into faulted granite such as is found at the EGS project at Soultz-sous-Forêts, France. At Soultz, observations suggested that flow and seismicity was confined to a small number of large scale faults. A more detailed discussion can be found in Section 4.1.4. In certain other EGS projects, injection into large scale fault zones is probably not an appropriate conceptual model, and so the results from this paper may be less applicable. However, as shown in Chapter 5, the EGS projects with large fault zones have been the projects where induced seismicity has been most significant.

4.1.2 Summary of Results

Major results of this chapter are summarized in this section. Many of the results were consistent with what has been described by other studies in the literature. There were several results that are novel and could have important practical implications.

The mechanism of growth of the stimulated region was a two-part cycle. The cycle began with a seismic event that spread slip and permeability enhancement into a region of the fracture where slip had not previously occurred and where there was low permeability and fluid pressure. The second part of the cycle was flow of water into the newly slipped patch of fracture, which eventually triggered the next seismic event. We refer to this process as episodic crack-like shear stimulation (ECSS). In modeling without frictional weakening (and seismic events), shear stimulation propagates along a fracture in a similar mechanism, but the propagation is smooth rather than episodic, referred to as smooth crack-like shear stimulation, SCSS (Section 3.4.2.2). In general, we refer to propagation of shear stimulation down a fracture (assisted by stress transfer) as crack-like shear stimulation, CSS (Section 3.4.2.2).

The CSS mechanism is distinctly different from a process that has been described in the literature in which pressure diffuses into unstimulated fracture regions, subsequently causing slip (Bruel, 2007; Shapiro et al., 1999). We refer to this process as the "diffusion controlled" (DC) mechanism.

The difference is that in the DC mechanism, slip follows fluid flow. In the CSS mechanism, fluid flow follows slip. CSS behavior will only occur in a model if stress interaction between elements is included, but CSS behavior is not unique to rate and state friction models. For example, ECSS behavior was described in McClure and Horne (2010b) using static/dynamic friction (described in Section 4.1.3), and SCSS behavior was observed in the simulations described in Section 3.4.2.2.

If the CSS, not the DC, mechanism controls the growth of the stimulated region, it would undermine several common assumptions. In the literature, unstimulated hydraulic diffusivity has been estimated using the assumption that it controls the rate of growth of the stimulated region during injection (Shapiro et al., 1999; Bruel, 2007). In the CSS

mechanism, the rate of growth of the stimulated region during injection does not depend on the unstimulated diffusivity.

The CSS mechanism could explain why injection pressure tends to increase only slightly when injection rate is increased during shear stimulation. Previously, such behavior has been interpreted as being caused by the opening of tensile fractures at a pore pressure equal to the least principal stress (Cornet and Bérard, 2003; Valley and Evans, 2007; Cornet et al., 2007). The CSS mechanism provides an alternative explanation that does not involve the propagation of opening mode tensile fractures and does not require the pore pressure to be equal to the least principal stress. The least principal stress would be underestimated if it was assumed incorrectly to be equal to the pore pressure during injection. This topic is discussed from the point of view of step rate tests in Section 3.4.7.

In the model, spreading and redistribution of pressure after the end of injection caused shut-in seismicity, a commonly observed phenomenon in which seismic events of significant magnitude continue to occur at the edge of the stimulated region after shut-in (Häring et al., 2007; Asanuma et al., 2006; Baisch et al., 2010). Redistribution of pressure has also been proposed as a mechanism for shut-in events by Baisch et al. (2006), Healy et al. (1968), and Hsieh and Bredehoeft (1981).

We investigated strategies to minimize induced seismicity. Reducing injection pressure over time reduced the maximum magnitude. With constant injection pressure over time, using a lower injection pressure led to fewer significant sized events but did not affect the maximum magnitude. Producing fluid back after injection reduced shut-in seismicity. Baisch et al. (2006) also suggested producing fluid could reduce shut-in events.

We investigated the effect of two geological uncertainties on the results, namely pore volume dilation during slip and the value of the rate and state characteristic length scale, d_c. A larger d_c caused slip to occur aseismically as opposed to seismically. Pore volume dilation caused slip to occur with a larger number of lower magnitude events. Both results were consistent with other studies in the literature (Ruina, 1983; Yamashita, 1999; Segall and Rice, 1995; Segall et al., 2010).

4.1.3 Seismicity Modeling in EGS

EGS modeling in the literature typically uses a treatment of friction in which elements do not slip until their shear stress exceeds their frictional ability to resist slip according to the Coulomb failure criterion:

$$| \tau | = S_0 + \mu_f (\sigma_n - P),$$ 4-1

where τ is shear stress, S_0 is a cohesion factor, μ_f is the coefficient of friction, σ_n is the normal stress, and P is the fluid pressure.

If μ_f is assumed constant (Kohl and Mégel, 2007; Ghassemi and Tarasovs, 2006; and Chapters 2 and 3), then slip is gradual and essentially aseismic because the only friction weakening mechanism is fluid flow.

Some recent modeling has implemented methods for abruptly weakening friction on slipping elements, as occurs in earthquakes. Bruel (2007) used a constant μ, but allowed S_0 to disappear when an element reached the slipping criterion. Baisch et al. (2010) imposed an instantaneous drop in stress on slipping elements. McClure and Horne (2010b) imposed an instantaneous (but subsequently recovered) drop in μ_f on slipping elements (also used in Chapter 2). In these approaches, slip occurs instantaneously and so is essentially seismic. We refer to the approach in McClure and Horne (2010b) as static/dynamic friction. All of these models are more generally in the class of "inherently discrete" earthquake models (Ben-Zion and Rice, 1993).

Rate and state friction has several advantages compared to other approaches. Constant friction approaches can model only aseismic slip, and abruptly weakening friction can only model seismic slip. Rate and state friction can model either seismic or aseismic clip. Rate and state friction simulation allows time to be discretized during slip, allowing slip velocity to evolve continuously, although potentially very rapidly.

A variety of approaches to stress transfer have been used in EGS modeling, including the block-spring model (Baisch et al., 2010), the distinct element model (Deng et al., 2011; Rachez and Gentier, 2010), the displacement discontinuity method (Ghassemi and Tarasovs, 2007) and neglecting stress transfer (Bruel, 2007; Kohl and Mégel, 2007). The

model in this chapter calculated stress transfer using the displacement discontinuity method (Crouch and Starfield, 1983). The displacement discontinuity method assumes linearly elastic deformation in an infinite, isotropic, homogenous medium.

4.1.4 Relationship of our Model to Actual EGS Reservoirs

Observations made during EGS projects demonstrate the context of the model used in this chapter. The European EGS project at Soultz-sous-Forêts can be used as an example of an EGS project. During the 1990s and 2000s several wells were drilled and stimulated hydraulically in faulted and fractured granite. During each stimulation, thousands of cubic meters of water were injected at high pressure into open wellbore. The injectivity of the wells increased by one to two orders of magnitude following stimulation (Hettkamp et al., 2004; Tischner et al., 2006; Genter et al., 2010).

Spinner and temperature logs of the Soultz wells indicated that during hydraulic stimulation, fluid exited the wellbore at a small number of preexisting fracture zones intersecting the wellbore. Caliper and wellbore imaging logs indicated that the newly permeable fractures had existed prior to stimulation but had been induced to shear, enhancing their permeability. In one example, 70% of flow during injection exited the wellbore GPK3 at a single location. (Evans, Genter, and Sausse, 2005; Evans, Moriya, et al., 2005; Baria et al., 2006; Tischner et al., 2006; Dezayes et al., 2010).

Wellbore core demonstrated that a typical fracture zone consisted of a fault core surrounded by an alteration zone up to 25 m thick. The fault cores were full of cataclasites, breccia, and secondary precipitation of quartz. The alterations zones had high fracture density and extensive chemical alteration leading to porosities as high as 25% (Genter et al., 2000).

The fault zones observed at Soultz could be considered more or less typical for medium to large scale faults in granite (Wibberley et al., 2008; Caine et al., 1996; Bruhn et al., 1994; Lockner et al., 2009). However, other fault zones geometries in granite have been described in the literature (Griffith et al., 2009).

In this chapter, injection into a single, isolated fracture 500 m long was modeled. While there may be a large number of fractures participating in flow at Soultz, they are located primarily in a small number of large scale fracture zones. The larger seismic events require a laterally extensive slip surface (Charlety et al., 2007) and so are likely associated with the fault core. The fracture in our model is intended to represent the fault core. Such a model cannot describe all of the smaller scale seismic events that occur on minor fractures, but it can describe slip on the large scale features.

One challenge for EGS modeling is how to specify the model storativity. Closed fractures in granite (which would be any fracture in frictional contact, and therefore capable of generating an earthquake) have apertures on the order of hundreds of microns (Esaki et al., 1999; Lee and Cho, 2002). A huge number of such fractures would be required to contain the thousands of cubic meters that are injected during EGS stimulation (also discussed in Sections 3.4.2.3 and 6.3). Because fluid typically exited the wellbore from a small number of fracture zones, a likely source of storativity is the high porosity, heavily fractured alteration zones that surround the fault cores.

In this chapter, we avoided any complexity associated with the details of fracture zone geometry. We modeled flow only in a single fracture. The storativity of the fracture was supplied by the increase in void aperture caused by increase in fluid pressure, which resulted in a decrease in effective normal stress (Equation 4-13). Void aperture values were on the order of 10^{-3} m, and so the fracture had quite limited volume and storativity.

Because the fracture storativity was low, it was necessary to use low flow rates, generally around 1 kg/s. During actual stimulations at Soultz, injection rates reached 50 kg/s or higher (Tischner et al., 2006).

4.2 Methods

4.2.1 Problem Definition

There are several differences between the numerical model used in this chapter and the model used in Chapters 2 and 3. A full description of the model used in this chapter is given in this section.

Our numerical model required solution of five equations for five primary variables. The variables were velocity (v), state (θ), mass of fluid in a cell (m), shear stress (τ), and cumulative shear displacement (D). A full list of symbols is given in Table 7-1. The equations solved were unsteady-state fluid mass balance (with Darcy's law), frictional force equilibrium (with a radiation damping approximation term), a stress strain relationship that related shear displacement to shear stress, the aging law for state evolution, and the time integral relationship between slip velocity and cumulative shear displacement.

The problem was solved on a one-dimensional fracture embedded in a two-dimensional homogenous, isotropic medium. It was assumed that the permeability of the surrounding medium was zero (reasonable for fractures embedded in granite), and so the injected water was located only in the fracture.

The two-dimensional stress/strain problems were solved using plane stress, which assumes the thickness of the medium in the third dimension is infinite. For some calculations, an infinite height fracture would lead to unrealistic results. For example, an infinite height fracture would have an infinite flow rate. Therefore, for calculations not involving stress and strain, fracture height was defined to be h, which we set to 100 m. The simulations were isothermal. The fluid was single-phase liquid water with no proppant.

The unsteady-state fluid mass balance equation in a fracture is (adapted from Aziz and Settari, 1979):

$$\frac{\partial(\rho E)}{\partial t} = \nabla(q_{flux}e) + s_a,$$

<div align="right">4-2</div>

where q_{flux} is the mass flux rate, s_a is a source term, t is time, E is the void aperture (the pore volume per cross-sectional area of fracture), e is the hydraulic aperture, and ρ is the fluid density. Darcy flow was assumed, in which mass flux in a direction x_i is (Aziz and Settari, 1979):

$$q_{flux} = \frac{k\rho}{\mu_l}\frac{\partial P}{\partial x_i},$$

<div align="right">4-3</div>

where P is fluid pressure, μ_l is fluid viscosity, and k is permeability.

The permeability k is given by the "cubic law" and defined as (Jaeger et al., 2007):

$$k = \frac{e^2}{12},$$

<div align="right">4-4</div>

where e is hydraulic aperture, which is the effective aperture for flow in the fracture. Hydraulic aperture is equal to void aperture between two smooth plates, but can be lower than void aperture between rough surfaces such as a rock fracture.

For flow in a one-dimensional fracture, the cross-sectional area A is $h*e$, and so the mass flow rate is:

$$q = \frac{\rho h e^3}{12\mu}\frac{\partial P}{\partial x_i}.$$

<div align="right">4-5</div>

For a closed fracture, force equilibrium requires that shear stress be equal to the frictional resistance to slip. An additional term, $v*\eta$, called the radiation damping term, can be included to approximate the damping effect of inertia on sliding at high velocities (Rice, 1993). The variable η is on the order of one to tens of MPa/(m/s), which means that the radiation damping term is negligible for $v \ll 1$ m/s. The frictional equilibrium equation is (Segall, 2010):

$$| \tau - \eta v | = \mu_f \sigma_n' ,$$
<div align="right">4-6</div>

where μ_f is the coefficient of friction and σ_n' is the effective normal stress, defined as (Segall, 2010):

$$\sigma_n' = \sigma_n - P ,$$
<div align="right">4-7</div>

where compressive stresses are taken to be positive. Following the rate and state friction law, the coefficient of friction is defined as a function of sliding velocity and state (Segall, 2010):

$$\mu_f = f_0 + a \ln \frac{v}{v_0} + b \ln \frac{\theta v_0}{d_c} ,$$
<div align="right">4-8</div>

where f_0, v_0, a, b, and d_c are material constants. The variable d_c is referred to as the characteristic displacement scale. The parameters a and b are ~0.01, much smaller than f_0, which is ~0.6. Their relatively small value is consistent with the observation that only a fraction of the stress borne by a fracture is usually released during a seismic event.

Under a rate and state framework, all fractures are slipping at all times. Fractures can have a tiny slip velocity. Very tiny velocities, ~10^{-10} m/s or less, are physically meaningless on the time scale of a hydraulic stimulation, but this is not a practical difficulty because these fractures behave approximately as if they were locked.

The state variable can be interpreted as the average contact time of asperities on the fault. The "aging law" of state evolution is (Segall, 2010):

$$\frac{\partial \theta}{\partial t} = 1 - \frac{\theta v}{d_c} .$$
<div align="right">4-9</div>

Dieterich (1979) associated the state variable with asperity contact time. Dieterich and Kilgore (1994) demonstrated experimentally that surface contact area increased with contact time due to creep of asperities.

The stresses induced by fracture slip were calculated according to the equations of quasistatic equilibrium in a continuum assuming that body forces are equal to zero. These stresses are given by the vector equation (Jaeger et al., 2007):

$$\nabla^T T_s = 0, \qquad\qquad\qquad\qquad\qquad\qquad\text{4-10}$$

where T_s is the stress tensor.

Linear elasticity in an isotropic, homogeneous body was assumed, which means that the relationship between stress and strain is given by Hooke's law (Jaeger et al, 2007):

$$T_s = \frac{2G\nu_p}{1-2\nu_p} trace(\varepsilon)I + 2G\varepsilon, \qquad\qquad\qquad\qquad\text{4-11}$$

where I is the unit matrix, ε is the strain tensor, ν_p is Poisson's ratio, and G is the shear modulus.

The cumulative displacement at any point is equal to the time integral of velocity:

$$D = \int vdt. \qquad\qquad\qquad\qquad\qquad\qquad\qquad\text{4-12}$$

Both void and hydraulic aperture are related to effective normal stress and cumulative displacement. There is not a universally accepted equation in the literature for the relationship between these variables. A modified version of the equation used by Willis-Richards et al. (1996), Rahman et al. (2002), Kohl and Mégel (2007), and others was used:

$$E = \frac{E_0}{1+9\sigma_n'/\sigma_{Enref}} + D_1 \tan \frac{\phi_{Edil1}}{1+9\sigma_n'/\sigma_{Enref}} + D_2 \tan \frac{\phi_{Edil2}}{1+9\sigma_n'/\sigma_{Enref}} + E_{res}, \qquad\text{4-13}$$

where E_0, σ_{Enref}, E_{res}, ϕ_{Edil1}, and ϕ_{Edil2} are material constants. We allowed these constants to be different for hydraulic aperture, e, and void aperture E. In most simulations, ϕ_{Edil1} and ϕ_{Edil2} were set to zero so that there was no shear-induced pore volume dilation, only hydraulic aperture dilation.

Prior authors have used only one term for aperture enhancement from shear displacement. We used two terms in order to take into account the laboratory observation that hydraulic aperture of a fracture tends to increase more slowly after the initial shear displacement. Such a property was not recognized in early laboratory testing of shear displacement and aperture coupling in granite (Barton et al., 1985). More recent laboratory work has observed this phenomenon. Esaki et al. (1999) and Lee and Cho (2002) both found that for a shearing fracture in granite, permeability increased rapidly at first, but permeability increased slowly or not at all after 5-10 mm of slip. Esaki et al. (1999) and Lee and Cho (2002) both observed an increase in mechanical aperture with slip beyond 10 mm of slip. It is not clear whether void aperture continued to increase after 10 mm of slip.

The parameters D_1 and D_2 were defined as follows:

$$D_1 = D \text{ (for } D < D_{max}) \qquad\qquad 4\text{-}14$$

$$D_1 = D_{max} \text{ (for } D > D_{max})$$

$$D_2 = 0 \text{ (for } D < D_{max})$$

$$D_2 = D - D_{max} \text{ (for } D > D_{max}) \ .$$

Fluid density and viscosity are related to fluid pressure (and temperature, but the simulations were isothermal). Values were interpolated from a large table of properties generated using the freeware Matlab code XSteam 2.6 (Holmgren, 2007).

A microseismic event was considered to have begun when the maximum velocity on the fracture exceeded 5 mm/s. A slip event was considered finished when the highest velocity on the fracture dropped below 2.5 mm/s. Event durations were variable but were at most a few seconds. Event hypocenters were defined as the location where slip velocity first exceeded 5 mm/s.

The total amount of displacement on the fracture during the event was correlated to seismic magnitude. The seismic moment M_0 is a measure of the size and energy release of an earthquake (Stein and Wysession, 2003). M_0 is defined as the integral of displacement over the fracture area times the shear modulus:

$$M_0 = G \int D_{cum} dA ,$$
<div align="right">4-15</div>

where D_{cum} is the cumulative shear displacement that occurred during the seismic event.

From Hanks and Kanamori (1979), the seismic moment magnitude M_w is defined as:

$$M_w = \frac{\log_{10} M_0}{1.5} - 6.06 ,$$
<div align="right">4-16</div>

where M_0 is defined in N-m. For calculation of slip surface area, the dimension of the fracture out of the plane (in the third dimension) was taken to be h. For a one-dimensional fracture, a patch of slip dA is equal to hdl, where dl is an increment of distance along the fracture.

Modeling a one-dimensional fracture instead of a two-dimensional fracture had some consequences but should not have had a major impact on the overall results. Total displacements were overestimated somewhat because in the two-dimensional plane strain elastic solution, displacement goes on infinitely in the third, out-of-plane coordinate direction. Surface area close to the wellbore was overestimated because flow from the wellbore was one-dimensional, not radial. As a result, the magnitudes of events near the wellbore were overestimated and the magnitudes of distant events were underestimated. Because the fracture in this study was one-dimensional, the magnitudes calculated should only be compared relative to each another and not be considered actual magnitude predictions.

Finally, the dimensionality of the fracture affected connectivity with respect to heterogeneity. For fluid or slip to travel from one location to another on a one-dimensional fracture, it has to travel through all points in between. For a two-dimensional fracture, fluid or slip can propagate around barriers.

We neglected elastodynamic transfer of stress. Stress changes were propagated instantaneously and calculated using the quasistatic boundary element solution. Dynamic stresses may have some effect on the results but are computationally intensive to calculate. Lapusta (2001) found for a single fracture case, calculations neglecting dynamic stresses could be made consistent with dynamic stress calculations by using a

radiation damping term (as done in this chapter). For geometries more complex than a single fracture, dynamic stress transfer would play a more complicated role.

The injection well was modeled by including a source term s_a in the mass balance equation for the two elements at the center of the fracture. The source term for each was set to half of the total flow rate. In most simulations, injection was carried out at a specified pressure. The injection pressure was not specified directly in the model. Instead, the source term was adjusted at each time step in order to bring the injection pressure to the target level. The injection pressure was calculated by assuming Darcy flow between the elements adjacent to the injector and a constant pressure boundary.

In one of the simulations, fluid was produced from the wellbore at a specified rate following injection. In that case, the source term was set constant until the wellbore pressure reached the initial fluid pressure of the reservoir. At that point, production was ended.

To include some modest heterogeneity, the permeability of each element was multiplied by a coefficient. The coefficients did not change during the simulations and were set to be a random number between 0.1 and 2.0.

4.2.2 Methods of Solution

The fracture was discretized into elements of constant length. The same discretization was used for the mechanical and the fluid flow parts of the problem.

The mass balance equation was solved using the finite volume method. The flow between two adjacent elements in a linear fracture was calculated from Darcy's law. The transmissibility between two elements was calculated using the harmonic average. Flow between fracture elements was calculated according to the method of Karimi-Fard et al. (2004).

The force equilibrium and stress/strain relations were solved with the two-dimensional displacement discontinuity method, a linear elastic boundary element method (BEM) from Crouch and Starfield (1983). The problem reduces to finding the

induced stresses $\Delta\tau$ at each element i caused by the cumulative shear displacements from each element j. Stresses and displacements are linearly related so that:

$$\Delta\tau_i = \sum_{j=1}^{n} (B_{D,\tau})_{ij} D_j \, , \qquad\qquad\qquad 4\text{-}17$$

where $B_{D,\tau}$ is a matrix of interaction coefficients calculated according to Crouch and Starfield (1983). Because the problem setup was a single, linear fracture, shear displacements only affected shear stresses, not normal stresses.

We neglected stresses induced by fracture normal displacement. Closed fractures can have some slight normal displacement due to loading or unloading, but these displacements are around 0.1 mm (Barton et al., 1985), and their effect should be slight compared to the effects of pore pressure change caused by injection. The fracture normal displacement in our model was around 0.1 mm. Fracture opening did not occur during any of the simulations.

As discussed in Section 4.1.4, during actual EGS stimulation, injection sometimes occurs into fault zones that have much greater storativity than the crack that was used in our model. For injection of larger volumes of fluid into a fault zone, it is possible that normal stress interaction between adjacent areas of a fault could play a larger role (also discussed in Section 2.2.3.3).

4.2.3 Time Discretization

The issue of solving mechanical and flow equations together has been discussed at length in the literature of poroelasticity. One way to solve the problem is to use implicit Euler time stepping on every equation simultaneously and solve the entire problem as a large coupled system of equations. This is a "fully coupled" scheme (Kim et al., 2011). The fully coupled strategy is stable and accurate but is expensive computationally. We used an "explicitly coupled" scheme in which a rate and state time step was taken, and then the time step was repeated for the flow problem using updated values from the rate and state calculation.

The rate and state update was performed with an explicit, third-order Runge-Kutta scheme (Abramowitz and Stegun, 1972). In this step, state, shear stress, and cumulative displacement were updated. The frictional equilibrium equation, Equation 4-6, was an algebraic constraint. At the end of each substep in the Runge-Kutta scheme, the frictional equilibrium equation was solved to find velocity for each individual element. Next the flow update was performed using implicit Euler to find m^{n+1}. After the flow update, the frictional equilibrium equation was solved a final time to find the sliding velocity.   The flow equations and the frictional equilibrium equation were solved using Newton-Raphson iteration.

Figure 4-1 summarizes the coupling strategy.

$$
\begin{array}{cccc}
v^n & v^{n+1/2} & v^{n-1} \\
\theta^n & \theta^{n+1} & \theta^{n+1} \\
m^n \longrightarrow & m^n \longrightarrow & m^{n+1} \\
\tau^n \quad \text{Explicit} & \tau^{n+1} \quad \text{Implicit} & \tau^{n+1} \\
\sigma_n{}^n & \sigma_n{}^{n-1} & \sigma_n{}^{n+1} \\
D^n & D^{n+1} & D^{n+1}
\end{array}
$$
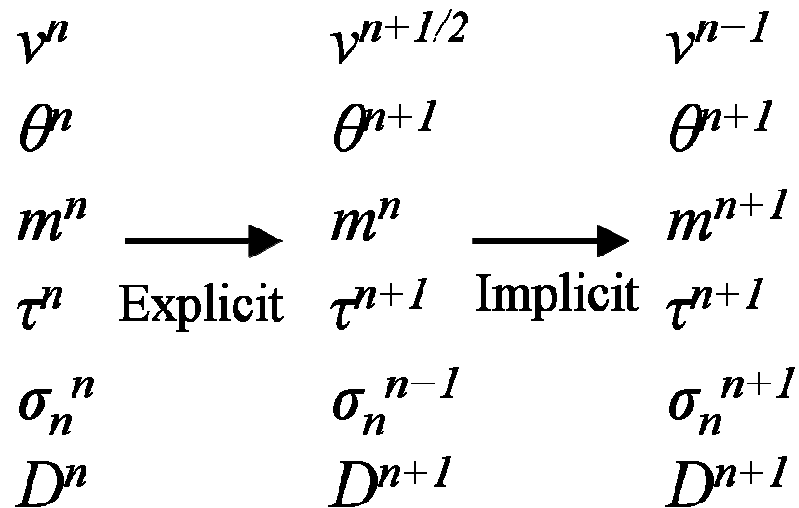
Figure 4-1: Explicit coupling scheme. The time step was split into two parts. First an explicit Runge-Kutta time step was taken to update D, θ, and τ (updating v as an algebraic constraint after every substep). Then an implicit time step was taken to update m, and v was updated for the last time after the update of m.

The advantage to splitting the problem is that different parts of the problem are most appropriately solved in different ways. The implicit Euler scheme is always numerically stable and is ideal for solving flow equations such as Equation 4-2. The Runge-Kutta scheme is more accurate and so is useful for solving the most non-linear part of the problem, the evolution of friction.

Adaptive time stepping was used. The time steps were chosen based on four criteria. The first criterion was error estimation based on the calculation of state and shear stress

from the third-order Runge-Kutta method. The second was the change in fluid pressure during the previous time step. The third was the number of iterations used by the flow simulator in solving the non-linear system of equations. The fourth was the relative amount of velocity change for each of the elements at the previous time step. There was a target value for each criterion, and a time step adjustment factor (either up or down) was calculated to move each value toward its target based on the result from the previous time step. The adjustment was chosen by taking the square root of the ratio of the target to the criterion. The subsequent time step was equal to the previous time step multiplied by the adjustment factor. Of the four criteria, the adjustment that resulted in the most conservative time step was used. If any of the criteria exceeded four times the target, the entire time step was discarded and repeated with a smaller time interval.

During seismic events when slip was very rapid, very small time steps on the order of microseconds were necessary. In between seismic events, time steps on the order of seconds, minutes, or hours were taken.

4.2.4 Problem Setup

Simulations were performed of injection into the center of a single, isolated, one-dimensional fracture embedded in a two-dimensional whole space.

The fracture was 500 m long and oriented 20° clockwise from the vertical y-axis. The two-dimensional problem could be interpreted as viewing a strike-slip fault in plan view, a normal fault in side view, or a reverse fault in side view, rotated 90°. The fracture was discretized into 2000 elements of length 25 cm.

The base case parameters are given in Table 4-1. T_{init} was the initial temperature and was the same as the injection temperature T_{inj}, 200°C, because the simulation was isothermal. The variables σ_{xx}^r, σ_{yy}^r, and σ_{xy}^r are the remote compressive stress in the x-direction, the y-direction, and the remote shear stress.

Table 4-1: Simulation base case parameters.

P_{init}	40 MPa	D_{emax}	5 mm
T_{init}	200 °C	D_{Emax}	-
θ_{init}	10e8 s	σ_{Enref}	95 MPa
$\sigma_{xx}{}^r$	65 MPa	σ_{enref}	95 MPa
$\sigma_{yy}{}^r$	100 MPa	f_0	0.6
$\sigma_{xy}{}^r$	0 MPa	d_c	.05 mm
a	0.011	v_0	10e-6 m/s
b	0.014	φ_{Edil1}	0.0º
G	10 GPa	φ_{Edil2}	0.0º
v_p	0.1	φ_{edil1}	1º
E_0	1 mm	φ_{edil2}	0.1º
e_0	.01 mm	P_{inj}	58 MPa
E_{res}	.002 mm	T_{inj}	200ºC
e_{res}	.0002 mm	h	100 m
η	20 MPa/(m/s)		

Once 75% of the fracture had slipped by a minimal amount, 0.1 mm, injection was ceased. The simulation was continued after injection stopped for a period equal to 20 times the duration of injection.

The frictional parameters a, b, and d_c deserve some discussion. In order for unstable slip to occur, a must be smaller than b (Ruina, 1983). This is because in order to achieve runaway velocity acceleration, the friction weakening effect of state decrease must be greater than the friction strengthening effect of velocity increase. The parameter d_c controls the minimum size of a patch of slip that can slip unstably and cause seismicity (Ruina, 1983). d_c also limits the size of the spatial discretization. The element size must

be significantly smaller than a characteristic length scale related to a, b, d_c, and $\sigma_n{}'$, otherwise the result is numerically unstable (Lapusta, 2001).

Several different simulations were carried out. The simulations were performed by specifying injection pressure. In practical EGS stimulations, positive displacement pumps are used so that the flow rate is controlled directly, not the injection pressure. However, in our simulations, trends in the injection pressure were most relevant to the behavior of the hydraulic stimulation, so injection pressure boundary conditions were used to control directly for these effects. In practice, injection pressure could be controlled indirectly by adjusting injection rate over time. In all simulations, injection pressure was low enough that the fluid pressure never exceeded the normal stress on the fault.

To investigate the effect of injection pressure, eight simulations were carried out using constant injection pressure (Cases A1-A8). All the simulations used pressures at 1 MPa increments from 51 MPa to 58 MPa.

To investigate the effect of decreasing injection pressure with time, 27 simulations were carried out that began with an injection pressure of 58 MPa and decreased the injection pressure over time. The injection rate was kept constant until the first microseismic event occurred, and then the injection pressure was decreased at a constant rate, defined as $P_{inj}{}'$. A variety of rates were used. In 14 of the simulations, Cases B1-B14, the injection pressure was kept constant if it dropped to 51 MPa. In 13 simulations, Cases C1-C13, the injection pressure was kept constant if it dropped to 53 MPa. In some of the cases, the minimum injection pressure was not reached before injection was stopped.

Three additional simulations were performed (Cases D1-D3). All used constant pressure injection at 58 MPa, like Case A8. D1 tested the effect of void aperture dilation with slip by using a value of φ_{Edil} equal to 1°, instead of the baseline value of 0° (no void dilation with slip). D2 used d_c equal to 5 mm, 100 times larger than the baseline value. D3 produced fluid at 3.0 l/s after the end of injection.

Table 4-2 specifies the settings for all the simulation runs. Table 4-3 provides the values for $P_{inj}{}'$ used in Cases B1-B14 and Cases C1-C13. Unless listed in Table 4-2, all parameters are the same as the baseline parameters given in Table 4-1.

Table 4-2: Parameters of the various simulations cases, A1-A8, B1-B14, C1-C13, and D1-D3. Further details about the B and C cases are given in Table 4-3.

A1-A8	Constant P_{inj} from 51 MPa to 58 MPa at 1 MPa increments
B1-B14	Decreasing P_{inj} with time from 58 MPa, minimum P_{inj} = 51 MPa
C1-C13	Decreasing P_{inj} with time from 58 MPa, minimum P_{inj} = 53 MPa
D1	Constant P_{inj} at 58 MPa, φ_{Edil1} = 1.0º
D2	Constant P_{inj} at 58 MPa, d_c = 5 mm
D3	Constant P_{inj} at 58 MPa, production at 2.5 kg/s after injection

Table 4-3: The rate of decrease in injection pressure, P_{inj}', for cases B1-B14 and C1-C13.

Case	P_{inj}' (MPa/hr)	Case	P_{inj}' (MPa/hr)
B1	-Infinity	C1	-Infinity
B2	-10.1	C2	-7.2
B3	-5.0	C3	-3.6
B4	-3.4	C4	-2.4
B5	-2.5	C5	-1.8
B6	-2.0	C6	-1.4
B7	-1.7	C7	-1.2
B8	-1.4	C8	-1.0
B9	-1.3	C9	-0.9
B10	-1.0	C10	-0.7
B11	-0.8	C11	-0.6
B12	-0.6	C12	-0.5
B13	-0.5	C13	-0.4
B14	-0.4		

4.3 Results

Plots of injection rate, injection pressure, and event magnitude versus time for Cases A3, A6, A8, B6, B10, D1, D2, and D3 are shown from Figure 4-2 to Figure 4-9. Summary metrics for Cases A1-A8 are given from Figure 4-10 to Figure 4-12. Figure 4-10 shows maximum magnitude and number of seismic events magnitude greater than two. Figure 4-11 shows the average injection rate during the period of time between the first seismic event and shut-in. Figure 4-12 shows the total fluid injected and total seismic moment released. Figure 4-13 and Figure 4-14 show the maximum event

magnitude and the number of events magnitude greater than two for Cases B1-B14 and Cases C1-C13. Table 4-4 and Table 4-5 give summary data for selected cases.
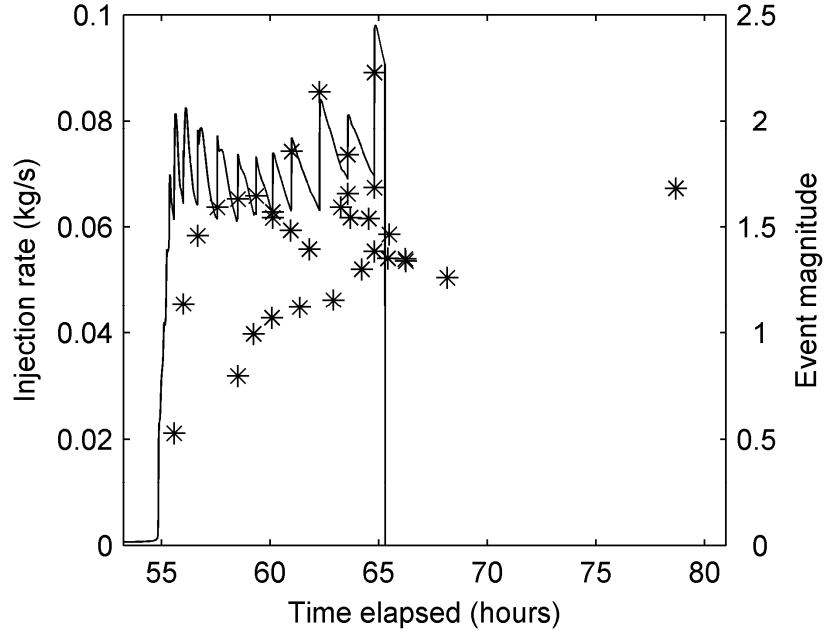
Figure 4-2: Injection rate (kg/s) and event magnitude for Case A3, constant pressure injection of 53 MPa.
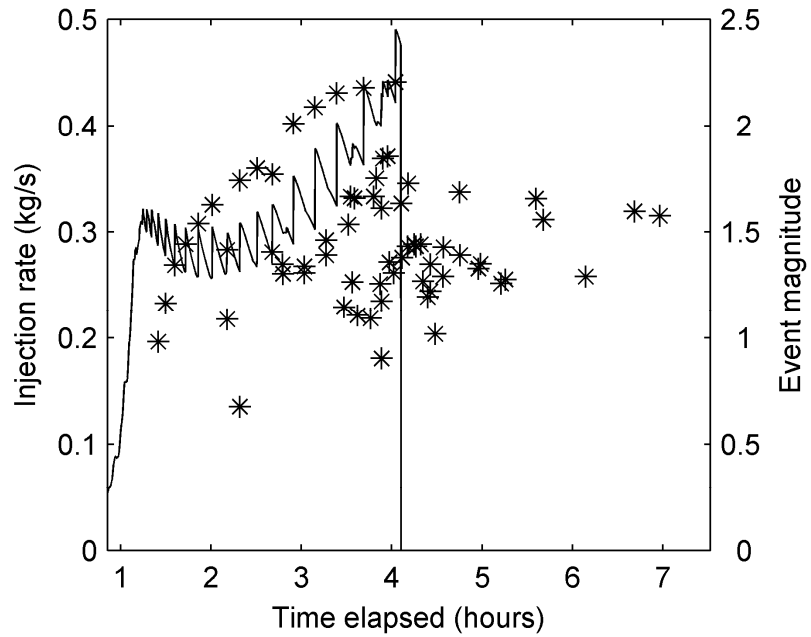
Figure 4-3: Injection rate (kg/s) and event magnitude for Case A6, constant pressure injection of 56 MPa.
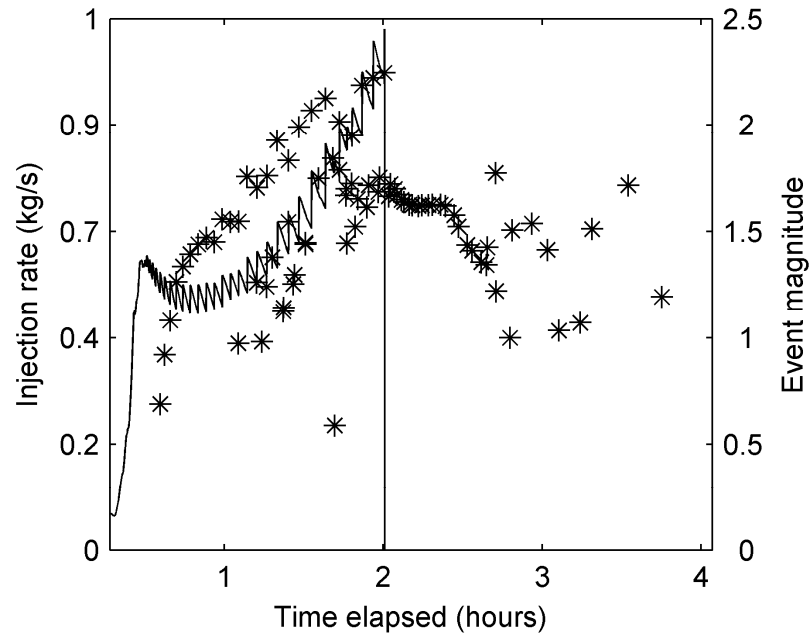
Figure 4-4: Injection rate (kg/s) and event magnitude for Case A8, constant pressure injection of 58 MPa.
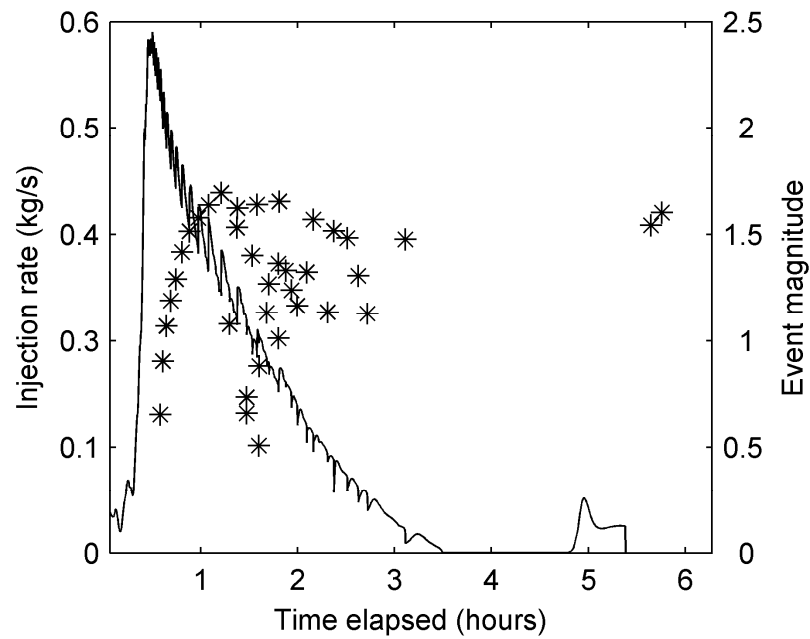
Figure 4-5: Injection rate (kg/s) and event magnitude for Case B6, decreasing injection rate from 58 MPa to 51 MPa with P_{inj}' equal to 2 MPa/hr.
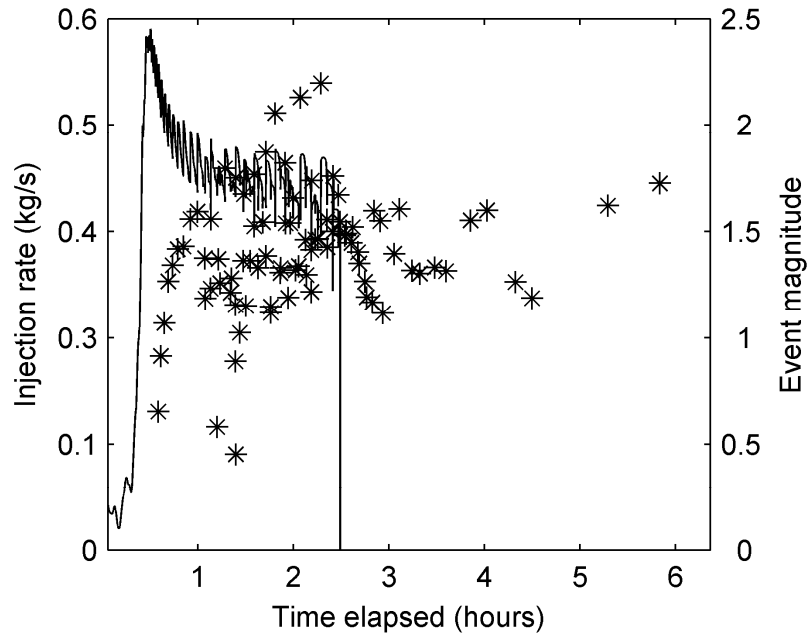
Figure 4-6: Injection rate (kg/s) and event magnitude for Case B10, decreasing injection rate from 58 MPa to 51 MPa with P_{inj}' equal to 1 MPa/hr. Note that in this case the injection was stopped before Pinj reached 51 MPa.
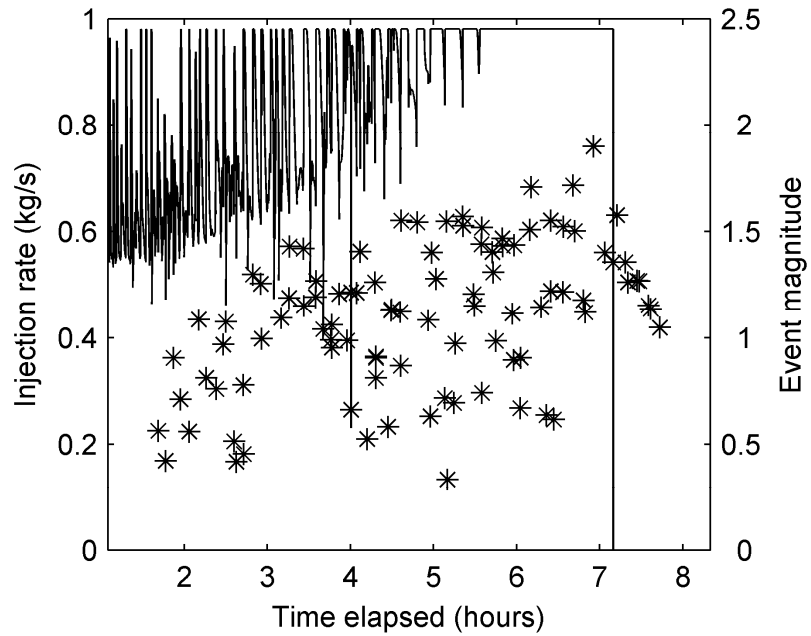
Figure 4-7: Injection rate (kg/s) and event magnitude for Case D1, constant pressure injection of 58 MPa with shear-induced pore volume dilation.
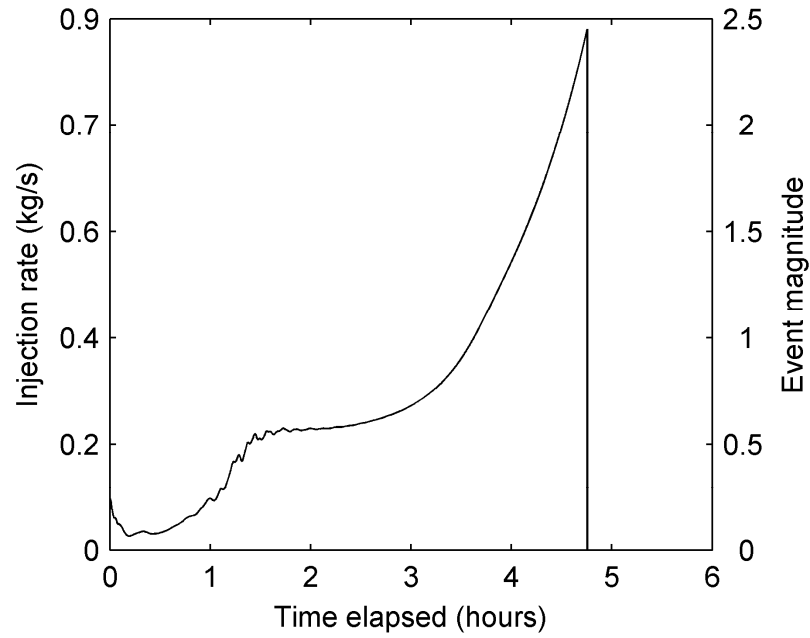
Figure 4-8: Injection rate (kg/s) and event magnitude for Case D2, constant pressure injection of 58 MPa with dc equal to 5 mm, 100 times larger than the default.
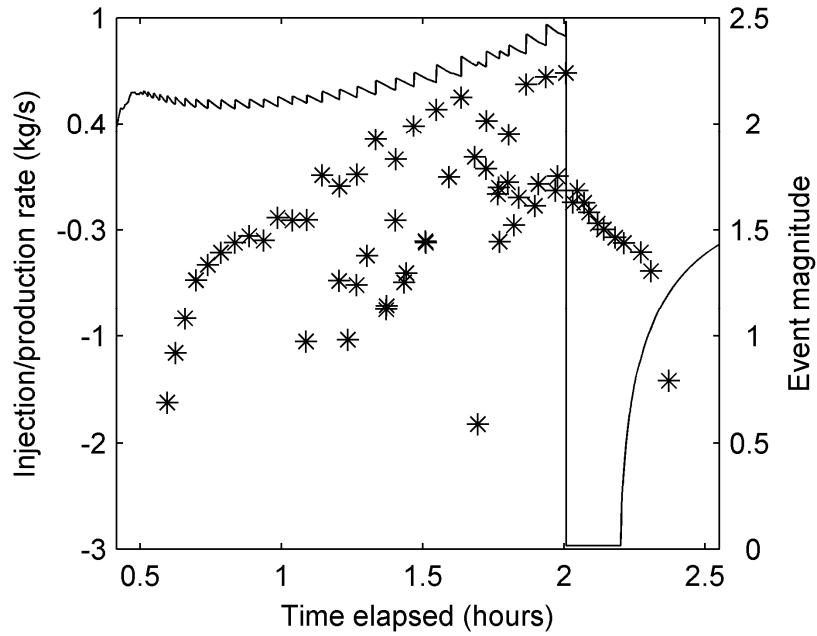
Figure 4-9: Injection rate (kg/s) and event magnitude for Case D3, constant pressure injection of 58 MPa with fluid production after injection.
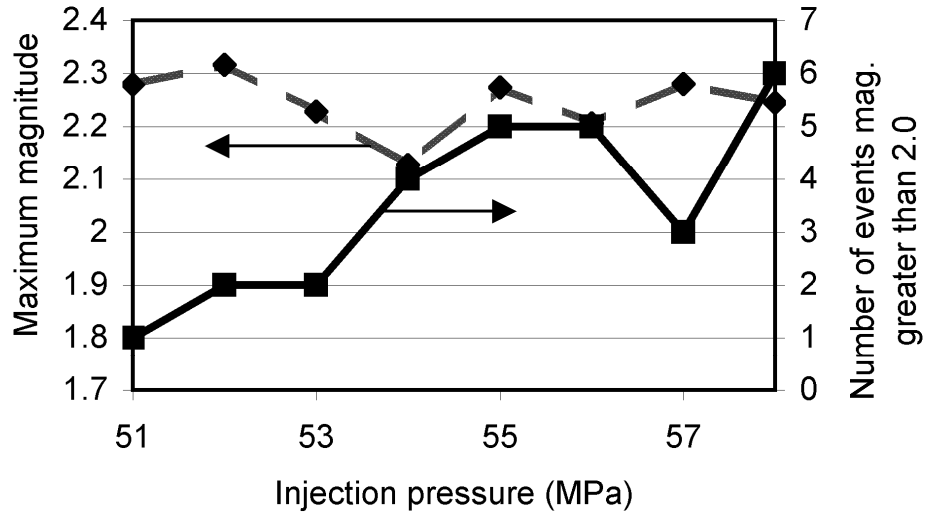
Figure 4-10: Maximum magnitude and the number of events with magnitude greater than 2.0 for Cases A1-A8, constant pressure injection.
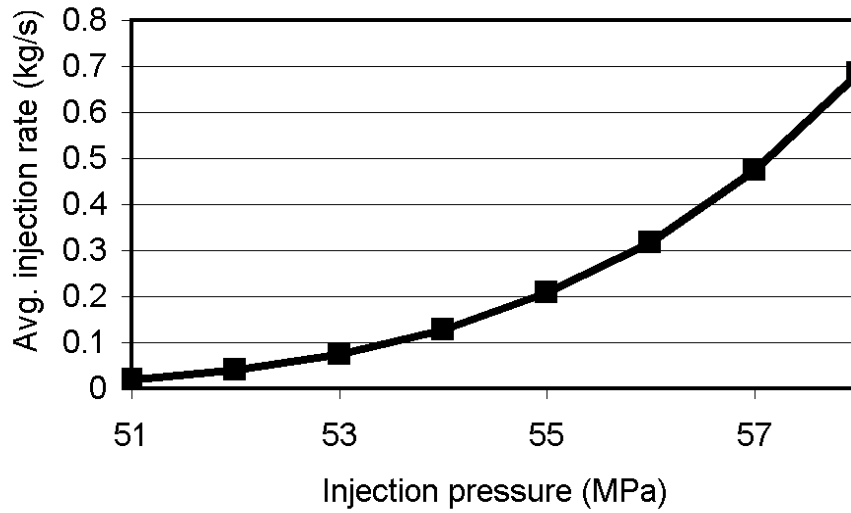
Figure 4-11: Average injection rate during stimulation for Cases A1-A8, constant pressure injection.
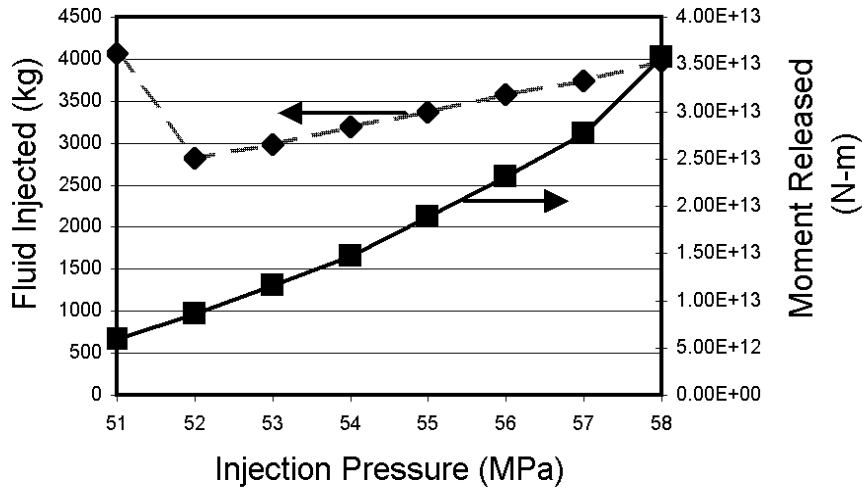
Figure 4-12: Total fluid injected (kg) and total seismic moment release (N-m) for Cases A1-A8, constant pressure injection.
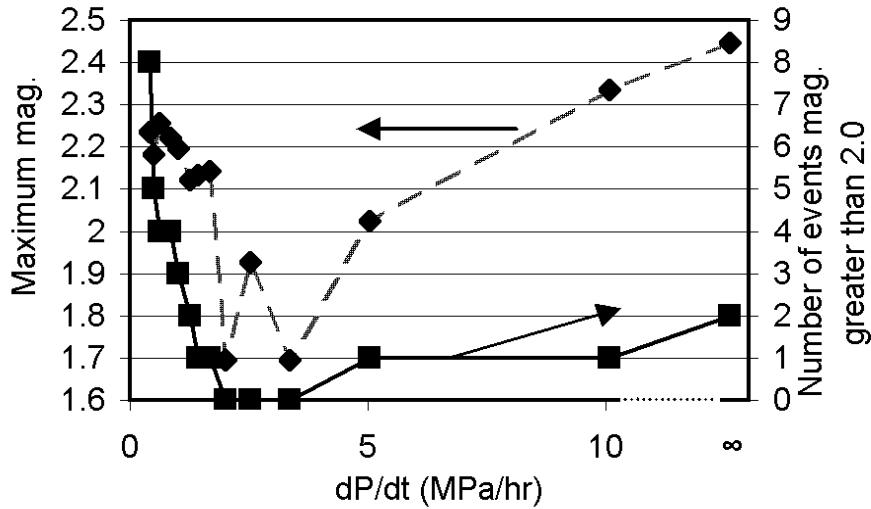
Figure 4-13: Maximum magnitude and the number of events with magnitude greater than 2.0 for Cases B1-B14, decreasing injection pressure with time from 58 MPa to a minimum of 51 MPa.
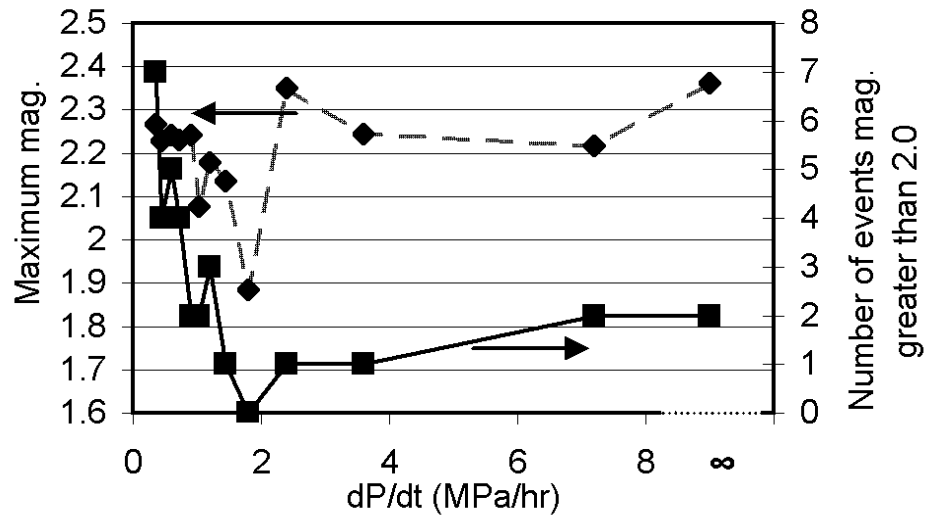
Figure 4-14: Maximum magnitude and the number of events with magnitude greater than 2.0 for Cases C1-C13, decreasing injection pressure with time from 58 MPa to a minimum of 53 MPa.

Table 4-4: Summary data for Cases A1, A3, A6, A8, B6, B10, and D1-D3. The number of events magnitude greater than 2.0, the maximum magnitude during injection, the maximum magnitude after injection, the total number of events during injection, the total number of events after injection.

Case	Events >2.0	Max. Mag. during Injection	Max. Mag. After Injection	Events During Injection	Events After Injection
A1	1	2.3	-	7	0
A3	2	2.2	1.7	26	6
A6	5	2.2	1.7	41	25
A8	6	2.2	1.8	51	32
B6	0	1.7	1.6	35	2
B10	3	2.2	1.7	61	24
D1	0	1.9	1.4	88	8
D2	0	-	-	0	0
D3	6	2.2	1.7	51	11

Table 4-5: Summary data for Cases A1, A3, A6, A8, B6, B10, and D1-D3. The total seismic moment release both during and after injection, the total duration of injection (including the period prior to the first seismic event), the total amount of fluid injected, and the maximum shear displacement along the fracture.

Case	Moment During Inj. (N-m)	Moment After Inj. (N-m)	Duration of Injection (s)	Fluid Injected (kg)	Maximum Displacement (m)
A1	5.90E+12	0.00E+00	42629200	4073	0.04
A3	1.06E+13	9.66E+11	235008	2982	0.07
A6	1.87E+13	4.44E+12	14759	3585	0.11
A8	2.75E+13	8.26E+12	7227	3981	0.14
B6	5.52E+12	3.15E+11	19374	2633	0.06
B10	1.81E+13	4.31E+12	8953	3622	0.11
D1	9.24E+12	6.08E+11	25781	20538	0.12
D2	0.00E+00	0.00E+00	17113	4752	0.15
D3	2.74E+13	2.19E+12	7227	3981	0.14

4.4 Discussion

A number of issues are discussed in the following subsections. First the overall behavior of the model is discussed, focusing on comparison to EGS field observations, the "episodic crack-like shear stimulation" mechanism that controlled the progression of the stimulation, shut-in events, and changes in injection rate with time. Subsequent subsections discuss estimation of least principal stress, estimation of initial hydraulic diffusivity, the effect of injection pressure for constant pressure injection, the effect of changing injection pressure with time, the effect of producing back fluid to reduce shut-in seismicity, a comparison of rate and state to static/dynamic friction, the effect of slip-induced void aperture dilation, and the effect of the characteristic displacement scale, d_c.

4.4.1 Similarity and Differences Compared to EGS Field

Observations

The behavior of the model was qualitatively consistent with a broad range of observations from EGS projects, with some differences. Similarities were migration of event hypocenters away from the stimulated region (Figure 4-20; Baisch et al., 2010; Shapiro et al., 1999), shut-in seismicity after injection stopped (Figure 4-2 to Figure 4-9; Charléty et al., 2007; Häring et al., 2007; Asanuma et al., 2006; Baisch et al., 2010), and large increases in injection pressure with small changes in injection rate (Figure 4-11; Cornet et al., 2003). Differences were an underestimation of the number of smaller events (Figure 4-2 to Figure 4-9; Baisch et al., 2010), a lack of event hypocenters that were *not* at the periphery of the stimulated region (Figure 4-20; Baisch et al., 2010), and shut-in seismicity magnitudes that were lower than magnitudes during injection (Figure 4-2 to Figure 4-9; Asanuma et al., 2006; Baisch et al., 2010; Majer et al., 2007). Because an unrealistically low value of storativity was used, it was necessary to keep the injection rate low by using a low value of permeability, as discussed in Section 4.1.4.

The differences between the model behavior and reality probably occurred because the model was significantly less heterogeneous than a natural system. The model contained a single, linear fracture with homogenous properties (other than permeability). Actual EGS stimulations could involves several fracture zones with multiple slip surfaces, nonuniform properties, and nonplanar geometry. All of these factors would encourage heterogeneity in the location of hypocenters and a greater number of smaller events.

As discussed in Section 4.4.10, shear-induced pore volume dilation could also cause hypocenters that are not located at the periphery of the stimulated region, especially because fractures in EGS stimulations are often embedded in high porosity damaged zones. As discussed in Section 4.4.11, d_c controls the minimum seismic event magnitude (Ruina, 1983; Dieterich, 2007). If a smaller value of d_c had been used, smaller events could have been simulated. In that case, it would have been necessary to use a finer discretization in order to avoid numerical instability (Lapusta, 2001). As discussed in

Section 4.4.3 the shut-in events had lower magnitude likely because the fracture modeled was one-dimensional, not two-dimensional.

In rate and state simulations with appropriately refined discretizations and homogenous (or mostly homogenous) properties on a single fracture, frequency-size distributions tend towards a "characteristic" distribution (Rice, 1993). In such models, seismic events, once nucleated, have a tendency to propagate across the entire fracture. In contrast, "inherently discrete" models have coarser discretizations and often use less realistic friction laws and tend to reproduce Gutenberg-Richter magnitude-frequency distributions that have a much greater number of smaller events than larger events (Rice, 1993; Ben-Zion and Rice, 1993; Ben-Zion, 2008). The development of characteristic frequency-size distributions in rate and state simulations suggests that Gutenberg-Richter distributions are not necessarily a consequence of frictional behavior, but rather may arise from heterogeneity in the earth itself. Hillers et al. (2006) replicated a Gutenberg-Richter distribution on a single fault using a rate and state model with spatial heterogeneity in frictional parameters. Aftershock distributions have been modeled successfully with rate and state friction using a distribution of faults (Gomberg et al., 2005).

4.4.2 Episodic Crack-Like Shear Stimulation

The advance of the stimulated region occurred through a specific mechanism, which we refer to as the episodic crack-like shear stimulation (ECSS) mechanism. A similar mechanism was described in McClure and Horne (2010b) based on results from a simpler shear stimulation model. If coefficient of friction is constant, a similar mechanism occurs, but the process is smooth instead of episodic (Section 3.4.2.2).

Conceptually, it is useful to divide the fracture into two regions. In the stimulated region, significant slip had already occurred. The permeability had increased dramatically, and as a result the fluid pressure had increased significantly. In the unstimulated region, slip had not yet occurred. The permeability was low, and the fluid pressure was near the initial pressure because fluid had not had time to flow beyond the stimulated region. The pressure distributions in the fracture at various times during Cases A8, A4, and A1 are shown from Figure 4-15 to Figure 4-17.
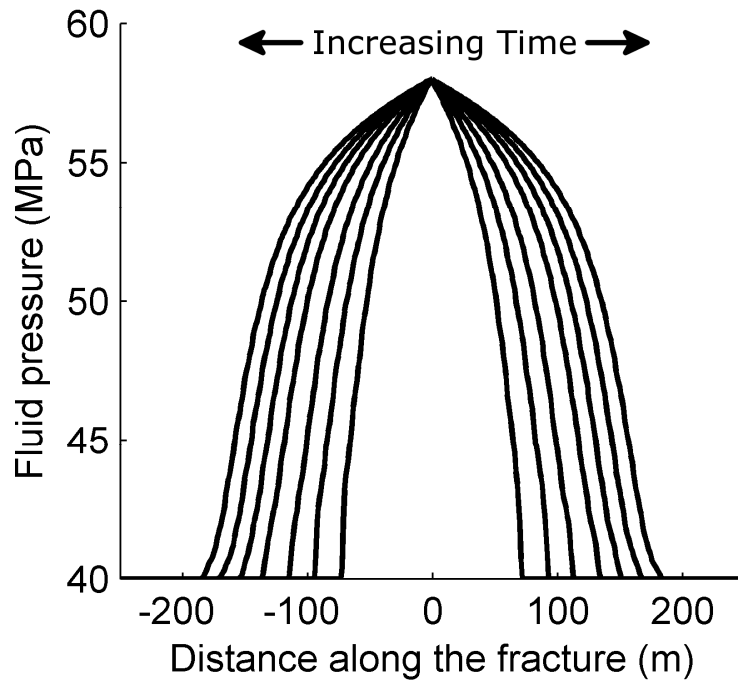
Figure 4-15: Pressure distribution along the fracture at various times during stimulation for Case A8, constant pressure injection at 58 MPa. The injector is located at the middle. The pressure front moves outward with time.
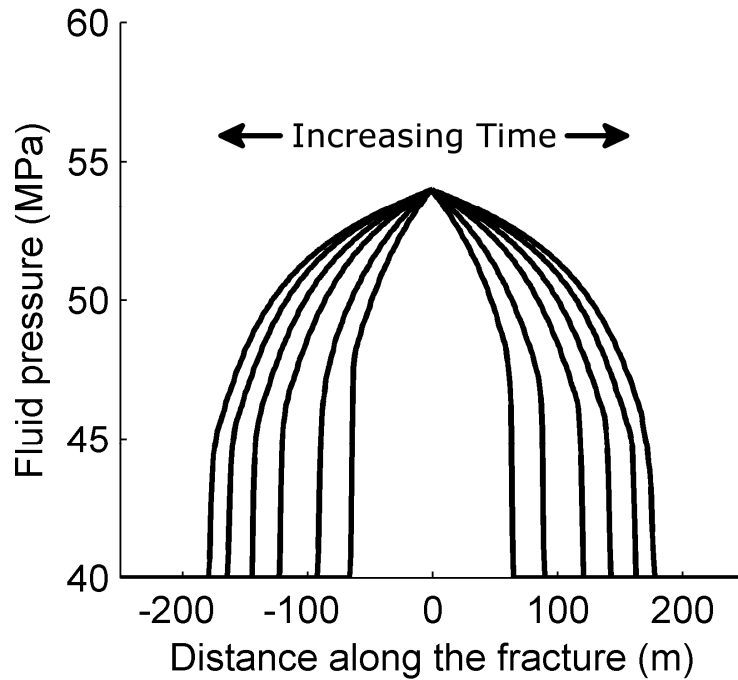
Figure 4-16: Pressure distribution along the fracture at various times during stimulation for Case A4, constant pressure injection at 54 MPa. The injector is located at the middle. The pressure front moves outward with time.
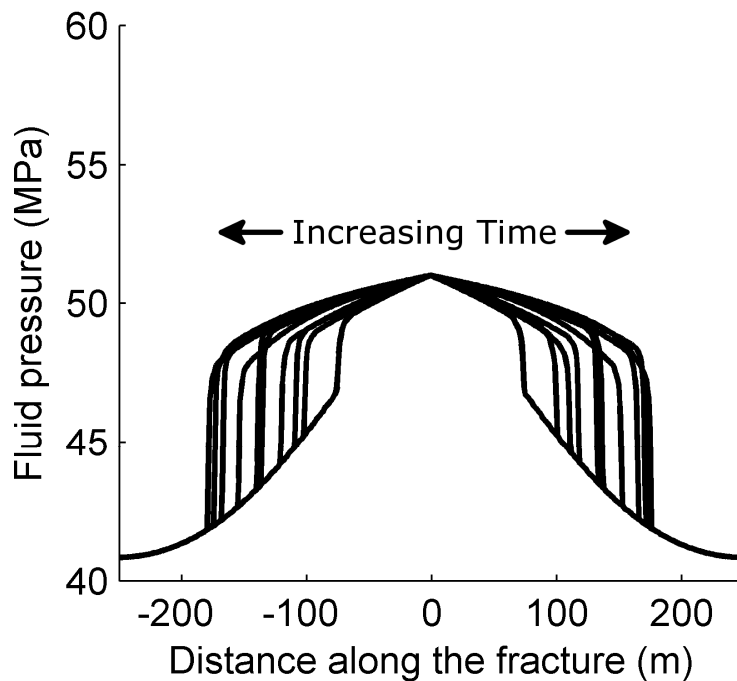
Figure 4-17: Pressure distribution along the fracture at various times during stimulation for Case A1, constant pressure injection at 51 MPa. The injector is located at the middle. The pressure front moves outward with time.

In the ECSS mechanism, slip events tended to nucleate at the edge of the stimulated region. Once nucleated, slip could propagate easily back across the stimulated region because in the stimulated region the fluid pressure was high and friction was relatively weak. It was more difficult for slip to propagate from the stimulated region into the unstimulated region because in the unstimulated region fluid pressure remained low and friction was relatively strong. Nevertheless, slip events were able to propagate some distance into the unstimulated region before stopping. When that happened, the permeability increased rapidly on the patch of fracture that had slipped for the first time. Fluid was able to rush into the newly slipped patch of fracture, weakening friction and nucleating the next seismic event. Figure 4-18 demonstrates the ECSS mechanism.

Figure 4-19 shows velocity profiles at different times of a rupture that nucleated at the edge of the stimulated region. The rupture can be seen nucleating, propagating, and dying out. The edge of the stimulated region is near the left of the figure. It is clear that the rupture traveled much further through the stimulated region, but also propagated some distance into the unstimulated region.
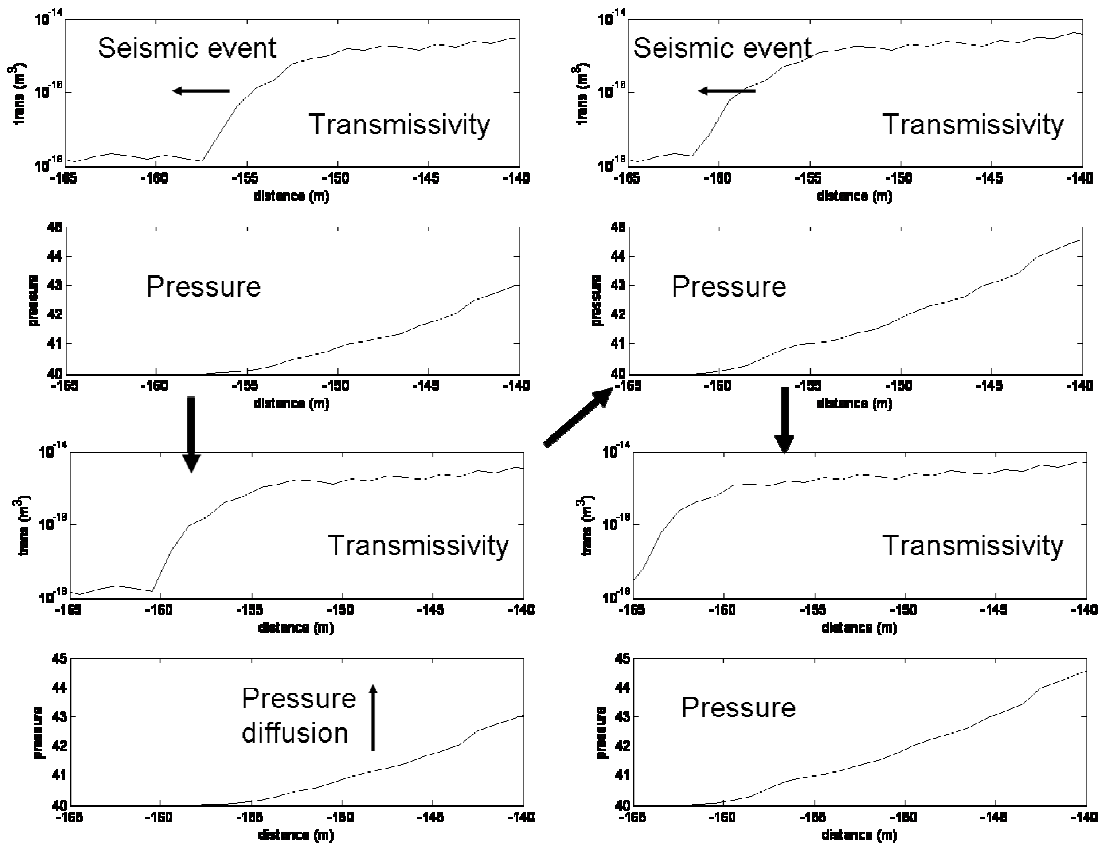
Figure 4-18: Example of episodic crack-like shear stimulation. Transmissivity and pressure are shown at four instants in time, progressing from upper left to lower left to upper right to lower right. Seismic events propagate slip and transmissivity enhancement very rapidly. Between seismic events, fluid flow raises fluid pressure across the stimulated region.
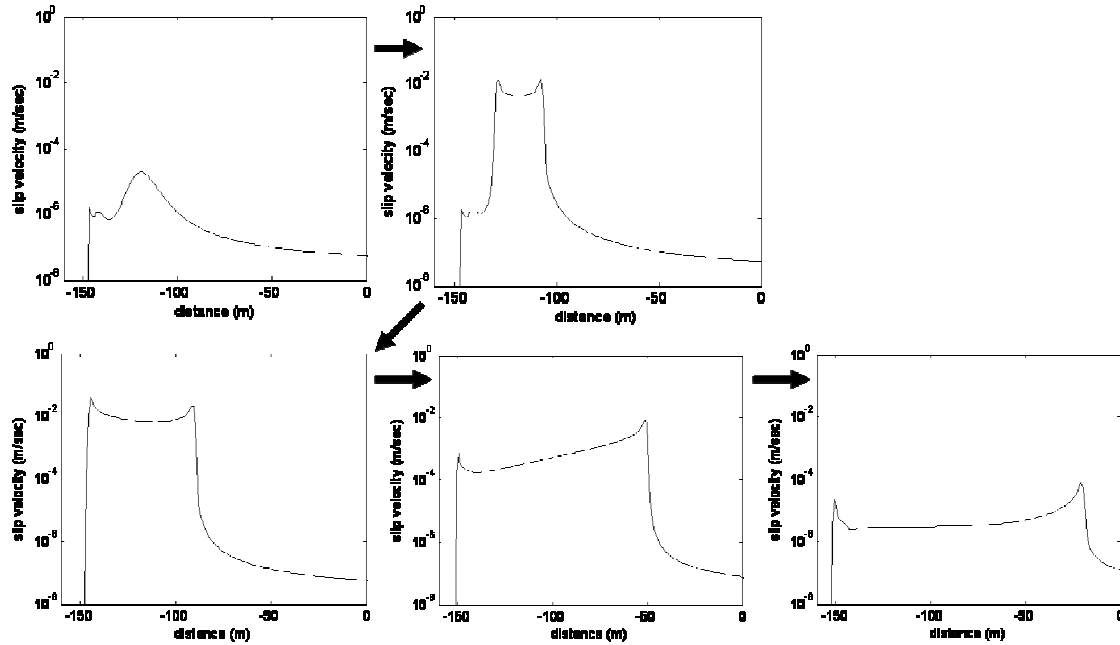
Figure 4-19: Rupture velocity profile at five snapshots in time. The rupture can be seen nucleating, spreading, and dying out. The edge of the stimulated region (which advances due to the rupture) is located near the left of the figure.

Figure 4-2, Figure 4-3, and Figure 4-4 show that for the base case with constant injection pressure, seismic events were relatively low in magnitude at the beginning of injection and grew larger over time. Magnitude increased over time because the largest events tended to propagate across the entire stimulated region. As the stimulated region grew larger over time, magnitude increased. A similar effect was observed in numerical simulations by McClure and Horne (2010b) and by Baisch et al. (2010).

4.4.3 Shut-in Events

Shut-in events occurred because of pressure redistribution. During injection, there was a pressure gradient away from the wellbore, which can be seen in Figure 4-15, Figure 4-16, and Figure 4-17. After injection stopped, the pressure redistributed to become uniform everywhere. The redistribution lowered pressure near the injector and increased pressure away from the injector. The fluid pressure at different times following shut-in during Case A8 is shown in Figure 4-21.
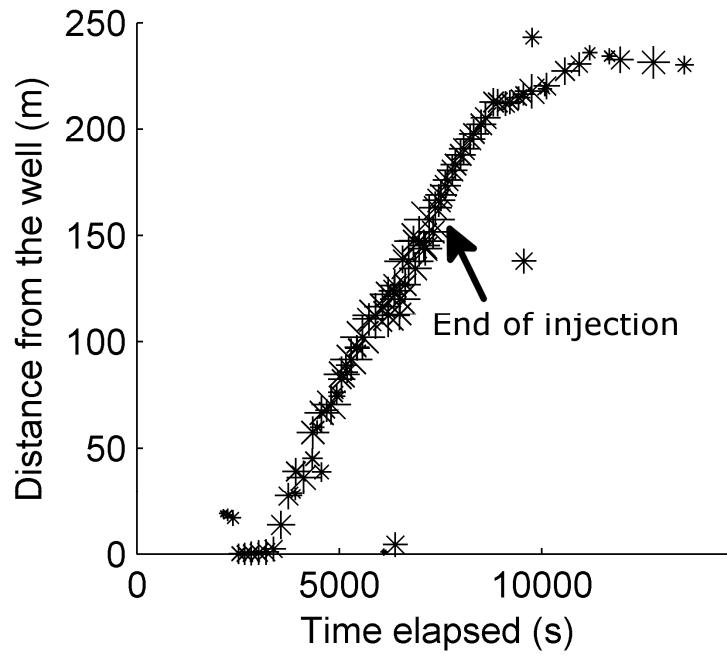
Figure 4-20: The distance of each seismic event hypocenter from the injector well as a function of duration of injection for Case A8, constant pressure injection at 58 MPa.
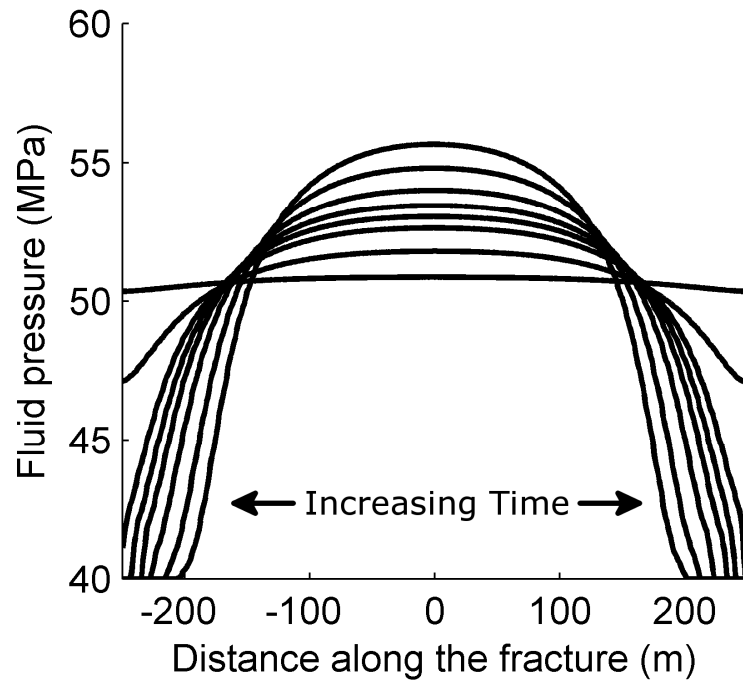
Figure 4-21: Pressure distribution along the fracture at various times during shut-in following injection for Case A8, constant pressure injection at 58 MPa. The injector is located at the middle. The pressure front flattens out with time.

The idea that fluid flow could cause an advance of the pressure front after shut-in has been proposed by other authors. Healy et al. (1968) and Hsieh and Bredehoeft (1981) discussed the possibility this may have occurred in association with a deep wastewater disposal well outside of Denver. Several numerical models have predicted this effect, including Bruel and Charlety (2007), McClure and Horne (2010b), Baisch et al. (2010), and Baisch et al. (2006). Similar mechanisms were investigated in modeling by Hayashi and Abe (1982) and Hayashi and Abe (1983).

In our simulations, shut-in events were smaller in magnitude than the largest events during injection (Figure 4-2 to Figure 4-7). In actual EGS stimulation, shut-in events are often larger than events during injection (Majer et al., 2007). The discrepancy may be an artifact of our use of a one-dimensional fracture. For a two-dimensional planar fracture, the periphery would have relatively more surface area than in the one-dimensional case. The shut-in events, which occur at the periphery, would be relatively larger.

In the one-dimensional simulations, peripheral events on either side of the fracture tended to be separated because the center region, which did not slip, prevented slip on one side from triggering slip on the other. For a two-dimensional, planar fracture, the periphery would be a ring-shaped region, and there would be no barrier to prevent slip anywhere in the periphery from inducing slip everywhere else in the periphery. Baisch et al. (2010) simulated induced seismicity in a two-dimensional planar fracture and observed larger events during shut-in than during injection.

4.4.4 Changes in Flow Rate with Time

The flow rate behavior with time for several cases can be seen in Figures 2-9. The flow rate tended to spike following a seismic event. Seismic events caused abrupt increases in permeability along the fracture without changing the pressure distribution (except in Case D1, which included the effect of shear-induced pore volume dilation). Because flow rate was proportional to both permeability and pressure gradient, increasing permeability while holding pressure gradient constant increased flow rate. Between seismic events, flow rate tended to decrease, as would be expected for constant injection pressure.

During an actual EGS stimulation, it is typical for flow rate to be held constant (except for occasional step changes) and the injection pressure to fluctuate with time. Abrupt changes in injection pressure of at least 0.6 MPa following large slip events have been observed during actual EGS stimulations (Weidler, 2000). The magnitude of the changes in injection pressure observed during EGS stimulations do not appear to be as great as the fluctuations in flow rate observed from Figure 4-2 to Figure 4-9. However, as discussed in Section 4.4.6, small changes in injection pressure can cause large changes in flow rate during shear stimulation. It follows that changes in fracture permeability would cause relatively small changes in injection pressure for constant injection rate and relatively large change in injection rate for constant injection pressure.

Outside of short term fluctuations, the long term behavior of the injection rate was generally increasing with time for most of the constant pressure injections but sometimes decreased or remained constant with time. The relationship between flow rate and injection pressure is complex but can be understood through the framework of the CSS mechanism. Increasing permeability across the stimulated region led to increasing injection rate with time. Injection rate tended to go down as the stimulated region extended. A more detailed discussion of this relationship can be found in McClure and Horne (2010b).

4.4.5 Implications of the Crack-like Shear Stimulation Mechanism for Estimation of the Unstimulated Hydraulic Diffusivity

It is sometimes assumed that the advance of the seismicity cloud during shear stimulation is caused by diffusion of pressure into the unstimulated reservoir (Shapiro et al., 1999; Bruel, 2007; Shapiro and Dinske, 2009). This process has been modeled assuming that the permeability is constant (Shapiro et al., 1999) or that permeability increases with fluid pressure (Shapiro and Dinske, 2009). The migration of event hypocenters from the injector has been used to estimate the unstimulated hydraulic diffusivity of the formation (Shapiro et al., 1999; Bruel, 2007). This method of estimating the unstimulated hydraulic diffusivity depends on the assumption that pressure diffuses through the unstimulated fractures ahead of the permeability stimulation front.

In the crack-like shear stimulation (CSS) mechanism, friction weakening allows slip and permeability enhancement to advance ahead of the pressure front (Sections 3.4.2.2 and 4.4.2). The growth of the stimulated region depends on the stimulated diffusivity and has no dependence on the unstimulated diffusivity (McClure and Horne, 2010b). In practice, which process can advance faster would depend on the relative hydraulic diffusivities of the stimulated and unstimulated fractures, the frictional characteristics of the fractures, the geometry of the fractures, and the initial stress state.

The initial hydraulic diffusivity could not be estimated from the growth of the seismic cloud if the stimulation front were able to advance faster than pressure can diffuse through the unstimulated region (also discussed in Section 3.4.2.2).

4.4.6 Implications of the Crack-like Shear Stimulation Mechanism for Estimation of the Least Principal Stress

It was proposed by Cornet and Bérard (2003) and subsequently assumed in Cornet et al. (2007) and Valley and Evans (2007) that during the hydraulic stimulation of the wells GPK1, GPK3, and GPK4 as a part of the EGS projects at Soultz, France, the fluid pressure reached the least principal stress at the top of the openhole section during stimulation. That assumption was used to estimate the magnitude of the least principal stress at Soultz field.

The justification for this assumption was that during the stimulation, large increases in injection rate resulted in relatively small increases in injection pressure. This behavior could be referred to as pressure limiting behavior. When pressure limiting behavior occurs during hydraulic stimulation involving the growth of tensile cracks, it is taken as evidence that tensile fractures are propagating away from the wellbore (Zoback, 2007).

Our model suggests that shear stimulation alone, without the presence of tensile fracturing, could cause pressure limiting behavior (also discussed in Section 3.4.7 and by Couzens-Schultz and Chan, 2010). Figure 4-11 shows the average flow rate for different constant injection pressures during stimulation between the first seismic event and shut-in. It is evident that for the lowest injection pressure case, 51 MPa in Case A1, the

average flow rate was extremely low. For an even lower injection pressure, the fluid pressure would not be high enough to propagate slip regardless of the duration of injection. That pressure could be called the shear stimulation threshold pressure.

For injection pressures below the shear stimulation threshold, increasing injection rate in increments would result in relatively large increases in injection pressure because injectivity would be related to the initial, low permeability.

Once shear stimulation began to occur, further increases in injection rate would result in much lower increases in injection pressure. From Figure 4-11, during Case A1 (51 MPa downhole, corresponding to a $\Delta P = P_{inj} - P_{init}$ of 11 MPa), the average flow rate (during the period between the first seismic event and shut-in) was 0.02 kg/s. Increasing the injection pressure by one additional MPa to 52 MPa in Case A2 (ΔP of 12 MPa, an increase of 9% from Case A1), doubled the flow rate to 0.04 kg/s. In Case A8, with an injection pressure of 58 MPa, the average flow rate was about 0.7 kg/s. From Case A1 to Case A8, a 64% increase in ΔP resulted in an increase in injection rate of 3400%.

The large increases in injection rate can be explained by considering the pressure distribution at different times during injection. The difference between the initial fluid pressure and the injection pressure can conceptually be decomposed into two parts. One part is the pressure drop in the stimulated region from the wellbore to the edge of the stimulated region. The second part is the front extension pressure at which the stimulated region was able to advance. The front extension pressure is approximately the fluid pressure that must be reached at the edge of the stimulated region to trigger seismicity that spreads slip into the unstimulated region. At the edge of the stimulated region, the fluid pressure drops rapidly from the front extension pressure to the initial fluid pressure.

Increasing the injection pressure lowered the front extension pressure. In Figure 4-17, injection at 51 MPa, the extension pressure was around 48 MPa. In Figure 4-16, injection at 55 MPa, the extension pressure was around 44 MPa. In Figure 4-15, injection at 58 MPa, the extension pressure apparently had reached nearly 40 MPa, the initial fluid pressure.

The pressure gradient was roughly the difference between the injection pressure and the front extension pressure divided by the distance to the fracture tip. Increasing

injection pressure increased pressure gradient in two ways: increasing the pressure at the center of the stimulated region and decreasing it at the edge (by lowering the extension pressure). Further discussion of the relationship between injection pressure and rate can be found in McClure and Horne (2010b).

From Equation 4-13, higher fluid pressure led to higher permeability. In addition, greater displacement occurred with higher injection pressure, which also led to greater permeability.

Therefore, when the CSS mechanism controlled stimulation, small increases in injection pressure led to large increases in injection rate.

If injection pressure were less than the shear stimulation threshold, significant slip would not occur, and permeability would remain low. With low permeability, the injection rate would remain low, and increases in injection pressure would cause small increases in injection rate.

Therefore, there are different mechanisms controlling the relationship between injection pressure and injection rate for injection pressures above and below the shear stimulation threshold. Injection rates at pressures below the stimulation threshold are related to the initial permeability. Injection rates at pressures above the stimulation threshold are related to the CSS mechanism and depend on the much higher stimulated permeability. The change in mechanism at the stimulation threshold causes a sharp change in the relationship between injection pressure and rate.

The shear stimulation threshold pressure could be significantly below the least principal stress. In our model, it was roughly 50 MPa, 15 MPa less than the least principal stress.

Our modeling suggests that pressure limited behavior could occur because of shear stimulation. If pressure limited behavior were incorrectly taken to be evidence of tensile fracturing, the least principal stress could be underestimated (also discussed in Section 3.4.7 and by Couzens-Schultz and Chan, 2010).

4.4.7 Effect of Injection Pressure for Constant Pressure Injection

Cases A1-A8 investigated the effect of injection pressure for constant pressure injection. Plots of flow rate and event magnitude with time for Cases A3, A6, and A8 are shown in Figure 4-2, Figure 4-3, and Figure 4-4.

The maximum event magnitude was not affected significantly by the injection pressure. Figure 4-10 shows that maximum magnitudes were clustered around 2.25 for all cases. The highest magnitudes occurred in Cases A1 and A2, the lowest injection pressures. They were larger because in those cases injection went on for a very long time before the first seismic event occurred (Figure 4-22). As a result, the pressure in the unstimulated region was significantly elevated by the time seismicity began (Figure 4-17).
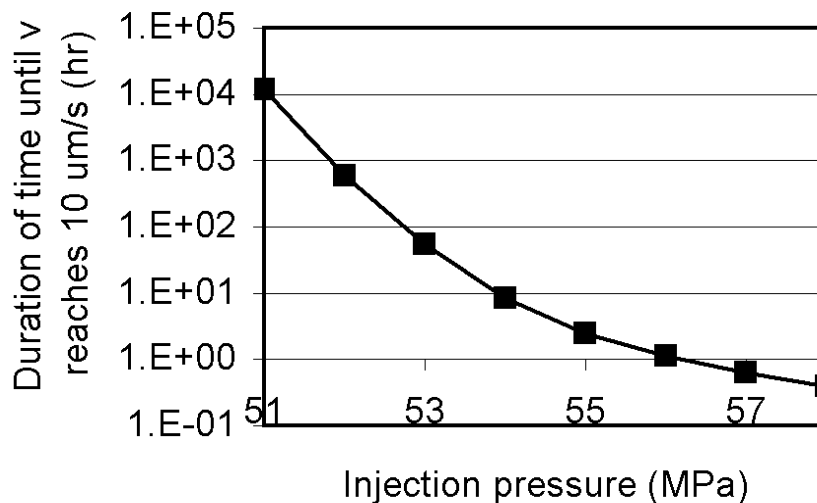
Figure 4-22: The duration of time until maximum slipping velocity on the fracture reached 10 μm/s for Cases A1-A8, constant pressure injection.

The maximum event magnitude was generally not affected by injection pressure because the stress drop during an earthquake is weakly sensitive to the fluid pressure. Magnitude is related to the product of the area of slip and the displacement. Displacement is related to the stress drop and area of slip. The maximum area of slip was roughly the same in each simulation because it was limited by the size of the fracture. The stress drop is related to the weakening of friction caused by a decrease in the θ variable in the rate and state friction law. The decrease in θ during an earthquake

depends on the rate and state parameters such as a, b, and η but not on the effective normal stress.

Higher injection pressure led to a greater release of seismic moment, a somewhat greater amount of total fluid injected, and a greater number of relatively large events. These effects can be seen in Figure 4-10 and Figure 4-12. The higher injection pressure caused a greater weakening of friction, which allowed more slip to occur, a greater release of seismic moment and more relatively large events.

4.4.8 Effect of Decreasing Injection Pressure over Time

Cases B1-B14 and Cases C1-C13 tested the effect of decreasing the injection pressure over time. Plots of flow rate and event magnitude with time for Cases B6 and B10 are shown in Figure 4-5 and Figure 4-6. In all cases, the initial injection pressure was 58 MPa. The injection pressure was kept constant at 58 MPa until the first seismic event, and then it began to be decreased. In the different cases, the pressure was decreased at different rates. In Cases B1-B14, injection pressure was kept constant once it reached 51 MPa. In Cases C1-C13, injection pressure was kept constant once it reached 53 MPa. The cases varied from instantaneous drop to the minimum injection pressure (Cases B1 and C1) to constant injection pressure at 58 MPa (Cases B14 and C13, the same as Case A8). It should be apparent that there was some overlap between Cases B1-B14 and Cases C1-C13.

Figure 4-10, Figure 4-13, and Figure 4-14 show that the cases with decreasing injection pressure over time had reduced seismicity compared to any of the constant injection pressure cases. There was a range of optimal values for $P_{inj}{}'$, the pressure derivative, that resulted in significantly smaller maximum magnitudes and fewer events magnitude greater than 2.0 than for either constant injection at 51 MPa, 53 MPa, or 58 MPa. The effect was more pronounced for Cases B1-B14 than Cases C1-C13.

There is a physical explanation for why decreasing injection pressure with time reduced seismicity. Magnitude is related to slip area and shear displacement. The largest events were able to propagate across the entire stimulated region, with the largest events occurring when the stimulated region was largest.

Decreasing the injection pressure over time tended to decrease the fluid pressure across the entire stimulated region over time. Because friction strengthens as pressure decreases, this had the effect of gradually strengthening friction across the fracture over time. Events continued to nucleate at the edge of the stimulated region, but they faced greater frictional resistance in spreading back across the stimulated region. This caused fewer events to spread across the entire stimulated region, and when they did, their total displacements were smaller.

The optimal values of $P_{inj}{}'$ corresponded to cases where the minimum injection pressure was reached either some time before or around the time that injection was complete. If injection pressure was lowered too rapidly, the minimum injection pressure was reached early in the stimulation, and the stimulation was subsequently carried out as a constant pressure injection. If injection pressure was lowered too slowly, the magnitude damping effect of lowering injection pressure over time was limited.

The effect of decreasing injection pressure over time was more pronounced for Cases B1-B14 than C1-C13. In Cases B1-B14, the minimum injection pressure was 51 MPa. Interestingly, in Case A1, injection at 51 MPa was almost too low to cause stimulation. Figure 4-22 shows that for Case A1 it took an exceptionally long time, over 1000 hours of injection, for slip velocity to reach 10^{-5} m/s. Prior to the initiation of significant slip, Case A1 was effectively constant pressure injection into a low permeability fracture. In Cases B1-B14 injection at 51 MPa was able to propagate stimulation across the fracture. It appears that a higher injection pressure was required to initiate seismicity in Case A1, but once seismicity was initiated, it was possible to propagate stimulation with a lower injection pressure.

The exact value of $P_{inj}{}'$ that would minimize seismicity is dependent on the details of the model. If decreasing injection pressure with time were to be attempted in practice, the optimal $P_{inj}{}'$ would be site specific and need to be estimated in advance with the construction of a full scale stimulation model.

It is possible that with a more complex, site specific model, the conclusions of this section may not hold or may not be feasible. On the other hand, with a more detailed model perhaps other opportunities to minimize induced seismicity would become

apparent. Perhaps injection pressure could be optimized in real time based on data such as microseismicity and injection rate that could be gathered during injection. Our results demonstrate in concept that minimizing induced seismicity by manipulating injection strategy could be possible but that to do so would require careful modeling and planning.

4.4.9 Effect of Producing Fluid Back after Injection

Case D3 tested the effect of producing fluid back after injection. Prior to the end of injection, Case D3 was identical to Case A8, with constant pressure injection at 58 MPa. The injection rate and event magnitudes for Cases A8 and D3 are shown in Figure 4-4 and Figure 4-9 (the vertical scales are different in the two figures). The figures show that producing from the well following injection resulted in reduced post-injection seismicity. The strategy of producing back fluid was also suggested by Baisch et al. (2006).

Producing fluid back mitigated the build-up of fluid pressure at the edge of the stimulated region after shut-in. The post-injection events immediately after the end of injection were not prevented because it took a period of time for the pressure transient caused by the production to reach the periphery of the fracture.

4.4.10   Effect of Shear-Induced Pore Volume Dilation

Case D1 investigated the potential effect of shear-induced pore volume dilation on seismicity. Laboratory experiments such as Marone et al. (1990) and Morrow and Byerlee (1989) found evidence of fracture pore volume dilation due to sliding. The effects of pore volume dilation have been investigated numerically by several authors, including Segall and Rice (1995), Yamashita (1999), and Segall et al. (2010). We are not aware of field evidence to indicate whether or not shear-induced pore volume dilation happens during EGS stimulation, but it is an interesting phenomenon to investigate.

Pore volume dilation had the effect of damping out seismicity, consistent with results from Yamashita (1999), Segall and Rice (1995), and Segall et al. (2010). This can be seen by comparing Cases D1 and A8 in Figure 4-7 and Figure 4-4, which show event magnitude with time. Both show constant pressure injection at 58 MPa. The only difference between the two cases is that there was shear-induced pore volume dilation in

Case D1. With pore volume dilation, a larger number of events occurred, but they were of relatively smaller magnitude.

Pore dilation damped out slip events because it caused a decrease in fluid pressure during slip. During rapid slip, fluid flow does not have time to occur, and so the mass of fluid at a given location is nearly fixed. Water density is relatively insensitive to pressure, so to conserve mass, the void aperture at a given location had to be nearly constant during slip. As slip tried to dilate the void aperture, the only way to keep void aperture constant was to decrease fluid pressure, increasing the effective normal stress (Equation 4-13). The higher effective normal stress strengthened friction and tended to inhibit slip from occurring. The same total amount of slip had to occur for the same injection pressure, and so slip was distributed into a larger number of smaller magnitude events.

There were several other differences between Case D1 and the other simulations. Due to pore dilation, the fluid pressure at the injector was decreased following seismic events. Because the well continued to inject at constant pressure, the flow rate spiked as a large pressure gradient was suddenly imposed between the injector and the fracture. Unrealistically high flow rates were possible, and so it was necessary to specify a maximum injection rate of 1 kg/s in the code. Because of the maximum flow rate, the injection rate would sometimes dip momentarily below the target of 58 MPa. Because of flow rate spiking following slip events, the flow rate history had a very erratic, unrealistic behavior as can be seen in Figure 4-7.

There were more event hypocenters near the injector in Case D1 than in Case A8. After seismic events, when fluid pressure was lowered near the injector, the fluid pressure increased again rapidly near the wellbore. Often that triggered another seismic event close to the injector.

A more realistic treatment of fracture zone geometry may have damped out the erratic variations in flow rate. If a fracture were surrounded by porous, permeable material, such as the alteration zones observed at Soultz (Section 4.1.4), fluid could flow rapidly back into the fracture from the surrounding porosity and raise the fluid pressure up again across the entire fracture. Such a mechanism could lead to complicated behavior that

could be interesting to investigate in future work. For example, a rapid decrease in fluid pressure during slip followed by a rapid increase in pressure due to fluid flow from a surrounding damage zone could lead to aftershock sequences with hypocenters distributed throughout the stimulated region as fluid pressure rapidly recovered following slip events.

A final difference between Case D1 and the other cases was that far more fluid was injected in Case D1 (Table 4-5). The reason was that because of the shear-induced pore volume dilation, a greater amount of fluid was required to increase the fluid pressure across the fracture.

4.4.11 Effect of d_c

In Case D2, a larger value for d_c inhibited seismicity. The entire fracture was stimulated, but the slip was slow and aseismic. The stimulated region grew slowly, as described by the smooth crack-like shear stimulation mechanism (Section 3.4.2.2). Figure 4-8 shows the injection rate and event magnitude with time for Case D2. The injection rate increased continuously during injection because of the shear-induced stimulation, but seismicity did not occur. This result is consistent with the theory of rate and state friction (Ruina, 1983), which predicts that the minimum size of a patch that can slip unstably increases with d_c. If the fracture in Case D2 had been large enough, the region of increased fluid pressure would have eventually grown large enough that it would have slipped unstably in a seismic event.

Differences in the rate and state parameters a, b, and d_c in nature help explain why sometimes fractures slip seismically, and sometimes they slip aseismically. Before initiating an injection experiment at a given location, characterization of the parameters a, b, and d_c could be useful for predicting seismic hazard (also discussed in Section 5.4.2).

4.4.12   Comparison of Rate/State Friction to Static/Dynamic Friction

Previously, in McClure and Horne (2010b), injection into a one-dimensional, isolated fracture was modeled using static/dynamic friction instead of rate and state friction (see Section 4.1.3 for a description of static/dynamic friction). The problem setup was similar, but not identical, to the problem setup used in this chapter. A similar approach was used by Baisch et al. (2010), who modeled injection induced seismicity in a two-dimensional planar fault using a block-spring treatment of stress interaction. Many results from McClure and Horne (2010b) and Baisch et al (2010) were consistent with the results from the rate and state modeling described in this chapter. In all three investigations, event magnitudes increased with time as the stimulated region grew larger. Hypocenters migrated away from the injector well. Post-injection events occurred because of redistribution of pressure. Investigation of the effect of injection schedule in McClure and Horne (2010b) were consistent with the results in this chapter. Decreasing injection pressure over time reduced seismicity relative to other strategies. Producing fluid after injection resulted in reduced seismicity.

A difference between the rate and state simulations in this chapter and the results from both Baisch et al. (2010) and McClure and Horne (2010b) is that there were fewer low magnitude events in the rate and state simulations. The models in Baisch et al. (2010) and McClure and Horne (2010b) are examples of "inherently discrete" models (Ben-Zion and Rice, 1993), which tend to model a greater number of smaller events.

4.5 Conclusions

Our modeling suggests that the treatment of friction and stress interaction between elements have a first order effect on the overall behavior of a shear stimulation model.

The episodic crack-like shear stimulation mechanism was identified as the process by which shear stimulation propagated along fractures (also discussed in Section 3.4.2.2). The crack-like shear stimulation mechanism contrasts with the diffusion controlled

mechanism because it involves slip and permeability enhancement advancing ahead of pore pressure perturbation.

If the crack-like shear stimulation mechanism describes shear stimulation realistically, it would undermine assumptions that are sometimes made for the estimation of initial hydraulic diffusivity and the estimation of least principal stress.

Shut-in seismic events occurred because of redistribution of pressure after injection was stopped, a mechanism proposed by several previous investigators. Producing fluid back after injection reduced post-injection seismicity, a strategy that was proposed by Baisch et al. (2006).

Reducing injection pressure over time was identified as a strategy that minimized maximum event magnitude, a result consistent with the findings of McClure and Horne (2010b) using a simpler treatment of friction. This result shows in principle that it may be possible to reduce the magnitude of induced events with injection strategy.

The effect of two geological factors, slip induced pore volume dilation and the characteristic length scale in the rate and state law, were investigated. Results were consistent with past investigators that dilation caused more, smaller events, and that a larger weakening length scale, d_c, led to aseismic slip.

Chapter 5

5 The Effect of Fault Zone Development on Induced Seismicity

It is widely assumed that induced slip on preexisting fractures is responsible for both the induced seismicity and the permeability enhancement in Enhanced Geothermal Systems (EGS). At a given location, the degree of brittle fault formation of the preexisting fractures can be classified along a spectrum from joints or crack-like faults to fully developed, thick faults with cataclasite fault cores. We reviewed data collected at nine projects around the world and found a striking variability in the character of the fractures and faults at each site. There was a correlation between the degree of brittle fault formation and the maximum magnitude of seismic events induced by stimulation. For long term circulation in which injection rate exceeded production rate, the correlation was weaker, but still present. We hypothesize that larger events tended to occur in places with thicker faults due to greater continuity of slip surfaces. An alternative explanation is that aseismic slip tended to occur in places with less developed faults. One factor not fully considered in this study is the predominant orientations of fractures in the preexisting stress field at the different sites, and this issue has the potential to be confounding factor for the correlation. The interactions between frictional properties, lithology, depth, geological heterogeneity, and seismic hazard are discussed. For projects

where only very small seismic events were induced, we offer alternative hypotheses to explain the mechanism of their generation. We conclude by discussing our findings in the context of induced seismic hazard analysis in general. Our results suggest that characterization of fault development should receive more emphasis, both in seismic hazard estimation and in reservoir engineering and modeling.

5.1 Introduction

5.1.1 Background

Fluid injection and production induced seismicity has been documented at many sites around the world (Nicholson and Wesson, 1990; McGarr et al., 2002). Induced seismicity occurs when stress is changed on preexisting fractures so that their shear stress exceeds their frictional resistance to slip according to the Coulomb failure criterion (Jaeger et al., 2007):

$$| \tau |= \mu_f (\sigma_n - P) + S_0, \qquad\qquad\qquad \text{5-1}$$

where τ is shear stress on a fracture, σ_n is normal stress, P is fluid pressure, S_0 is the fracture cohesion, and μ_f is the coefficient of friction. When the failure criterion is exceeded on a fracture, slip occurs. Alternative mechanisms for very small seismic events are discussed later in Section 5.4.5.

Slip is seismic when it occurs rapidly enough to generate seismic waves. Seismic slip occurs because of rapid weakening and restrengthening of the friction coefficient. Rate and state friction theory describes how the coefficient of friction can weaken rapidly as a result of tiny asperities on a fracture surface coming out of contact during slip (Dieterich, 1979, 1992, 2007; Dieterich and Kilgore, 1994). The tendency to slip seismically depends on several factors, including the material properties of the materials contacting in the fracture plane, the temperature, and the stress state (Dieterich et al., 1992; Blanpied et al., 1985; Tembe et al., 2010).

From Equation 5-1, it can be seen that seismicity can be caused by changes in shear stress, normal stress, fluid pressure, or coefficient of friction. Fluid injection and production can induce stress through several mechanisms. These mechanisms include (1) increase in pore pressure from fluid injection and (2) poroelastic or thermoelastic expansion or contraction of the reservoir due to changes in pressure or temperature (Majer et al., 2007). A third mechanism (3) is that slip induced by mechanisms (1) and (2) can cause stress change. Mechanisms (2) and (3) can act at distances greater than the region of pressure or thermal perturbation because stresses can be transferred through the earth at distances beyond the sources of strain that caused them. Stresses induced by these different processes are heterogeneous and anisotropic, and whether they encourage or inhibit seismicity on a given fracture depends on the fracture's orientation and relative location (Segall, 1989). Stress triggering and stress shadow effects have been well documented in studies of seismic hazard (Harris, 2000).

Induced slip in EGS stimulation usually causes extensive microseismicity. In some cases, projects have been associated with seismic events strong enough to be felt at the surface and which may have caused very minor property damage (Majer et al., 2007, 2011; Cladouhos et al., 2010; Evans et al., 2012). For this reason, estimation of induced seismicity hazard has become an important issue for EGS. Experience with EGS could also help understand induced seismicity as it applies to other settings, such as oil and gas hydraulic fracturing (Holland, 2011; Baisch and Vörös, 2011) or CO_2 sequestration (Cappa and Rutqvist, 2011; Nicol et al., 2011; Zoback and Gorelick, 2012).

Several models have been proposed for use in estimation of induced seismicity hazard. In general, a major shortcoming is that they require injection to calibrate their use. It would be desirable to predict induced seismicity hazard prior to initiating injection or prior to drilling a well.

McGarr (1976) proposed that the seismic moment release during injection should be proportional to the volume of fluid injected, a prediction generally supported by subsequent experience comparing seismicity at different locations (McGarr et al., 2002; Nicol et al., 2011; Evans et al., 2012) and during injection at a single location (Bommer et al., 2006; Section 4.2 of Baisch and Vörös, 2009). This effect is also has been

observed in some numerical modeling (Chapter 4; Baisch et al., 2010). However, the scatter in the data is very large. The seismic moment release induced at different EGS projects around the world has varied hugely, even among projects involving similar volumes of water (Evans et al., 2012).

Shapiro et al. (2007) and Shapiro and Dinske (2009) combined the assumption that seismic moment release is proportional to fluid injection with an assumed Gutenberg-Richter (GR) magnitude-frequency distribution. But they did not suggest how the parameters of the GR distribution could be determined prior to injection. The GR distribution might be characterized from observations of background seismicity, but it is not necessarily the case that natural seismicity in a region should have the same GR parameters as induced seismicity. Furthermore, in some settings, there may not be enough natural seismicity to characterize the natural GR distribution.

In order to monitor seismicity in real time during injection, Bommer et al. (2006) proposed the traffic light system. They proposed fitting observed seismicity to a GR distribution in real time during injection. Injection would be stopped if the empirical GR distribution predicted that an event larger than a given threshold might occur during injection (Bommer et al., 2006). This approach was further refined in Bachmann et al. (2011), who investigated the use of different statistical models of seismicity. A potential problem with these approaches is that post-injection seismicity tends to follow a different GR distribution than seismicity during injection (Section 4.1 of Baisch and Vörös, 2009) with a tendency towards larger events (Häring et al., 2008; Baisch et al., 2010). Numerical modeling has suggested that this behavior is likely due to the continued spreading of fluid after injection stops (Section 4.4.3; Baisch et al., 2006; Baisch et al., 2010). Bachmann et al. (2011) examined seismicity at the EGS project in Basel, Switzerland and proposed that the post-injection seismicity could be matched with an Omori-Utsu aftershock distribution. Another important problem is that these methods cannot be used to predict hazard prior to initiating injection.

Triggered seismicity occurs when induced stresses cause a natural earthquake to happen sooner than it would have otherwise. There is an extensive literature on natural triggered seismicity (Freed, 2005; King, 2007; Hill and Prejean, 2007). In EGS seismic

hazard analysis, triggered seismicity has been handled with numerical modeling and consideration of the natural rate of seismicity. The stresses induced by geothermal exploitation are calculated on nearby mapped faults, and those stresses are used to estimate the degree to which the occurrence of natural earthquakes may have been accelerated on those faults (Hunt and Morelli, 2006; Vörös and Baisch, 2009).

Computational modeling could be a useful tool for predicting seismicity prior to injection. A typical strategy in EGS shear stimulation modeling is discrete fracture modeling. The standard workflow is to stochastically or deterministically generate a realization of the preexisting fracture network and then numerically simulate the injection (Chapters 3 and 2; Willis-Richards et al., 1996; Rahman et al., 2002; Ghassemi et al., 2007; Kohl and Mégel, 2007; Bruel, 2007; Baisch et al., 2010; Rachez and Gentier, 2010; Deng et al., 2011). Discrete fracture modeling has the potential to predict seismic hazard directly, by simulating individual seismic events on faults. However, to simulate seismic events in a predictive way, a model would need to compute both the stresses induced by slip and the evolution of friction during an earthquake, which only a few EGS models have attempted (Chapter 4; Baisch et al., 2010). Some modeling studies have attempted to model EGS seismicity without including evolution of friction (Bruel, 2007; Kohl and Mégel, 2007) or as the breaking of bonds between rock particles (Hazzard et al, 2002). Continuum based modeling has been used for modeling of seismicity caused by thermal contraction (Rutqvist and Oldenburg, 2008). Continuum modeling is appropriate for this application because strain cause by thermal contraction is volumetric, and so the induced stresses are less dependent on the details of flow or deformation on individual fractures.

One value of modeling is that by stepping through the workflow necessary to parameterize a model, it can become apparent which uncertainties give rise to the significant model behaviors. This study was inspired by the need for better characterization of fracture system geometry and fault frictional behavior in discrete simulation modeling of EGS. Model inputs regarding fractures that need characterization include frictional properties, storativity, shape and spatial extent, patterns of clustering and connectivity, and permeability anisotropy (within individual fractures, as opposed to bulk permeability).

There are countless situations where fault geometry would have a profound effect on model behavior. For example, Ghassemi et al. (2007) investigated the effect of thermoelastic strains in EGS by modeling injection into a single, planar crack. However, in some EGS projects, flow occurs in fault zones with thicknesses of ten meters or more (Genter et al., 2000). The temperature field and thermal stresses that would develop due to injection into a crack would be very different than injection into a thick fault zone.

In Chapter 6 it is shown how the pressure transient caused by injection would be affected strongly by the inner geometry of storativity and permeability within a fault. In Section 3.4.2.3, it is described how fault storativity may affect the stimulation mechanism. In Section 2.2.3.3, it is described how fault thickness affects calculations of stresses induced by the filling of the fault with fluid.

5.1.2 Effect of Fault Development

A geological unit can be categorized according to its degree of fault development (Fetterman and Davatzes, 2011). Faults can form with a variety of modes of deformation from highly localized and brittle to distributed and ductile (Wibberley et al., 2008). Because in this study we are interested in the development of brittle fault zones, we use a categorization of faulting based on the degree of cataclasite formation, from joints or crack-like faults to well-developed faults with thick cataclasite core and meter scale damage zones.

Intuition would suggest that only fractures that are well oriented to slip in the local stress state contribute to seismic hazard. However, we have not attempted to filter the classifications of fault development based on orientation, primarily because the data was not available in all cases.

These progressive stages reflect the understanding that faults form by the progressive shear and link up smaller faults into larger thoroughgoing features (Segall and Pollard, 1983; Martel et al., 1988; Cladouhos and Marrett, 1996; Wibberley et al., 2008; Griffith et al., 2009; Faulkner et al, 2010). It has also been observed, with significant scatter, that fault thickness scales with displacement and spatial extent (Wibberley et al., 2008).

As an example of a well-developed fault, Figure 5-1 is an illustration from Genter et al. (2000) that depicts a typical fault encountered at the EGS project in Soultz, France. Figure 5-1 is a good schematic but is not the only possible brittle fault geometry. For example, hydrothermal alteration, shown in Figure 5-1, is not necessary. Also, Figure 5-1 does not clearly illustrate a damage zone, which is composed of a high density of fracturing decreasing with distance from the fault core (Faulkner et al., 2010).
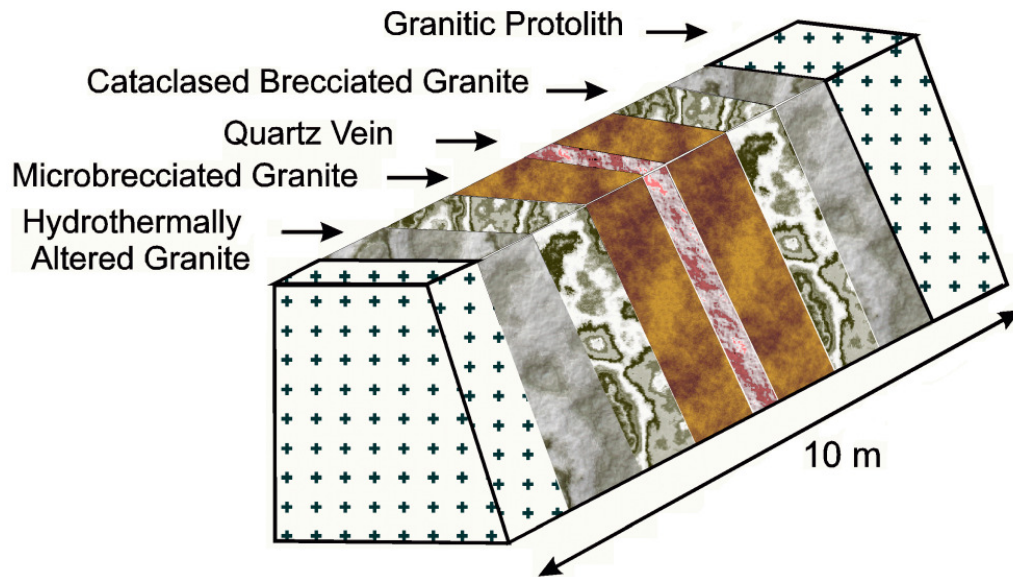
Figure 5-1: Conceptual image of a hydrothermally altered and fractured fault zone at Soultz. From Genter et al., (2000).

Seismic event magnitude scales with the surface area of slip. The seismic moment release during an earthquake is:

$$M_0 = G \int D_{cum} dA ,$$

5-2

where M_0 is the seismic moment, G is the shear modulus, D_{cum} is the shear displacement during the event, and dA is an increment of surface area on the fault (Stein and Wysession, 2003). From Hanks and Kanamori (1979), the seismic moment magnitude M_w is defined as

$$M_w = \frac{\log_{10} M_0}{1.5} - 6.06 \,,$$

where M_w is the moment magnitude and M_0 is defined in units of N-m.

In general, thicker faults have greater spatial extent, and slip over greater spatial extent leads to greater magnitude. Therefore, it would seem reasonable to seek a correlation between fault thickness and induced seismic magnitude. Faults can form in ductile deformation, which could lead to thick, large faults but not a tendency for seismicity. Therefore we categorize faults not only by thickness, but by their degree of cataclasite formation, which should correlate with the degree to which brittle, strain weakening failure has occurred on the fault.

5.1.3 Summary of Results

We reviewed reports from nine projects around the world that involved injection into crystalline rock (mostly EGS projects) and categorized each according to the degree of brittle fault development (DFD). The projects were Soultz, France, Basel, Switzerland, Rosemanowes, United Kingdom, Bad Urach, Germany, Fjällabacka, Sweden, Ogachi, Japan, the KTB Borehole, Germany, Groβ Schönebeck, Germany, and Cooper Basin, Australia. Some major EGS projects, such as Hijiori, Japan, Fenton Hill, USA, and Desert Peak, USA, were not included because we were not able to find enough information to classify DFD with confidence. We investigated only projects in crystalline rock because induced seismicity has been observed to be much more significant in crystalline than sedimentary rocks (Evans et al., 2012). The subject of lithology is discussed further in Section 5.4.2.

In the projects reviewed, degree of fault development was very well correlated with the maximum magnitude induced during or soon after stimulation. In two cases, events during long term circulation (with net injection) were significantly greater in magnitude than events associated with stimulation. Including these circulation events, the correlation between maximum magnitude and DFD was weaker but still present. We

speculate these differences may be caused by geological heterogeneity, discussed in Section 5.4.7.

One possible explanation for the greater magnitudes in places with more developed faults is that larger faults have more spatially continuous slip surfaces that are more conductive to larger magnitudes. This topic is discussed in Section 5.4.1.

Another possible explanation is that there was a correlation between aseismic slip and less developed faulting. This topic is discussed from the point of view of magnitude-frequency distributions in Section 5.4.8.

A possible confounding factor is whether fractures were well oriented to slip in the local stress state. We have not attempted to characterize each project by this criterion. This issue is discussed in Section 5.4.3.

The frictional properties of the materials contacting in the fracture planes affect both the degree of seismicity and the formation of faults. This topic is discussed in Sections 5.4.2 and 5.4.4.

At Rosemanowes, there were joints with spatial extent of tens of meters. Because the seismic magnitudes were so small, these larger joints evidently did not slip entirely during individual seismic events.   We theorize this may have been caused by heterogeneity in frictional properties on fractures (discussed in Section 5.4.2). Another possibility is that the smallest seismic events were caused by mechanisms other than rate and state friction (discussed in the Section 5.4.5).

We conclude by discussing in Section 5.4.9 how our results fit into the larger topic of induced seismicity hazard analysis.

We are not aware of a prior study comparing the effect of fault development between EGS projects. Clearly, degree of fault development is not the only variable that affects induced seismicity hazard, but our results suggest that it should be considered an important variable for estimating hazard.

The striking variety in fault development between different locations suggests that degree of fault development is an important factor for not only induced seismicity hazard, but also EGS reservoir engineering and stimulation design in general. Our results show

the value of performing detailed fracture characterization beyond merely mapping fracture orientations and mapping density with depth.

5.2 Methodology

For each project considered, we categorized the degree of fault development (DFD) and determined the maximum magnitude induced by stimulation. Our results were based on published reports and personal communication with individuals involved in the projects.

In determining the maximum magnitude, we considered only event that occurred during or shortly after stimulation. In most cases, stimulation related events were the largest events observed at these projects. In cases where maximum magnitudes were observed during long term circulation, the results were reported as a separate data point. In one case, an outlier in the maximum magnitude during stimulation was reported as a separate data point.

Classifications of DFD were based only on direct observation: from wellbore core, surface outcrop, mineshaft, and wellbore imaging logs. Imaging logs are not as useful as direct lithological analysis, but comparisons between core and image logs have shown that it is possible to identify large fault zones from image logs (Genter et al., 1997). Observations from the injector wells were preferred, but in some cases observations from nearby wells, outcrops or mines were used.   Because we were concerned with development of brittle deformation, the categories of DFD were focused primarily on the thickness of cataclasite zones. In some cases, a distinctive categorization of DFD could not be made, and the categorization was given in a range.

A more detailed analysis would have made an exhaustive review of the orientations of all fractures observed and calculated their tendency to slip in the present day stress field. Fractures used for categorization would only be drawn from the fractures that were well oriented for slip at the injection pressure. However, in many cases, fracture orientations in the local stress state were not available, and so we did not attempt to integrate fracture orientation into our categorizations.

The categories of DFD were (1) no fractures present, (2) only joints (opening mode fractures) and crack-like faults (thin, planar shear discontinuities) (3) very small faults with at most a few mm thickness of cataclasite, (4) developing faults with a cataclasite zone beginning to develop in a zone with thickness of mm to a few cm, and an altered/damaged zone less than one meter in thickness, and (5) fully developed fault(s) with one or more significant cataclasite fault core zones thickness of tens of cm and an altered/damaged zone with thickness of meters or more. Figure 5-1 is a depiction of what a DFD (5) fault might look like.

5.3 Results

5.3.1 Summary

In the following sections, we briefly summarize the observations of seismicity and DFD at each project. Most projects were in granite, but the KTB and Bad Urach projects were in gneiss.

The results are summarized in Figure 5-2, which shows a plot of degree of fault development versus maximum magnitude.
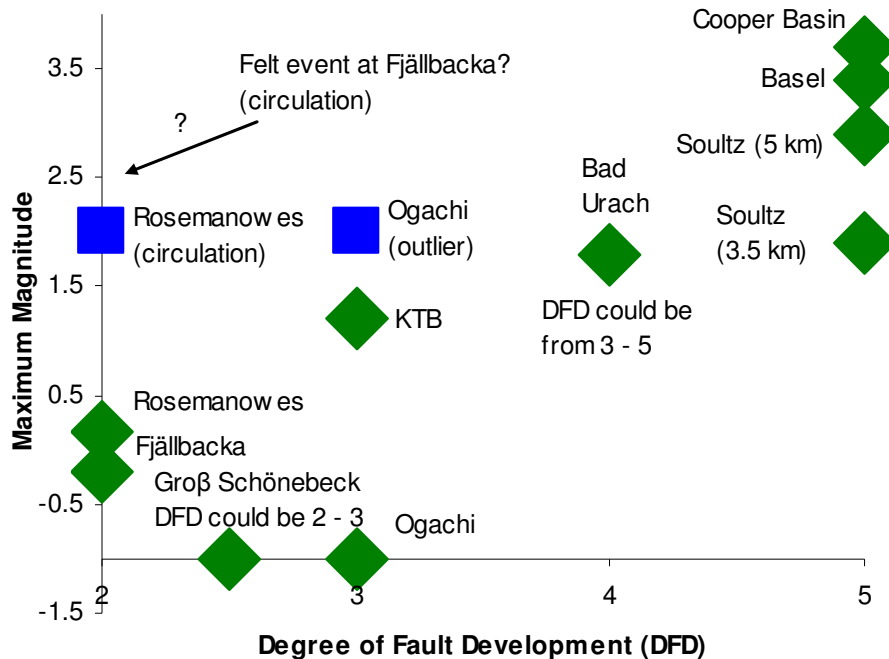
Figure 5-2: Maximum magnitude and degree of fault development. Green diamonds show maximum magnitudes during stimulation. Separately tabulated events that are either outliers or associated with long term circulation are shown with blue squares. See Methodology section, for definition of "degree of fault development."

5.3.2 Soultz

The Soultz project involved several wells that were stimulated in granite at depths around 3.5 km and 5 km during the 1990s and 2000s. Injections involved volumes of tens of thousands of cubic meters of water at flow rates of tens of l/s and wellhead pressures of 5 – 15 MPa (Evans et al., 2012).

The maximum magnitude of the events at 3.5 km depth was $M_w = 1.7$ during injection and $M_w = 1.9$ in the days after injection. During the stimulations of the deeper wells, hundreds of events $M_w > 1.0$ were observed, with the largest reaching $M_w = 2.9$ (Evans et al., 2012). Circulations tests have been performed at Soultz over the course of months, generally with injection rates less than or equal to production rates, and the largest event associated with those tests was $M_w = 2.3$ (Cuenot et al., 2011).

We rated the DFD at Soultz (5). Well core and imaging logs at Soultz showed cataclasite fault cores with thickness of tens of centimeters and damaged/altered zones

with dimensions of ten meters or more (Genter and Traineau, 1996; Genter et al., 2000; Evans, Genter, and Sausse, 2005).

5.3.3 Ogachi

The Ogachi project involved several wells that were stimulated at depths from 700 m to 1100 m during the 1990s (Kitano et al, 2000) in granodiorite (Ito and Kaieda, 2002). Injections for stimulation involved volumes on the order of 3000-10,000 m^3 at rates of tens of l/s and wellhead pressures of 18-22 MPa (Kitano et al., 2000).

Kaieda et al. (2010) reported that the maximum magnitude during stimulation at Ogachi was -1.0, except for a single 2.0 event. We tabulated the maximum magnitude as -1.0, and plotted the $M_w = 2.0$ event separately because it was such a strong outlier.

Permeable zones prior to stimulation were correlated on wellbore image logs to fractures intersecting the wellbore (Ito and Kaieda, 2002). Detailed investigation of a continuous core of one well from 700 to 1100 m showed that the permeable zones were fractures, not faults (Ito, 2003).

Permeability was associated with open fractures at the edges of dykes, in veins and in individual fractures (Ito, 2003). According to Ito (2003), "faults with gouge greater than 5 mm thick were not found at the Ogachi cores, but faults with slickenside and thin gouge (< 2mm) are abundant ... sporadic minor faults without gouge and up to 3 cm of displacement occasionally displace anhydrite veins and andesite dykes."

Hydrothermal breccia zones were identified at Ogachi (Ito, 2003), but we did not count them in our categorization of fault development. Hydrothermal breccias form from implosion of rock into a void space, perhaps associated with fluid boiling (Sibson, 1986). Because hydrothermal breccia forms from opening mode strain, they would not be expected to form continuous cataclasite slip surfaces required for earthquakes. Hydrothermal breccias can be associated with faults, but only at dilatational fault jogs (Sibson, 1986). The hydrothermal breccias at Ogachi are not permeable because they are filled with a very fine grained matrix enclosing clasts, nor are they associated with seismicity (Ito, 2003).

On the basis of these observations, we categorize the DFD at Ogachi as (3), containing faults with no more than millimeter scale gouge.

5.3.4 Basel

The Basel project involved a single well that was drilled into granite to a depth around 5 km and stimulated with around 11,500 m^3 at rates up to 60 l/s and wellhead pressures of 10 – 30 MPa (Häring et al, 2008). Many seismic events occurred during or soon after stimulation that were greater than M_w = 2.0, with the largest being M_w = 3.4 (Häring et al., 2008).

The wellbore was not cored continuously, and there are no any interpretations of the wellbore image logs available in the literature that addressed the topic of fracture zone/fault development. However, on the basis of several sources, we categorized the DFD at Basel as (5) with medium confidence.

Häring et al. (2008) reported that there were two "major cataclasite fracture zones" in the openhole interval of the well. Kaeser et al. (2007) performed a petrological study of cuttings and core at selected intervals from the Basel well. From cuttings Kaeser et al. (2007) concluded "only based on cuttings, no clear conclusions on the extent of deformation can be made ... either true ultra-cataclasite (i.e., composed of very fine-grained material with matrix contents > 90%) ... or fragments of the matrix of a protocataclasite or cataclasite *s.s.* (<50% or 50-90% matrix, respectively, with embedded larger mm- cm-sized rock fragments)" (Section 5.6 in Kaeser et al., 2007). There were five zones in the openhole section of the well where cuttings with evidence of cataclasite were observed (Appendix 2 in Kaeser et al., 2007), including at 4700 m and 4835m, the depths where Häring et al. (2008) reported cataclasite fracture zones.

From these sources (Häring et al., 2008; Kaeser et al., 2007) it is clear that cataclasite fault zones exist in the Basel well, but it is not possible to estimate their thickness. The likely thickness of the faults in Basel can be estimated from comparison with several other wells that were cored nearby in the crystalline basement of northern Switzerland and the southern Black Forest region of Germany (Mazurek et al., 1998). Figure 1-1 in Mazurek et al. (1998) shows the locations of the cored wells and the city of Basel. The

cored wells are located from less than 20 km away to roughly 100 km from Basel. Mazurek et al. (1998) describes pervasive presence of large, well-developed fault zones with decimeter scale cataclasite zones and overall thickness on the order of meters (Appendix F in Mazurek et al., 1998). On the basis of consistent observations from nearby analog wells, cuttings from the Basel well that indicate cataclasite, and the report of Häring et al. (2008) of "major cataclasite zones," we categorized the DFD at Basel as (5).

5.3.5 Bad Urach

The Bad Urach project involved drilling of a single well to a depth of 4444m into gneiss in three stages between 1977 and 1992. The casing shoe was set at 3320 m. The lower part of the casing was perforated within three sections. During the early history of the project, small volume (<100 m^3) high pressure stimulations were carried out at the true vertical depth (TVD) of the wellbore at that time, around 3334. In 2002, after the well had been deepened, 5600 m^3 was injected at rates of tens of l/s and wellhead pressures of 15-34 MPa over the more than 1000 m of openhole at the bottom of the well (Stober, 2011). During the 2002 stimulation, 420 events were detected ranging in magnitude from M_w = -0.6 to M_w = 1.8 (Evans et al., 2012). Prior to the 2002 stimulation, there were no observations concerning seismicity at Urach, and so the maximum magnitude during earlier stimulations is not known (Ingrid Stober, personal communication).

The openhole section penetrates successions of biotite-amphibolite gneiss, migmatitc gneiss, quartz-diorite gneiss, and biotite-cordierite gneiss. Fractures frequently cut across the wellbore, and leached zones are found on either side of the fractures (Stober, 2011).

We were not able to gather enough data to characterize DFD with complete confidence. Here we summarize the available data. Genter (1994) analyzed two cores from Urach, one with length 9m and the other with length 4m. In the 9m long core, K57, cataclasite structures were observed. The thickest cataclasite structure was 5 mm (Albert Genter, personal communication). It is very likely that thicker cataclasite zones were intersected by the well, as the core sampled less than 2% of the openhole section.

Cuttings analyzed from the wellbore contained cataclasite and ultracataclasite. It is believed that larger hydrothermally altered zones were in the range of tens of centimeters and not larger than one meter. From a depth of 2500-3000 m, several hundred meters above the injection zone, there was a very disturbed borehole section with alteration zones, fracture zones and cataclastic zones. (Ingrid Stober, personal communication).

It is clear that fractures were present and cataclasite had formed in some faults. Therefore, the DFD should not be categorized as (1) or (2). The thickest cataclasite zone directly observed in the wellbore was 5 mm, which would be on the border between (3) and (4). Because the wellbore was sampled across only a small percentage of its total length, it is very likely that thicker cataclasite zones than 5 mm are present. There is no data to suggest fault zones wider than one meter were found in the wellbore, but it cannot be ruled out. Therefore we assigned Urach a DFD of (3) to (5), with (4) being the most likely.

5.3.6 Rosemanowes

The Rosemanowes project involved the drilling of three wells to depths around 2 km in the Carnmenellis granite in the UK. The project was active from 1978 to 1991. Several stimulations were carried out involving thousands of m^3 of water at flow rates up to 90 l/s and pressures up to 11 MPa (Evans et al., 2012).

The largest event during stimulation was $M_w = 0.16$. From 1985 to 1989, various circulation tests were carried out with fluid losses averaging 20% over periods of months, effectively constituting long term injection. In 1987, a magnitude 2.0 event occurred several kilometers from the injector, and in 1988 a magnitude 1.8 event occurred near the hypocenter of the first (Evans et al., 2012).

The Rosemanowes project is located in the Cornubian granite batholith in southwest England. Regionally, there is a general trend of NW-SE wrench faulting. Regional scale mapping suggests that large scale faults likely pass through the Carnmenellis granite (Whittle and McCartney, 1989; Whittle, 1989). Therefore, it is known that in the general region of the Rosemanowes project faulting occurs, at least on the regional scale. These

regional studies do not give any information about the nature of the deformation at the inferred faults.

On a smaller scale, the fractures of the Carnmenellis granite have been studied extensively through outcrop study, quarries, and underground mapping from mine shafts. In addition, wellbore imaging logs were run in the Rosemanowes wells. Studies of fracturing in the Carnmenellis granite and at the Rosemanowes site have focused overwhelmingly on descriptions of jointing and have not described observation of cataclasite formation (Ghosh, 1934; Heath, 1985; Randall et al., 1990; Whittle, 1989; Pearson et al, 1989; Richards et al., 1991).

Ghosh (1934) described frequent slickensides in the Carnmenellis granite, but not formation of cataclasite zones. Heath (1985) studied fracture permeability in the Carnmenellis granite in several wells up to 700 m deep that were drilled and cored roughly 10 km from the Rosemanowes EGS project. Heath (1985) reported that displacements of a few mm could be observed on some joints with development of slickensides. Heath (1985) observed that permeability was associated with joints, dykes and veins. Major surface and underground mapping studies were performed as part of the Rosemanowes project, and reports on these studies describe only observation of jointing (Randall et al., 1990; Whittle, 1989). Analyses of wellbore imaging logs at the Rosemanowes wells do not mention any indication of fault development (Pearson et al., 1991).

Studies of fracturing within the Carnmenellis granite consistently describe joints, dykes, veins, and very simple crack-like faults. We assigned the DFD at Rosemanowes to be (2).

5.3.7 Fjällbacka

The Fjällbacka project involved drilling, stimulation, and circulation between two wells roughly 500 m deep in granite. During the main stimulation in 1986, 400 m^3 of viscous gel and water were injected at rates from 20 - 30 l/s (Wallroth et al., 1999) into a 31 m zone near the bottom of the well, sealed by an inflatable packer (Eliasson et al., 1990) at injection pressure up to 13 MPa (Evans et al., 2012). It should be noted that this

project involved a shallower depth and a lower volume of water than the other projects discussed in this study.

During the 1986 stimulation, 74 events were recorded, with magnitudes ranging from $M_w = -1.3$ to $M_w = -0.2$ (Evans et al., 2012). During a 1989 circulation experiment, which had 50% recovery of fluid, a seismic event occurred that was felt by project employees. The magnitude was not determined (Evans et al., 2012).

One of the wells at the Fjällabacka project was cored continuously to 511 m. Hydrothermally altered fractured zones were observed, including the development of smectite. There was no report that cataclasite or any development of faults was observed in the wellbore core (Eliasson et al., 1990).

In contrast with the direct wellbore observations, Eliasson et al. (1988) reported that surface mapping showed "morphological lineaments (fracture zones and large fractures)" with "not seldom a length of several kilometers thus indicating a large vertical extension." Details of these lineaments, such as whether they contained cataclasite, were not provided.

Because subvertical fracture zones were not observed in the wellbore, despite 511 m of continuous core, the Eliasson et al. (1988) report was not included in the classification, and DFD was classified as (2). Because Eliasson et al. (1988) gave at least some evidence (though vague) that there could have been more developed faults in the area, there is some uncertainty in the DFD classification of (2). Clearly, no larger faults intersected the wellbore, but we cannot be completely sure that there were not larger faults nearby, which would justify a larger rating, possibly up to (5).

Fault classification did not incorporate orientation, but if they had, the potentially present larger, subvertical fractures would have been ruled out due to the local stress state. At the depth of stimulation, the vertical principal stress was the least principal stress (Jupe et al., 1992; Wallroth et al., 1999). Jupe et al. (1992) performed critical stress analysis on the fractures observed on the borehole televiewer and found that the subhorizontal fractures were much more likely to slip. They reported that the injection pressure may have been just at the threshold of making it possible for the subvertical fractures to slip. Jupe et al. (1992) also reported that focal mechanisms from events were

consistent with slip on subhorizontal fractures. Hydraulic tests from the wellbore demonstrated that flow zones correlated with subhorizontal fractures and that vertical permeability was low (Wallroth et al., 1999). Finally, the overall spatial shape of the microseismic showed horizontal propagation (Jupe et al., 1992).

5.3.8 KTB

The KTB project involved a continuously cored pilot hole to 4000 m from 1987 to 1989 and a deep borehole to a depth of 9101m from 1990 to 1994. The wells were drilled through paragneisses and metabasites (Hirschmann et al., 1997). Three major injections were carried out. In 1994, about 200 m^3 was injected into the main borehole at up to 9 l/s. The water was injected into the 70 m openhole section at the bottom of the well (Zoback and Harjes, 1997). In 2000, 4000 m^3 of water was injected into the main borehole at rates up to 1.2 l/s. During the second experiment, seismicity clustered at 3.3 km, 5.4 km, and 6.6 km in addition to the bottom of the wellbore, likely because of casing leaks at the shallower depths (Evans et al., 2012). From 2004-2005, 84,600 m^3 water was injected over ten months into the pilot hole openhole section from about 3850-4000 m depth (Shapiro et al., 2006).

In the depth range of 3-6 km, the largest seismic event observed during any of the injection experiments was $M_w = 0.5$. At the depth of 9 km, the largest magnitude event observed was $M_w = 1.2$. The $M_w = 1.2$ event occurred during the initial injection test, and in the subsequent injection tests, there was never an event larger than $M_w = 0.5$ (Evans et al., 2012).

The continuously cored pilot hole to 4000 m is the best source of information about the character of the fracture network. It is not certain how well those data can be extrapolated to the depth of 9000 m of the full hole, which introduces significant uncertainty. Our assignment of DFD was based on the cored pilot hole. Various significant fault zones were observed at various depths throughout the both the pilot and deep boreholes (Hirschmann et al., 1997). Zulauf (1992) did a detailed examination of the fracture networks intersecting the pilot hole. Zulauf (1992) inferred various stages of deformation leading to different sets of fractures and faults. In the upper 2000 m of the

wellbore, cataclasite zones with thickness up to 5 cm were observed. This depth range is far above the injections, and so these observations were not used for the assignment of DFD. Below 2000 m, the thickest cataclasite zones were a few millimeters. There were fault zones with thickness of meters. Within the fault zones, there were many thin cataclasite zones spaced from a few centimeters to decimeters apart. These faults do not appear to be associated with purely brittle faulting mechanisms. The deformation is significantly less localized than in faults with layers of cataclasite centimeters or decimeters thick. Instead, deformation is spread across a large number millimeter thickness cataclasite zones. In many cataclasite zones, there were high concentrations of graphite (Zulauf et al., 1990). In some cases, there was evidence of semibrittle deformation, with quartz minerals fracturing, but biotite and muscovite minerals deforming plastically (Zulauf, 1990). Brittle deformation is associated with the strongest strain weakening, which tends to localize failure (Ben-Zion and Sammis, 2003). The rather distributed strain in the fault zones is likely due to ductile failure.

On the basis of the observations from the cored pilot holed, the DFD at KTB is categorized as (3). Meter scale thickness faults were present, but they were associated with ductile or mixed ductile-brittle deformation and contained zones of cataclasite no thicker than a few millimeters.

5.3.9 Groβ Schönebeck

The Groβ Schönebeck project involved the stimulation of a well drilled to a depth around 4175m with casing set about 40 m above the bottom of the wellbore. The bottom section of the hole was drilled through volcanic andesites, and above that the well was completed with perforations through casing in sandstone. The volcanic section of the wellbore was stimulated with 13,170 m^3 at flow rates alternating between around 20 l/s and around 150 l/s. The injection well head pressures alternated between around 30 MPa and around 50 MPa (Zimmermann et al., 2008; Moeck et al., 2009). Subsequently, the sedimentary layer was stimulated at two depths with about 500 m^3 of water and 100 tons of proppant. The largest magnitude earthquake detected was -1.0 (Moeck et al., 2009).

The only data available to characterize DFD is wellbore imaging logs and a few meters of core from the volcanic section. Neither the core nor the wellbore imaging logs showed any indication of fault or fracture zones (Günter Zimmermann, personal communication). Therefore we categorized DFD as either (2) or (3).

5.3.10   Cooper Basin

The Cooper Basin project involved the drilling of four wells between depths of 4-5 km in granite, starting in 2003. The largest event that occurred at the Cooper Basin site was M_w = 3.7 and occurred during the stimulation of the well Habanero 1 in 2003. During that stimulation, 20,000 m^3 was injected at flow rates up to 50 l/s, and injection pressures up to 60 MPa (Asanuma et al., 2005).

Wellbore imaging logs have been run over approximately a 2000 m combined in the granite sections of the four wells at the Cooper Basin project. Thick fault zones have been observed in the image logs. In the wellbore imaging logs, the major fault zones contain a core with thickness of a few meters, surrounded by subsidiary fracturing within ten meters of the core (Doone Wyborn, personal communication). This observation is consistent with the standard model of a brittle fault in granite (Figure 5-1; Genter et al., 2000; Faulkner et al., 2010). Therefore, even though core is not available to confirm, the wellbore imaging logs give strong evidence of large scale faulting. We categorized the DFD as (5).

5.4 Discussion

5.4.1 Slip Surface Continuity

Figure 5-2 shows that there is an excellent correlation between the degree of fault development and the severity of induced seismicity. The simplest explanation is that thicker, more developed faults have greater spatial extent, and greater surface area of slip during a seismic event causes greater magnitude. Ruptures should find it much easier to propagate across a continuous, large fault than a collection of smaller faults or joints.

Any discontinuity in a slip surface should be considered a barrier to rupture propagation. A powerful stress concentration is generated at the rupture front of an earthquake, and the stress concentration helps the earthquake to propagate (Freund, 1990). Stress concentration weakens with distance from the rupture, and so any discontinuity in the slip surface will tend to create a barrier to propagation. Wesnousky (2006) found that ruptures tended to terminate at fault steps during earthquakes on the San Andreas Fault.

It is conceivable that multiple fractures or faults could slip during a single seismic event, combining their surface area to effectively form a larger surface area than their thickness would suggest possible. The case of many smaller faults organizing into a single large event has been hypothesized to be the mechanism of seismicity at Basel (Häring et al., 2008). Häring et al. (2008) observed strike-slip focal mechanisms oriented in NS-EW planes but seismicity organized into a planar feature oblique to that orientation at NNW-SSE. Häring et al. (2008) also observed several distinct arrivals in the seismic signal, suggesting that the seismic events consisted of slip on several slip surfaces. This mechanism is consistent with outcrop studies of faults granite that describe en echelon arrays of faults connected by tensile steps (Segall and Pollard, 1983; Martel et al., 1988; Griffith et al., 2009). In the brittle regime, faults form complex geometries generally made up of many shear fractures that have linked together (Faulkner et al., 2010). A feedback loop develops between strain weakening and localization of deformation that lead to progressive localization of strain onto fewer, more significant features (Ben-Zion and Sammis, 2003). Therefore, even large fault zones likely do not have perfectly continuous slip planes. But they are likely to be formed of collections of slip planes that have naturally developed over time to align and be spatially clustered in such a way as to be conducive to rupture propagation. These closely aligned slip planes might be considered a single fault. Faults consisting of many slip planes have far greater spatial continuity than distributions of joints or fractures that formed in mechanisms other than brittle faulting.

Continuity of slip surfaces may not be the full explanation. At Rosemanowes, surface outcrops suggested that joints commonly had spatial extents of 80 m or more (Whittle, 1989). The seismic moment of a circular crack embedded in a linear elastic material is (Kanamori and Anderson, 1975):

$$M_0 = \frac{16}{7} r^3 \Delta\sigma \, ,$$

where r is the radius and $\Delta\sigma$ is the stress drop. Assuming a radius of 40 m and a stress drop of 1 MPa, the moment would be 1.5×10^{11} N-m, which corresponds (Equation 5-3) to a magnitude of 1.39.   Other than the two events that occurred during long term circulation, no events at Rosemanowes came close to being that large. Based on this analysis, entire joints almost never failed in a single seismic event at Rosemanowes.

It is not clear how to explain the observation that entire large joints apparently never failed during a single seismic event at Rosemanowes. One possibility is that joint sizes based on surface outcrop are not representative of joint sizes at depth. A second possibility is that reported individual joints were not actually single, continuous fractures. A third is that the natural surface roughness of the joints inhibited rupture propagation. A fourth is that the frictional properties of the joints and their infilling was not favorable for seismic slip, and seismic events were limited to small regions of heterogeneity on the joints where unstable slip was frictionally favorable (Section 5.4.2). A fifth is that seismic slip was entirely unfavorable according to a rate and state framework (discussed in Section 5.4.2), and other mechanisms are needed to explain the presence of seismicity (discussed in Section 5.4.5). A different possibility is that stress drops on the fractures were very low, a phenomenon that would be related to the frictional characteristics of the fault.

5.4.2 Seismic and Aseismic Slip

Whether faults tend to slip seismically or aseismically clearly matters for induced seismicity.   Seismic slip occurs when friction weakens rapidly on a fault as a consequence of tiny asperities on a fracture surface coming out of contact during slip (Dieterich, 1979, 1992, 2007). According to rate and state friction theory, the friction on a fault is function of sliding velocity v, and the average duration of contact for contacting asperities (called state), θ:

$$\mu_f = f_0 + a\log(\frac{v}{v_0}) + b\log(\frac{\theta v_0}{d_c}),$$

<div style="text-align: right">5-5</div>

where f_0, v_0, a, and b are constants and d_c is the characteristic weakening distance. According to rate and state friction theory, seismic slip should only be possible if the parameter a is less than the parameter b, a condition referred to as velocity weakening. The condition $b > a$, is referred to as velocity strengthening (Dieterich, 2007).

Whether or not rate strengthening or weakening conditions exist depends strongly on composition of the fault gouge and the temperature. The exact composition of a fault gouge would depend on the protolith and the history of mineral alteration. Unfortunately, rate and state experiments have not been carried out in a wide range of gouges and temperatures. The most relevant experiments to faulting in granite were carried out by Blanpied et al. (1995), who performed experiments on wet fractures in granite and found two transitions between velocity strengthening and weakening. They found a transition from strengthening to weakening around 25°C-100°C and a transition from velocity weakening to strengthening around 250°C-300°C. These results are risky to apply in general because the frictional dependence on temperature may vary depending on the specifics of gouge. For example, den Hartog et al. (2012) studied the temperature dependence of friction for simulated fault gouge of illite shale and found rate strengthening behavior for the temperatures up to 250°C. He et al. (2007) studied the temperature dependence of friction in fractures in gabbro and found rate weakening behavior only in the temperature range 200°C to 310°C. Tembe et al. (2010) investigated the frictional behavior of mixtures of quartz, montmorillonite, and illite at room temperature in wet conditions. They found a general trend of increasing rate strengthening and decreasing friction coefficient with increasing clay content in the mixtures.

These results are obviously highly relevant to the issue of induced seismicity, but it is not clear how reliably they could be applied in practice because of the complexity of natural systems and the limited number of the experiments that have been carried out. Nevertheless, the understanding that seismicity depends on the frictional properties of the fault can be instructive. Several general principles can be gleaned from experiments.

First, increasing clay content contributes to aseismic slip and a weaker coefficient of friction. Second, temperature plays a role, with seismic slip favored only in certain temperature ranges.

Frictional behavior appeared to play a role in seismicity at the KTB borehole, where seismicity was mild. In this case, there was clear evidence of ductile and aseismic slip from core (Zulauf et al., 1990, 1992). Even at Soultz, where there were large cataclasite zones and significant seismicity, evidence suggested considerable aseismic slip may have taken place, at least in the shallower reservoir at 3.5 km (Cornet et al., 1997). Some fault zones at Soultz contained significant concentrations of illite (Evans, Genter, and Sausse, 2005), which has been associated with weaker friction (Tembe et al., 2010) and aseismic deformation (den Hartog et al., 2012). The experience at the shallower Soultz wells suggests that aseismic slip could be possible even in places with thick cataclasite zones. This is especially true because faults could have formed in the past under brittle failure but have subsequently begun to deform aseismically due to alteration related changes in mineralogy, changes in depth, or changes in temperature. The implication is that characterization of mineralogy within faults could be important for induced seismicity hazard estimation.

Evans et al. (2012) noted that induced seismicity is far more likely to be an issue in crystalline than sedimentary rock. We can speculate that this may be a result of a tendency for aseismic, rather than seismic slip on faults that form in sedimentary rocks. This could be a consequence of the different minerals that are likely to form in gouge from different protoliths.

5.4.3 Fracture Orientation

It is well known that orientation affects whether or not a fracture will slip in the local stress field. The fracture shear stress, τ, and normal stress, σ_n, in Equation 5-1 are functions of both the stress state and orientation. This relationship is typically displayed graphically with a Mohr's circle diagram (Jaeger et al., 2007). While there is always a particular fracture orientation that is most optimal to slide in the local stress state

(assuming particular values for μ and S_0), increased fluid pressure can allow fractures of a wide variety of orientations to be able to slide (Zoback et al., 2012).

In a particular location, fracture orientations tend to be clustered into a small number of fracture sets. Given data about fracture orientation, the local stress state, and fluid pressure, critical stress analysis can be performed to calculate which fractures will be able to slide. Clearly, if there are few (if any) fractures oriented optimally to slide in the local stress field, seismicity would be expected to be significantly reduced.

We have not attempted to perform a critical stress analysis for all of the projects in this study. Therefore, fracture orientation remains a potentially confounding factor that is not accounted for in this study. However, a comparison between two projects, Soultz and Rosemanowes, shows that fracture orientation alone is not capable of explaining the observations. It has been well documented that there were abundant fractures well oriented to slip in the local stress field at Soultz (Evans, 2005) and Rosemanowes (Pine and Batchelor, 1984). Yet these two projects had very different maximum magnitudes, 2.9 and 0.16, respectively (Figure 5-2).

5.4.4 Dependence on Depth

In the projects we studied, there was a correlation between project depth and maximum magnitude. Evans et al. (2012) also a noted a relationship between depth and seismicity. This was particularly evident at the Soultz project, where the shallower reservoir had a significantly lower maximum magnitude than the deeper reservoir.

Based on the results discussed in Section 5.4.2, we can speculate that the higher temperatures at greater depth contribute to more friction weakening behavior. Another possible depth effect is that clays, which are generally associated with aseismic slip, are not stable at higher temperatures. For example, clay minerals have been observed to occur no deeper than certain horizons at the Coso and the Desert Peak geothermal fields (Kovac et al., 2005; Davatzes and Hickman, 2009, 2010; Lutz et al., 2010). The clay smectite was identified in the shallowest and lowest temperature project that we reviewed, Fjällbacka (Eliasson, 1990). At Soultz, illite was found in some fault zones (Evans, Genter, and Sausse, 2005), which may explain the lower magnitudes at shallower

depth at Soultz. Davatzes and Hickman (2010) described how temperature, clay formation, and fault development interact to control the thermal and permeability regime of the Coso geothermal field.

Another obvious effect of depth is that deeper faults are under greater stress, which would tend to lead to greater stress drops and higher magnitudes. However, stress could account for only rather mild variations in induced magnitudes.

To fully detangle the effects of depth and fault zone development would require more data. Unfortunately, in our dataset there were no deep projects in granite with undeveloped fault zones nor were there shallow projects with well-developed faults.

5.4.5 Alternative Mechanisms of Acoustic Emission

It is widely acknowledged that earthquakes are caused by slip on preexisting faults, and rate and state friction is the leading theory to explain the frictional evolution that leads to seismic slip. However, in this section we discuss an alternative hypothesis to explain seismicity in locations where seismic events were very small. In this hypothesis, seismic slip was not favorable at these locations according to a rate and state mechanism. Instead, events may have been caused by alternative mechanisms. Rate and state is by far the most likely explanation for larger events, perhaps $M_w > 0$, but these alternative mechanisms may be reasonable hypotheses to explain smaller events.

This discussion is motivated especially by the observations at Rosemanowes, where joints with spatial extent up to 80 m have been observed in outcrops, yet the maximum magnitude during stimulation was $M_w = 0.16$. As discussed Section 5.4.1, these small magnitudes imply that entire joints never slipped during a single event. Yet this is somewhat surprising, because if a seismic event was able to nucleate, the intense concentration of stress at the rupture front would tend to cause the rupture to continue to propagate (Chapter 4). There may be a rupture mechanics explanation for this phenomenon that is consistent with rate and state friction. The most obvious is that due to heterogeneity, seismic events were only frictionally favorable on small patches of the fractures. They nucleated on those patches and then arrested as they propagated into

regions where seismic slip was not favorable. However, in this section we investigate the alternative hypothesis.

During triaxial compression tests, intact samples of rock are strained axially until failure while a confining radial stress is applied. Acoustic emissions are observed consistently during these experiments. Prior to failure, the acoustic emissions are distributed throughout the rock sample, but during failure they localize around the failure surface (Lockner et al., 1991; Lockner, 1993; Jaeger et al., 2007). Experiments with intact samples of granite (Lockner et al., 1991; Jaeger et al., 2007) show that deviatoric stresses of hundreds of MPa are necessary to induce the generation of a new shear fracture. The greater the confining pressure, the greater the deviatoric stress required to initiate failure (Jaeger et al., 2007).

Because of the great strength of intact rock, especially granite, it is unlikely that major fracturing occurs through the failure of intact rock during stimulation. Supporting this conclusion, zones of enhanced permeability are correlated with zones of preexisting fractures (Pearson et al., 1989; Wallroth et al., 1999; Ito and Kaieda, 2002; Evans et al., 2005). The tensile strength of granite, and all rocks, is far less than the compressive strength, on the order of MPa (Jaeger et al., 2007). Both failure of intact rock and failure of preexisting fractures can be described using Equation 5-1, the Coulomb failure criterion, but the cohesion, S_0, of intact rock is on the order of tens or hundreds of MPa, while the cohesion of an individual fracture is on the order of MPa (Jaeger et al., 2007). Because of these different strength thresholds, shear slip of preexisting fractures or propagation of tensile cracks would be expected to happen during injection, not extensive failure of intact rock.

Keeping in mind these strength considerations, we can speculate about alternative mechanisms that could lead to very small seismic events. One possibility is abrupt loss of cohesion, S_0. This might occur, for example, if a joint were sealed shut by mineralization. The chemical bonds of the mineralization might be abruptly broken in a section of a joint. The shear strength of a mineralized joint would be much lower than the strength of intact rock (Papaliangas et al., 1993; Armand et al., 1998). Flow is known to be highly channelized during flow within individual fractures (Auradou et al., 2006),

and so events might be caused by the breaking of mineralization in low permeability regions of a fracture surrounded by higher permeability channels. Fluid pressure would be elevated in the higher permeability channels, leading to their slipping earlier and then subsequently triggering rapid slip on the surrounded lower permeability regions as the mineralization is broken. This mechanism involves slip on preexisting fractures but is quite different from the mechanism described by evolution of rate and state friction in Equation 5-5. Rate and state friction would allow seismic slip to occur repeatedly at a given location on a fracture (Chapter 4), which would make slip across an entire joint more likely. Abrupt failure of mineralization could only happen once at a location, making it possible that fractures could fail in a series of smaller events that never encompass the surface area of an entire large fracture.

Stress concentrations can be very strong locally near the tip of a fracture that has slipped. Concentrations of stress can generate both compressive and tensile forces in different locations relative to the tip (Sibson, 1986). These local stress heterogeneities might cause development of either tensile fracturing or possibly even compressive failure of intact rock. Aki et al. (1977) theorized that jerky growth of a tensile fracture could result in microseismicity. Observations from triaxial tests demonstrate that compressive failure of intact rock can result in emission of acoustic waves (Lockner et al., 1991; Lockner, 1993).

These alternative mechanisms would not be able to generate significantly sized microseismic events. However, they could explain the occurrence of seismicity in places where magnitudes are very small. These mechanisms could explain microseismicity in places where fractures do not have rate and state frictional characteristics needed for rapid slip.

5.4.6 Background Seismicity

Evans et al. (2012) noted that induced events tended to be more significant in places with stronger natural seismicity. It is natural that seismically active regions would tend to contain more significant fault zones because seismicity occurs because of slip on faults and over time seismicity helps form faults. However, low natural seismicity does not

preclude the occurrence of significant induced seismicity. The natural seismic hazard at Soultz is rather low (Evans et al., 2012), yet relatively large events were triggered ($M_w >$ 2.5). Even if modern strain rates are too low to generate seismicity and cause significant fault formation, faults may have formed in the past and could slip seismically if placed under elevated fluid pressure.

5.4.7 Outlier Events and Geological Heterogeneity

At the Ogachi, Rosemanowes, and Fjällbacka projects, there were one or two events that were much greater in magnitude than the others. At Rosemanowes and Fjällbacka, these events occurred during long term unbalanced circulation experiments. These circulations involved the injection of more water than was produced, which means that they constituted long term injection (Evans et al., 2012; Kaieda et al., 2010). It is not possible to give a certain explanation for these events, but we speculate they may have been caused by geological heterogeneity.

In a statistically homogeneous region, a fault could not be present that was radically larger or otherwise different than the population of faults sampled in a statistically significant length of a wellbore. Power law distributions of fault sizes are commonly observed, and this has been theorized to be caused by the mechanism of fault growth by which smaller faults progressively link up to develop larger features (Cladouhos and Marrett, 1996). However, sharp discontinuities in statistical homogeneity are common in the earth. Because of heterogeneity, faults observed at a wellbore do not necessarily have to be representative of faults in the surrounding earth. In adjacent lithological units, potentially with different ages, and chemical and mechanical properties, faulting might develop differently. Even in a seemingly homogeneous region such as a granitic batholith, different units of granite can exist with significantly different fracture densities and orientations. For example, several different lithological units have been described in the granite at Soultz (Dezayes et al., 2010).

Large faults can be found at the interface between facies. One possible explanation is that interfaces are mechanically weaker, which would encourage strain localization. Another possible explanation is that large faults create large offsets, juxtaposing two

different facies. For example, at Soultz, a large fault is located at the boundary between two types of granite (Dezayes et al., 2010). A fracture zone is reported at a lithological boundary at the EGS project at Desert Peak in Nevada (Davatzes and Hickman, 2009). A fault juxtaposing granite and volcanic rocks is inferred to be located roughly 500 m from the Ogachi test project (Suzuki and Kaieda, 2000).

During long term net injection, injected fluid could spread a greater distance away from the wellbore than during stimulation, increasing the possibility that the pressure could be perturbed on a fault that is statistically differently than the faults in the immediate vicinity of the wellbore. In addition, thermal contraction of the reservoir due to injection of cooler water would cause volumetric strain, which could perturb stress a considerable distance from the injector and producer wells (Segall, 1989; McGarr et al., 2002).

The circulation related event at Rosemanowes was around $M_w = 2.0$, and the magnitude of the circulation related event at Fjällbacka is unknown, but it was strong enough to be felt at the surface (Evans et al., 2012; Kaieda et al., 2010). During circulation tests in the deep reservoir at Soultz from 2005-2010, many seismic events occurred, with a maximum magnitude of $M_w = 2.3$. These circulation tests at Soultz were generally carried out with production rates equal to or greater than reinjection rates (Cuenot et al., 2011). Events during circulation were much larger than events during stimulation only for projects where the stimulation events were very small. For the case of Soultz, where the stimulation events were relatively large, the circulation events were of somewhat lesser magnitude.

5.4.8 Magnitude-Frequency Distribution

It is widely acknowledged that natural earthquake magnitude-frequency distributions roughly follow a power law scaling of frequency and size. The most widely used is the Gutenberg-Richter distribution:

$$\log n(M) = a - bM \;,$$
<div style="text-align: right">5-6</div>

where $n(M)$ is the cumulative number of events with magnitude M or higher over a given time period, and a and b are constants, distinct from the a and b constants used in the rate and state friction law, Equation 5. The variable a reflects the general level of seismic activity. The variable b reflects the relative frequency of different magnitudes. In natural earthquakes, the value of b is typically found between 0.6 and 1.1 (Utsu, 2002). The value of b is often higher in the case of volcanic tremors (Rierola, 2005; Farrell et al., 2009) and induced seismicity (Downie et al., 2010).

The value of b is available in the literature for several of the projects investigated in this chapter: 1.58 during injection at Basel and 1.15 after injection at Basel (Bachmann et al., 2011), 0.83 at Cooper Basin (Baisch et al., 2009), 0.86 at KTB (Haney et al., 2011), 1.5 at Soultz (estimated from Figure 9 in Baisch et al., 2010), and 1.1 at Ogachi (Hideshi Kaieda, personal communication). The b value at Fenton Hill (which is not investigated in this chapter) was 1.5-1.9 (Fehler and Phillips, 1991).

In this limited sample, there is no trend between b value and maximum magnitude. The KTB and Ogachi projects had b values lower than Basel or Soultz, yet had much lower maximum magnitudes. Therefore, not only were the maximum magnitudes smaller at KTB and Ogachi, there were far fewer smaller events as well. Yet in all four projects, 1000s of m^3 of water were injected at comparable fluid pressures, triggering slip on preexisting fractures. This observation demonstrates that most of the deformation taking place at KTB and Ogachi must have been aseismic. The constant of proportionality between seismic moment release and injected fluid volume (as postulated by McGarr, 1976) is many orders of magnitude lower for KTB and Ogachi.

It is worthwhile to ask whether the magnitude-frequency distribution is related to the distribution of fault sizes. If every fracture in a stimulated rock volume slips once, independently, and fully in a single event, then the magnitude-frequency distribution will reflect the distribution of fracture sizes. Of course, this is a simplification because fractures can slip multiple times, only part of a fracture may slip, or multiple fractures may slip during a single event.

If significant aseismic slip occurs, magnitudes and fracture sizes could be decoupled. For example, seismic slip could be frictionally unfavorable ($a > b$) everywhere in the formation except for certain patches of material heterogeneity. These patches could be smaller than the maximum fracture size, and as a result, only parts of fractures (not whole fractures) would slip seismically. In this case, the magnitude-frequency distribution would be related to both the distribution of material heterogeneity and fracture size.

According to the discussion in Section 5.4.1, more developed faults tend to be larger, and larger faults are required for larger earthquakes. An implication of this theory would be that at sites without large faults (but ample seismic slip), there should be a truncation of the magnitude-frequency distribution, with a large number of smaller events, but sharp reduction in the number of larger events.

Are truncations in magnitude ever observed? An example from the literature is the sandstone/shale hydraulic fracturing treatment described by Downie et al. (2010). Figure 11 of Downie et al. (2010) shows a clear truncation of magnitude frequency starting around -1.0. Extrapolation of the trend line would suggest that the maximum magnitude should have been around 0.5, yet it was actually -0.5. Fehler and Phillips (1991) analyzed events at Fenton Hill. Figure 11 of Fehler and Phillips (1991) shows that extrapolation of the "PC-1" line suggests that the maximum seismic moment should have been around 10^{19} dyne-cm ($M_w = 1.9$) but was actually around $10^{17.5}$ dyne-cm ($M_w = 0.9$) (from the "TENT" dataset). Elevated b values during earthquake swarms may be a consequence of a large amount of strain taking place in a section of the subsurface where large faults are not present, forcing to the strain to occur in a larger number of small events. These results are interesting, but further data would be needed to draw any firm conclusions.

Overall, it appears that one possible explanation for the correlation between degree of fault development and maximum magnitude is that regions with undeveloped faults tend to have aseismic slip.

5.4.9 Seismic Hazard Analysis

In this section, we discuss how this study fits into the broader topic of seismic hazard analysis. As discussed in the introduction, there are two important mechanisms of

induced seismicity: direct pressure perturbation and volumetric contraction/expansion of the field from poroelastic or thermoelastic forces. The spatial and time scales of these mechanisms may be different.

In EGS stimulation, direct pressure perturbation during injection occurs over a period of days in a region that is localized around a wellbore. In this case, induced seismicity is unmistakably correlated to the injection. The largest seismic event ever caused by EGS stimulation is probably the $M_w = 3.7$ event during the Cooper Basin project (Majer et al., 2007).

If long term EGS circulation is unbalanced (more fluid is injected than produced), there will be a long term spreading of a pressure perturbation over greater time and length scales than during stimulation. Unbalanced EGS circulation could be compared to deep injection projects in crystalline rock such as at Rocky Mountain Arsenal, Colorado, Rangely, Colorado, and Ashtabula, Ohio (Nicholson and Wesson, 1990; McGarr et al., 2002). The maximum magnitudes associated with injection at these sites was $M_w = 4.85$, $M_w = 3.6$, and $M_w = 3.1$, respectively. These projects involved injection over months and years of much greater volumes of water than are injected during EGS stimulation.

Thermal contraction of a reservoir occurs slowly and the stress perturbation can be spread some distance from the region where the rock is actually cooled (Segall, 1989; McGarr et al., 2002). Induced seismicity from thermal contraction may also be correlated to the geothermal production, but it is not as obvious and direct. Hazard from thermal contraction induced seismicity is the same for EGS projects as it is for geothermal projects in general. The largest geothermal field in the world, the Geysers, California, has hosted some of the largest induced events, the largest being $M_w = 4.6$ (Majer et al., 2007). These are likely caused by thermal contraction from massive injection of cool water into the reservoir (Rutqvist and Oldenburg, 2008).

As noted in Section 5.1.1, McGarr (1976) proposed that the seismic moment release during injection should be proportional to the volume of fluid injected. His prediction has generally been supported by subsequent experience comparing seismicity at different locations (McGarr et al., 2002; Nicol et al., 2011; Evans et al., 2012) and during injection at individual sites (Bommer et al., 2006; Baisch and Vörös, 2009, section 4.2).

To extend the idea of McGarr (1976) somewhat, the induced seismic hazard scales with spatial extent of the stress perturbation, whether it is direct fluid injection or thermal contraction. With that in mind, it is evident that the scale of the stress perturbation caused by EGS stimulation is smaller than the scale of long term injection or thermal contraction. Therefore, in the long term, seismic hazard from thermal contraction and unbalanced circulation should be greater than hazard from EGS stimulation. This suggests that long term unbalanced circulation in an EGS system would significantly increase seismic hazard, as it would for any subsurface project. In the case of long term balanced circulation, seismic hazard would arise mainly from thermal contraction. Seismic hazard from thermal contraction should be the same for EGS as for geothermal in general.

Both theoretical considerations and the empirical results from this study suggest that short term hazard from EGS stimulation are well predicted by characterization of the faults and fractures intersecting the wellbore. Observations of outlier events at Ogachi, Rosemanowes and Fjällbacka suggest that long term seismic hazard may be less well predicted by characterization of fracture networks. This is probably due to geological heterogeneity. Therefore, while investigation of local fault properties appears to be useful for stimulation induced seismic hazard analysis, it is not completely reliable, especially for long term hazard.

5.5 Conclusion

Comparative study of the effect of fault development on EGS has not previously been carried out. Our survey of fracture networks at different projects around the world suggests that fault and fracture characterization may be effective for estimation of hazard associated with EGS stimulation. The review in this chapter did not incorporate fracture orientation exhaustively, but nevertheless a good correlation was observed between the thickness of cataclasite zones and maximum induced event magnitude. There are several potential explanations for correlation.

One explanation is that ruptures propagate more easily on the spatially extensive and continuous slip surfaces in well-developed faults. An alternative hypothesis is that less developed faults that lack thick cataclasite zones are more likely to slip aseismically. Degree of fault development tended to be correlated with depth. Finally, our study did not address the topic of natural fracture orientation comprehensively, and this could be a confounding variable.

Identification of mineralogy of fault infill was identified as being important in order to identify the presence of clays or other minerals that would promote aseismic deformation. A correlation of seismicity with depth was also identified, which may be related to the greater tendency of some gouge materials to slip seismically at higher temperature.

In two places where only tiny seismic events occurred during stimulation, long term net injection led to a small number of relatively much larger events. This was probably due to geological heterogeneity and the larger region of stress perturbation caused by long term net injection relative to stimulation.

At the Rosemanowes project, surface outcrop studies described joints with dimensions of tens of meters. However, very small observed magnitudes suggest that entire joints were not able to slip during individual seismic events. This suggests that seismic slip may have only been frictionally favorable on small patches within joints. An alternative hypothesis is that smaller magnitude events seen at Rosemanowes and other locations may not have been caused by rate and state frictional sliding mechanisms.

This study suggests characterization of the degree of fault development should be a priority in EGS field demonstrations. The extreme variation in fault development at different historical EGS projects is striking, especially because this point has not been emphasized in the EGS literature. Basic aspects of reservoir engineering and stimulation modeling would be affected by the degree of fault development. Fundamentally different reservoir behaviors might be expected depending on the degree of fault development. For example, the storativity of the faults affects the mechanism of stimulation (Section 3.4.2.3).

From the point of view of seismic hazard analysis, gathering data on fracture orientations in the local stress field is insufficient. Fractures must not only be well oriented to slip, but also large enough to cause significant sized events and have frictional characteristics conducive to rapid slip.

Chapter 6

6 Pressure Transient Analysis of Fracture Zone Permeability at Soultz-sous-Forêts

During the EGS project at Soultz-sous-Forêts in France, several wells were drilled and hydraulically in faulted and fractured granite during the 1990s and 2000s. During each stimulation, thousands of cubic meters of water were injected at high pressure into open wellbore, triggering slip on pre-existing fractures, inducing seismicity, and permanently enhancing the productivity of the wells.

Understanding how storativity and permeability is distributed and created at Soultz is critical to design of future hydraulic stimulations and prediction of reservoir performance. This chapter investigates the permeability distribution at Soultz using pressure transient analysis in conjunction with qualitative observations from other sources of data.

Pressure transient analysis is an inverse problem, which means that multiple mathematical models may be capable of matching the same data set. In this chapter, we propose three candidate conceptual models based on well log and core observations. A few parameters in each model were varied until a good fit to the data was achieved. The objective was to evaluate whether the parameters used to match the data were physically

plausible. A model that requires unrealistic physical parameters to match data should be discarded.

At Soultz, several lines of data indicate that flow from each well is localized in a small number of fracture zones with an effective width of several meters. Given that interpretation, we investigated three conceptual models that were considered candidates to explain the distribution of permeability in the fracture zones.

The three conceptual models were (A) flow in a crack, (B) flow in a crack embedded in an intermediate permeability and porosity damage zone, and (C) flow in a damage zone with uniform permeability and porosity. Overall, Model A was ruled out, and Model C was found to be most consistent with the observations.

6.1 Introduction

At Soultz-sous-Forêts in France, a European Enhanced Geothermal project drilled and hydraulically stimulated several wells in faulted and fractured granite during the 1990s and 2000s. During each stimulation, thousands of cubic meters of water were injected at high pressure into open wellbore, triggering slip on pre-existing fractures and inducing seismicity. The injectivity of the wells increased by one to two orders of magnitude following stimulation (Hettkamp et al., 2004; Tischner et al., 2006; Genter et al. 2010).

This chapter focuses on a few fundamental questions about the Soultz reservoir. What was the mechanism of permeability creation? Where in the formation were the massive volumes of injected fluid stored? What was the spatial distribution of the newly created permeability?

This chapter starts by reviewing the body of data that has been gathered at the Soultz site and the general conceptual reservoir model that has emerged over the years. The premise of this chapter is that flow in the Soultz reservoir occurs primarily in a relatively small number of discrete preexisting fracture zones. In wellbore core, the fracture zones were generally observed to contain a fault core surrounded by a hydrothermally altered and fractured zone with a thickness on the order of meters. Our analysis was based on an

injection experiment carried out at fluid pressure well below estimates for the least principal stress, precluding the possibility that new tensile fractures propagated through the formation (Zoback, 2007).

Given that premise, our investigation used pressure transient analysis to investigate how permeability was distributed throughout the fracture zones. Was the permeability distributed roughly uniformly through the fracture zones or was it confined primarily to the fault core with fluid leakoff into the damage zone?

Pressure transient analysis can be used to interpret the change in wellbore pressure with time given a known injection rate (Horne, 1995). The pressure transients during hydraulic stimulations at Soultz were complex because the permeability was changing with time and because of uncertainty in the geometry of the fracture zone network. However, the early time transients, perhaps the first hour or few hours after a step change in injection rate, may be interpretable because flow can initially be assumed to be roughly radial away from the wellbore through the fracture zones.

We analyzed two pressure transients from the hydraulic stimulation of GPK2 in June and July of 2000. A downhole pressure gauge took a pressure reading roughly every second.

We attempted to match the pressure transients with three models: a crack embedded in unfractured granite (Model A), a crack embedded in a damage zone of finite thickness (Model B), and a damage zone of uniform permeability and porosity embedded in unfractured granite (Model C).

The exact numerical parameters of the models were less important than identifying whether the models could match the data in a qualitatively reasonable way. All three models were able to match both transients. By examining the numerical parameters required, it was possible to identify whether those interpretations were reasonable.

The single crack model (Model A) required extremely unrealistic values for hydraulic diffusivity and skin to match the data. In addition, because the model did not provide adequate storativity, it appeared to be the least plausible.

The most plausible match was the model using homogenous permeability and porosity (Model C). It matched the transients with reasonable hydraulic diffusivity and skin. The moderate negative skin effect from that match could be fully explained by the geometric skin effect from slanted wellbore penetration.

The crack with damage zone model (Model B) could not be ruled out but was challenging to interpret. It required a very negative skin. A possible explanation for the very negative skin could be fracture opening in the vicinity of the wellbore, possibly due to thermal stresses. However calculations suggested that thermal stresses should not have been strong enough to induce fracture opening. Furthermore, Model B predicted a more complicated pressure transient behavior than Model A or Model C, and it was unclear whether that behavior could be reconciled with the transients observed.

6.1.1 The Soultz Reservoir

Spinner and temperature logs in all of the Soultz wells showed that fluid exited and entered the wellbores at a small number of discrete locations.   These zones of concentrated flow were associated with fracture zones intersecting the well that contained a high density of fracturing and hydrothermal alteration.   Seismicity observations, wellbore imaging logs and caliper logs indicated that the zones of increased flow contained fracture that had slipped in shear (Genter et al., 2000; Genter and Traineau, 1996; Evans, Genter, and Sausse, 2005; Evans, Moriya, et al., 2005; 2006; Tischner et al, 2006; Dezayes et al., 2010). In GPK3 at Soultz, 70% of flow from the wellbore exited from a single location (Baria et al., 2004).

Baisch et al. (2010) showed that the seismic events around GPK3 were clustered along a distinct, planar feature corresponding to the feed zone in GPK3. Charlety et al. (2007) looked only at large magnitude events that occurred during the stimulations of GPK2 (deep), GPK3, and GPK4, and found that they located along distinct planar features. In contrast, Michelet and Toksöz (2007) found that the seismic events formed a broader cloud, but Baisch et al. (2010) argued that the volumetric distribution of events was an artifact of the sparse seismometer network used by Michelet and Toksöz (2007).

Permeability enhancement primarily via slip on preexisting fractures has been observed at other EGS projects in crystalline basement such as at Cornwallis, UK, (Pine and Batchelor, 1984) and Hijiori, Japan (Tezuka and Niitsuma, 2000).

6.1.2 Fracture Opening vs. Fracture Slip

It is not clear to what extent significant new opening mode cracks were created during the hydraulic stimulations at Soultz. Formation of new opening mode cracks is usually considered the primary mechanism of stimulation in oil and gas hydraulic stimulation (Economides and Nolte, 2000). To propagate new opening mode cracks, the fluid pressure P must exceed the minimum principal stress, σ_3 (Zoback, 2007). Some early conceptual models of stimulation at Soultz involved propagation of new tensile cracks (Jung and Weidler, 2000). However, it is now more widely believed that the primary stimulation mechanism was shear of preexisting fractures (Evans, 2005).

Valley and Evans (2007), Cornet and Bérard (2003), and Cornet et al. (2007) interpreted the pressure and flow rate behavior during the hydraulic stimulation of the GPK1 (Jung et al., 1992), GPK3 (Hettkamp et al., 2004), and GPK4 (Baria et al., 2006) as indicating that tensile fractures were formed at the top of the openhole section of these wells. Their rational was that a "stabilization of pressure" occurred during the stimulations. It is common in oil and gas hydraulic fracturing to observe an abrupt change in slope in the relationship between injection pressure and injection rate when downhole pressure reaches the σ_3 and fractures have begun to propagate through the formation (Gulrajani and Nolte, 2000). Such a change in slope in the relationship between injection pressure and injection rate has been consistently observed during the stimulations at Soultz (Jung and Weidler, 2000) and this "stabilization of pressure" is interpreted to indicate tensile fractures are propagating through the formation with the fluid pressure nearly equal to the least principal stress.

The interpretation of pressure stabilization could be complicated by the process of shear stimulation of preexisting fractures. In Sections 3.4.7 and 4.4.6 it is described how shear stimulation could cause a change in the slope between injection pressure and rate that would be indistinguishable from tensile fracturing.

The shear stimulation mechanism could explain why injection pressure stabilization occurred during the deep stimulation of GPK2 (Weidler et al., 2002) in June and July 2000 even though the fluid pressure was several MPa below the Valley and Evans (2007) or Cornet et al. (2007) profiles for σ_3.

If it was assumed incorrectly that P reached σ_3 during injection, then σ_3 would be underestimated.   This may explain why critical stress analyses at Soultz have been required to invoke unusually high values for the coefficient of friction, 0.8-1.0, and/or significant fracture cohesions in order for the fractures to initially (prestimulation) be at mechanical equilibrium (Cornet et al, 2007; Evans, 2005).

Even if there was some tensile fracturing during the Soultz stimulation, the evidence suggests that it did not control flow through the reservoir because major exit points for fluid have been identified at all depths throughout the openhole sections (not just the top, which is where tensile fracturing would occur).   As mentioned above, these exit points were correlated with preexisting fracture zones crossed by the wellbore and microseismicity.

Regardless of the above arguments, during the pressure transients analyzed in this chapter, from the June and July stimulation of GPK2, the pore pressure was several MPa below σ_3 (also referred to as σ_{hmin}), and so significant propagation of opening mode fractures can be ruled out.   According to the Valley and Evans (2007) stress and pressure profile, at 4500 m, the top of the openhole section, σ_{hmin} was 61.5 MPa, and P was 45 MPa.   Therefore it would have required 16.1 MPa of fluid overpressure to cause the propagation of tensile fractures into the formation.   At its highest, the overpressure during the stimulation of GPK2 was around 12 MPa.

6.1.3 Flow in the Unfractured Granite

Simple calculations can be used to estimate the potential impact of fluid flow into the granite matrix surrounding the fracture zones. Such fluid leakoff from the fracture zones into the surrounding matrix could provide storativity and possibly affect pressure transients. The injection pressure for constant rate injection, assuming radial flow from a line source, is (Horne, 1995):

$$p_D = -1/2 Ei(\frac{-1}{4t_D}),$$ 6-1

where

$$p_D = \frac{2\pi kh}{q\mu_l}\Delta P,$$ 6-2

and

$$t_D = \frac{kt}{\phi\mu_l c_t r_w^2},$$ 6-3

and k is permeability, μ_l is viscosity, q is the injection rate, h is height, φ is porosity, r_w is well radius, c_t is total compressibility, and ΔP is the difference in the injection pressure and the initial pressure. Ei is the exponential integral function.

Jung (1992) estimated an upper limit on the permeability of the intact granite in the shallow GPK1 borehole (around 3 km depth) based on *in situ* hydraulic testing at 3.5×10^{-17} m^2. The permeability during the deeper stimulation of GPK2 (around 5 km depth) would be even lower. Rummel (1992) measured permeability in cores taken from GPK1 and estimated that the granite permeability varied from 10^{-17} to 10^{-16} m^2 at atmospheric confining pressure to 10^{-19} to 10^{-17} m^2 at 100 MPa confining pressure.

For k equal to 10^{-17} m^2, φ equal to 0.003, r_w equal to 0.1 m, c_t equal to 6.7×10^{-4} MPa^{-1}, μ_l equal to 2×10^{-4} Pa-s, h equal to 500 m, and q equal to 0.5 l/s, the injection pressure after 1 hour would be 16 MPa, greater than the increase in fluid pressure during the 2000 stimulation of GPK2. The flow rate during that stimulation was on the order of tens of liters per second, much higher than the 0.5 l/s used in the calculation above. This rough calculation makes clear that solid granite is not capable of accepting the flow rates observed during injection from radial flow alone.

It is plausible that a significant amount of fluid could leak off into the intact granite from the fracture zones. The fracture zones could have very large surface area, which makes significant leakoff possible.

From Bird et al. (2007), the solution for one dimensional flow into a semi-infinite slab with constant pressure at one side gives a volumetric flow rate of:

$$q = \frac{kA}{\mu_l \sqrt{t\alpha\pi}} \Delta P \,,$$

<div align="right">6-4</div>

where ΔP is defined as the difference between initial and the boundary condition pressure. Using the same values as above, A equal to 10^6 m^2, and with hydraulic diffusivity α defined as $k/(\varphi c_t \mu)$, the volumetric flow rate would be about 30 l/s after one hour. This was a rough calculation, but it illustrates that significant flow could occur into the solid granite, as long as it is leaking off from a very large stimulated fracture surface area.

The penetration depth can be estimated using these parameters. The pressure will be perturbed by 15% of the difference between the initial pressure and the boundary pressure at a distance of $\sqrt{t\alpha}$. That would correspond to a depth of about 90 m from each fracture zone after 10 days. There is a lot of uncertainty in these calculations, but they demonstrate that it is at least plausible that pressure perturbations could fill a large volume of rock, and therefore create a large volume of induced seismicity, even if the large scale permeability is localized to a small number of discrete zones.

These calculations seem to suggest that leakoff into the formation could affect pressure transients. It cannot be ruled out that leakoff into the matrix could affect pressure transients at late time. However at early time, when flow away from the wellbore is roughly radial, a low surface area of fracture would be affected by the transient, and leakoff into the surrounding granite would be a minor effect because of the relatively smaller surface area. In Models A and C, low permeability granite was included surrounding the main permeability zone, and it was observed to have a negligible effect on the pressure transient.

6.1.4 EGS Modeling

Because flow is confined to a handful of major flow pathways, discrete fracture modeling is most commonly used to model the hydraulic stimulations at Soultz and for

EGS in general. Flow through the bulk of intact granite is typically neglected and flow is assumed to be occurring only in preexisting fractures (Kohl et al., 1995; Yamamoto et al., 1997; Willis-Richards et al. 1996; Hossain et al., 2002; Kohl and Mégel, 2007; Bruel, 2007; Rahman et al., 2002; Sausse et al., 2008; Baisch et al., 2010).

In discrete fracture models, flow is typically conceptualized as flowing through discrete fractures. Functions relating slip to permeability increase are used that are based on laboratory tests of permeability increase in granite fractures and often incorporate the cubic law to relate transmissibility to aperture (Willis-Richards et al., 1996; Bruel, 2007; Kohl and Mégel, 2007). These functions are broadly consistent with a large number of laboratory studies that have noted increases in granite fracture permeability with shear displacement (Barton et al, 1985; Esaki et al. 1999; Lee and Cho, 2002; Chen et al. 2000; Yeo et al, 1998; Auradou et al., 2006; Matsuki et al., 2010).

However, modeling flow in an EGS reservoir with cracks is problematic because cracks are very narrow, and it would require a large number of them to contain the volume of fluid that is injected during a hydraulic stimulation. For example, during the hydraulic stimulation of GPK2 in June 2000, roughly 25,000 m^3 of water was injected (Weidler, 2000). Sanjuan et al. (2007) analyzed tracer tests between GPK2 and GPK3 and estimated that the most direct fluid pathway between the two wells had a volume of roughly 3900 m^3 (Sanjuan et al., 2006). The areal extent of seismicity surrounding GPK2 should roughly delineate the area where the injected fluid was contained, and it was roughly 2.5 km by 0.5 km (Weidler et al., 2002), which would be roughly 1.25 km^2.

To contain 25,000 m^3 of fluid in that areal extent would require an average of 0.02 m^3 of water contained per areal square meter. The aperture of a closed crack in granite is on the order of hundreds of microns (Esaki et al, 1999, Lee and Cho, 2002). Assuming the water was contained in new cracks with aperture of 1 mm and area 1.25 km^2, it would require 20 cracks to contain 25,000 m^3 of water. Assuming that the water was contained in preexisting cracks with compressibility roughly that of water, around 6.8×10^{-4} MPa^{-1} at 200ºC, an increase in pressure of 10 MPa, and an initial aperture of 1 mm, it would require roughly 3,000 cracks of area 1.25 km^2 to contain 25,000 m^3 of water. If the water were contained in a layer of porous material with compressibility 6.8×10^{-4} MPa, an

increase in pressure of 10 MPa, an area of 1.25 km^2, and a porosity of 10%, the layer would have to be roughly 30 m thick.

It is a major concern how to reconcile these mass balance concerns with spinner logs that show only a small number of discrete locations for fluid to exit the wellbore.

Geological evidence suggests that fluid at Soultz may not be confined only to cracks, but may also be stored in fault damage zones, wider regions of alteration and microfracturing surrounding the major fault slip planes. Genter and Traineau (1996) analyzed a core of EPS1, one of the shallow wells at Soultz. They described faults intersecting the well which contained cores full of secondary precipitation of quartz and cataclasites, breccia, and microbreccia and highly altered zones up to 25 m thick. The altered zones contained a high density of fractures and had experienced extensive dissolution of primary minerals and precipitation of secondary minerals. The damage zones had porosities of 5% to 25% (Genter et al., 2000). These high porosity alteration zones could provide the storativity necessary to contain the volumes of water injected during stimulations.

Fluid storativity in damage zones are already effectively incorporated into many EGS models, which generally use storativity values that are too high to be individual cracks. Unitless storativity S_u is defined as:

$$S_u = \rho \phi c_t b_t g \, , \tag{6-5}$$

where ρ is fluid density, φ is porosity, c_t is compressibility, b_t is thickness, and g is the gravitational constant. Storativity could be high because either the layer thickness b_t is high or because the fracture compressibility c_t is high.

For example, Bruel (2007) assumed a unitless fracture storativity of 10^{-6}. It is possible to calculate what combination of parameters would result in a fracture with storativity equal to 10^{-6}. Assuming a compressibility of 6.8×10^{-4} MPa, a water density of 890 kg/m^3, a porosity of one, and a storativity of 10^{-6}, the crack thickness b_t would be about 17 cm. Assuming that b_t is equal to 1 mm, the compressibility would be 1.1 MPa^{-1}. Neither a fracture compressibility of 1.1 MPa^{-1} nor a fracture aperture of 17 cm are realistic values for individual cracks. However, these storativity values would be

consistent with a damaged zone mode.   A 1.7 m wide zone of 10% porosity, compressibility equal to $6.8{\times}10^{-4}$ MPa^{-1}, and fluid density equal to 890 kg/m^3 would have a storativity of 10^{-6}.

Other examples of fracture storativities used in EGS modeling are Baisch et al. (2010), who modeled a crack with aperture of 1 mm but very high storativity, and Sausse et al. (2008), who modeled fractures with apertures on the order of centimeters, and explicitly stated high apertures were used to take into account the storativity of fault zones.

6.1.5 Fault Zones

It seems highly likely that the primary storativity of the EGS reservoirs at Soultz lies in the fault zones. It is not clear how permeability is distributed throughout the fault zones. From the literature it is evident that fault damage zones in granite most commonly have higher permeability than the fault core.

A wide range of fault zone structures have been described in the literature. Faults are generally described in terms of three distinct mechanical and hydraulic units: fault core, which is where slip is primarily localized and containing cataclastic rocks, a damage zone containing extensive fracturing and possibly hydrothermal alteration, and the protolith consisting of the undisturbed rock (Wibberley et al., 2008; Caine et al., 1996; Bruhn et al., 1994).

Within the framework of these three units, fault zone geometry shows a great deal of variability. Chester and Logan (1986) described a single fault core surrounded by a damage zone at the Punchbowl Fault in California. Griffith et al. (2009) described Bear Creek fault zones in California consisting of two cracks accommodating slip bounding a damage zone several meters thick. Faulkner et al. (2003) described the Carboneras Fault in Spain, a zone that is over 1 km wide, consisting of many bands of fault gouge embedded in a complex zone of damage zone and distributed deformation.

Fault cores in granite have been measured to have lower permeability than the surrounding damaged zones (Chester and Logan, 1986; Lockner et al., 2009; Evans et al.,

1997; Seront et al., 1998; Morrow et al., 1984). On the other hand, very strong quartz mineralization at Soultz in the fault cores (Genter et al, 2000) suggests that, at least immediately following slip events, there is a significant amount of fluid flowing in the fault core, and it may have significant permeability. Because of the variability in mineralogy of fault cores at different locations, fault core measurements in the literature do not necessarily apply to Soultz. Low permeability fault cores are most associated with the presence of clay minerals (Morrow et al., 1984), but fault cores at Soultz are filled primarily with quartz (Genter et al., 2000). It may also be that fault core permeability may be temporarily elevated following earthquakes. Fluid discharge is frequently observed after earthquakes, suggesting that along fault permeability is enhanced immediately after seismic events, but is sealed relatively rapidly by mineralization, a mechanism called the fault valve model (Sibson, 1990). However, it is not clear from the fault valve model whether the transient permeability creation after an earthquake occurs in the fault core or in the damage zone.

If the permeability is concentrated primarily on a slip plane in the fault core, then the mechanism of permeability enhancement is likely the mismatch of asperities along the slip plane following slip. As noted above, many laboratory studies have observed such a phenomenon during slip on granite fractures (Barton et al, 1985; Esaki et al. 1999; Lee and Cho, 2002; Chen et al. 2000; Yeo et al, 1998; Auradou et al., 2006; Matsuki et al., 2009).

If permeability is distributed throughout the damage zone, the mechanism of permeability enhancement is not as obvious. One possibility would be that the damage zone contains a large number of fractures that slip in shear. The relatively large seismic events at Soultz must involve slip areas of tens of thousands of square meters. Presumably, such laterally extensive slip surfaces could only exist in the fault cores. There was a roughly fractal distribution of event magnitudes during the stimulations at Soultz (Bruel and Charlety, 2007). The many smaller events could be due to slip on the small ancillary fractures that are located in the damaged zones, and as a result they could have increased permeability. This interpretation would be supported by the observation of Evans (2005) and Evans, Genter, and Sausse (2005) that a significant number of newly permeable fractures were clustered in the damaged zones of faults in GPK1, one of the

shallow wells at Soultz. On the other hand, Evans, Genter, and Sausse (2005) also observed that 95% of flow appeared to be exiting from 10 major flowing fractures.

Another possible source of permeability creation in the damage zone is dynamic stresses induced during propagation of seismic events along the fault cores. Very strong stresses are induced at the rupture front during the propagation of a seismic event (Aki and Richards, 2009). These powerful stresses during rupture propagation could cause significant secondary fracturing and permeability enhancement in the damage zone (Paul et al., 2007).

6.2 Pressure Transient Analysis of GPK2

To address the question of how permeability is distributed throughout the damaged zones at Soultz, we analyzed two pressure transients from the deep hydraulic stimulation of GPK2 at Soultz in June and July 2000. The GPK2 transients were ideal for interpretation, because according to the Valley and Evans (2007) stress profile, the pore pressure was several MPa less than σ_{hmin} during the stimulation. Therefore the pressure transients should not be complicated by the possibility of new fractures propagating into the formation. Stress heterogeneities could cause small scale tensile fracturing, but these fractures would be confined to those localized regions of stress perturbation.

The pressure transients were taken from a downhole pressure gauge that took measurements at intervals of roughly one second. GPK2 had originally been completed at around 3 km depth, but GPK2 was deepened to 5 km and that was the depth of the June and July 2000 stimulation. This was the first hydraulic stimulation carried out at 5 km depth at Soultz.

Unfortunately, a borehole restriction prevented the running of a spinner log to identify where fluid was exiting GPK2. However, Jung et al. (2010) used a brine displacement test to identify that there were three primary zones where fluid was exiting the wellbore. They estimated 15% left from a zone at 3860 through a leak in the casing. Another 15% left around 4420 at the casing shoe. The remaining 70% of flow exited the well from a zone at about 4670 m. These results are consistent with spinner logs run in

the other Soultz wells, which showed fluid exiting the wellbores from a small number of discrete fracture zones (Tischner et al., 2006).

A casing leak would have the potential to complicate analysis of the pressure transients. However, this leak did not begin until after the transients analyzed in this chapter. The transients analyzed in this chapter occurred during the hydraulic stimulation that ended July 6. The casing leak originated on July 12 when a seismic event caused the casing to shear off (Weidler, 2000).

6.2.1 Data

The full record of flow rate and downhole pressure is shown in Figure 6-1. The time axis was measured in hours from 7:34:50 PM on June 30, 2000. Two pressure transients were analyzed, Transient A and Transient B, and they are labeled on Figure 6-1. The downhole gauge was located at 4412 m depth until roughly 136 hours, when it was moved to 4436 m. The change is depth caused a small discontinuity in the downhole pressure, which can be seen in Figure 6-1. The depth change of the pressure gauge did not occur during either Transient A or B, so does not affect the analysis.
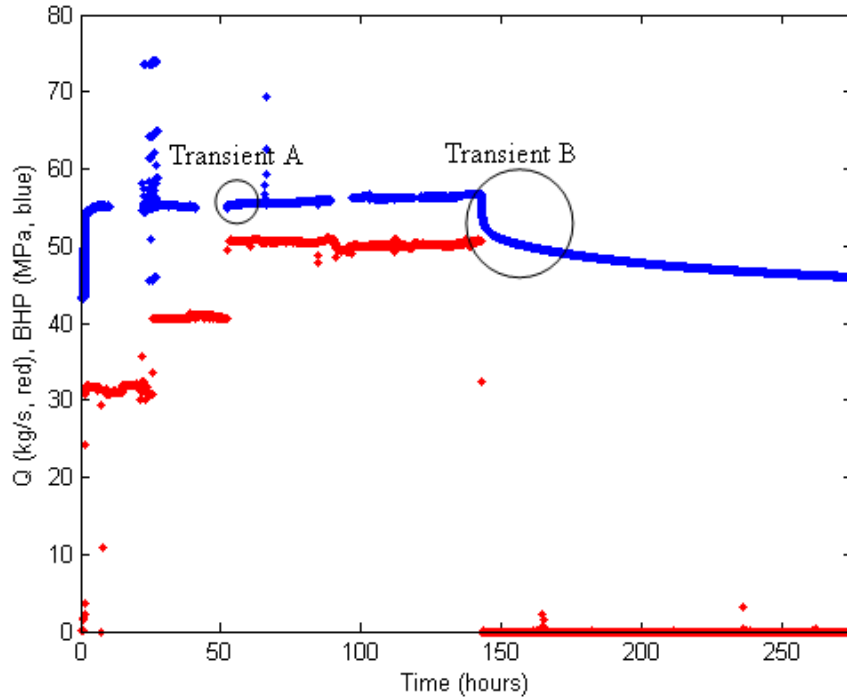
Figure 6-1: Injection rate and bottom hole pressure in the stimulation of the deepened GPK2 in June and July 2000.

Transient B is the transient following shut-in after stimulation. Transient A is the transient during injection when the injection rate was stepped from roughly 40 kg/s to 50 kg/s. Flow rate measurements are available at five minute intervals, so it is impossible from those records to know precisely when the transients began in the pressure record, which was at intervals of seconds. By inspecting the pressure records, the beginning of the transients was identified from abrupt change in pressure.

Figure 6-2 and Figure 6-3 show Transients A and B, respectively, on a log-log plot. The blue line shows ΔP, the absolute value of the change in pressure relative to the beginning of the transient. The red line shows the pressure derivative curve, $dP/d(\ln(t))$. Pressure derivative plots are routinely used in pressure transient analysis because they are highly sensitive to changes in the transient behavior and are therefore useful diagnostic tools.

Low amplitude, high frequency fluctuations in the pressure record cause significant noise in the pressure derivative calculation but do not affect the overall shape of the transient. To smooth the pressure derivative, the pressure record was sampled with logarithmic spacing so that the data was sampled with increasing sparseness with

increasing time.   In Transient A, a moving average filter with a window of five was applied to the sampled data for further smoothing. Figure 6-1 shows both the full data set and the sampled, smooth data set.

Because Transient A was during the hydraulic stimulation, the long term transient was affected by the stimulation process itself and is not suitable for pressure transient analysis.   After about 1500 seconds, a seismic event occurred and caused an abrupt behavior in the pressure transient (even though flow rate remained constant). Transient A is only considered up until 1500 seconds.
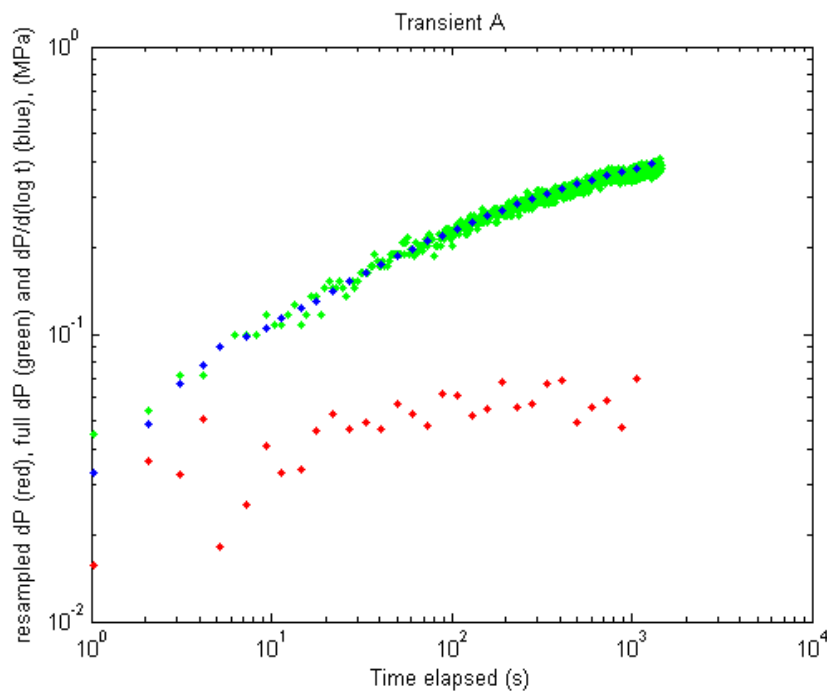
Figure 6-2: Transient A. The change in pressure following stimulation injection pressure increase from 40 kg/s to 50 kg/s.
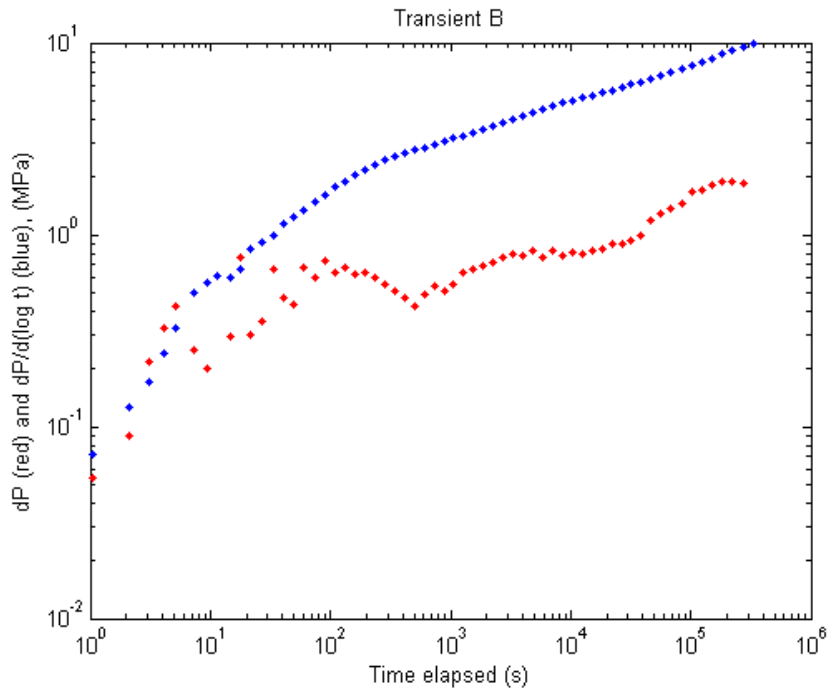
Figure 6-3: Transient B. The change in pressure following the termination of injection.

6.2.2 Model Construction

Numerical models were constructed to describe three conceptual ideas about how flow might occur through the fracture zones (shown in Figure 6-4). In Model A, there was a high permeability fracture embedded in very low permeability, low porosity solid granite. In Model B, there was a high permeability fracture embedded in a several meters thick damaged zone of intermediate permeability and porosity. In Model C, there was a several meters thick zone of homogenous permeability and porosity embedded in low permeability granite. The numerical model was written in Matlab.
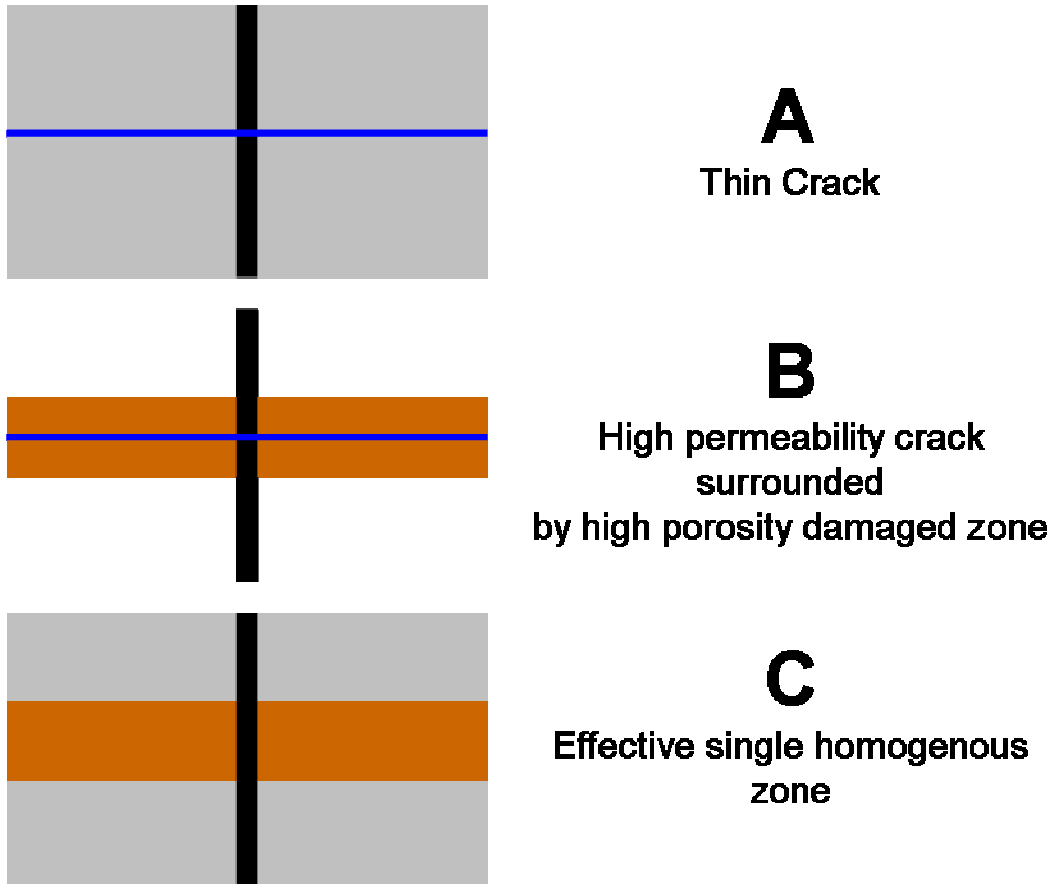
Figure 6-4: Schematic of the three conceptual models for flow in fracture zones. The black line is the wellbore. The blue line represents a "crack-like" fracture. The brown rectangle represents a zone of porous material. The grey background represents very low permeability granite.

The diffusivity equation was solved in cylindrical coordinates considering only radial and vertical flow. The diffusivity equation is written (Aziz and Settari, 1979):

$$\nabla^2 P = \frac{\phi \mu_l c_t}{k} \frac{\partial P}{\partial t} + q .$$

6-6

The model assumed constant fluid viscosity, compressibility, and single phase flow. It is isothermal and neglected thermoelastic and poroelastic effects. It used a finite volume discretization with implicit time stepping. Adaptive time stepping was used such that the maximum change in pressure per time step was limited within a certain threshold. Logarithmic grid spacing was used so that the grid was highly refined in the neighborhood of the wellbore and less refined with increasing distance. For vertical flow, the grid was more refined near the high permeability fracture/damage zone in the

middle. The radial and vertical extent of the model was large enough such that it was effectively infinite on the time scale of the simulations. An exception was Model B, where the damaged zone had a finite thickness. Sensitivity analysis to discretization was performed on both the spatial and the temporal discretizations to ensure that the discretization was resolved adequately. To verify accuracy, the simulator was compared to the analytical solution for radial flow.

Within rock types, the permeability was constant, but contrasts in permeability occurred at fracture/granite interfaces in Model A, fracture/damage zone interfaces in Model B, and damage zone/granite interfaces in Model C. At permeability contrasts, the transmissibility was calculated using a harmonic average.

The wellbore was modeled as a single grid block with a volume of 131 m^3, equal to the volume of the GPK2 wellbore (Baumgärtner et al., 2000). The wellbore was connected to each element in the innermost radius.

Wellbore skin is a parameter used in well test analysis to account for anomalously high or low pressure drop in neighborhood the wellbore. Skin was incorporated into the model by using an effective wellbore radius according to (Horne, 1995):

$$r_{weff} = r_w e^{-s}.$$

<div align="right">6-7</div>

Permeability and wellbore skin were varied manually until the models matched the observations. In Model B, the damaged zone permeability was chosen so that the *kh* of the fracture was ten times higher than the *kh* of the matrix zone. If the *kh* of the damage zone were allowed to be similar or greater in magnitude to the *kh* of the fracture, the model would have similarly to Model C, which was a wide zone of uniform permeability.

The initial condition of the model at the beginning of both transients was homogenous. This is a simplification because the prior injection history would have some impact on the transients. Because the injection rate had been constant for an extended period of time prior to the beginning of both transients, the prior injection history should only a small effect on the early time pressure transient. These models were used only to match the short time behavior of the transients in the observations.

The flow rate during the simulations was set to constant. It was 10 l/s injection during the simulations of Transient A and 50 l/s of production during the simulations of Transient B. From superposition, 50 l/s of production is equivalent to stopping injection after a long period of injecting at 50 l/s (Horne, 1995).

All parameters besides permeability and skin were specified beforehand and not altered during the matching. The constant parameters are specified in Table 6-1.

Table 6-1: Parameters used in Models A, B, and C.

Total compressibility (all rock types)	$6.8 \times 10^{-10}\ Pa^{-1}$
Wellbore compressibility	$4.5 \times 10^{-10}\ Pa^{-1}$
Fracture porosity	1.0
Damage zone porosity	0.1
Granite porosity	0.003
Granite permeability	$10^{-18}\ m^2$
Fluid viscosity	$2 \times 10^{-4}\ Pa\text{-}s$
Wellbore radius	.108 m
Wellbore volume	$130\ m^3$
Fracture aperture	5 mm
Damage zone thickness	25 m
Initial pressure	43 MPa

The assumed thickness of the fractures was 5 mm. Closed fractures have aperture significantly less than 5 mm, typically hundreds of microns. However, our model assumed that only a single fracture zone was intersecting the wellbore. In reality several, perhaps 3-6, would be intersecting the wellbore. Using a 5 mm fracture aperture effectively accounts for the possibility of flow into several fracture zones.

6.2.3 Data Matching

We focused on interpreting the early time transient. The geometry of flow at some distance from the wellbore is highly uncertain as it depends on the specific geometry of the fracture network. But before the fracture zone edges are felt, flow should be roughly radial away from the wellbore within the fracture zones. Therefore, we sought to match the early time data with radial flow models.

Our models assumed only a single fracture zone taking flow from the well. It is likely that multiple zones were taking flow. The effect of having multiple zones would be to reduce the flow rate into each individual zone, but that would not affect the overall behavior of the model. To account for the possibility of flow in multiple fractures, the assumed fracture aperture was about ten times larger than would be realistic for a single closed fracture.

Our best matches to the two transients with the three models are shown from Figure 6-5 to Figure 6-10. The six matches are subsequently referred to as TAMA, TBMA, TAMB, TBMB, TAMC, and TBMC. The second letter refers to the Transient being matched, either A or B, and the fourth letter refers to the model being matched, either A, B, or C.
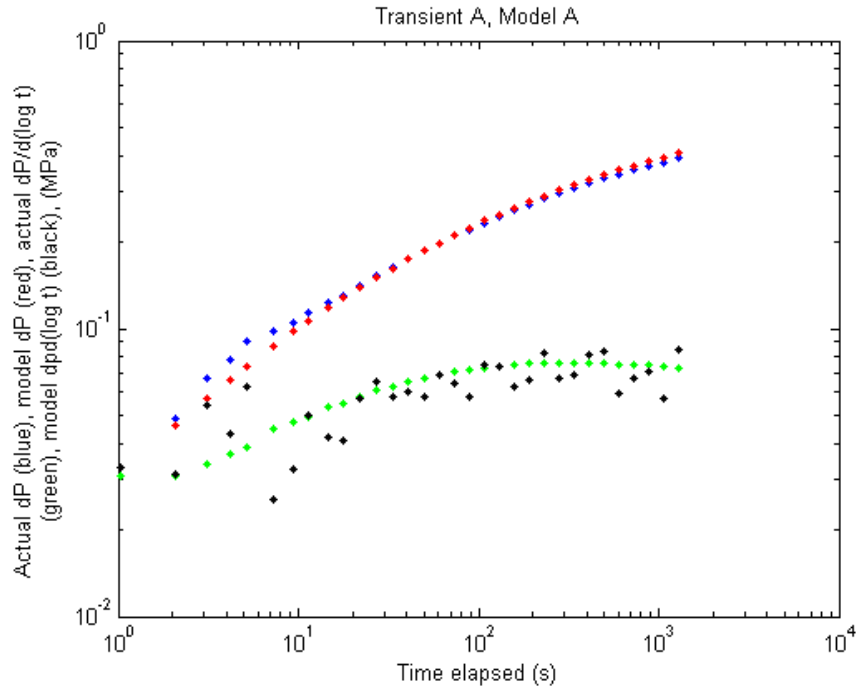
Figure 6-5: Model A match to Transient A.
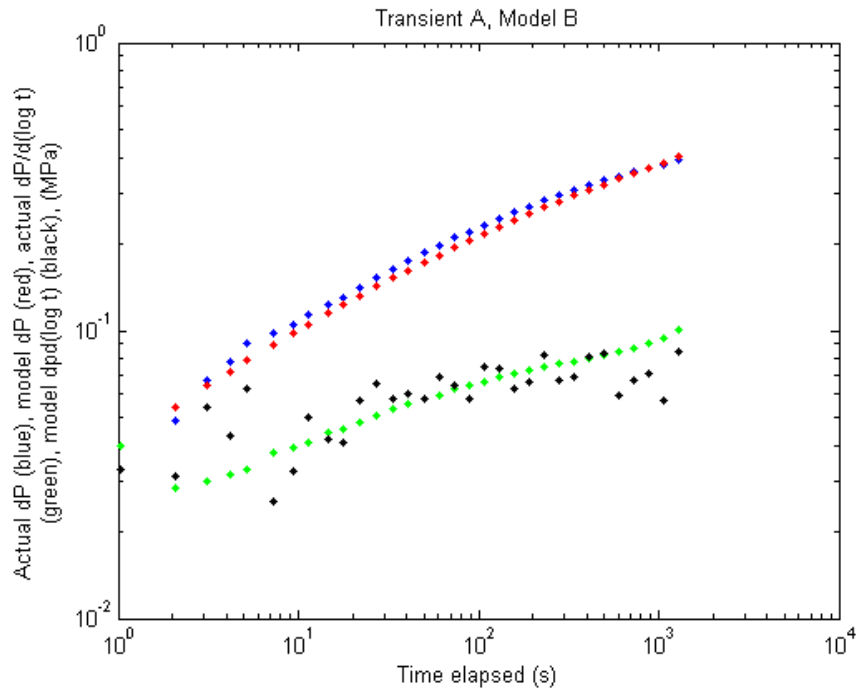
Figure 6-6: Model B match to Transient A.
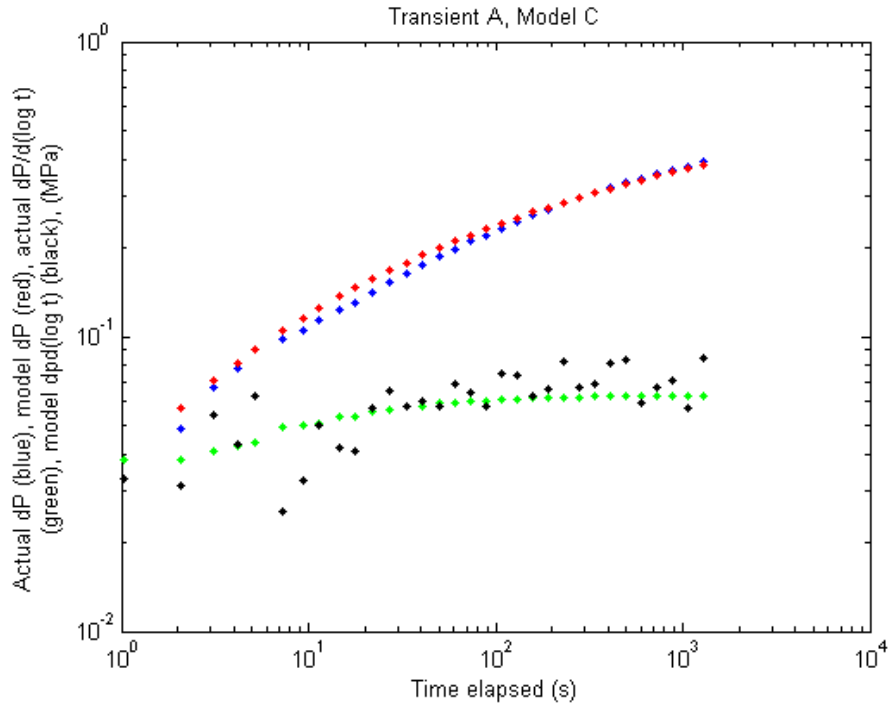
Figure 6-7: Model C match to Transient A.
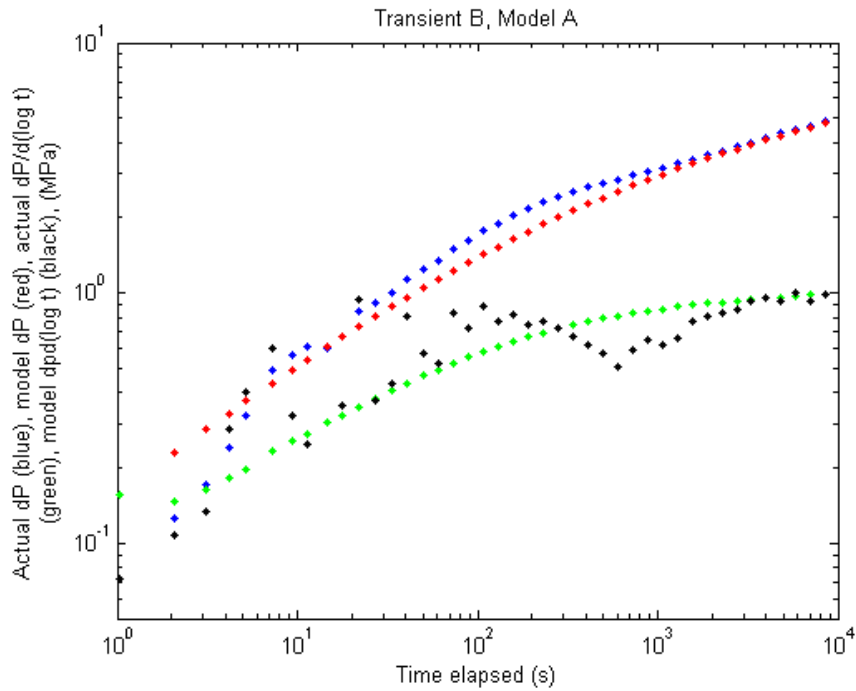
Figure 6-8: Model A match to Transient B.
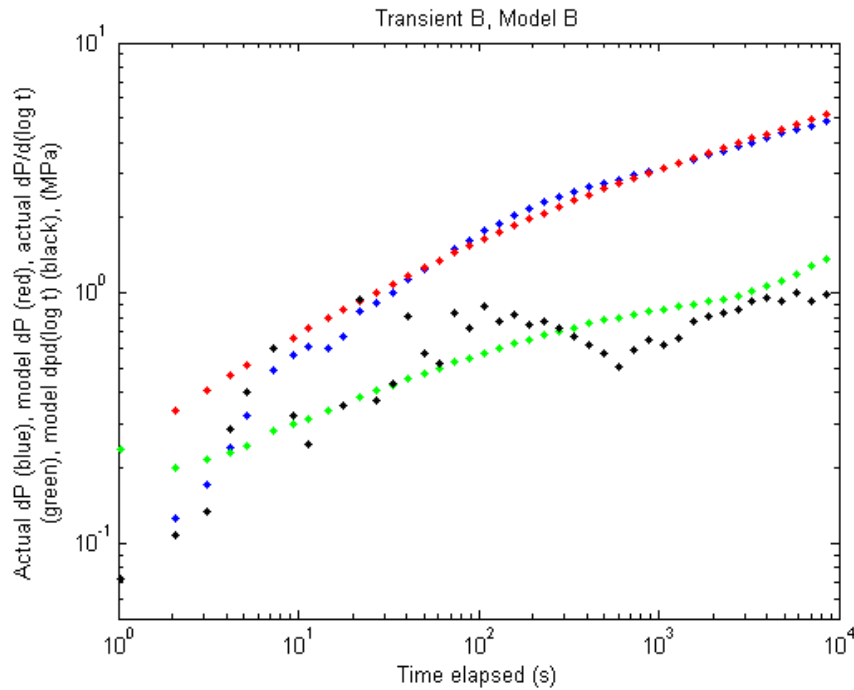
Figure 6-9: Model B match to Transient B.
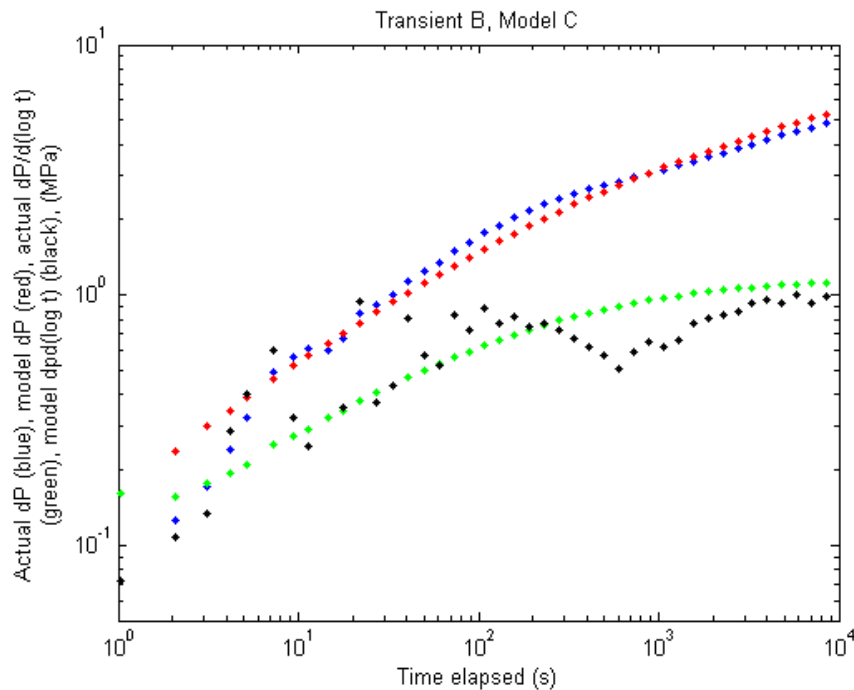
Figure 6-10: Model C match to Transient B.

The values of permeability and skin that were used in each model are given in Table 6-2. The derived values r_{weff}, kh, α (hydraulic diffusivity, defined as $k/(c_t \varphi \mu)$), and r_{inv} are also shown. For Model B, there was some ambiguity on how to calculate α because there

were two permeabilities and porosities, the damaged zone and the fracture. Effective properties were calculated for both using the arithmetic thickness weighted average.

The radius of investigation for radial flow can be approximated as Horne (1995):

$$r_{inv} = 2\sqrt{\alpha t} \ .$$

6-8

In Table 6-2, r_{inv} was calculated after 1000 seconds for the Transient A models and after 10,000 seconds for the Transient B models.

Table 6-2: Parameters used in the six matched models. k and s were the only variables varied to perform the model match to the data. The values r_{weff}, kh, α, and r_{inv} can be calculated from other model parameters.

Model	$k\ (m^2)$	s	$r_{weff}\ (m)$	$kh\ (m^3)$	$\alpha\ (m^2/s)$	$r_{inv}\ (m)$
TAMA	2.8E-10	-7.8	263.6	1.4E-12	2058.8	2869.7
TBMA	6.6E-11	-8.8	681.6	3.3E-13	485.3	4405.9
TAMB	3.0E-10	-6.0	43.6	1.7E-12	5.5	148.3
TBMB	8.0E-11	-6.0	43.6	4.4E-13	1.5	242.2
TAMC	1.1E-13	-4.0	5.9	2.8E-12	8.1	179.9
TBMC	3.0E-14	-4.0	5.9	7.5E-13	2.2	297.0

6.3 Discussion

The estimated parameters for Transients A and B were roughly similar for all three models, which verifies that the methodology was repeatable. The estimated k from Transient A was about four times higher than for Transient B for all three models. This may indicate that permeability was actually different during the two transients or may be some artifact of the simplifications being made, such as neglecting prior injection history. The radius of investigation was larger for the Transient B matches than the Transient A matches, but this makes sense because the radius of investigation in the Transient B matches was calculated at a later time.

All three models were able to reasonably match both transients. But examination of the parameters required for the matches shows that some of the matches were not physically plausible.

The Model A matches to Transients A and B required an equivalent wellbore radius of 264 m and 682 m and hydraulic diffusivities of 2059 m^2/s and 485 m^2/s, respectively. These values are extremely unrealistic. The cloud of seismicity, which roughly outlines the region where pressure was perturbed during the stimulation, was about 500 m by 2500 m (Weidler et al., 2002). Hydraulic diffusivities on the order of hundreds of m^2/s would allow pressure signals to propagate to the edge of the stimulated region extremely rapidly, in under an hour. If that had occurred, the pressure transients would have shown evidence of boundary behavior at similar time scales. The high diffusivities were required to match the data because Model A did not have the storativity needed to contain the volumes of fluid required in an area of 1.25 km^2.

Models B and C both required a very negative skin, but Model C required a significantly more negative skin. Skin scales exponentially, so a skin of -6 is much stronger than a skin of -4.

The negative skin in Model C could be explained by geometric skin from slanted well penetration. The negative skin in Model B was exceptionally strong, but if injection was near σ_{hmin}, it could possibly be explained by fracture opening due to thermal stresses.

Geometric skin can occur due to penetration of a wellbore at an angle θ to a layer. Geometric skin can be approximated as (Bourdet, 2002):

$$s_\theta = -(\frac{\theta_w^{'}}{41})^{2.06} - (\frac{\theta_w^{'}}{56})^{1.865} \log(\frac{h}{100 r_w} \sqrt{\frac{k_H}{k_V}}) ,$$

6-9

where $\theta_w^{'}$ equals θ if k_H equals k_V, which is what we assumed. Geometric skin is negligible for very thin layers, such as for the fracture in Case A and B. In Case B, there would be some s_θ in the damaged zone, but the kh of the damaged zone was much smaller than the central fracture, so the effect of the geometric skin would be significantly reduced.

For Model C, assuming θ equals 70º, s_θ would be -3.6. Using an h of 10 m, s_θ would be -3.0. For h of 50 m, s_θ would be -4.0.

The geometrical skin effect could potentially account all of the negative skin in Model C. In sensitivity analysis, it was found that increasing the thickness allowed Model C to match the data using a less negative skin. With a thickness of 50 m, Model C matched the data with a skin of -3.5. In reality, there was than one fracture zone intersecting the well. The thickness could be distributed over multiple layers, and if so, then the appropriate value to use for the calculation of s_θ would be the thickness of the individual layers, not the aggregate thickness. According to Genter et al. (2000), the maximum thickness of a fracture zone observed at Soultz was 28.5 m.

The negative skin in the Model B match was exceptionally strong and would require a very large increase in permeability in the neighborhood of the wellbore. Fracture opening due to thermal stresses could potentially supply such a strong enhancement of permeability. Ghassemi et al. (2005) calculated that after seven days of injecting 30ºC water at 25 l/s into a fracture at 175ºC, there would be a zone of induced tensile stresses within 50 m of the wellbore. The magnitude of the induced fracture normal tensile stresses would be around 3.5 MPa at the wellbore, reducing with distance. If the induced tensile stress were not enough to overcome the compressive *in situ* stress, then the fracture would remain closed. If the injection were occurring very near σ_{hmin}, then the tensile thermal stresses could exceed the *in situ* compressive stress and put the fracture into tension. In that case, fracture opening could occur and permeability could increase dramatically.

A problem with this interpretation is that it is unlikely that the fracture could be induced to open, even if experiencing a thermal tension of 3.5 MPa. Assuming that the fracture zone were at the top of the openhole section of GPK2 (where σ_{hmin} is smallest relative to P), then according to the Valley and Evans (2007) stress profile, P was about 4 MPa below σ_{hmin}. Another problem is that the fracture zones at Soultz were not observed to be oriented perpendicular to σ_{hmin} (in fact, if they were, they wouldn't bear any shear stress and could not fail in shear). Fractures not oriented perpendicular to σ_{hmin} bear a normal stress that is greater than σ_{hmin}. By definition, the orientation of σ_{hmin} is the

orientation that would minimize compressive stress. At 4.4 km, the depth of the top of the openhole section of GPK2, the Valley and Evans (2007) profile predicts that σ_{hmin} is 60 MPa and σ_v is 111 MPa. The fluid pressure at that depth reached about 56 MPa during the June and July stimulation of GPK2. Using a stress rotation, it can be calculated (Jaeger et al., 2007) that a fracture zone dipping 70º and striking perpendicular to σ_{hmin} would experience a normal stress of 66 MPa. With the fluid pressure at 56 MPa, thermal stresses would need to induce 10 MPa of tensile stress in order to cause opening of the fracture.

Another problem with Model B is that it while it could match Transients A and B, which are relatively short, when the model was run for longer periods, it showed anomalous behavior that may not be consistent with the observations.

Model B was effectively a dual permeability MINC (Multiple Interacting Continua) model. However the *kh* within the damaged zone was set to be 10% of the *kh* in the core, so Model B was close to being a MINC dual porosity model (in a dual porosity model, flow from adjacent matrix blocks is not possible, unlike in dual permeability models). The pressure derivative of a typical MINC model shows an initial increase, then a sharp decrease followed by a long level period, and finally a late time increase (Bourdet, 2002). The initial decrease is caused by fluid diffusion into the matrix, which reduces the rate at which the pressure derivative can increase. When the matrix becomes filled, the rate of pressure increases rises back, causing the late time increase in pressure derivative.

An initial decrease in the pressure derivative curve, which is a characteristic behavior of MINC behavior, is not observed in the GPK2 pressure transients. A possible explanation could be that the initial drop in the pressure derivative was masked by an extremely negative skin, which would significantly reduce the early time pressure derivative. Model B is shown for three values of skin in Figure 6-11. The skin values are zero, *-3,* and *-6.* Note that Figure 6-9 only showed the transient until 10,000 seconds, but Figure 6-11 shows the full duration of the transient.
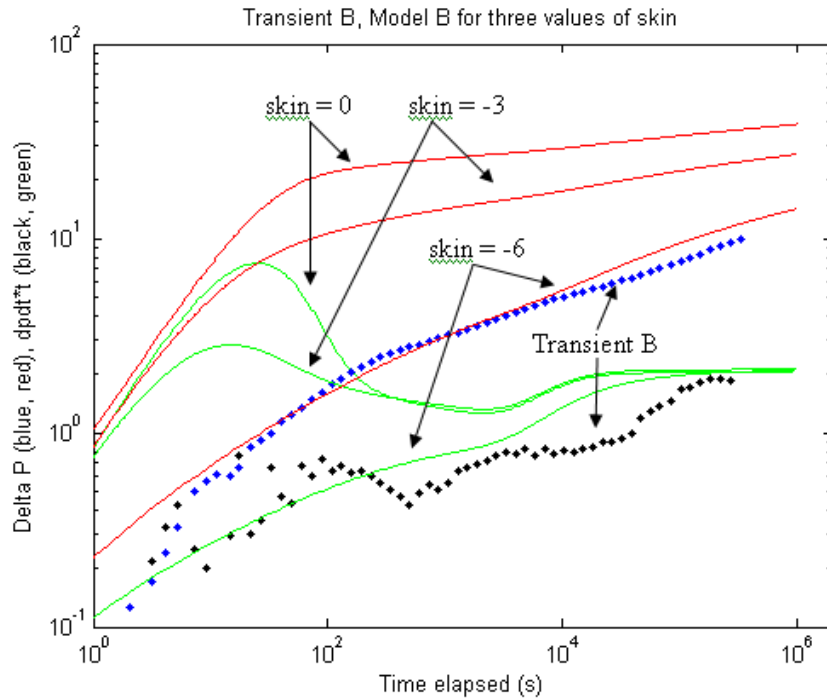
Figure 6-11: Model B match to Transient B, showing the full time history. In addition, the same model is shown for two other values of skin, -3 and 0.

Figure 6-11 demonstrates how negative skin reduces the early time change in pressure and can mask the hump in the pressure derivative curve caused by the MINC.

The Model B match to Transient B is shown above in Figure 6-11 as the line with skin = -6. Seen in the context of the full Transient B, the Model B does not appear to match as well as it did in Figure 6-9, when only the first 10,000 seconds were shown. The problem is that Model B had a late time hump in the pressure derivative curve. That hump was caused by the increase in the derivative of the pressure transient because of the finite size of the damage zone. If Model B is the correct conceptual model to describe the Soultz fracture zones, then the damage zone boundary hump should be in the pressure transient. A late time hump was present in the full Transient B, but it occurred so late that it was likely caused with boundary effects associated with the edge of the stimulated region.

6.4 Conclusions

Understanding how storativity and permeability are distributed and created at Soultz is critical to design of future hydraulic stimulations and prediction of reservoir performance.

This chapter reviewed the evidence that flow is primarily localized in small number of fracture zones with width of several meters. That interpretation is most consistent with combined interpretation of spinner logs, wellbore imaging logs, core analysis, microseismic relocation, mass balance calculations, tracer tests interpretations, and pressure transient analysis.

It appears unlikely that creation of new opening mode tensile fractures is a major source of permeability and storativity creation at Soultz, but that mechanism cannot be completely discounted. Valley and Evans (2007) and Cornet et al. (2007) interpreted injection pressure records and concluded that fracture opening occurred at the top of the openhole sections during most of the Soultz stimulations. In this chapter, it was assumed that the pressure transients occurred due to flow in only closed, preexisting fractures. Even according to the Valley and Evans (2007) and Cornet et al. (2007) stress profiles, injection occurred below the minimum principal stress during the stimulations analyzed in this chapter.

In order to investigate the permeability distribution in the Soultz fracture zones, analysis was carried out on two pressure transients associated with the June and July 2000 hydraulic stimulation of GPK2. During these stimulations, the downhole pressure was well below the minimum principal stress according to the Valley and Evans (2007) profiles, and so propagation of new opening mode fractures was not possible. Numerical models corresponding to three conceptual models were constructed. The models corresponded to a fracture embedded in granite, a fracture surrounded by an intermediate permeability and porosity damage zone, and a homogenous permeability and porosity damage zone embedded in granite. Combinations of parameters were identified for all three models that matched each of the two transients. Roughly consistent values were estimated for each of the two transients.

The exact numerical values calculated were less important than their general magnitude. The objective was to see if the conceptual models could plausibly explain the observations.

The isolated fracture model required an unrealistically large hydraulic diffusivity and negative skin to match the data, and so seems unlikely to be the correct interpretation.

The two fracture zone models were able to match the data, but differed in the amount of negative skin they required. The homogenous property fracture zone required a skin of -4. That skin could be explained by the geometrical effect of the well intersecting the fracture zone at an acute angle. The fracture and damage zone model required a skin of -6. Such a negative skin is very unusual and would require an exceptionally high permeability in the near wellbore region. A possible explanation is that the fracture could be opening, possibly due to thermal stresses. However, calculations indicated that thermal stresses could not account for enough stress to put the fracture plane into tension. Another problem for the damaged zone model was that it predicted a period of significant increase in the pressure derivative curve due to the pressure transient reaching the vertical edge of the damaged zone.

Overall, the pressure transient analysis suggested that the homogenous property fracture zone was the most consistent with the data, but it could not rule out the fracture embedded in a damaged zone model. The literature on fault zones suggests that it is common for damaged zones to have higher permeabilities than fault cores. On the other hand, large scale quartz deposition in the fault cores at Soultz suggests that they may sometimes be sites for significant fluid flow.

It may be possible to reduce the ambiguities in interpretation by looking at other pressure transients at Soultz. Because fracture opening emerged as a possibly confounding factor in the analysis, determining whether and to what extent it is happening at Soultz should be a priority for future work.

Chapter 7

7 Conclusion

7.1 Future Work

There are many opportunities to extend the work described in this dissertation. These opportunities can be divided into (1) applications of modeling to hydraulic stimulation, (2) code development, and (3) induced seismicity.

For code development, moving to three-dimensional simulations is a priority. With three dimensions, problem size will increase, and so code parallelization may become necessary. Further work is needed for efficient, robust methods of earthquake modeling that can be performed on large problems and are convergent to grid refinement (as discussed in Section 2.2.5.4). The code could be extended to include multiphase flow, thermal effects, thermoelasticity, and (for gas shale) production from the matrix. These extensions are divided between techniques that would not require discretizing the matrix (which would be either less accurate and/or useful only for short-duration problems in which one-dimensional approximations can be used) and techniques that would involve discretizing the matrix (which would be much more computationally intensive). As an alternative, upscaling algorithms could be applied to transfer the detailed DFN results from the model to an effective continuum model for modeling of long term reservoir

behavior. Currently, stress interaction between elements at low angle intersections cause major problems in the simulator. Mitigation requires either using networks that do not contain low angle intersections (Section 2.2.4.1) or using a method of applying penalty stresses when problems arise (Section 2.2.5.6). A more rigorous and robust method for handling intersections is needed.

The modeling methodology described in this dissertation requires simulations to be initialized with realizations of the preexisting fracture network. In this dissertation, methods of generating realistic fracture networks were discussed only briefly. The conclusions from the modeling in this dissertation were not dependent on the details of the networks (aside from overall properties like percolation and fracture orientation statistics), nor were any actual field sites modeled, and so it was not necessary to use highly realistic fracture networks. However, realistic generation of fracture networks could be highly valuable for practical field scale modeling and basic research. Further work could include (1) outcrop and borehole study to generate conceptual ideas about what realistic fracture networks look like in different settings, and (2) development of geostatistical algorithms for turning these conceptual ideas into stochastic realizations of fracture networks that can be conditioned to wellbore image logs.

There are opportunities to use the modeling and concepts in this dissertation to applied problems. A priority is to apply the methodologies for diagnosing stimulation mechanism from Chapter 3 to actual field data. Even though the needed data could be routinely collected, often they are not. Work is needed to build field scale models using actual data and attempt to match observed behavior. Field scale modeling will become more viable with further code development, particularly the ability to perform three-dimensional simulations. Field scale modeling will be valuable in learning how to parameterize these models and validating the modeling approach. The goal is to use field scale models for routine design and optimization of hydraulic stimulation.

As demonstrated in this dissertation, there is great value to generic modeling. There is much more work that could be pursued in this direction. Processes can be examined and described in detail, and the relative importance of different uncertainties can be investigated. Generic modeling can also be useful for experimenting with novel ideas

about stimulation design.   Numerical experiments are much cheaper than field experiments, and while field experiments must ultimately be done to verify model results, modeling can help identify the ideas that are most promising for testing in the field and the data that needs to be collected.

For EGS, an important goal is to identify the best geological settings and stimulation techniques. Different stimulation techniques may be best suited for different settings (and stimulation mechanisms), and modeling could identify the strategies optimized for each setting. Ultimately, modeling could be used to identify the best overall design for an EGS system, taking into account both geological setting and stimulation design. In some cases, technologies needed for EGS do not yet exist (such as reliable high temperature openhole packers), and modeling could quantify the value of these technologies, helping in allocation of research funding by the public and private sector. Having a correct conceptual model for stimulation mechanism will be critical for these studies, which is one reason by stimulation mechanism was a major topic of this dissertation.

For gas shale, differences in mechanisms could account for variations in productivity between stages or fields. The concepts in this dissertation could be used to explain variations in productivity and assist in formation evaluation. Further development of modeling will be valuable for selection of routine stimulation design parameters, such as stage spacing, well spacing, and pumped volumes. Stimulation techniques could be better optimized for the geological conditions specific to a particular site. The model could be used to invent novel stimulation techniques that would improve ultimate recovery and/or reduce cost. Improved understanding of fundamental processes, which is dissertation is focused on, will enable engineers to design stimulation techniques more effectively and bypass the trial and error approach that is often used in industry.

Estimation of induced seismicity hazard analysis is a major application of the modeling described in this dissertation. Our vision is that models to estimate induced seismicity hazard could be constructed routinely prior to a project. The main obstacle to using modeling for seismic hazard analysis is the difficulty of parameterizing a model. In Chapter 5, it is argued that induced seismicity hazard can be reduced to the following

question: are there significant sized faults that will slip seismically in response to the pressure and stress perturbations caused by this injection? Key questions are: (1) how can we predict whether induced slip on a fault will be seismic or aseismic and (2) in crystalline rock, where seismic data cannot be used to identify faults, how can we estimate the largest size of fault that may be present? As discussed in Section 5.1.1, induced seismicity hazard analysis often relies on statistical techniques. Our proposed method for induced seismicity hazard analysis is based understanding the fundamental physical processes.

Finally, more work is needed to establish realistic estimates of seismic hazard from earthquake triggering. Event magnitudes from induced seismicity can be expected to be limited to the size of the subsurface where pressure and stress have been perturbed, but theoretically, triggered events could be disproportionately large relative to the size of the perturbation. Whether such events have ever occurred, even after decades of human activity that have perturbed the fluid pressure and stress in the Earth, is an issue that needs to be addressed in order to determine how or whether triggered events should be considered in hazard analysis.

7.2 Summary

This dissertation contains many detailed conclusions on a variety of related topics. In Section 1.3, many of the specific findings are listed, and the chapter introductions summarize the findings of each chapter.

The overall concept of this research has been to integrate field observation with carefully designed computational modeling to develop better understanding of the process of hydraulic stimulation and deliver practically useful recommendations.

In Chapter 2, the details of the model used in Chapter 3 are described. The model couples fluid flow, stresses induced by fracture opening and sliding, transmissivity coupling to deformation, friction evolution, and fracture propagation in two-dimensional discrete fracture networks. The model is efficient enough to simulate networks with thousands of fractures. A variety of novel techniques were developed to enable the

model to be accurate, efficient, realistic, and convergent to discretization refinement in time and space. Various simulations options were tested and optimal settings were identified. Testing demonstrated that simulation results are profoundly affected by the stresses induced by fracture deformation, justifying the considerable effort required to include these stresses in the model.

In Chapter 3, four conceptual models are presented that represent the main hypotheses about stimulation mechanism from the literature of hydraulic fracturing. We refer to the stimulation mechanisms as Pure Opening Mode (PSS), Pure Shear Stimulation (PSS), Mixed-Mechanism Stimulation (MMS), and Primary Fracturing with Shear Stimulation Leakoff (PFSSL). Computation models were used to investigate the properties of each mechanism. Geological factors that affect stimulation mechanism were identified. Techniques for diagnosing stimulation mechanism were devised, including interpretation of bottom hole pressure during injection, shut-in, and production, microseismic relocations, and wellbore image logs. A Tendency to Shear Stimulation (TSS) test was proposed as a way to directly measure a formation's ability to experience shear stimulation and to help diagnose mechanism. Several physical mechanisms were identified that could have important practical implications: crack-like shear stimulation, fluid trapping due to snapoff, and confusion of shear stimulation and tensile fracturing.

In Chapter 4, a model was used that couples fluid flow with rate and state earthquake simulation. The model was used to investigate the interaction of fluid flow, permeability evolution, deformation, and friction evolution. A variety of observations about induced seismicity in EGS were explained. Producing fluid back after injection and gradually reducing injection pressure during stimulation were identified as strategies for minimizing induced seismicity.

In Chapter 5, a review of historical EGS projects demonstrated that the severity of induced seismicity was strongly correlated to the degree of brittle fault zone development. While degree of fault zone development is not the only parameter that affects induced seismicity hazard, the results suggest that it may be an important parameter. The fracture networks at each project were categorized along a continuum from thick, porous fault zones to thin cracks. Observations from specific EGS projects

fell across the full continuum, a result that has important implications not only for induced seismicity, but for fractured reservoirs in general.

In Chapter 6, a pressure transient analysis was performed using data from the EGS project at Soultz-sous-Forêts. At Soultz, fluid injection induced slip and transmissivity enhancement in large fault zones. The pressure transient analysis showed that these fault zones are best described as a slabs of single porosity, single permeability material. Evidence of dual porosity behavior was not found.

References

1. Abelin, H., L. Birgersson, L. Moreno, H. Widén, T. Ågren, and I. Neretnieks (1991), A large-scale flow and tracer experiment in granite: 2. Results and interpretation, *Water Resources Research*, *27*(12), 3119-3135, doi:10.1029/91WR01404.

2. Abramowitz, M., and I. A. Stegun (1972), *Handbook of Mathematical Functions with Formulas, Graphs, and Mathematical Tables*, Knovel, U.S. Dept. of Commerce: U.S. G.P.O., Washington, D.C.

3. Adachi, J., E. Siebrits, A. Peirce, and J. Desroches (2007), Computer simulation of hydraulic fractures, *International Journal of Rock Mechanics and Mining Sciences*, *44*(5), 739-757, doi:10.1016/j.ijrmms.2006.11.006.

4. Aki, K., M. Fehler, and S. Das (1977), Source mechanism of volcanic tremor: fluid-driven crack models and their application to the 1963 Kilauea eruption, *Journal of Volcanology and Geothermal Research*, *2*(3), 259-287, doi:10.1016/0377-0273(77)90003-8.

5. Aki, K., and P. G. Richards (2002), *Quantitative Seismology*, 2nd ed., University Science Books, Sausalito, Calif.

6. Amestoy, P. R., T. A. Davis, and I. S. Duff (1996), An approximate minimum degree ordering algorithm, *SIAM Journal on Matrix Analysis and Applications*, *17*(4), 886-905, doi:10.1137/S0895479894278952.

7. Amestoy, P. R., T. A. Davis, and I. S. Duff (2004), Algorithm 837: AMD, an approximate minimum degree ordering algorithm, *ACM Transactions on Mathematical Software*, *30*(3), 381-388, doi:10.1145/1024074.1024081.

8. Anderson, E., Z. Bai, C. Bischof, S. Blackford, J. Demmel, J. Dongarra, J. Du Croz, A. Greenbaum, S. Hammarling, A. McKenney, and D. Sorensen (1999), *LAPACK Users' Guide*, Third ed., Society for Industrial and Applied Mathematics, Philadelphia, PA.

9. Armand, G., M. Boulon, N. Hoteit, and S. Cannic (1998), Mechanical behavior of natural joints of granodiorite under high normal stress, in *Mechanics of Jointed and Faulted Rock: Proceedings of the Third International Conference on the Mechanics of Jointed and Faulted Rock, MJFR-3, Vienna, Austria, 6-9 April 1998*, edited by H. P. Rossmanith, pp. 217-222, A.A. Balkema, Rotterdam; Brookfield.

10. Asanuma, H., H. Nozaki, T. Uhara, H. Niitsuma, R. Baria, and D. Wyborn (2006), Spatial and temporal distribution of larger seismic events at European and Australian HDR sites, paper presented at the Thirty-First Workshop on Geothermal Reservoir Engineering, Stanford University, <http://www.geothermal-energy.org/pdf/IGAstandard/SGW/2006/asanuma.pdf>.

11. Asanuma, H., N. Soma, H. Kaieda, Y. Kumano, T. Izumi, K. Tezuka, H. Niitsuma, and D. Wyborn (2005), Microseismic monitoring of hydraulic stimulation at the Australian HDR project in Cooper Basin, paper presented at the World Geothermal Congress, Antalya, Turkey, <http://www.geothermal-energy.org/pdf/IGAstandard/WGC/2005/1615.pdf>.

12. Asgian, M. (1989), A numerical model of fluid-flow in deformable naturally fractured rock masses, *International Journal of Rock Mechanics and Mining Sciences & Geomechanics Abstracts*, *26*(3–4), 317-328, doi:10.1016/0148-9062(89)91980-3.

13. Auradou, H., G. Drazer, A. Boschan, J.-P. Hulin, and J. Koplik (2006), Flow channeling in a single fracture induced by shear displacement, *Geothermics*, *35*(5–6), 576-588, doi:10.1016/j.geothermics.2006.11.004.

14. Aziz, K., and A. Settari (1979), *Petroleum Reservoir Simulation*, Applied Science Publishers, London.

15. Bachmann, C. E., S. Wiemer, J. Woessner, and S. Hainzl (2011), Statistical analysis of the induced Basel 2006 earthquake sequence: introducing a probability-based monitoring approach for Enhanced Geothermal Systems, *Geophysical Journal International*, *186*(2), 793-807, doi:10.1111/j.1365-246X.2011.05068.x.

16. Baisch, S., and R. Vörös (2009), Deep heat mining Basel -- seismic risk analysis: AP 3000, induced seismicity. Q-Con Report, <http://www.wsu.bs.ch/geothermie.htm>.

17. Baisch, S., and R. Vörös (2011), Geomechanical study of Blackpool seismicity. Q-Con Report, <http://www.cuadrillaresources.com/cms/wp-content/uploads/2011/12/Q-con_CUA001_v8.pdf>.

18. Baisch, S., R. Vörös, E. Rothert, H. Stang, R. Jung, and R. Schellschmidt (2010), A numerical model for fluid injection induced seismicity at Soultz-sous-Forêts, *International Journal of Rock Mechanics and Mining Sciences*, *47*(3), 405-413, doi:10.1016/j.ijrmms.2009.10.001.

19. Baisch, S., R. Vörös, R. Weidler, and D. Wyborn (2009), Investigation of fault mechanisms during geothermal reservoir stimulation experiments in the Cooper Basin, Australia, *Bulletin of the Seismological Society of America*, *99*(1), 148-158, doi:10.1785/0120080055.

20. Baisch, S. W., Ralph; Voros, Robert; Jung, Reinhard (2006), A conceptual model for post-injection seismicity at Soultz-sous-Forêts, *Geothermal Resources Council Transactions*, *30*, 601-606.

21. Baria, R., Michelet, S., Baumgärtner, J., Dyer, B., Gerard, A., Nicholls, J., Hettkamp, T., Teza, D., Soma, N., Asanuma, H., Garnish, J., and Megel, T. (2004), Microseismic monitoring of the world's largest potential HDR reservoir, paper presented at the Twenty-Ninth Workshop on Geothermal Reservoir Engineering, Stanford University, <https://pangea.stanford.edu/ERE/db/IGAstandard/record_detail.php?id=1702>.

22. Baria, R., R. Jung, T. Tischner, J. Nicholls, S. Michelet, B. Sanjuan, N. Soma, H. Asanuma, B. Dyer, and J. Garnish (2006), Creation of an HDR reservoir at 5000 m depth at the European HDR Project, paper presented at the Thirty-First Workshop on Geothermal Reservoir Engineering, Stanford University, <http://www.geothermal-energy.org/pdf/IGAstandard/SGW/2006/baria1.pdf?>.

23. Barton, N., S. Bandis, and K. Bakhtar (1985), Strength, deformation and conductivity coupling of rock joints, *International Journal of Rock Mechanics and Mining Sciences & Geomechanics Abstracts*, *22*(3), 121-140, doi:10.1016/0148-9062(85)93227-9.

24. Baumgärtner, J., A. Gerard, R. Baria, and J. Garnish (2000), Progress at the European HDR Project at Soultz-sous-Forêts: preliminary results from the deepening of the well GPK2 to 5000m, paper presented at the Twenty-Fifth Workshop on Geothermal Reservoir Engineering, Stanford University, <https://pangea.stanford.edu/ERE/db/IGAstandard/record_detail.php?id=216>.

25. Baumgärtner, J., and M. D. Zoback (1989), Interpretation of hydraulic fracturing pressure-time records using interactive analysis methods, *International Journal of Rock Mechanics and Mining Sciences & Geomechanics Abstracts*, *26*(6), 461-469, doi:10.1016/0148-9062(89)91422-8.

26. Beckwith, R. (2010), Hydraulic fracturing: the fuss, the facts, and the future, *Journal of Petroleum Technology*, *62*(12), 34-40.

27. Ben-Zion, Y. (2008), Collective behavior of earthquakes and faults: continuum-discrete transitions, progressive evolutionary changes, and different dynamic regimes, *Reviews of Geophysics*, *46*(4), doi:10.1029/2008RG000260.

28. Ben-Zion, Y., and J. R. Rice (1993), Earthquake failure sequences along a cellular fault zone in a three-dimensional elastic solid containing asperity and nonasperity regions, *Journal of Geophysical Research*, *98*(B8), 14109-14131, doi:10.1029/93JB01096.

29. Ben-Zion, Y., and C. G. Sammis (2003), Characterization of fault zones, *Pure and Applied Geophysics*, *160*(3), 677-715, doi:10.1007/PL00012554.

30. Berkowitz, B. (1995), Analysis of fracture network connectivity using percolation theory, *Mathematical Geology*, *27*(4), 467-483, doi:10.1007/BF02084422.

31. Bird, R. B., W. E. Stewart, and E. N. Lightfoot (2006), *Transport Phenomena, Revised 2nd Edition*, 2nd ed., John Wiley & Sons, Inc.

32. Blanpied, M. L., D. A. Lockner, and J. D. Byerlee (1995), Frictional slip of granite at hydrothermal conditions, *Journal of Geophysical Research*, *100*(B7), 13045-13064, doi:10.1029/95JB00862.

33. Blanton, T. (1982), An experimental study of interaction between hydraulically induced and pre-existing fractures, SPE 10847, paper presented at the SPE Unconventional Gas Recovery Symposium, Pittsburgh, Pennsylvania, doi:10.2118/10847-MS.

34. Bommer, J. J., S. Oates, J. M. Cepeda, C. Lindholm, J. Bird, R. Torres, G. Marroquín, and J. Rivas (2006), Control of hazard due to seismicity induced by a Hot Fractured Rock geothermal project, *Engineering Geology*, *83*(4), 287-306, doi:10.1016/j.enggeo.2005.11.002.

35. Bourdet, D. (2002), *Well Test Analysis: the Use of Advanced Interpretation Models*, Elsevier, Amsterdam; Boston.

36. Bowker, K. A. (2007), Barnett Shale gas production, Fort Worth Basin: issues and discussion, *AAPG Bulletin*, *91*(4), 523-533, doi:10.1306/06190606018.

37. Bradley, A. M. (2012), H-matrix and block error tolerances, *arXiv:1110.2807v2*, source code available at http://www.stanford.edu/~ambrad, paper available at http://arvix.org/abs/1110.2807.

38. Brown, D. W. (1989), The potential for large errors in the inferred minimum earth stress when using incomplete hydraulic fracturing results, *International Journal of Rock Mechanics and Mining Sciences & Geomechanics Abstracts*, *26*(6), 573-577, doi:10.1016/0148-9062(89)91437-X.

39. Brown, D. W., D. V. Duchane, G. Heiken, and V. T. Hriscu (2012), *Mining the Earth's Heat: Hot Dry Rock Geothermal Energy*, Springer-Verlag.

40. Bruel, D. (1995), Heat extraction modelling from forced fluid flow through stimulated fractured rock masses: application to the Rosemanowes Hot Dry Rock reservoir, *Geothermics*, *24*(3), 361-374, doi:10.1016/0375-6505(95)00014-H.

41. Bruel, D. (2007), Using the migration of the induced seismicity as a constraint for fractured Hot Dry Rock reservoir modelling, *International Journal of Rock Mechanics and Mining Sciences*, *44*(8), 1106-1117, doi:10.1016/j.ijrmms.2007.07.001.

42. Bruel, D., and J. Charlety (2007), Moment-frequency distribution as a constraint for hydro-mechanical modelling in fracture networks, paper presented at the 11th Congress of the International Society for Rock Mechanics, Lisbon, Portugal.

43. Bruhn, R. L., W. T. Parry, W. A. Yonkee, and T. Thompson (1994), Fracturing and hydrothermal alteration in normal fault zones, *Pure and Applied Geophysics*, *142*(3), 609-644, doi:10.1007/BF00876057.

44. Cacas, M. C., E. Ledoux, G. d. Marsily, A. Barbreau, P. Calmels, B. Gaillard, and R. Margritta (1990), Modeling fracture flow with a stochastic discrete fracture network: calibration and validation: 2. The transport model, *Water Resources Research*, *26*(3), 491-500, doi:10.1029/WR026i003p00491.

45. Caine, J. S., J. P. Evans, and C. B. Forster (1996), Fault zone architecture and permeability structure, *Geology*, *24*(11), 1025-1028, doi:10.1130/0091-7613(1996)024<1025:FZAAPS>2.3.CO;2.

46. Cappa, F., and J. Rutqvist (2011), Impact of CO2 geological sequestration on the nucleation of earthquakes, *Geophysical Research Letters*, *38*(17), doi:10.1029/2011GL048487.

47. Cathles, L., L. Brown, M. Taam, and A. Hunter (2012), A commentary on "The greenhouse-gas footprint of natural gas in shale formations" by R.W. Howarth, R. Santoro, and Anthony Ingraffea, *Climatic Change*, *113*(2), 525-535, doi:10.1007/s10584-011-0333-0.

48. Charléty, J., N. Cuenot, L. Dorbath, C. Dorbath, H. Haessler, and M. Frogneux (2007), Large earthquakes during hydraulic stimulations at the geothermal site of Soultz-sous-Forêts, *International Journal of Rock Mechanics and Mining Sciences*, *44*(8), 1091-1105, doi:10.1016/j.ijrmms.2007.06.003.

49. Chen, Z., S. P. Narayan, Z. Yang, and S. S. Rahman (2000), An experimental investigation of hydraulic behaviour of fractures and joints in granitic rock, *International Journal of Rock Mechanics and Mining Sciences*, *37*(7), 1061-1071, doi:10.1016/S1365-1609(00)00039-3.

50. Cheng, Y. (2009), Boundary element analysis of the stress distribution around multiple fractures: implications for the spacing of perforation clusters of hydraulically fractured horizontal wells, SPE 125769, paper presented at the SPE Eastern Regional Meeting, Charleston, West Virginia, USA, doi:10.2118/125769-MS.

51. Chester, F. M., and J. M. Logan (1986), Implications for mechanical properties of brittle faults from observations of the Punchbowl Fault Zone, California, *Pure and Applied Geophysics*, *124*(1), 79-106, doi:10.1007/BF00875720.

52. Cipolla, C., N. Warpinski, M. Mayerhofer, E. Lolon, and M. Vincent (2008), The relationship between fracture complexity, reservoir properties, and fracture treatment design, SPE 115769, paper presented at the SPE Annual Technical Conference and Exhibition, Denver, Colorado, USA, doi:10.2118/115769-MS.

53. Cipolla, C., X. Weng, M. Mack, U. Ganguly, H. Gu, O. Kresse, and C. E. Cohen (2011), Integrating microseismic mapping and complex fracture modeling to characterize fracture complexity, SPE 140185, paper presented at the SPE Hydraulic Fracturing Technology Conference, The Woodlands, Texas, USA, doi:10.2118/140185-MS.

54. Cipolla, C. L., and E. P. Lolon (2010), Reservoir modeling in shale-gas reservoirs, *SPE Reservoir Evaluation & Engineering*, *13*(4), 638-653, doi:10.2118/125530-PA.

55. Cladouhos, T., S. Petty, G. Foulger, B. Julian, M. Fehler (2010), Injection induced seismicity and geothermal energy, *Geothermal Resources Council Transactions*, *34*, 1213-1220.

56. Cladouhos, T. T., M. Clyne, M. Nichols, S. Petty, W. L. Osborn, and L. Nofziger (2011), Newberry Volcano EGS demonstration stimulation modeling, *Geothermal Resources Council Transactions*, *35*, 317-322.

57. Cladouhos, T. T., and R. Marrett (1996), Are fault growth and linkage models consistent with power-law distributions of fault lengths?, *Journal of Structural Geology*, *18*(2–3), 281-293, doi:10.1016/S0191-8141(96)80050-2.

58. Cornet, F., and T. Bérard (2003), A case example of integrated stress profile evaluation, in *Rock Stress: Proceedings of the Third International Symposium on Rock Stress: RS Kumatomo '03, 4-6 November, 2003, Kumatomo, Japan*, edited by A. Sato, Y. Obara and K. Sugawara, p. 586, A.A. Balkema, Rotterdam; Exton, Pennsylvania.

59. Cornet, F. H., T. Bérard, and S. Bourouis (2007), How close to failure is a granite rock mass at a 5 km depth?, *International Journal of Rock Mechanics and Mining Sciences*, *44*(1), 47-66, doi:10.1016/j.ijrmms.2006.04.008.

60. Cornet, F. H., J. Helm, H. Poitrenaud, and A. Echecopar (1997), Seismic and aseismic slips induced by large-scale fluid injections, *Pure and Applied Geophysics*, *150*(3), 563-583, doi:10.1007/s000240050093.

61. Couzens-Schultz, B. A., and A. W. Chan (2010), Stress determination in active thrust belts: an alternative leak-off pressure interpretation, *Journal of Structural Geology*, *32*(8), 1061-1069, doi:10.1016/j.jsg.2010.06.013.

62. Cramer, D. (2008), Stimulating unconventional reservoirs: lessons learned, successful practices, areas for improvement, SPE 114172, paper presented at the SPE Unconventional Reservoirs Conference, Keystone, Colorado, USA, doi:10.2118/114172-MS.

63. Crouch, S. L., and A. M. Starfield (1983), *Boundary Element Methods in Solid Mechanics: with Applications in Rock Mechanics and Geological Engineering*, Allen & Unwin, London; Boston.

64. Cuenot, N., M. Frogneux, C. Dorbath, and M. Calo (2011), Induced microseismic activity during recent circulation tests at the EGS site of Soultz-sous-Forêts (France), paper presented at the Thirty-Sixth Workshop on Geothermal Reservoir Engineering, Stanford University, <http://www.geothermal-energy.org/pdf/IGAstandard/SGW/2011/cuenot.pdf?>.

65. Dahi-Taleghani, A., and J. Olson (2011), Numerical modeling of multistranded-hydraulic-fracture propagation: accounting for the interaction between induced and natural fractures, *SPE Journal*, *16*(3), doi:10.2118/124884-PA.

66. Damjanac, B., I. Gil, M. Pierce, and M. Sanchez (2010), A new approach to hydraulic fracturing modeling in naturally fractured reservoirs, ARMA 10-400, paper presented at the 44th U.S. Rock Mechanics Symposium and 5th U.S.-Canada Rock Mechanics Symposium, Salt Lake City, Utah.

67. Davatzes, N. C., and S. H. Hickman (2009), Fractures, stress and fluid flow prior to stimulation of Well 27-15, Desert Peak, Nevada, EGS Project, paper presented at the Thirty-Fourth Workshop on Geothermal Reservoir Engineering, Stanford University, <http://www.geothermal-energy.org/pdf/IGAstandard/SGW/2009/davatzes.pdf?>.

68. Davatzes, N. C., and S. H. Hickman (2010), The feedback between stress, faulting, and fluid flow: lessons from the Coso Geothermal Field, CA, USA, paper presented at the World Geothermal Congress, Bali, Indonesia, <http://www.geothermal-energy.org/pdf/IGAstandard/WGC/2010/1267.pdf?>.

69. Davis, T. A. (2004a), A column pre-ordering strategy for the unsymmetric-pattern multifrontal method, *ACM Transactions on Mathematical Software*, *30*(2), 165-195, doi:10.1145/992200.992205.

70. Davis, T. A. (2004b), Algorithm 832: UMFPACK, an unsymmetric-pattern multifrontal method, *ACM Transactions on Mathematical Software*, *30*(2), 196-199, doi:10.1145/992200.992206.

71. Davis, T. A. (2006), *Direct Methods for Sparse Linear Systems*, SIAM, Philadelphia, PA.

72. Davis, T. A., and I. S. Duff (1997), An unsymmetric-pattern multifrontal method for sparse LU factorization, *SIAM Journal on Matrix Analysis and Applications*, *18*(1), 140-158, doi:10.1137/S0895479894246905.

73. Davis, T. A., and I. S. Duff (1999), A combined unifrontal/multifrontal method for unsymmetric sparse matrices, *ACM Transactions on Mathematical Software*, *25*(1), 1-19, doi:10.1145/305658.287640.

74. Delaney, P. T., D. D. Pollard, J. I. Ziony, and E. H. McKee (1986), Field relations between dikes and joints: emplacement processes and paleostress analysis, *Journal of Geophysical Research*, *91*(B5), 4920-4938, doi:10.1029/JB091iB05p04920.

75. den Hartog, S. A. M., C. J. Peach, D. A. M. de Winter, C. J. Spiers, and T. Shimamoto (2012), Frictional properties of megathrust fault gouges at low sliding velocities: new data on effects of normal stress and temperature, *Journal of Structural Geology*, *38*(0), 156-171, doi:10.1016/j.jsg.2011.12.001.

76. Deng, S., R. Podgorney, and H. Huang (2011), Discrete element modeling of rock deformation, fracture network development and permeability evolution under hydraulic stimulation, paper presented at the Thirty-Sixth Workshop on Geothermal Reservoir Engineering, Stanford University, <http://www.geothermal-energy.org/pdf/IGAstandard/SGW/2011/deng.pdf?>.

77. Dershowitz, W. S., M. G. Cottrell, D. H. Lim, and T. W. Doe (2010), A discrete fracture network approach for evaluation of hydraulic fracture stimulation of naturally fractured reservoirs, ARMA 10-475, paper presented at the 44th U.S. Rock Mechanics Symposium and 5th U.S.-Canada Rock Mechanics Symposium, Salt Lake City, Utah.

78. Detournay, E. (2004), Propagation regimes of fluid-driven fractures in impermeable rocks, *International Journal of Geomechanics*, *4*(1), 35-45, doi:10.1061/(ASCE)1532-3641(2004)4:1(35).

79. Dezayes, C., A. Genter, and B. Valley (2010), Overview of the fracture network at different scales within the granite reservoir of the EGS Soultz site (Alsace, France), paper presented at the World Geothermal Congress, Bali, Indonesia, <http://www.geothermal-energy.org/pdf/IGAstandard/WGC/2010/3116.pdf?>.

80. Dieterich, J. H. (1979), Modeling of rock friction: 1. Experimental results and constitutive equations, *Journal of Geophysical Research*, *84*(B5), 2161-2168, doi:10.1029/JB084iB05p02161.

81. Dieterich, J. H. (1992), Earthquake nucleation on faults with rate-and state-dependent strength, *Tectonophysics*, *211*(1–4), 115-134, doi:10.1016/0040-1951(92)90055-B.

82. Dieterich, J. H. (1995), Earthquake simulations with time-dependent nucleation and long-range interactions, *Nonlinear Processes in Geophysics*, *2*, 109-120.

83. Dieterich, J. H. (2007), 4.04 - Applications of rate- and state-dependent friction to models of fault slip and earthquake occurrence, in *Treatise on Geophysics*, edited by S. Gerald, pp. 107-129, Elsevier, Amsterdam.

84. Dieterich, J. H., and B. D. Kilgore (1994), Direct observation of frictional contacts: new insights for state-dependent properties, *Pure and Applied Geophysics*, *143*(1), 283-302, doi:10.1007/BF00874332.

85. Dieterich, J. H., and K. B. Richards-Dinger (2010), Earthquake recurrence in simulated fault systems, in *Seismogenesis and Earthquake Forecasting: The Frank Evison Volume II*, edited by M. K. Savage, D. A. Rhoades, E. G. C. Smith, M. C. Gerstenberger and D. Vere-Jones, pp. 233-250, Springer Basel.

86. Dieterich, J. H., and D. E. Smith (2010), Nonplanar faults: mechanics of slip and off-fault damage, in *Mechanics, Structure, and Evolution of Fault Zones*, edited by Y. Ben-Zion and C. Sammis, pp. 1799-1815, Birkhäuser Basel, doi:10.1007/978-3-0346-0138-2_12.

87. Doe, T. W., and G. Boyce (1989), Orientation of hydraulic fractures in salt under hydrostatic and non-hydrostatic stresses, *International Journal of Rock Mechanics and Mining Sciences & Geomechanics Abstracts*, *26*(6), 605-611, doi:10.1016/0148-9062(89)91441-1.

88. Dongarra, J. J., J. D. Croz, S. Hammarling, and R. J. Hanson (1988a), An extended set of FORTRAN Basic Linear Algebra Subprograms, *ACM Transactions on Mathematical Software*, *14*(1), 1-17, doi:10.1145/42288.42291.

89. Dongarra, J. J., J. D. Croz, S. Hammarling, and R. J. Hanson (1988b), Algorithm 656: an extended set of basic linear algebra subprograms: model implementation and test programs, *ACM Transactions on Mathematical Software*, *14*(1), 18-32, doi:10.1145/42288.42292.

90. Dongarra, J. J., J. Du Croz, S. Hammarling, and I. S. Duff (1990a), A set of level 3 basic linear algebra subprograms, *ACM Transactions on Mathematical Software*, *16*(1), 1-17, doi:10.1145/77626.79170.

91. Dongarra, J. J., J. Du Croz, S. Hammarling, and I. S. Duff (1990b), Algorithm 679: A set of level 3 basic linear algebra subprograms: model implementation and test programs, *ACM Transactions on Mathematical Software*, *16*(1), 18-28, doi:10.1145/77626.77627.

92. Downie, R. C., E. Kronenberger, and S. C. Maxwell (2010), Using microseismic source parameters to evaluate the influence of faults on fracture treatments: a geophysical approach to interpretation, SPE 134772-MS, paper presented at the SPE Annual Technical Conference and Exhibition, Florence, Italy, doi:10.2118/134772-MS.

93. Du, C., L. Zhan, J. Li, X. Zhang, S. Church, K. Tushingham, and B. Hay (2011), Generalization of dual-porosity-system representation and reservoir simulation of hydraulic fracturing-stimulated shale gas reservoirs, SPE 146534, paper presented at the SPE Annual Technical Conference and Exhibition, Denver, Colorado, USA, doi:10.2118/146534-MS.

94. Economides, M. J., and K. G. Nolte (2000), *Reservoir Stimulation*, 3rd ed., John Wiley, Chichester, England; New York.

95. Eliasson, T. M., U. Sundquist, and T. Wallroth (1988), Rock mass characteristics at the HDR geothermal research site in the Bohus granite, SW Sweden. Department of Geology, Chalmers University of Technology and University of Göteborg.

96. Eliasson, T. M., E.-L. Tullborg, and O. Landström (1990), Fracture filling mineralogy and geochemistry at the Swedish HDR research site, Robertson Scientific Publications, paper presented at the Hot Dry Rock: Proceedings Camborne School of Mines International Hot Dry Rock Conference.

97. Esaki, T., S. Du, Y. Mitani, K. Ikusada, and L. Jing (1999), Development of a shear-flow test apparatus and determination of coupled properties for a single rock joint, *International Journal of Rock Mechanics and Mining Sciences*, *36*(5), 641-650, doi:10.1016/S0148-9062(99)00044-3.

98. Evans, J. P., C. B. Forster, and J. V. Goddard (1997), Permeability of fault-related rocks, and implications for hydraulic structure of fault zones, *Journal of Structural Geology*, *19*(11), 1393-1404, doi:10.1016/S0191-8141(97)00057-6.

99. Evans, K. F. (2005), Permeability creation and damage due to massive fluid injections into granite at 3.5 km at Soultz: 2. Critical stress and fracture strength, *Journal of Geophysical Research*, *110*(B4), doi:10.1029/2004JB003169.

100. Evans, K. F., A. Genter, and J. Sausse (2005), Permeability creation and damage due to massive fluid injections into granite at 3.5 km at Soultz: 1. Borehole observations, *Journal of Geophysical Research*, *110*(B4), doi:10.1029/2004JB003168.

101. Evans, K. F., H. Moriya, H. Niitsuma, R. H. Jones, W. S. Phillips, A. Genter, J. Sausse, R. Jung, and R. Baria (2005), Microseismicity and permeability enhancement of hydrogeologic structures during massive fluid injections into granite at 3 km depth at the Soultz HDR site, *Geophysical Journal International*, *160*(1), 389-412, doi:10.1111/j.1365-246X.2004.02474.x.

102. Evans, K. F., A. Zappone, T. Kraft, N. Deichmann, and F. Moia (2012), A survey of the induced seismic responses to fluid injection in geothermal and CO2 reservoirs in Europe, *Geothermics*, *41*(0), 30-54, doi:10.1016/j.geothermics.2011.08.002.

103. Fakcharoenphol, P., L. Hu, and Y. Wu (2012), Fully-implicit flow and geomechanics model: application for Enhanced Geothermal reservoir simulations, paper presented at the Thirty-Seventh Workshop on Geothermal Reservoir Engineering, Stanford University, <https://pangea.stanford.edu/ERE/db/IGAstandard/record_detail.php?id=8254>.

104. Fan, L., J. Thompson, and J. Robinson (2010), Understanding gas production mechanism and effectiveness of well stimulation in the Haynesville Shale through reservoir simulation, SPE 136696, paper presented at the Canadian Unconventional Resources and International Petroleum Conference, Calgary, Alberta, Canada, doi:10.2118/136696-MS.

105. Farrell, J., S. Husen, and R. B. Smith (2009), Earthquake swarm and b-value characterization of the Yellowstone volcano-tectonic system, *Journal of Volcanology and Geothermal Research*, *188*(1–3), 260-276, doi:10.1016/j.jvolgeores.2009.08.008.

106. Fast, R. E., A. S. Murer, and R. S. Timmer (1994), Description and analysis of cored hydraulic fractures – Lost Hills Field, Kern County, California, *SPE Production & Facilities*, *9*(2), doi:10.2118/24853-PA.

107. Faulkner, D. R., C. A. L. Jackson, R. J. Lunn, R. W. Schlische, Z. K. Shipton, C. A. J. Wibberley, and M. O. Withjack (2010), A review of recent developments concerning the structure, mechanics and fluid flow properties of fault zones, *Journal of Structural Geology*, *32*(11), 1557-1575, doi:10.1016/j.jsg.2010.06.009.

108. Faulkner, D. R., A. C. Lewis, and E. H. Rutter (2003), On the internal structure and mechanics of large strike-slip fault zones: field observations of the Carboneras fault in southeastern Spain, *Tectonophysics*, *367*(3–4), 235-251, doi:10.1016/S0040-1951(03)00134-3.

109. Fehler, M., and W. S. Phillips (1991), Simultaneous inversion for Q and source parameters of microearthquakes accompanying hydraulic fracturing in granitic rock, *Bulletin of the Seismological Society of America*, *81*(2), 553-575.

110. Fetterman, J. A., and N. C. Davatzes (2011), Evolution of porosity in fractures in the Newberry Volcano geothermal system, Oregon, USA: feedback between deformation and alteration, *Geothermal Resources Council Transactions*, *35*, 339-346.

111. Fisher, M. K., J. R. Heinze, C. D. Harris, D. B.M, C. A. Wright, and K. P. Dunn (2004), Optimizing horizontal completion techniques in the Barnett Shale using microseismic fracture mapping, SPE 90051, paper presented at the SPE Annual Technical Conference and Exhibition, Houston, Texas, doi:10.2118/90051-MS.

112. Fredd, C. N., S. B. McConnell, C. L. Boney, and K. W. England (2001), Experimental study of fracture conductivity for water-fracturing and conventional fracturing applications, *SPE Journal*, *6*(3), 288-298, doi:10.2118/74138-PA.

113. Freed, A. M. (2005), Earthquake triggering by static, dynamic, and postseismic stress transfer, *Annual Review of Earth and Planetary Sciences*, *33*, 335-367, doi:10.1146/annurev.earth.33.092203.122505.

114. Freund, L. B. (1990), *Dynamic Fracture Mechanics*, Cambridge University Press, Cambridge; New York.

115. Fu, P., S. M. Johnson, and C. R. Carrigan (2012), An explicitly coupled hydro-geomechanical model for simulating hydraulic fracturing in arbitrary discrete fracture networks, *International Journal for Numerical and Analytical Methods in Geomechanics*, doi:10.1002/nag.2135.

116. Gaarenstroom, L., R. a. J. Tromp, M. C. d. Jong, and A. M. Brandenburg (1993), Overpressures in the Central North Sea: implications for trap integrity and drilling safety, *Geological Society, London, Petroleum Geology Conference series*, *4*, 1305-1313, doi:10.1144/0041305.

117. Gale, J. F. W., and J. Holder (2008), Natural fractures in the Barnett Shale: constraints on spatial organization and tensile strength with implications for hydraulic fracture treatment in shale-gas reservoirs, ARMA 08-096, paper presented at the 42nd U.S. Rock Mechanics Symposium (USRMS), San Francisco, CA.

118. Gale, J. F. W., R. M. Reed, and J. Holder (2007), Natural fractures in the Barnett Shale and their importance for hydraulic fracture treatments, *AAPG Bulletin*, *91*(4), 603-622, doi:10.1306/11010606061.

119. Geertsma, J., and F. de Klerk (1969), A rapid method of predicting width and extent of hydraulically induced fractures, *Journal of Petroleum Technology*, *21*(12), doi:10.2118/2458-PA.

120. Genter, A. (1994), Structural analysis of core in the crystalline section of the borehole Urach 3 (Swabian Alb, Germany)*.* Bureau de recherches géologiques et minières (BRGM).

121. Genter, A., C. Castaing, C. Dezayes, H. Tenzer, H. Traineau, and T. Villemin (1997), Comparative analysis of direct (core) and indirect (borehole imaging tools) collection of fracture data in the Hot Dry Rock Soultz reservoir (France), *Journal of Geophysical Research*, *102*(B7), 15419-15431, doi:10.1029/97JB00626.

122. Genter, A., X. Goerk, J.-J. Graff, N. Cuenot, G. Krall, M. Schindler, and G. Ravier (2010), Current status of the EGS Soultz geothermal project (France), paper presented at the World Geothermal Congress, Bali, Indonesia, <http://www.geothermal-energy.org/pdf/IGAstandard/WGC/2010/3124.pdf?>.

123. Genter, A., and H. Traineau (1996), Analysis of macroscopic fractures in granite in the HDR geothermal well EPS-1, Soultz-sous-Forêts, France, *Journal of Volcanology and Geothermal Research*, *72*(1–2), 121-141, doi:10.1016/0377-0273(95)00070-4.

124. Genter, A., H. Traineau, B. Ledésert, B. Bourgine, and S. Gentier (2000), Over 10 years of geological investigations within the HDR Soultz project, France, paper presented at the World Geothermal Congress, Kyushu – Tohoku, Japan, <http://www.geothermal-energy.org/pdf/IGAstandard/WGC/2000/R0710.PDF?>.

125. Ghassemi, A., and S. Tarasovs (2006), Fractures slip and opening in response to fluid injection into a geothermal reservoir, paper presented at the Thirty-First Workshop on Geothermal Reservoir Engineering, Stanford University, <http://www.geothermal-energy.org/pdf/IGAstandard/SGW/2006/ghassemi.pdf?>.

126. Ghassemi, A., S. Tarasovs, and A. H. D. Cheng (2005), Integral equation solution of heat extraction-induced thermal stress in enhanced geothermal reservoirs, *International Journal for Numerical and Analytical Methods in Geomechanics*, *29*(8), 829-844, doi:10.1002/nag.440.

127. Ghassemi, A., S. Tarasovs, and A. H. D. Cheng (2007), A 3-D study of the effects of thermomechanical loads on fracture slip in enhanced geothermal reservoirs, *International Journal of Rock Mechanics and Mining Sciences*, *44*(8), 1132-1148, doi:10.1016/j.ijrmms.2007.07.016.

128. Ghosh, P. K. (1934), The Carnmenellis Granite: its petrology, metamorphism and tectonics, *Quarterly Journal of the Geological Society*, *90*(1-4), 240-276, doi:10.1144/GSL.JGS.1934.090.01-04.09.

129. Golder Associates (2009), User documentation: FracMan 7: interactive discrete feature data analysis, geometric modeling, and exploration simulation*.*

130. Gomberg, J., M. E. Belardinelli, M. Cocco, and P. Reasenberg (2005), Time-dependent earthquake probabilities, *Journal of Geophysical Research*, *110*(B5), doi:10.1029/2004JB003405.

131. Grabowski, J. W., P. K. Vinsome, R. Lin, G. A. Behie, and B. Rubin (1979), A fully implicit general purpose finite-difference thermal model for in situ combustion and steam, SPE 8396, paper presented at the SPE Annual Technical Conference and Exhibition, Las Vegas, Nevada, doi:10.2118/8396-MS.

132. Griffith, W., P. Sanz, and D. Pollard (2009), Influence of outcrop scale fractures on the effective stiffness of fault damage zone rocks, *Pure and Applied Geophysics*, *166*(10), 1595-1627, doi:10.1007/s00024-009-0519-9.

133. Griffith, W. A., S. Nielsen, G. D. Toro, and S. A. F. Smith (2010), Rough faults, distributed weakening, and off-fault deformation, *Journal of Geophysical Research*, *115*(B8), doi:10.1029/2009JB006925.

134. Gu, H., and X. Weng (2010), Criterion for fractures crossing frictional interfaces at non-orthogonal angles, ARMA 10-198, paper presented at the 44th U.S. Rock Mechanics Symposium and 5th U.S.-Canada Rock Mechanics Symposium, Salt Lake City, Utah.

135. Gu, H., X. Weng, J. Lund, M. Mack, U. Ganguly, and R. Suarez-Rivera (2011), Hydraulic fracture crossing natural fracture at non-orthogonal angles, a criterion, its validation and applications, SPE 139984, doi:10.2118/139984-MS.

136. Gulrajani, S. N., and K. G. Nolte (2000), Appendix: background for hydraulic fracturing pressure analysis techniques, in *Reservoir Stimulation*, edited by M. J. Economides and K. G. Nolte, John Wiley, Chichester, England; New York.

137. Haimson, B., and C. Fairhurst (1967), Initiation and extension of hydraulic fractures in rocks, *Society of Petroleum Engineers Journal*, *7*(3), doi:10.2118/1710-PA.

138. Haney, F., J. Kummerow, C. Langenbruch, C. Dinske, S. A. Shapiro, and F. Scherbaum (2011), Magnitude estimation for microseismicity induced during the KTB 2004/2005 injection experiment, *Geophysics*, *76*(6), WC47-WC53, doi:10.1190/geo2011-0020.1.

139. Hanks, T. C., and H. Kanamori (1979), A moment magnitude scale, *Journal of Geophysical Research*, *84*(B5), 2348-2350, doi:10.1029/JB084iB05p02348.

140. Häring, M., F. Ladner, U. Schanz, and T. Spillman (2007), Deep heat mining Basel, preliminary results, paper presented at the European Geothermal Conference, <http://www.geothermal-energy.org/pdf/IGAstandard/EGC/2007/184.pdf>.

141. Häring, M. O., U. Schanz, F. Ladner, and B. C. Dyer (2008), Characterisation of the Basel 1 enhanced geothermal system, *Geothermics*, *37*(5), 469-495, doi:10.1016/j.geothermics.2008.06.002.

142. Harris, R. A. (2000), Earthquake stress triggers, stress shadows, and seismic hazard. 1215-1225 pp, United States Geological Survey, <http://pubs.er.usgs.gov/publication/70022355>.

143. Hayashi, K., and H. Abé (1982), Opening of a fault and resulting slip due to injection of fluid for the extraction of geothermal heat, *Journal of Geophysical Research*, *87*(B2), 1049-1054, doi:10.1029/JB087iB02p01049.

144. Hayashi, K., and H. Abé (1983), Opening of a fault and resulting slip due to injection of fluid for the extraction of geothermal heat: 2. Further details, *Journal of Geophysical Research*, *88*(B10), 8299-8304, doi:10.1029/JB088iB10p08299.

145. Hayashi, S., N. Yamashita, and M. Fukushima (2005), A combined smoothing and regularization method for monotone second-order cone complementarity problems, *SIAM Journal on Optimization*, *15*(2), 593-615, doi:10.1137/S1052623403421516.

146. Hazzard, J. F., R. P. Young, and S. J. Oates (2002), Numerical modeling of seismicity induced by fluid injection in a fractured reservoir, paper presented at the 5th North American Rock Mechanics Symposium, Toronto, Canada.

147. He, C., Z. Wang, and W. Yao (2007), Frictional sliding of gabbro gouge under hydrothermal conditions, *Tectonophysics*, *445*(3–4), 353-362, doi:10.1016/j.tecto.2007.09.008.

148. Healy, J. H., W. W. Rubey, D. T. Griggs, and C. B. Raleigh (1968), The Denver Earthquakes, *Science*, *161*, 1301-1310, doi:10.1126/science.161.3848.1301.

149. Heath, M. J. (1985), Geological control of fracture permeability in the Carnmenellis granite, Cornwall: implications for radionuclide migration, *Mineralogical Magazine*, *49*(351), 233-244.

150. Hettkamp, T., J. Baumgärtner, R. Baria, A. Gérard, T. Gandy, S. Michelet, and D. Teza (2004), Electricity production from hot rocks, paper presented at the Twenty-Ninth Workshop on Geothermal Reservoir Engineering, Stanford University, <http://www.geothermal-energy.org/pdf/IGAstandard/SGW/2004/Hettkamp.pdf>.

151. Heuze, F. E., R. J. Shaffer, A. R. Ingraffea, and R. H. Nilson (1990), Propagation of fluid-driven fractures in jointed rock. Part 1—development and validation of methods of analysis, *International Journal of Rock Mechanics and Mining Sciences & Geomechanics Abstracts*, *27*(4), 243-254, doi:10.1016/0148-9062(90)90527-9.

152. Hicks, T. W., R. J. Pine, J. Willis-Richards, S. Xu, A. J. Jupe, and N. E. V. Rodrigues (1996), A hydro-thermo-mechanical numerical model for HDR geothermal reservoir evaluation, *International Journal of Rock Mechanics and Mining Sciences & Geomechanics Abstracts*, *33*(5), 499-511, doi:10.1016/0148-9062(96)00002-2.

153. Hill, D. P., and S. G. Prejean (2007), 4.09 - Dynamic triggering, in *Treatise on Geophysics*, edited by S. Gerald, pp. 257-291, Elsevier, Amsterdam.

154. Hillel, D. (1971), *Soil and Water; Physical Principles and Processes*, Academic Press, New York.

155. Hillers, G., Y. Ben-Zion, and P. M. Mai (2006), Seismicity on a fault controlled by rate- and state-dependent friction with spatial variations of the critical slip distance, *Journal of Geophysical Research*, *111*(B1), doi:10.1029/2005JB003859.

156. Hirschmann, G., J. Duyster, U. Harms, A. Kontny, M. Lapp, H. d. Wall, and G. Zulauf (1997), The KTB superdeep borehole: petrography and structure of a 9-km-deep crustal section, *Geologische Rundschau*, *86*(0), S3-S14.

157. Holland, A. (2011), Examination of possibly induced seismicity from hydraulic fracturing in the Eola Field, Garvin County, Oklahoma. Oklahoma Geological Survey, <http://www.eenews.net/assets/2011/11/02/document_pm_01.pdf>.

158. Holmgren, M. (2007), XSteam: water and steam properties according to IAPWS IF-97. <www.x-eng.com>.

159. Horne, R. N. (1995), *Modern Well Test Analysis: a Computer-Aided Approach*, 2nd ed., Petroway, Inc., Palo Alto, CA.

160. Hossain, M. M., M. K. Rahman, and S. S. Rahman (2002), A shear dilation stimulation model for production enhancement from naturally fractured reservoirs, *SPE Journal*, *7*(2), doi:10.2118/78355-PA.

161. Howarth, R., R. Santoro, and A. Ingraffea (2011), Methane and the greenhouse-gas footprint of natural gas from shale formations, *Climatic Change*, *106*(4), 679-690, doi:10.1007/s10584-011-0061-5.

162. Hsieh, P. A., and J. D. Bredehoeft (1981), A reservoir analysis of the Denver earthquakes: a case of induced seismicity, *Journal of Geophysical Research*, *86*(B2), 903-920, doi:10.1029/JB086iB02p00903.

163. Hunt, S. P., and C. Morelli (2006), Cooper Basin HDR hazard evaluation: predictive modeling of local stress changes due to HFR geothermal energy operations in South Australia. South Australia Department of Primary, Industries and Resources, <http://www.iea-gia.org/documents/InducedSeismicityReportSHuntDraftOctober2006Malvazos4Jan07.pdf>.

164. Ito, H. (2003), Inferred role of natural fractures, veins, and breccias in development of the artificial geothermal reservoir at the Ogachi Hot Dry Rock site, Japan, *Journal of Geophysical Research*, *108*(B9), doi:10.1029/2001JB001671.

165. Ito, H., and H. Kaieda (2002), Review of 15 years experience of the Ogachi Hot Dry Rock Project with emphasis on geological features, paper presented at the 24th New Zealand Geothermal Workshop, <http://www.geothermal-energy.org/pdf/IGAstandard/NZGW/2002/Ito.pdf?>.

166. Ito, T., and K. Hayashi (2003), Role of stress-controlled flow pathways in HDR geothermal reservoirs, *Pure and Applied Geophysics*, *160*(5), 1103-1124, doi:10.1007/PL00012563.

167. Jaeger, J. C., N. G. W. Cook, and R. W. Zimmerman (2007), *Fundamentals of Rock Mechanics*, 4th ed., Blackwell Pub., Malden, MA.

168. Jeffrey, R., Wu, B., Zhang, X. (2012), The effect of thermoelastic stress change in the near wellbore region on hydraulic fracture growth, paper presented at the Thirty-Seventh Workshop on Geothermal Reservoir Engineering, Stanford University, <https://pangea.stanford.edu/ERE/db/IGAstandard/record_detail.php?id=8287>.

169. Jeffrey, R., A. Bunger, B. Lecampion, X. Zhang, Z. Chen, A. van As, D. Allison, W. De Beer, J. Dudley, E. Siebrits, M. Thiercelin, and M. Mainguy (2009), Measuring hydraulic fracture growth in naturally fractured rock, SPE 124919, paper presented at the SPE Annual Technical Conference and Exhibition, New Orleans, Louisiana, doi:10.2118/124919-MS.

170. Jeffrey, R., X. Zhang, and M. Thiercelin (2009), Hydraulic fracture offsetting in naturally fractured reservoirs: quantifying a long-recognized process, SPE 119351, paper presented at the SPE Hydraulic Fracturing Technology Conference, The Woodlands, Texas, doi:10.2118/119351-MS.

171. Jing, L. (2003), A review of techniques, advances and outstanding issues in numerical modelling for rock mechanics and rock engineering, *International Journal of Rock Mechanics and Mining Sciences*, *40*(3), 283-353, doi:10.1016/S1365-1609(03)00013-3.

172. Jing, Z., J. Willis-Richards, K. Watanabe, and T. Hashida (2000), A three-dimensional stochastic rock mechanics model of engineered geothermal systems in fractured crystalline rock, *Journal of Geophysical Research*, *105*(B10), 23663-23679, doi:10.1029/2000JB900202.

173. Jung, R. (1992), Hydraulic fracturing and hydraulic testing in the granitic section of borehole GPK1, Soultz-sous-Forêts, in *Geothermal Energy in Europe: the Soultz Hot Dry Rock Project*, edited by J. C. Bresee, p. 309, Gordon and Breach Science Publishers, Montreux, Switzerland; Philadelphia, USA.

174. Jung, R., M. Schindler, P. Nami, and T. Tischner (2010), Determination of flow exits in the Soultz borehole GPK2 by using the brine displacement method, *Comptes Rendus Geoscience*, *342*(7–8), 636-643, doi:10.1016/j.crte.2009.06.002.

175. Jung, R., and R. Weidler (2000), A Conceptual Model for the Stimulation Process of the HDR System at Soultz, *Transactions Geothermal Resources Council*, *24*, 143-147.

176. Jupe, A. J., A. S. P. Green, and T. Wallroth (1992), Induced microseismicity and reservoir growth at the Fjällbacka hot dry rocks project, Sweden, *International Journal of Rock Mechanics and Mining Sciences & Geomechanics Abstracts*, *29*(4), 343-354, doi:10.1016/0148-9062(92)90511-W.

177. Kaeser, B., A. Kalt, and J. Borel (2007), The crystalline basement drilled at the Basel-1 geothermal site, a preliminary petrological-geochemical study. Institut de Géologie et d'Hydrogéologie, Université de Neuchâtel, Switzerland.

178. Kaieda, H., S. Sasaki, and D. Wyborn (2010), Comparison of characteristics of micro-earthquakes observed during hydraulic stimulation operations in Ogachi, Hijiori, and Cooper Basin HDR projects, paper presented at the World Geothermal Congress, Bali, Indonesia, <http://www.geothermal-energy.org/pdf/IGAstandard/WGC/2010/3157.pdf?>.

179. Kanamori, H., and D. L. Anderson (1975), Theoretical basis of some empirical relations in seismology, *Bulletin of the Seismological Society of America*, *65*(5), 1073-1095.

180. Karimi-Fard, M., L. J. Durlofsky, and K. Aziz (2004), An efficient discrete-fracture model applicable for general-purpose reservoir simulators, *SPE Journal*, *9*(2), doi:10.2118/88812-PA.

181. Kaven, J., S. Hickman, N. Davatzes, and O. Mutlu (2012), Linear complementarity formulation for 3D frictional sliding problems, *Computational Geosciences*, *16*(3), 613-624, doi:10.1007/s10596-011-9272-0.

182. Kazemi, H., M. L.S, K. L. Porterfield, and P. R. Zeman (1976), Numerical simulation of water-oil flow in naturally fractured reservoirs, *Society of Petroleum Engineers Journal*, *16*(6), doi:10.2118/5719-PA.

183. Kelkar, S., K. Lewis, S. Hickman, N. C. Davatzes, D. Moos, and G. Zyvoloski (2012), Modeling coupled thermal-hydrological-mechanical processes during shear stimulation of an EGS well, paper presented at the Thirty-Seventh Workshop on Geothermal Reservoir Engineering, Stanford University, <https://pangea.stanford.edu/ERE/db/IGAstandard/record_detail.php?id=8295>.

184. Keshavarzi, R., and S. Mohammadi (2012), A new approach for numerical modeling of hydraulic fracture propagation in naturally fractured reservoirs, SPE 152509, paper presented at the SPE/EAGE European Unconventional Resources Conference and Exhibition, Vienna, Austria, doi:10.2118/152509-MS.

185. Ketter, A., J. Daniels, J. Heinze, and G. Waters (2006), A field study optimizing completion strategies for fracture initiation in Barnett Shale horizontal wells, SPE 103232, paper presented at the SPE Annual Technical Conference and Exhibition, San Antonio, Texas, USA, doi:10.2118/103232-MS.

186. Khristianovich, S. A., and Y. P. Zheltov (1959), Theoretical principles of hydraulic fracturing of oil strata, paper presented at the Fifth World Petroleum Congress, New York, New York.

187. Kim, J., H. Tchelepi, and R. Juanes (2011), Stability, accuracy, and efficiency of sequential methods for coupled flow and geomechanics, *SPE Journal*, *16*(2), doi:10.2118/119084-PA.

188. King, G. (2010), Thirty years of gas shale fracturing: what have we learned?, SPE 133456, paper presented at the SPE Annual Technical Conference and Exhibition, Florence, Italy, doi:10.2118/133456-MS.

189. King, G. C. P. (2007), 4.08 - Fault interaction, earthquake stress changes, and the evolution of seismicity, in *Treatise on Geophysics*, edited by S. Gerald, pp. 225-255, Elsevier, Amsterdam.

190. Kitano, K., Y. Hori, and H. Kaieda (2000), Outline of the Ogachi HDR project and character of the reservoirs, paper presented at the World Geothermal Congress, Kyushu - Tohoku, Japan, <http://www.geothermal-energy.org/pdf/IGAstandard/WGC/2000/R0435.PDF?>.

191. Kohl, T., K. F. Evans, R. J. Hopkirk, and L. Rybach (1995), Coupled hydraulic, thermal and mechanical considerations for the simulation of Hot Dry Rock reservoirs, *Geothermics*, *24*(3), 345-359, doi:10.1016/0375-6505(95)00013-G.

192. Kohl, T., and T. Mégel (2007), Predictive modeling of reservoir response to hydraulic stimulations at the European EGS site Soultz-sous-Forêts, *International Journal of Rock Mechanics and Mining Sciences*, *44*(8), 1118-1131, doi:10.1016/j.ijrmms.2007.07.022.

193. Kovac, K. M., J. N. Moore, and S. J. Lutz (2005), Geological framework of the East Flank, Coso Geothermal Field: implications for EGS development, paper presented at the Thirtieth Workshop on Geothermal Reservoir Engineering, Stanford University, <http://www.geothermal-energy.org/pdf/IGAstandard/SGW/2005/kovac.pdf?>.

194. Lanyon, G. W., A. S. Batchelor, and P. Ledingham (1993), Results from a Discrete Fracture Network model of a Hot Dry Rock system, paper presented at the Eighteenth Workshop on Geothermal Reservoir Engineering, Stanford University, <https://pangea.stanford.edu/ERE/db/IGAstandard/record_detail.php?id=2245>.

195. Lapusta, N. (2001), Elastodynamic analysis of sliding with rate and state friction, PhD thesis, Harvard University.

196. Last, N. C., and T. R. Harper (1990), Response of fractured rock subject to fluid injection. Part I. Development of a numerical model, *Tectonophysics*, *172*(1–2), 1-31, doi:10.1016/0040-1951(90)90056-E.

197. Lawson, C. L., R. J. Hanson, D. Kincaid, and F. T. Krogh (1979), Basic Linear Algebra Subprograms for FORTRAN usage, *ACM Transactions on Mathematical Software*, *5*(3), 308-323, doi:10.1145/355841.355847.

198. Ledésert, B., R. Hebert, A. Genter, D. Bartier, N. Clauer, and C. Grall (2010), Fractures, hydrothermal alterations and permeability in the Soultz Enhanced Geothermal System, *Comptes Rendus Geoscience*, *342*(7–8), 607-615, doi:10.1016/j.crte.2009.09.011.

199. Lee, H. S., and T. F. Cho (2002), Hydraulic characteristics of rough fractures in linear flow under normal and shear load, *Rock Mechanics and Rock Engineering*, *35*(4), 299-318, doi:10.1007/s00603-002-0028-y.

200. Lee, S. H., and A. Ghassemi (2011), Three-dimensional thermo-poro-mechanical modeling of reservoir stimulation and induced seismicity in geothermal reservoir, paper presented at the Thirty-Sixth Workshop on Geothermal Reservoir Engineering, Stanford University, <https://pangea.stanford.edu/ERE/db/IGAstandard/record_detail.php?id=7261>.

201. Lehman, L. V., and R. F. Shelley (2010), Survey of over 1000 frac stage database with net pressure in the Barnett Shale. Part 1, SPE 138277, paper presented at the SPE Tight Gas Completions Conference, San Antonio, TX, doi:10.2118/138277-MS.

202. Lemonnier, P., and B. Bourbiaux (2010), Simulation of naturally fractured reservoirs. State of the art, *Oil & Gas Science and Technology – Revue de l'Institut Français du Pétrole*, *65*(2), 239-262, doi:10.2516/ogst/2009066.

203. Liu, E. (2005), Effects of fracture aperture and roughness on hydraulic and mechanical properties of rocks: implication of seismic characterization of fractured reservoirs, *Journal of Geophysics and Engineering*, *2*(1), 38-47, doi:10.1088/1742-2132/2/1/006.

204. Lockner, D. (1993), The role of acoustic emission in the study of rock fracture, *International Journal of Rock Mechanics and Mining Sciences & Geomechanics Abstracts*, *30*(7), 883-899, doi:10.1016/0148-9062(93)90041-B.

205. Lockner, D., H. Tanaka, H. Ito, R. Ikeda, K. Omura, and H. Naka (2009), Geometry of the Nojima Fault at Nojima-Hirabayashi, Japan – I. A simple damage structure inferred from borehole core permeability, *Pure and Applied Geophysics*, *166*(10), 1649-1667, doi:10.1007/s00024-009-0515-0.

206. Lockner, D. A., J. D. Byerlee, V. Kuksenko, A. Ponomarev, and A. Sidorin (1991), Quasi-static fault growth and shear fracture energy in granite, *Nature*, *350*(6313), 39-42.

207. Lutz, S. J., S. Hickman, N. Davatzes, E. Zemach, P. Drakos, and A. Robertson-Tait (2010), Rock mechanical testing and petrological analysis in support of well stimulation activities at the Desert Peak Geothermal Field, Nevada, paper presented at the Thirty-Fifth Workshop on Geothermal Reservoir Engineering, Stanford University, <http://www.geothermal-energy.org/pdf/IGAstandard/SGW/2010/lutz.pdf?>.

208. Mahrer, K. D. (1999), A review and perspective on far-field hydraulic fracture geometry studies, *Journal of Petroleum Science and Engineering*, *24*(1), 13-28, doi:10.1016/S0920-4105(99)00020-0.

209. Majer, E., J. Nelson, A. Robertson-Tai, J. Savy, and I. Wong (2011), Protocol for addressing induced seismicity associated with Enhanced Geothermal Systems. <http://www1.eere.energy.gov/geothermal/pdfs/egs-is-protocol-final-draft-20110531.pdf>.

210. Majer, E. L., R. Baria, M. Stark, S. Oates, J. Bommer, B. Smith, and H. Asanuma (2007), Induced seismicity associated with Enhanced Geothermal Systems, *Geothermics*, *36*(3), 185-222, doi:10.1016/j.geothermics.2007.03.003.

211. Marone, C., C. B. Raleigh, and C. H. Scholz (1990), Frictional behavior and constitutive modeling of simulated fault gouge, *Journal of Geophysical Research*, *95*(B5), 7007-7025, doi:10.1029/JB095iB05p07007.

212. Martel, S. J., D. D. Pollard, and P. Segall (1988), Development of simple strike-slip fault zones, Mount Abbot Quadrangle, Sierra Nevada, California, *Geological Society of America Bulletin*, *100*(9), 1451-1465, doi:10.1130/0016-7606(1988)100<1451:DOSSSF>2.3.CO;2.

213. Martin, A., and M. Economides (2010), Best practices for candidate selection, design and evaluation of hydraulic fracture treatments, SPE 135669, paper presented at the SPE Production and Operations Conference and Exhibition, Tunis, Tunisia, doi:10.2118/135669-MS.

214. Matsuki, K., Y. Kimura, K. Sakaguchi, A. Kizaki, and A. A. Giwelli (2010), Effect of shear displacement on the hydraulic conductivity of a fracture, *International Journal of Rock Mechanics and Mining Sciences*, *47*(3), 436-449, doi:10.1016/j.ijrmms.2009.10.002.

215. Mayerhofer, M., E. Lolon, N. Warpinski, C. Cipolla, D. Walser, and C. Rightmire (2010), What Is Stimulated Reservoir Volume?, *SPE Production & Operations*, *25*(1), doi:10.2118/119890-PA.

216. Mazurek, M. (1998), Technical report 93-12: geology of the crystalline basement of northern Switzerland and derivation of geological input data for safety assessment models. National Cooperative for the Disposal of Radioactive Waste, Switzerland, <http://www.nagra.ch/documents/database/dokumente/%24default/Default%20Folder/Publikationen/NTBs%201991-1993/e_ntb93-12.pdf>.

217. McCabe, W. J., B. J. Barry, and M. R. Manning (1983), Radioactive tracers in geothermal underground water flow studies, *Geothermics*, *12*(2–3), 83-110, doi:10.1016/0375-6505(83)90020-2.

218. McClure, M. W., and R. N. Horne (2010a), Discrete fracture modeling of hydraulic stimulation in Enhanced Geothermal Systems, paper presented at the Thirty-Fifth Workshop on Geothermal Reservoir Engineering, Stanford University, <https://pangea.stanford.edu/ERE/db/IGAstandard/record_detail.php?id=5675>.

219. McClure, M. W., and R. N. Horne (2010b), Numerical and analytical modeling of the mechanisms of induced seismicity during fluid injection, *Geothermal Resources Council Transactions*, *34*, 381-396.

220. McClure, M. W., and R. N. Horne (2012), Opening mode stimulation or shear stimulation?, *Geothermal Resources Council Transactions*, *36*, 515-522.

221. McGarr, A. (1976), Seismic moments and volume changes, *Journal of Geophysical Research*, *81*(8), 1487-1494, doi:10.1029/JB081i008p01487.

222. McGarr, A., D. Simpson, and L. Seeber (2002), 40. Case histories of induced and triggered seismicity, in *International Geophysics*, edited by W. H. K. Lee and H. Kanamori, pp. 647-661, Academic Press.

223. Meyer and Associates, I. (2011), Meyer fracturing simulators, ninth edition. <http://www.mfrac.com/documentation.html>.

224. Meyer, B., and L. Bazan (2011), A discrete fracture network model for hydraulically induced fractures: theory, parametric and case studies, SPE 140514, paper presented at the SPE Hydraulic Fracturing Technology Conference, The Woodlands, Texas, USA, doi:10.2118/140514-MS.

225. Michelet, S., and M. N. Toksöz (2007), Fracture mapping in the Soultz-sous-Forêts geothermal field using microearthquake locations, *Journal of Geophysical Research*, *112*(B7), doi:10.1029/2006JB004442.

226. Miller, C., G. Waters, and E. Rylander (2011), Evaluation of production log data from horizontal wells drilled in organic shales, SPE 144326, paper presented at the North American Unconventional Gas Conference and Exhibition, The Woodlands, Texas, USA, doi:10.2118/144326-MS.

227. Miyairi, M., and M. Sorimachi (1996), Characterization of effective fractures by production logging at Hijiori HDR test site, paper presented at the Second Well Logging Symposium of Japan, Chiba, Japan, <www.japexrc.com/ptfd.files/PTF2ndSymp.pdf>.

228. Moeck, I., G. Kwiatek, and G. Zimmermann (2009), Slip tendency analysis, fault reactivation potential and induced seismicity in a deep geothermal reservoir, *Journal of Structural Geology*, *31*(10), 1174-1182, doi:10.1016/j.jsg.2009.06.012.

229. Moniz, E. J., Chair, (2011), The future of natural gas. Massachusetts Institute of Technology, <http://mitei.mit.edu/publications/reports-studies/future-natural-gas>.

230. Moore, P. W., and R. A. Pearson (1989), Production logging results, in *Hot Dry Rock Geothermal Energy: Phase 2B Final Report of the Camborne School of Mines Project*, edited by R. H. Parker, Pergamon Press, Oxford; New York.

231. Moos, D., A. Lacazette, G. Vassilellis, R. Cade, J. Franquet, E. Bourtembourg, and G. Daniel (2011), Predicting shale reservoir response to stimulation: the Mallory 145 multi-well project, SPE 145849-MS, paper presented at the SPE Annual Technical Conference and Exhibition, Denver, Colorado, USA, doi:10.2118/145849-MS.

232. Morris, J. P., and S. C. Blair (2000), Efficient Displacement Discontinuity Method using fast multipole techniques, paper presented at the 4th North American Rock Mechanics Symposium, Seattle, WA, <http://www.osti.gov/energycitations/servlets/purl/791449-ZAgLs5/native/>.

233. Morrow, C. A., and J. D. Byerlee (1989), Experimental studies of compaction and dilatancy during frictional sliding on faults containing gouge, *Journal of Structural Geology*, *11*(7), 815-825, doi:10.1016/0191-8141(89)90100-4.

234. Morrow, C. A., L. Q. Shi, and J. D. Byerlee (1984), Permeability of fault gouge under confining pressure and shear stress, *Journal of Geophysical Research*, *89*(B5), 3193-3200, doi:10.1029/JB089iB05p03193.

235. Mullen, M., J. Pitcher, D. Hinz, M. Everts, D. Dunbar, G. Carlstrom, and G. Brenize (2010), Does the presence of natural fractures have an impact on production? A case study from the Middle Bakken Dolomite, North Dakota, SPE 135319, paper presented at the SPE Annual Technical Conference and Exhibition, Florence, Italy, doi:10.2118/135319-MS.

236. Murphy, H. D., and M. C. Fehler (1986), Hydraulic fracturing of jointed formations, SPE 14088, paper presented at the International Meeting on Petroleum Engineering, Beijing, China, doi:10.2118/14088-MS.

237. Mutlu, O., and D. D. Pollard (2008), On the patterns of wing cracks along an outcrop scale flaw: a numerical modeling approach using complementarity, *Journal of Geophysical Research*, *113*(B6), doi:10.1029/2007JB005284.

238. Nagel, N., I. Gil, M. Sanchez-Nagel, and B. Damjanac (2011), Simulating hydraulic fracturing in real fractured rocks - overcoming the limits of pseudo3d models, SPE 140480, paper presented at the SPE Hydraulic Fracturing Technology Conference, The Woodlands, Texas, USA, doi:10.2118/140480-MS.

239. Nicholson, C., and R. Wesson (1990), Earthquake hazard associated with deep well injection - a report to the U.S. Environmental Protection Agency. U. S. Geological Survey <pubs.usgs.gov/bul/1951/report.pdf>.

240. Nicol, A., R. Carne, M. Gerstenberger, and A. Christophersen (2011), Induced seismicity and its implications for CO2 storage risk, *Energy Procedia*, *4*(0), 3699-3706, doi:10.1016/j.egypro.2011.02.302.

241. Nolte, K. (1979), Determination of fracture parameters from fracturing pressure decline, SPE 8341, paper presented at the SPE Annual Technical Conference and Exhibition, Las Vegas, Nevada, doi:10.2118/8341-MS.

242. Nolte, K. G. (1993), Discussion of examination of a cored hydraulic fracture in a deep gas well, SPE 26302, *SPE Production and Facilities*, *8*(3), 159-164.

243. Nordgren, R. P. (1972), Propagation of a vertical hydraulic fracture, *Society of Petroleum Engineers Journal*, *12*(4), doi:10.2118/3009-PA.

244. Olson, J., and A. Dahi-Taleghani (2009), Modeling simultaneous growth of multiple hydraulic fractures and their interaction with natural fractures, SPE 119739, paper presented at the SPE Hydraulic Fracturing Technology Conference, The Woodlands, Texas, doi:10.2118/119739-MS.

245. Olson, J., and D. D. Pollard (1989), Inferring paleostresses from natural fracture patterns: a new method, *Geology*, *17*(4), 345-348, doi:10.1130/0091-7613(1989)017<0345:IPFNFP>2.3.CO;2.

246. Olson, J. E. (2004), Predicting fracture swarms — the influence of subcritical crack growth and the crack-tip process zone on joint spacing in rock, *Geological Society, London, Special Publications*, *231*(1), 73-88, doi:10.1144/GSL.SP.2004.231.01.05.

247. Oreskes, N., K. Shrader-Frechette, and K. Belitz (1994), Verification, validation, and confirmation of numerical models in the earth sciences, *Science*, *263*(5147), 641-646, doi:10.1126/science.263.5147.641.

248. Palmer, I., Z. Moschovidis, and J. Cameron (2007), Modeling shear failure and stimulation of the Barnett Shale after hydraulic fracturing, SPE 106113, paper presented at the SPE Hydraulic Fracturing Technology Conference, College Station, Texas, U.S.A., doi:10.2118/106113-MS.

249. Papaliangas, T., S. R. Hencher, A. C. Lumsden, and S. Manolopoulou (1993), The effect of frictional fill thickness on the shear strength of rock discontinuities, *International Journal of Rock Mechanics and Mining Sciences & Geomechanics Abstracts*, *30*(2), 81-91, doi:10.1016/0148-9062(93)90702-F.

250. Paul, P., M. Zoback, and P. Hennings (2009), Fluid flow in a fractured reservoir using a geomechanically constrained fault-zone-damage model for reservoir simulation, *SPE Reservoir Evaluation & Engineering*, *12*(4), doi:10.2118/110542-PA.

251. Pearson, R. A., P. W. Moore, C. Harker, and G. W. Lanyon (1989), Logging results, section 1 - proprietary logging results, in *Hot Dry Rock Geothermal Energy: Phase 2B Final Report of the Camborne School of Mines Project*, edited by R. H. Parker, pp. 423-558, Pergamon Press, Oxford; New York.

252. Perkins, T. K., and L. R. Kern (1961), Widths of hydraulic fractures, *Journal of Petroleum Technology*, *13*(9), doi:10.2118/89-PA.

253. Pine, R. J., and A. S. Batchelor (1984), Downward migration of shearing in jointed rock during hydraulic injections, *International Journal of Rock Mechanics and Mining Sciences & Geomechanics Abstracts*, *21*(5), 249-263, doi:10.1016/0148-9062(84)92681-0.

254. Pine, R. J., and P. A. Cundall (1985), Applications of the fluid-rock interaction program (FRIP) to the modelling of hot dry rock geothermal energy systems, paper presented at the International Symposium on Fundamentals of Rock Joints, Bjorkliden, Sweden.

255. Pollard, D. D., P. Segall, and P. T. Delaney (1982), Formation and interpretation of dilatant echelon cracks, *GSA Bulletin*, *93*(12), 1291-1303, doi:10.1130/0016-7606(1982)93<1291:FAIODE>2.0.CO;2.

256. Potyondy, D. O., and P. A. Cundall (2004), A bonded-particle model for rock, *International Journal of Rock Mechanics and Mining Sciences*, *41*(8), 1329-1364, doi:10.1016/j.ijrmms.2004.09.011.

257. Rachez, X., and S. Gentier (2010), 3D-hydromechanical behavior of a stimulated fractured rock mass, paper presented at the World Geothermal Congress, Bali, Indonesia, <http://www.geothermal-energy.org/pdf/IGAstandard/WGC/2010/3152.pdf>.

258. Rahman, M., and M. Rahman (2009), A fully coupled numerical poroelastic model to investigate interaction between induced hydraulic fracture and pre existing natural fracture in a naturally fractured reservoir: potential application in tight gas and geothermal reservoirs, SPE 124269, paper presented at the SPE Annual Technical Conference and Exhibition, New Orleans, Louisiana, doi:10.2118/124269-MS.

259. Rahman, M. K., M. M. Hossain, and S. S. Rahman (2002), A shear-dilation-based model for evaluation of hydraulically stimulated naturally fractured reservoirs, *International Journal for Numerical and Analytical Methods in Geomechanics*, *26*(5), 469-497, doi:10.1002/nag.208.

260. Randall, M. M., G. W. Lanyon, J. Nicolls, and J. Willis-Richards (1990), Evaluation of jointing in the Carnmenellis Granite, Robertson Scientific Publications, paper presented at the Hot Dry Rock: Proceedings Camborne School of Mines International Hot Dry Rock Conference.

261. Ravindran, A. (1972), Algorithm 431: a computer routine for quadratic and linear programming problems [H], *Communications of the ACM*, *15*(9), 818-820, doi:10.1145/361573.1015087.

262. Renshaw, C. E., and D. D. Pollard (1995), An experimentally verified criterion for propagation across unbounded frictional interfaces in brittle, linear elastic materials, *International Journal of Rock Mechanics and Mining Sciences & Geomechanics Abstracts*, *32*(3), 237-249, doi:10.1016/0148-9062(94)00037-4.

263. Rice, J. R. (1992), Chapter 20: fault stress states, pore pressure distributions, and weakness of the San Andreas Fault, *International Geophysics*, *51*, 475-503, doi:10.1016/S0074-6142(08)62835-1.

264. Rice, J. R. (1993), Spatio-temporal complexity of slip on a fault, *Journal of Geophysical Research*, *98*(B6), 9885-9907, doi:10.1029/93JB00191.

265. Richards, H. G., R. H. Parker, A. S. P. Green, R. H. Jones, J. D. M. Nicholls, D. A. C. Nicol, M. M. Randall, S. Richards, R. C. Stewart, and J. Willis-Richards (1994), The performance and characteristics of the experimental Hot Dry Rock geothermal reservoir at Rosemanowes, Cornwall (1985–1988), *Geothermics*, *23*(2), 73-109, doi:10.1016/0375-6505(94)90032-9.

266. Richards, H. G., J. Willis-Richards, and J. Pye (1991), A review of geological investigations associated with the UK Hot Dry Rock programme, Ussher Society, paper presented at the Ussher society. Annual conference.

267. Rierola, M. (2005), Temporal and spatial transients in b-values beneath volcanoes, PhD thesis, Swiss Federal Institute for Technology Zurich.

268. Ritz, E., and D. D. Pollard (2012), Stick, slip, and opening of wavy frictional faults: a numerical approach in two dimensions, *Journal of Geophysical Research*, *117*(B3), doi:10.1029/2011JB008624.

269. Rjasanow, S., and O. Steinbach (2006), *The Fast Solution of Boundary Integral Equations*, 1st ed., Springer, New York.

270. Rogers, S., D. Elmo, R. Dunphy, and D. Bearinger (2010), Understanding hydraulic fracture geometry and interactions in the Horn River Basin through DFN and numerical modeling, SPE 137488, paper presented at the Canadian Unconventional Resources and International Petroleum Conference, Calgary, Alberta, Canada, doi:10.2118/137488-MS.

271. Rooke, D. P., D. J. Cartwright, and Great Britain. Ministry of Defence. Procurement Executive. (1976), *Compendium of Stress Intensity Factors*, H.M.S.O., London.

272. Roussel, N., and M. Sharma (2011), Strategies to minimize frac spacing and stimulate natural fractures in horizontal completions, SPE 146104, paper presented at the SPE Annual Technical Conference and Exhibition, Denver, Colorado, USA, doi:10.2118/146104-MS.

273. Ruina, A. (1983), Slip instability and state variable friction laws, *Journal of Geophysical Research*, *88*(B12), 10359-10370, doi:10.1029/JB088iB12p10359.

274. Rummel, F. (1992), Physical properties of the rock in the granitic section of borehole GPK1, Soultz-sous-Forêts, in *Geothermal Energy in Europe: the Soultz Hot Dry Rock Project*, edited by J. C. Bresee, p. 309, Gordon and Breach Science Publishers, Montreux, Switzerland; Philadelphia, USA.

275. Rutqvist, J., and C. M. Oldenburg (2008), Analysis of injection-induced micro-earthquakes in a geothermal steam reservoir, The Geysers Geothermal Field, California, ARMA 08-151, paper presented at the 42nd U.S. Rock Mechanics Symposium, San Francisco, CA.

276. Safari, M. R., and A. Ghassemi (2011), 3D analysis of huff and puff and injection tests in geothermal reservoirs, paper presented at the Thirty-Sixth Workshop on Geothermal Reservoir Engineering Stanford University, <https://pangea.stanford.edu/ERE/db/IGAstandard/record_detail.php?id=7217>.

277. Sanjuan, B., J.-L. Pinault, P. Rose, A. Gérard, M. Brach, G. Braibant, C. Crouzet, J.-C. Foucher, A. Gautier, and S. Touzelet (2006), Tracer testing of the geothermal heat exchanger at Soultz-sous-Forêts (France) between 2000 and 2005, *Geothermics*, *35*(5–6), 622-653, doi:10.1016/j.geothermics.2006.09.007.

278. Sausse, J., C. Dezayes, A. Genter, and A. Bisset (2008), Characterization of fracture connectivity and fluid flow pathways derived from geological interpretation and 3D modelling of the deep seated EGS reservoir of Soultz (France), paper presented at the Thirty-Third Workshop on Geothermal Reservoir Engineering, Stanford University, <https://pangea.stanford.edu/ERE/db/IGAstandard/record_detail.php?id=5270>.

279. Schultz, R. A. (1988), Stress intensity factors for curved cracks obtained with the Displacement Discontinuity Method, *International Journal of Fracture*, *37*(2), R31-R34, doi:10.1007/BF00041718.

280. Segall, P. (1989), Earthquakes triggered by fluid extraction, *Geology*, *17*(10), 942-946, doi:10.1130/0091-7613(1989)017<0942:ETBFE>2.3.CO;2.

281. Segall, P. (2010), *Earthquake and Volcano Deformation*, Princeton University Press, Princeton, N.J.

282. Segall, P., and D. D. Pollard (1983), Joint formation in granitic rock of the Sierra Nevada, *Geological Society of America Bulletin*, *94*(5), 563-575, doi:10.1130/0016-7606(1983)94<563:JFIGRO>2.0.CO;2.

283. Segall, P., and D. D. Pollard (1983), Nucleation and growth of strike slip faults in granite, *Journal of Geophysical Research*, *88*(B1), 555-568, doi:10.1029/JB088iB01p00555.

284. Segall, P., and J. R. Rice (1995), Dilatancy, compaction, and slip instability of a fluid-infiltrated fault, *Journal of Geophysical Research*, *100*(B11), 22155-22171, doi:10.1029/95JB02403.

285. Segall, P., A. M. Rubin, A. M. Bradley, and J. R. Rice (2010), Dilatant strengthening as a mechanism for slow slip events, *Journal of Geophysical Research*, *115*(B12), doi:10.1029/2010JB007449.

286. Sesetty, V., and A. Ghassemi (2012), Modeling and analysis of stimulation for fracture network generation, paper presented at the Thirty-Seventh Workshop on Geothermal Reservoir Engineering, Stanford University, <https://pangea.stanford.edu/ERE/db/IGAstandard/record_detail.php?id=8356>.

287. Shapiro, S. A., P. Audigane, and J.-J. Royer (1999), Large-scale in situ permeability tensor of rocks from induced microseismicity, *Geophysical Journal International*, *137*(1), 207-213, doi:10.1046/j.1365-246x.1999.00781.x.

288. Shapiro, S. A., and C. Dinske (2009), Fluid-induced seismicity: pressure diffusion and hydraulic fracturing, *Geophysical Prospecting*, *57*(2), 301-310, doi:10.1111/j.1365-2478.2008.00770.x.

289. Shapiro, S. A., C. Dinske, and J. Kummerow (2007), Probability of a given-magnitude earthquake induced by a fluid injection, *Geophysical Research Letters*, *34*(22), doi:10.1029/2007GL031615.

290. Shapiro, S. A., J. Kummerow, C. Dinske, G. Asch, E. Rothert, J. Erzinger, H. J. Kümpel, and R. Kind (2006), Fluid induced seismicity guided by a continental fault: injection experiment of 2004/2005 at the German Deep Drilling Site (KTB), *Geophysical Research Letters*, *33*(1), doi:10.1029/2005GL024659.

291. Shlyapobersky, J. W. (1985), Energy analysis of hydraulic fracturing, ARMA 85-0539-1, paper presented at the 26th U.S. Symposium on Rock Mechanics (USRMS), Rapid City, SD.

292. Shou, K. J., and S. L. Crouch (1995), A higher order Displacement Discontinuity Method for analysis of crack problems, *International Journal of Rock Mechanics and Mining Sciences & Geomechanics Abstracts*, *32*(1), 49-55, doi:10.1016/0148-9062(94)00016-V.

293. Sibson, R. H. (1986), Brecciation processes in fault zones: inferences from earthquake rupturing, *Pure and Applied Geophysics*, *124*(1), 159-175, doi:10.1007/BF00875724.

294. Sibson, R. H. (1990), Conditions for fault-valve behaviour, *Geological Society, London, Special Publications*, *54*(1), 15-28, doi:10.1144/GSL.SP.1990.054.01.02.

295. Smith, M. B., and J. W. Shlyapobersky (2000), Basics of hydraulic fracturing, in *Reservoir Stimulation*, edited by M. J. Economides and K. G. Nolte, pp. 5-1 to 5-28, John Wiley, Chichester, England; New York.

296. Starfield, A. M., and P. A. Cundall (1988), Towards a methodology for rock mechanics modelling, *International Journal of Rock Mechanics and Mining Sciences & Geomechanics Abstracts*, *25*(3), 99-106, doi:10.1016/0148-9062(88)92292-9.

297. Stein, S., and M. Wysession (2002), *An Introduction to Seismology, Earthquakes, and Earth Structure*, Blackwell Science, Malden, MA.

298. Stober, I. (2011), Depth- and pressure-dependent permeability in the upper continental crust: data from the Urach 3 geothermal borehole, southwest Germany, *Hydrogeology Journal*, *19*(3), 685-699, doi:10.1007/s10040-011-0704-7.

299. Suk Min, K., Z. Zhang, and A. Ghassemi (2010), Hydraulic fracturing propagation in heterogeneous rock using the VMIB method, paper presented at the Thirty-Fifth Workshop on Geothermal Reservoir Engineering Stanford University, <https://pangea.stanford.edu/ERE/db/IGAstandard/record_detail.php?id=7229>.

300. Suzuki, K., and H. Kaieda (2000), Geological structure around the Ogachi Hot Dry Rock test site using seismic reflection and CSAMT surveys, paper presented at the World Geothermal Congress Kyushu -- Tohoku, Japan, <http://www.geothermal-energy.org/pdf/IGAstandard/WGC/2000/R0670.PDF?>.

301. Swenson, D., and B. Hardeman (1997), The effects of thermal deformation on flow in a jointed geothermal reservoir, *International Journal of Rock Mechanics and Mining Sciences*, *34*(3–4), 308.e301-308.e320, doi:10.1016/S1365-1609(97)00285-2.

302. Tarasovs, S., and A. Ghassemi (2012), On the role of thermal stress in reservoir stimulation, paper presented at the Thirty-Seventh Workshop on Geothermal Reservoir Engineering Stanford University, <https://pangea.stanford.edu/ERE/db/IGAstandard/record_detail.php?id=8372>.

303. Taron, J., and D. Elsworth (2009), Thermal–hydrologic–mechanical–chemical processes in the evolution of engineered geothermal reservoirs, *International Journal of Rock Mechanics and Mining Sciences*, *46*(5), 855-864, doi:10.1016/j.ijrmms.2009.01.007.

304. Tembe, S., D. A. Lockner, and T.-F. Wong (2010), Effect of clay content and mineralogy on frictional sliding behavior of simulated gouges: binary and ternary mixtures of quartz, illite, and montmorillonite, *Journal of Geophysical Research*, *115*(B3), doi:10.1029/2009JB006383.

305. Tester, J., ed. (2007), The future of geothermal energy: impact of Enhanced Geothermal Systems (EGS) on the United States in the 21st century. Massachusetts Institute of Technology, <http://geothermal.inel.gov/publications/future_of_geothermal_energy.pdf>.

306. Teufel, L. W., and J. A. Clark (1984), Hydraulic fracture propagation in layered rock: experimental studies of fracture containment, *SPE Journal*, *24*(1), 19-32, doi:10.2118/9878-PA.

307. Tezuka, K., and H. Niitsuma (2000), Stress estimated using microseismic clusters and its relationship to the fracture system of the Hijiori hot dry rock reservoir, *Engineering Geology*, *56*(1–2), 47-62, doi:10.1016/S0013-7952(99)00133-7.

308. Tezuka, K., T. Tamagawa, and K. Watanabe (2005), Numerical simulation of hydraulic shearing in fractured reservoir, paper presented at the World Geothermal Congress, Antalya, Turkey, <https://pangea.stanford.edu/ERE/db/IGAstandard/record_detail.php?id=1000>.

309. Tischner, T., M. Pfender, and D. Teza (2006), Hot Dry Rock projekt Soultz: erste phase der erstellung einer wissenschaftlichen pilotanlage: Final project report. Bundesanstalt für Geowissenschaften und Rohstoffe (BGR), <http://www.bgr.bund.de/DE/Themen/Energie/Downloads/soultz_abschlussbericht.pdf?__blob=publicationFile& v=2>.

310. Utsu, T. (2002), 43. Statistical features of seismicity, in *International Geophysics*, edited by W. H. K. Lee and H. Kanamori, pp. 719-732, Academic Press.

311. Valley, B., and K. Evans (2007), Stress state at Soultz-sous-Forêts to 5 km depth from wellbore failure and hydraulic observations, paper presented at the Thirty-Second Workshop on Geothermal Reservoir Engineering, Stanford University, <http://www.geothermal-energy.org/pdf/IGAstandard/SGW/2007/valley.pdf>.

312. Vassilellis, G., V. Bust, C. Li, R. Cade, and D. Moos (2011), Shale engineering application: the MAL-145 project in West Virginia, SPE 146912, paper presented at the Canadian Unconventional Resources Conference, Alberta, Canada, doi:10.2118/146912-MS.

313. Vörös, R., and S. Baisch (2009), Deep heat mining Basel -- seismic risk analysis: AP 4000, triggered seismicity. Q-Con Report, <http://www.wsu.bs.ch/geothermie.htm>.

314. Wallroth, T., T. Eliasson, and U. Sundquist (1999), Hot dry rock research experiments at Fjällbacka, Sweden, *Geothermics*, *28*(4–5), 617-625, doi:10.1016/S0375-6505(99)00032-2.

315. Wang, X., and A. Ghassemi (2012), A 3D thermal-poroelastic model for geothermal reservoir stimulation, paper presented at the Thirty-Seventh Workshop on Geothermal Reservoir Engineering, Stanford University, <https://pangea.stanford.edu/ERE/db/IGAstandard/record_detail.php?id=8382>.

316. Warpinski, N., R. Kramm, J. Heinze, and C. Waltman (2005), Comparison of single- and dual-array microseismic mapping techniques in the Barnett Shale, SPE 95568, paper presented at the SPE Annual Technical Conference and Exhibition, Dallas, Texas, doi:10.2118/95568-MS.

317. Warpinski, N. R., J. C. Lorenz, P. T. Branagan, F. R. Myal, and B. L. Gall (1993), Examination of a cored hydraulic fracture in a deep gas well, SPE 22876, *SPE Production & Facilities*, *8*(3), doi:10.2118/22876-PA.

318. Warpinski, N. R., M. J. Mayerhofer, M. C. Vincent, C. L. Cipolla, and E. P. Lolon (2009), Stimulating unconventional reservoirs: maximizing network growth while optimizing fracture conductivity, *Journal of Canadian Petroleum Technology*, *48*(10), doi:10.2118/114173-PA.

319. Warpinski, N. R., W. S.L, and C. A. Wright (2001), Analysis and prediction of microseismicity induced by hydraulic fracturing, SPE 71649, paper presented at the SPE Annual Technical Conference and Exhibition, New Orleans, Louisiana, doi:10.2118/71649-MS.

320. Warpinski, N. R., R. A. Schmidt, and D. A. Northrop (1982), In-situ stresses: the predominant influence on hydraulic fracture containment, *Journal of Petroleum Technology*, *34*(3), 653-664, doi:10.2118/8932-PA.

321. Warpinski, N. R., and L. W. Teufel (1987), Influence of geologic discontinuities on hydraulic fracture propagation, *Journal of Petroleum Technology*, *39*(2), doi:10.2118/13224-PA.

322. Warren, J. E., and P. J. Root (1963), The behavior of naturally fractured reservoirs, *Society of Petroleum Engineers Journal*, *3*(3), doi:10.2118/426-PA.

323. Weidler, R. (2000), Hydraulic stimulation of the 5 km deep well GPK-2. Bureau de recherches géologiques et minières (BRGM).

324. Weidler, R., A. Gerard, A. Baria, J. Baumgärtner, and R. Jung (2002), Hydraulic and micro-seismic results of a massive stimulation test at the 5 km depth at the European Hot-Dry Rock test site Soultz, France, paper presented at the Twenty-Seventh Workshop on Geothermal Reservoir Engineering, Stanford University, <https://pangea.stanford.edu/ERE/db/IGAstandard/record_detail.php?id=62>.

325. Weng, X., O. Kresse, C.-E. Cohen, R. Wu, and H. Gu (2011), Modeling of hydraulic-fracture-network propagation in a naturally fractured formation, *SPE Production & Operations*, *26*(4), doi:10.2118/140253-PA.

326. Wesnousky, S. G. (2006), Predicting the endpoints of earthquake ruptures, *Nature*, *444*(7117), 358-360, doi:10.1038/nature05275.

327. Whittle, R. (1989), The granites of South West England, Section 2 -- jointing in the Carnmenellis Granite, in *Hot Dry Rock Geothermal Energy: Phase 2B Final Report of the Camborne School of Mines Project*, edited by R. H. Parker, pp. 119-182, Pergamon Press, Oxford; New York.

328. Whittle, R., and R. A. McCartney (1989), The granites of South West England, Section 1 -- lithology, minerology and structure, in *Hot Dry Rock Geothermal Energy: Phase 2B Final Report of the Camborne School of Mines Project*, edited by R. H. Parker, pp. 41-118, Pergamon Press, Oxford; New York.

329. Wibberley, C. A. J., G. Yielding, and G. D. Toro (2008), Recent advances in the understanding of fault zone internal structure: a review, *Geological Society, London, Special Publications*, *299*(1), 5-33, doi:10.1144/SP299.2.

330. Willis-Richards, J., K. Watanabe, and H. Takahashi (1996), Progress toward a stochastic rock mechanics model of engineered geothermal systems, *Journal of Geophysical Research*, *101*(B8), 17481-17496, doi:10.1029/96JB00882.

331. Wu, R., O. Kresse, X. Weng, C. Cohen, and H. Gu (2012), Modeling of interaction of hydraulic fractures in complex fracture networks, paper presented at the SPE Hydraulic Fracturing Technology Conference, The Woodlands, Texas, USA, doi:10.2118/152052-MS.

332. Wyborn, D., L. de Graaf, S. Davidson, and S. Hann (2005), Development of Australia's first Hot Fractured Rock (HFR) underground heat exchanger, Cooper Basin, South Australia, paper presented at the World Geothermal Congress, Antalya, Turkey, <https://pangea.stanford.edu/ERE/db/IGAstandard/record_detail.php?id=1473>.

333. Xu, W., M. Thiercelin, U. Ganguly, X. Weng, H. Gu, H. Onda, j. sun, and J. Le Calvez (2010), Wiremesh: a novel shale fracturing simulator, SPE 132218, paper presented at the International Oil and Gas Conference and Exhibition, Beijing, China, doi:10.2118/132218-MS.

334. Yamamoto, T., K. Kitano, Y. Fujimitsu, and H. Ohnishi (1997), Application of simulation code, GEOTH3D, on the Ogachi HDR site, paper presented at the 22nd Annual Workshop on Geothermal Reservoir Engineering, Stanford University, <https://pangea.stanford.edu/ERE/db/IGAstandard/record_detail.php?id=463>.

335. Yamashita, T. (1999), Pore creation due to fault slip in a fluid-permeated fault zone and its effect on seismicity: generation mechanism of earthquake swarm, *Pure and Applied Geophysics*, *155*(2), 625-647, doi:10.1007/s000240050280.

336. Yeo, I. W., M. H. de Freitas, and R. W. Zimmerman (1998), Effect of shear displacement on the aperture and permeability of a rock fracture, *International Journal of Rock Mechanics and Mining Sciences*, *35*(8), 1051-1070, doi:10.1016/S0148-9062(98)00165-X.

337. Zhai, Z., and M. Sharma (2005), A new approach to modeling hydraulic fractures in unconsolidated sands, SPE 96246, paper presented at the SPE Annual Technical Conference and Exhibition, Dallas, Texas, doi:10.2118/96246-MS.

338. Zhang, X., and R. G. Jeffrey (2006), The role of friction and secondary flaws on deflection and re-initiation of hydraulic fractures at orthogonal pre-existing fractures, *Geophysical Journal International*, *166*(3), 1454-1465, doi:10.1111/j.1365-246X.2006.03062.x.

339. Zhao, X., and R. P. Young (2011), Numerical modeling of seismicity induced by fluid injection in naturally fractured reservoirs, *Geophysics*, *76*(6), WC167-WC180, doi:10.1190/geo2011-0025.1.

340. Zhou, J., M. Chen, Y. Jin, and G.-q. Zhang (2008), Analysis of fracture propagation behavior and fracture geometry using a tri-axial fracturing system in naturally fractured reservoirs, *International Journal of Rock Mechanics and Mining Sciences*, *45*(7), 1143-1152, doi:10.1016/j.ijrmms.2008.01.001.

341. Zhou, X., and A. Ghassemi (2011), Three-dimensional poroelastic analysis of a pressurized natural fracture, *International Journal of Rock Mechanics and Mining Sciences*, *48*(4), 527-534, doi:10.1016/j.ijrmms.2011.02.002.

342. Zimmermann, G., A. Reinicke, W. Brandt, G. Blöcher, H. Milsch, H.-G. Holl, I. Moeck, T. Schulte, A. Saadat, and E. Huenges (2008), Results of stimulation treatments at the geothermal research wells in Groβ Schönebeck/Germany, paper presented at the Thirty-Third Workshop on Geothermal Reservoir Engineering, Stanford University, <http://www.geothermal-energy.org/pdf/IGAstandard/SGW/2008/zimmerma.pdf?>.

343. Zoback, M., A. Kohli, I. Das, and M. McClure (2012), The importance of slow slip on faults during hydraulic fracturing stimulation of shale gas reservoirs, SPE 155476, paper presented at the SPE Americas Unconventional Resources Conference, Pittsburgh, Pennsylvania USA, doi:10.2118/155476-MS.

344. Zoback, M. D. (2007), *Reservoir Geomechanics*, Cambridge University Press, Cambridge.

345. Zoback, M. D., and S. M. Gorelick (2012), Earthquake triggering and large-scale geologic storage of carbon dioxide, *Proceedings of the National Academy of Sciences*, *109*(26), 10164-10168, doi:10.1073/pnas.1202473109.

346. Zoback, M. D., and H.-P. Harjes (1997), Injection-induced earthquakes and crustal stress at 9 km depth at the KTB deep drilling site, Germany, *Journal of Geophysical Research*, *102*(B8), 18477-18491, doi:10.1029/96JB02814.

347. Zoback, M. D., F. Rummel, R. Jung, and C. B. Raleigh (1977), Laboratory hydraulic fracturing experiments in intact and pre-fractured rock, *International Journal of Rock Mechanics and Mining Sciences & Geomechanics Abstracts*, *14*(2), 49-58, doi:10.1016/0148-9062(77)90196-6.

348. Zulauf, G. (1992), Late to post-Variscan deformation phases and palaeostresses in the KTB pilot research well (Bohemian Massif, Germany), *Tectonophysics*, *202*(1), 1-21, doi:10.1016/0040-1951(92)90452-C.

349. Zulauf, G., G. Kleinschmidt, and O. Oncken (1990), Brittle deformation and graphitic cataclasites in the pilot research well KTB-VB (Oberpfalz, FRG), *Geological Society, London, Special Publications*, *54*(1), 97-103, doi:10.1144/GSL.SP.1990.054.01.10.

List of Variables

Table 7-1: List of variables.

A	Fracture surface area, m^2
a	Element half-length, m
a_{const}	Element half-length for initial discretization, m
a_{frac}	Fracture half-length, m
a_{min}	Minimum element half-length, m
a_{rs}	Rate-state friction, coefficient for velocity term, unitless
$B_{E,\sigma},\ B_{D,\sigma},$ $B_{E,\tau},\ B_{D,,\tau}$	Matrices of interaction coefficients, MPa/mm
b	Rate-state friction, coefficient for state term, unitless
b_t	Thickness of a layer or fracture, mm
c_t	Total compressibility, MPa^{-1}
D	Cumulative shear displacement discontinuity, mm
D_{cum}	Cumulative rapid slip during a seismic event, mm
$D_{E,eff},\ D_{e,eff}$	Effective cumulative displacement discontinuity (used in Chapters 2 and 3), mm

$D_{e,eff,max},$ $D_{E,eff,max}$	*Maximum effective cumulative sliding displacement used for calculating aperture in Chapters 2 and 3 (mm)*
D_{emax}	*Maximum hydraulic aperture displacement (used in Chapter 4), mm*
D_{Emax}	*Maximum void aperture displacement (used in Chapter 4), mm*
D_1	*Cumulative shear displacement discontinuity variable used for calculation of aperture in Chapter 4, mm*
D_2	*Cumulative shear displacement discontinuity variable used for calculation of aperture in Chapter 4, mm*
d_c	*Rate-state friction, characteristic weakening distance, m*
dt	*Duration of a time step, s*
dX	*Update to vector of unknowns, various units*
E	*Void aperture, mm*
E_0	*Reference void aperture, mm*
$E_{hfresid}$	*Residual closed aperture, mm*
E_{open}	*Open aperture, physical separation between walls, mm*
E_{res}	*Residual void aperture, mm*
e	*Hydraulic aperture, mm*
e_0	*Reference hydraulic aperture, mm*
e_{hmat}	*Relative error for h-matrix approximation, unitless*
e_j	*Relative difference between simulations, defined in a variety of ways*
e_{proc}	*Process zone hydraulic aperture, mm*
e_{res}	*Residual hydraulic aperture, mm*
f_0	*Rate and state friction term, unitless*
G	*Shear modulus, GPa*

G_{adj}	Olson (2004) adjustment factor to interaction coefficients, unitless
g	Gravitational constant, ~9.8 m/s^2
h	Out of plane fracture width, or height, m
I	Unit matrix, unitless
$itertol$	Convergence tolerance for iterative coupling, MPa
J	Iteration matrix formed as an incomplete Jacobian matrix, various forms
$J_{mech,thresh}$	Threshold parameter for including mechanical interaction terms in the iteration matrix, unitless
K_I	Stress intensity factor, MPa-m$^{1/2}$
K_{Ic}	Critical stress intensity factor, MPa-m$^{1/2}$
$K_{I,crithf}$	Critical stress intensity factor for propagation of a new fracture, MPa-m$^{1/2}$
$K_{I,crit}$	Critical stress intensity factor for propagation of opening on a preexisting fracture, MPa-m$^{1/2}$
K_{frac}	Fracture stiffness, MPa^{-1}
K_{hf}	Stiffness of closed, newly formed fractures, MPa^{-1}
k	Permeability, m^2
k_H	Horizontal permeability, m^2
k_V	Vertical permeability, m^2
l	Increment of length along a fracture, m
l_c, l_o, l_s, l_f	Parameters used for discretization refinement, m, unitless, unitless, and unitless
M_0	Seismic moment, N-m
M_w	Moment magnitude, unitless
m	Mass of fluid in a discretization element, kg

mechtol	Convergence tolerance for the shear stress residual equations, MPa
opentol	Tolerance for including elements with adaptive domain adjustment, MPa
P	Pressure, MPa
P_{init}	Initial formation fluid pressure (MPa)
P_{inj}	Injection pressure, MPa
P_{inj}'	Injection Pressure Derivative, MPa/s
p_D	Dimensionless pressure, unitless
$P_{prodmin}$	Minimum production pressure, MPa
P_{injmax}	Maximum injection pressure, MPa
Q	Calculated injection rate, kg/s
q	Mass flow rate, kg/s
q_{flux}	Mass flux, $kg/(s\text{-}m^2)$
q_{injmax}	Maximum injection rate, kg/s
$q_{prodmax}$	Maximum production rate, kg/s
R	Residual equation, various units
r	Fracture radius, m
r_{inv}	Radius of investigation, m
r_w	Wellbore radius, m
r_{weff}	Effective wellbore radius, m
S	Specified total injection rate, kg/s
S_0	Cohesion, MPa
Su	Storativity, unitless

$S_{0,open}$	Cohesion term for open elements, MPa
s	Wellbore skin, unitless
s_a	Mass source term per area, $kg/(s\text{-}m^2)$
s_m	Mass source term, kg/s
s_θ	Geometric wellbore skin, unitless
$slidetol$	Tolerance for including elements with adaptive domain adjustment, MPa
T	Transmissivity, m^3
$T_{hf,fac}$	Factor for calculating residual transmissivity of newly formed fractures, m^2
T_{inj}	Injection temperature, °C
T_{init}	Initial temperature, °C
T_g	Geometric transmissibility between elements, m^3
T_s	Stress tensor, MPa
t	Time, s
t_D	Dimensionless time, unitless
v	Sliding velocity, m/s
v_0	Rate-state friction, reference velocity, m/s
v_s	Shear wave velocity, m/s
X	Vector of unknowns, various forms
x	Dummy variable to specify an arbitrary direction, m
α	Hydraulic diffusivity, m^2/s
$\Delta D, \Delta E$	Change in displacement discontinuity during a time step, mm
$\Delta\sigma_{k,strainadj}$	Stress applied during high strain penalty method, MPa

$\Delta\sigma$	Stress drop during an earthquake, MPa
ΔP	Difference between injection pressure and initial pressure, MPa
δ	Parameter used in adaptive time stepping, sum of absolute value of change in shear stress and effective normal stress, MPa
$\delta_{strainadj}$	The largest value of $\Delta\sigma_{k,strainadj}$ during a time step, MPa
ε	Strain tensor, unitless
ε_k	Displacement discontinuity strain, used for high strain penalty method, unitless
$\varepsilon_{k,lim}$	Limit to displacement discontinuity strain, unitless
ε_{tol}	User specified relative tolerance for h-matrix assembly, unitless
η	Radiation damping coefficient, MPa/(m/s)
η_{targ}	Target change in stress change parameter for adaptive time stepping, MPa
$\eta_{targ,strainadj}$	Target change in ε_k for time stepping, unitless
θ	Rate-state friction, state variable, s
$\theta_w{}'$	Factor used for calculation of geometric wellbore skin, unitless
μ_d	Dynamic coefficient of friction, unitless
μ_f	Coefficient of friction, unitless
μ_l	Fluid viscosity, Pa-s
μ_s	Static coefficient of friction from S/D friction, unitless
ρ	Density, kg/m^3
π	Mathematical constant Pi, unitless
σ_3	Minimum principal stress, MPa
σ_{hmin}	Minimum horizontal principal stress, MPa
$\sigma_n{}'$	Effective normal stress, MPa

σ_n	Normal stress, MPa
$\sigma_{n,Eref}$, $\sigma_{n,eref}$	Reference fracture stiffness, mm
σ_v	Vertical principal stress, MPa
$\sigma_{yy}{}^r$	Remote compressive stress in the y direction, MPa
$\sigma_{xy}{}^r$	Remote shear stress, MPa
$\sigma_{xx}{}^r$	Remote compressive stress in the x direction, MPa
τ	Shear stress, MPa
υ_p	Poisson's ratio, unitless
$\varphi_{E,dil}$, $\varphi_{e,dil}$	Aperture dilation angle, °